Pharmaceutical Impact of the Different Ionization States of a Weakly Basic Drug within a Living Organism

by

Mikhail D. Murashov

A dissertation submitted in partial fulfillment
of the requirements for the degree of
Doctor of Philosophy
(Pharmaceutical Sciences)
In The University of Michigan
2019

Doctoral Committee:

Professor Gustavo R. Rosania, Chair
Professor James J. Moon
Professor Anna Schwendeman
Professor Kathleen A. Stringer
Professor Duxin Sun

Mikhail D. Murashov

murashov@umich.edu

ORCID iD: 0000-0001-6300-6109

Be Like a Doctor, Have Some Patience!

Acknowledgements

First, I would like to thank my advisor, Dr. Gus Rosania, for his mentorship throughout my Ph.D. experience. He always kept me on my toes and helped me to succeed at everything I had put my hands on. He helped me to become a better scientist, writer, and an independent thinker, whose ideas can make a positive and influential difference in the world.

Next, I would like to thank my committee members, Dr. Kathleen A. Stringer, Dr. James J. Moon, Dr. Anna Schwendeman, and Dr. Duxin Sun for their support, guidance, insightful comments, and suggestions throughout my dissertation work.

I would also like to thank all members of the Dr. Rosania lab who helped me with my experiment methodology development and data analysis throughout my dissertation work: Vernon LaLone, Jennifer Diaz-Espinosa, Phil Rzeczycki, Tehetina Woldemichael, Gi Yoon, Rahul Keswani, and Sudha Sud.

Finally, I would like to thank my family for their support and belief in me throughout this whole journey. Special appreciation goes to my mom, Elvira, and my beautiful wife, Gabrielle. I thank my mom for sacrificing everything, sending me to the US on my own when I was only 15, and giving me this opportunity to achieve my educational and career goals. I thank my beautiful wife for the unconditional support, belief, and putting up with me throughout my undergraduate and graduate school experience. I owe everything to them, and without them, I would have never become the man I am today.

Table of Contents

List of Figures

List of Tables

List of Appendices

Abstract

Clofazimine (CFZ), an oral FDA-approved antibiotic for over 40 years, has been used effectively against leprosy and multi-drug resistant tuberculosis (MDR-TB). Due to its atypical pharmacokinetic parameters, orally administered CFZ free base is associated with extensive intracellular bioaccumulation of the solid drug, primarily in tissue macrophages, in a form of crystal-like drug inclusions (CLDIs) that chemically and structurally resemble CFZ hydrochloride salt (CFZ-HCl) crystals. These biocrystals are biocompatible, stable, long-lived, relatively non-toxic, and have anti-inflammatory properties.

In this dissertation, I hypothesized that CFZ-HCl is a more therapeutically efficacious form of CFZ compared to CFZ free base that could be potentially used in the repurposing CFZ for other indications. To test this hypothesis, first, I established the physicochemical parameters of CFZ (e.g. $pH_{max,}$ apparent pK_a, CFZ-HCl aqueous solubility, CFZ free base intrinsic solubility, K_{sp}, etc.) that allowed me to understand the different ionization states of CFZ and their relationship to the drug's physicochemical, pharmacokinetic, and pharmacodynamic properties. In fact, these physicochemical parameters explained the thermodynamic mechanism of differential stabilization and accumulation of the HCl salt form of CFZ in macrophage lysosomes. Based on this mechanism, I developed a specific buffer system that mimics the macrophage intralysosomal microenvironment, which ultimately helped me to determine that CFZ free base is associated with the major side effect from CFZ treatment, drug-induced skin pigmentation, that results from its partitioning into subcutaneous fat layer of the skin.

Next, I developed a biomimetic formulation of CFZ drug biocrystals, micronized CFZ-HCl salt crystals, and investigated its stability in macrophages *in vitro* and *in vivo*. As a result, I determined that macrophages internalize and stabilize CFZ-HCl microcrystals, just as well as CLDIs, without any detectable toxicological effects. Furthermore, no skin pigmentation was observed when an equivalent total amount of CFZ-HCl to the total oral dose that causes maximal skin pigmentation was administered. Thus, parenteral biomimetic formulations of CFZ-HCl could be instrumental in avoiding the pigmentation side effect of oral CFZ therapy.

Finally, I explored the inflammatory status and efficacy of my formulation of CFZ-HCl salt microcrystals in gouty arthritis under local administration *in vivo*, utilizing an FDA-recognized rat model. As a result, local injection of CFZ-HCl microcrystals led to the recruitment of macrophages to the site of action, a pro-inflammatory response, and did not facilitate the dissolution and clearance of monosodium urate (MSU) crystals from the joint, the main source of inflammation, by lowering the local pH of the synovium. Even though the results of this study suggested that my formulation is not suitable for gouty arthritis, further investigation is required to determine efficacy and anti-inflammatory action of my formulation in MDR-TB and other potential new indications.

Overall, this dissertation augments the understanding of drug distribution and mechanism of action by effectively demonstrating how it is possible to distinguish the differential contribution of different ionization states of a drug (e.g. CFZ) to the drug's efficacy and toxicity properties. Furthermore, this dissertation has advanced the rational design of formulations, in terms of being the first to develop a biomimetic form of a small molecule drug and demonstrating how the role of macrophages in determining the stability of biomimetic formulations can be probed.

Chapter 1

Introduction

1.1 Macrophages

Macrophages (and their precursors, monocytes) reside in every tissue of the body, although in different guises depending on the anatomic location (e.g. microglia, Kupffer cells, and osteoclasts) [1]. They are the 'big eaters' and the first line of defense of the immune system [1]. Through their ability to clear pathogens and instruct other immune cells, these cells have a central role in protecting the host [1]. Upon tissue damage or infection, monocytes are rapidly recruited to the tissue, where they differentiate into tissue macrophages that engulf apoptotic cells, pathogens, and drug molecules and produce immune effector cytokines.

Macrophages are involved in a variety of disease states, such as inflammatory, infectious, cardiovascular, autoimmune diseases, and many more [2]. The role of macrophages as phagocytic and antigen-presenting cells is very well established. However, over or underactivity of these cells can result in the onset and/or progression of pathologic conditions such as growth and spread of malignant tumors, sepsis, chronic inflammation in rheumatoid arthritis, lysosomal storage disease, atherosclerosis, and major infections, including HIV/AIDS and tuberculosis [3]. Thus, therapies targeting macrophages appears to be a very promising strategy. Furthermore, the ability of the macrophages to migrate to the sites of inflammation, infection, and tissue degeneration makes them attractive vehicles to deliver contrast agents for diagnosis or drugs as therapeutic modalities [4, 5].

There have been several reports showing that macrophages are also responsible for drug accumulation of weakly basic drugs based on ion trapping in the acidic endo-lysosomal system [6]. Chemicals with a propensity to accumulate in the endo-lysosomal system are commonly referred to as lysosomotropic agents. The trapping and accumulation of a drug within the lysosome, which is the subcellular organelle in macrophages that digests unwanted materials delivered from the cytoplasm and extracellular environment, has a variety of consequences. There are several studies that show that the drug entrance into the macrophage activates the macrophage which leads to several cellular responses. Studies by Krise et. al have demonstrated that drug accumulation by lysosomotropic agents results in an expanded volume of the lysosome, and further work by this group has demonstrated that lysosomal drug accumulation results in nuclear localization of the transcription factor EB (TFEB), which regulates lysosomal biogenesis and leads to an increase in the number of lysosomes and degradation rate of complex molecules [6-11]. Furthermore, lysosomal drug accumulation was also associated with macrophage activation and proton and chloride channel upregulation [6-9]. However, the mechanisms that stabilize the accumulating drug within endo-lysosomal system are not well understood yet. Therefore, further investigation is required.

The trapping and accumulation of a drug within the lysosome has significant biological outcomes and can greatly impact the pharmacokinetics and pharmacodynamics of an accumulating drug. It is generally known that intracellular accumulation of the drug, especially of insoluble form, can lead to serious complications, including cell toxicity, blockage, and organ failure. However, in some cases, there are insoluble drug complexes that are not toxic and actually improve the parent's drug pharmacokinetic parameters. The great example of that is clofazimine (CFZ).

1.2 Clofazimine (CFZ)

Clofazimine is a weakly basic, very lipophilic, phenazine compound that is FDA-approved antibiotic [12]. It has been used effectively against leprosy for over 40 years, curing over 14 million people worldwide, which makes it to be a part of World Health Organization's list of essential medications [13]. Currently, CFZ is in clinical trials for multi-drug resistant tuberculosis (MDR-TB) [14].

Due to its unique pharmacokinetic parameters, orally administered CFZ free base has a half-life of up to 70 days and is associated with extensive intracellular bioaccumulation of the solid drug, primarily in tissue macrophages, in a form of Crystal-Like Drug Inclusions (CLDIs) [15-17]. Even though prolonged CFZ treatment is associated with massive drug biocrystal accumulation within resident tissue macrophages, there are no obvious toxicological manifestations from these biocrystals. Instead, CLDIs are biocompatible, stable, long-lived, relatively non-toxic, and have anti-inflammatory properties [18]. By analyzing the isolated CLDIs from spleen and liver in mice, it was shown that CLDIs chemically and structurally resemble CFZ hydrochloride salt (CFZ-HCl) crystals (FITC(-) Cy5(+)), which is a different form of the drug from orally administered CFZ free base (FITC(+) Cy5(-)) [19]. These results indicate that a salt form of CFZ is much more stable within macrophages of the spleen and liver than a CFZ free base form, which is contradictive to general knowledge of pharmaceutical drug design. Salification usually enhances solubility of a parent drug, making it less stable or less prone to precipitation [20]. Therefore, it makes it very interesting to study why macrophages preferentially stabilize the salt form of the drug rather than free base form, which leads to massive drug bioaccumulation and an anti-inflammatory response, which needs further characterization.

In terms of its toxicological properties and regardless of the indication, the major side effect of orally administered CFZ is a strong red skin pigmentation, observed in more than 94% of patients [21, 22]. Patients may also experience ichthyosis or gastrointestinal symptoms, but at the normal dosage of 50 to 100 mg/day, no other major side effects have been reported [21, 23-25]. It has been generally assumed that the skin pigmentation is due to the massive bioaccumulation of Cy5(+) CFZ-HCl within the organism, specifically within skin tissue macrophages; however, no one has ever determined exactly what form of the drug causes this major side effect from orally administered CFZ treatment.

It is critical to understand and acknowledge the importance of off-target drug accumulation-related side effects from weakly basic drugs. For example, doxorubicin, chemotherapy medication, accumulates in the heart muscle mitochondria leading to cardiotoxicity [26]. By studying the drug's physicochemical parameters, ionization states, its interaction with cellular membranes and ions, and ultimately, determining the thermodynamic mechanism that leads to its off-target accumulation, it is possible to circumvent these side effects through appropriate targeted formulation (e.g. liposomal doxorubicin, Doxil, avoids cardiotoxicity) [26].

Therefore, by determining the physicochemical parameters and the thermodynamic mechanism of differential stabilization and accumulation of the HCl salt vs free base form of CFZ in lysosomes of macrophages, I can properly develop solid nano/microparticulate formulations that target macrophages and are stabilized inside of them for more efficacious drug response. Furthermore, some of the methods on how to determine the physicochemical parameters and the thermodynamic mechanism leading to differential stability of the salt form vs the free base of a precipitated weak base have already been established and used for several

decades [27]. Overall, this will aid in the selection of superior performing formulations for future studies of other weakly basic drugs that are similar to CFZ for long-acting drug delivery systems designed to improve the dosing strategy and patient compliance. Also, since macrophages are distributed throughout the body in different tissues, they can be potentially utilized as drug delivery vehicles to prevent and treat macrophage related diseases [3].

1.3 Microparticulate Formulation for Macrophage Targeting (Passive Targeting)

Passive targeting refers to the accumulation of the drug or drug-carrier nano/microsystem by exploiting the pathophysiological condition and anatomical route [3]. For example, nanoparticle systems that are >100 nm are readily opsonized and removed from the circulation by the mononuclear phagocyte system (MPS, aka reticuloendothelial system) and degraded by the macrophages in the liver and spleen [3]. Thus, the tendency of unmodified nanoparticles to localize in the MPS has been exploited as a way to passively deliver the payload to macrophages. In fact, the presence of macrophages at the site of action presents an excellent opportunity to passively target these cells.

Particle size reduction has been a nonspecific formulation approach for many years that is applicable to almost any drug [26]. Micronization means transfer of relatively coarse drug powder to micrometer size crystals using colloid mills or jet mills. The mean diameter of such micronized drug powders is in the range of approximately 1 to 5 μm, corresponding to a size distribution of approximately 0.1 to 20 μm [3, 26]. Owing to their particle size distribution, such formulations in general cannot be used for intravenous (IV) injections (unless nanonized), but more suitable for local administration [26]. In order to achieve a cellular delivery (i.e. macrophage delivery) of drug particles, the next consequent step is to go down one further dimension in size, which means to reduce the particle size in the nanometer range. In case of

drug nanocrystals, as far as they reach the site of action where macrophages are present, macrophages should technically engulf these drug nanocrystals via passive targeting.

According to Thassu et al., drug nanocrystals are pure solid drug particles with a mean diameter below 1000 nm. A nanosuspension consists of drug nanocrystals, stabilizing agents (e.g. surfactants, lipids, and/or polymeric stabilizers), and a liquid dispersion medium. The dispersion media can be water, aqueous solutions, or non-aqueous media. The term "drug nanocrystals" implies a crystalline state of the discrete particles, but depending on the production method they can also be partially or completely amorphous. Drug nanocrystals have to be distinguished from polymeric nanoparticles, which consist of a polymeric matrix and an incorporated drug. Drug nanocrystals do not consist of any matrix material [26].

1.4 Central Hypothesis

Even though clofazimine hydrochloride (CFZ-HCl) and clofazimine (CFZ) free base have the same active pharmaceutical ingredient (API), I hypothesize that CFZ-HCl is a more therapeutically efficacious form of CFZ that could be potentially used in repurposing this drug for other indications.

1.5 Specific Aims

1.5.1 Specific Aim 1

In Specific Aim 1, I aim to establish the physicochemical parameters of CFZ that explain the thermodynamic mechanism of differential stabilization and accumulation of the HCl salt vs free base form of drug in lysosomes of macrophages. These parameters will allow us to determine what form of the drug causes the major side effect from clofazimine treatment – skin pigmentation. I hypothesize that CFZ has unique physicochemical parameters that allow it to

stabilize and accumulate as HCl salt form in the lysosomes of macrophages throughout the body, including macrophages of the skin, causing the drug-induced skin pigmentation.

1.5.2 Specific Aim 2

In Specific Aim 2, I aim to develop a biomimetic formulation of CFZ drug biocrystals, micronized CFZ-HCl salt crystals, and investigate its stability in macrophages *in vitro* and *in vivo*. I hypothesize that biomimetic formulation of micronized CFZ-HCl crystals will be stable under lysosomal conditions *in vitro* and *in vivo.*

1.5.3 Specific Aim 3

Explore the inflammatory status and efficacy of the biomimetic formulation of micronized CFZ-HCl salt crystals in gouty arthritis under local administration *in vivo*. I hypothesize that local injection of the biomimetic formulation of CFZ-HCl microcrystals *in vivo* will decrease inflammation, pain, and swelling associated with gout and facilitate the dissolution and clearance of monosodium urate (MSU) crystals from the joint by lowering the local pH of the synovium.

1.6 References

1. Nature Reviews: Immunology. *Monocytes and Macrophages*. 2011 [cited 2016 Aug 19]; Available from: http://www.nature.com/nri/focus/macrophages/index.html?WT.ec_id=SLBU_COMMS.

2. Barin, J.G., N.R. Rose, and D. Cihakova, *Macrophage diversity in cardiac inflammation: a review.* Immunobiology, 2012. **217**(5): p. 468-75.

3. Svenson, S. and R.K. Prud'homme, *Multifunctional Nanoparticles for Drug Delivery Applications: Imaging, Targeting, and Delivery*. Nanostructure Science and Technology, ed. D.J. Lockwood. 2012, New York, USA: Springer Science+Business Media, LLC.

4. Beduneau, A., et al., *Facilitated monocyte-macrophage uptake and tissue distribution of superparmagnetic iron-oxide nanoparticles.* PLoS One, 2009. **4**(2): p. e4343.

5. Kingsley, J.D., et al., *Nanotechnology: a focus on nanoparticles as a drug delivery system.* J Neuroimmune Pharmacol, 2006. **1**(3): p. 340-50.

6. Kaufmann, A.M. and J.P. Krise, *Lysosomal sequestration of amine-containing drugs: analysis and therapeutic implications.* J Pharm Sci, 2007. **96**(4): p. 729-46.

7. Funk, R.S. and J.P. Krise, *Cationic amphiphilic drugs cause a marked expansion of apparent lysosomal volume: implications for an intracellular distribution-based drug interaction.* Mol Pharm, 2012. **9**(5): p. 1384-95.

8. Logan, R., et al., *Amine-containing molecules and the induction of an expanded lysosomal volume phenotype: a structure-activity relationship study.* J Pharm Sci, 2014. **103**(5): p. 1572-80.

9. Logan, R., A.C. Kong, and J.P. Krise, *Time-dependent effects of hydrophobic amine-containing drugs on lysosome structure and biogenesis in cultured human fibroblasts.* J Pharm Sci, 2014. **103**(10): p. 3287-96.

10. Sardiello, M., et al., *A gene network regulating lysosomal biogenesis and function.* Science, 2009. **325**(5939): p. 473-7.

11. Visvikis, O., et al., *Innate host defense requires TFEB-mediated transcription of cytoprotective and antimicrobial genes.* Immunity, 2014. **40**(6): p. 896-909.

12. Arbiser, J.L. and S.L. Moschella, *Clofazimine: a review of its medical uses and mechanisms of action.* J Am Acad Dermatol, 1995. **32**(2 Pt 1): p. 241-7.

13. World Health Organization. *Leprosy Report*. 2014 [cited 2016 Aug 16]; Available from: http://www.who.int/mediacentre/factsheets/fs101/en.

14. Dey, T., et al., *Outcomes of clofazimine for the treatment of drug-resistant tuberculosis: a systematic review and meta-analysis.* J Antimicrob Chemother, 2013. **68**(2): p. 284-93.

15. Baik, J. and G.R. Rosania, *Macrophages sequester clofazimine in an intracellular liquid crystal-like supramolecular organization.* PLoS One, 2012. **7**(10): p. e47494.

16. Baik, J. and G.R. Rosania, *Molecular imaging of intracellular drug-membrane aggregate formation.* Mol Pharm, 2011. **8**(5): p. 1742-9.

17. Baik, J., et al., *Multiscale distribution and bioaccumulation analysis of clofazimine reveals a massive immune system-mediated xenobiotic sequestration response.* Antimicrob Agents Chemother, 2013. **57**(3): p. 1218-30.

18. Yoon, G.S., et al., *Phagocytosed Clofazimine Biocrystals Can Modulate Innate Immune Signaling by Inhibiting TNFalpha and Boosting IL-1RA Secretion.* Mol Pharm, 2015. **12**(7): p. 2517-27.

19. Keswani, R.K., et al., *Chemical Analysis of Drug Biocrystals: A Role for Counterion Transport Pathways in Intracellular Drug Disposition.* Mol Pharm, 2015. **12**(7): p. 2528-36.

20. Bansal, A.K., L. Kumar, and A. Amin, *Salt Selection in Drug Development.* Pharmaceutical Technology, 2008. **32**(3).

21. Maia, M.V., G. Cunha Mda, and C.S. Cunha, *Adverse effects of alternative therapy (minocycline, ofloxacin, and clofazimine) in multibacillary leprosy patients in a recognized health care unit in Manaus, Amazonas, Brazil.* An Bras Dermatol, 2013. **88**(2): p. 205-10.

22. Tang, S., et al., *Clofazimine for the treatment of multidrug-resistant tuberculosis: prospective, multicenter, randomized controlled study in China.* Clin Infect Dis, 2015. **60**(9): p. 1361-7.

23. Singh, H., et al., *Adverse effects of multi-drug therapy in leprosy, a two years' experience (2006-2008) in tertiary health care centre in the tribal region of Chhattisgarh State (Bastar, Jagdalpur).* Lepr Rev, 2011. **82**(1): p. 17-24.

24. Hastings, R.C., et al., *Leprosy.* Clin Microbiol Rev, 1988. **1**(3): p. 330-48.

25. Jamet, P., et al., *Short-term trial of clofazimine in previously untreated lepromatous leprosy.* Int J Lepr Other Mycobact Dis, 1992. **60**(4): p. 542-8.

26. Thassu, D., M. Deleers, and P. Y., *Drugs and the Pharmaceutical Sciences*. Nanoparticulate Drug Delivery Systems. Vol. 166. 2007, New York, USA: Informa Healthcare USA, Inc.

27. Kramer, S.F. and G.L. Flynn, *Solubility of organic hydrochlorides.* J Pharm Sci, 1972. **61**(12): p. 1896-904.

Chapter 2

Clofazimine Biocrystal Accumulation in Macrophages Upregulates Interleukin 1 Receptor Antagonist Production to Induce a Systemic Anti-Inflammatory State

2.1 Relevance to Thesis

This chapter was adapted from the following publication:

Yoon GS, Keswani RK, Sud S, Rzeczycki PM, ***Murashov MD****, Koehn TA, Standiford TJ, Stringer KA, Rosania GR.* ***2016****. Clofazimine biocrystal accumulation in macrophages upregulates interleukin 1 receptor antagonist production to induce a systemic anti-inflammatory state.* ***Antimicrob Agents Chemother*** *60:3470 –3479. doi:10.1128/AAC.00265-16.*

In this study, we designed an experimental strategy to probe the site-specific accumulation of the Cy5(+) CFZ-HCl salt form (in the chapter referred to as "intracellular biocrystals") and its downstream immunological effects to help us to distinguish between the potential adverse effects of CFZ-HCl from those of the soluble molecules of CFZ. We tested the specific hypothesis that CFZ-HCl that accumulate in resident tissue macrophages can modulate (or activate) these cells' inflammatory signaling pathways *in vivo* that lead to systemic changes in the inflammatory response. My contribution in this study involved mice clofazimine treatment and cytokine measurements from organ homogenates via ELISA, SDS-PAGE, and Western Blotting. As the result, by monitoring key inflammatory cytokines in the vital organs and blood of CFZ-treated mice, it was demonstrated that CFZ-HCl salt form in macrophages, but not the

soluble form of CFZ free base, is specifically associated with an IL-1RA-mediated anti-inflammatory response.

The results from this study were critical because this study suggested that drug CFZ-HCl salt form is biocompatible, stable, long-lived, relatively non-toxic, and have anti-inflammatory properties compared to the soluble form of CFZ free base. In other words, CFZ-HCl, being a different form of the drug from the orally-administered CFZ free base, is a more therapeutically efficacious form of CFZ that could be potentially used in repurposing this drug for other indications, such as inflammatory and infectious diseases, supporting my central hypothesis.

2.2 Abstract

Clofazimine (CFZ) is a poorly soluble antibiotic and anti-inflammatory drug indicated for the treatment of leprosy. In spite of its therapeutic value, CFZ therapy is accompanied by the formation of drug biocrystals that accumulate within resident tissue macrophages, without obvious toxicological manifestations. Therefore, to specifically elucidate the off-target consequences of drug bioaccumulation in macrophages, we compared the level of inflammasome activation in CFZ-accumulating organs (spleen, liver and lung) in mice after 2 and 8 weeks of CFZ treatment when the drug exists in soluble and insoluble (biocrystalline) forms, respectively. Surprisingly, the results showed a drastic reduction in caspase 1 and interleukin-1β (IL-1β) cleavage in the livers of mice treated with CFZ for 8 weeks (8-week-CFZ-treated mice) compared to 2-week-CFZ-treated and control mice, which was accompanied by a 3-fold increase in hepatic IL-1 receptor antagonist (IL-1RA) production and a 21-fold increase in serum IL-1RA levels. In the lung and spleen, IL-1β cleavage and tumor necrosis factor alpha expression were unaffected by soluble or biocrystal CFZ forms. Functionally, there was a drastic reduction of carrageenan- and lipopolysaccharide-induced inflammation in the footpads and lungs,

respectively, of 8-week-CFZ-treated mice. This immunomodulatory activity of CFZ biocrystal accumulation was attributable to the upregulation of IL-1RA, since CFZ accumulation had minimal effect in IL-1RA knockout mice or 2-week-CFZ-treated mice. In conclusion, CFZ accumulation and biocrystal formation in resident tissue macrophages profoundly altered the host's immune system and prompted an IL-1RA-dependent, systemic anti-inflammatory response.

2.3 Introduction

Clofazimine (CFZ) is an antimycobacterial agent listed in the World Health Organization's List of Essential Medicines that has been in use as part of the standard treatment of leprosy since the 1960s [1, 2]. The number of leprosy cases has drastically dropped from 12 million/year in 1981 to 216,000/year in 2013 [3], a testament to the effectiveness of CFZ, which has gained considerable attention recently as part of a treatment regimen for drug-resistant tuberculosis [4-6]. The efficacy of oral CFZ against leprosy is due, in part, to its well-documented anti-inflammatory activity [2]. However, CFZ's mechanism of anti-inflammatory action and atypical pharmacokinetic properties are not well understood, and its high oral bioavailability and poor solubility leads to significant bioaccumulation in tissues [7].

In previous studies, it has been shown that following prolonged oral administration of CFZ, the drug massively bioaccumulates as intracellular biocrystals in resident tissue macrophages [8-12]. Therefore, it is natural to assume that this bioaccumulation phenomenon contributes to the drug's toxicity, whereas the soluble form of CFZ, which circulates and partitions to and from the different organs, is responsible for CFZ's mechanism of action. Indeed, insoluble particles and crystals that accumulate in macrophages under various pathological conditions are known to activate immune signaling pathways that lead to caspase 1

(Casp 1) activation and increased interleukin-1β (IL-1β) secretion [13-16]. This so-called "inflammasome" activation pathway is often associated with many downstream pathological changes, as has been shown by the accumulation of cholesterol monohydrate crystals in atherosclerosis [13], monosodium urate crystals in gout [14], and inhaled foreign particles in the case of asthma and other chronic inflammatory lung diseases [15, 16].

In spite of its bioaccumulation, several clinical trials have established CFZ as a potentially useful therapeutic agent for treating a variety of chronic inflammatory diseases [17-22]. Furthermore, *in vitro* studies have shown that intracellular CFZ biocrystals dampen proinflammatory pathways while enhancing anti-inflammatory signals [23].

In order to distinguish between the potential adverse effects of insoluble drug biocrystals from those of the soluble molecules, we designed an experimental strategy to compare how the accumulation of insoluble drug biocrystals might influence the immune signaling response of macrophages in live mice. We reasoned that macrophages exposed to the soluble form of CFZ (after 2 weeks of treatment) may behave differently from those that are exposed to its biocrystalline form (after 8 weeks of treatment). Accordingly, we tested the specific hypothesis that CFZ biocrystals that accumulate in resident tissue macrophages can modulate (or activate) these cells' inflammatory signaling pathways *in vivo* that lead to systemic changes in the inflammatory response. By assessing tumor necrosis factor alpha (TNF-α) and IL-1 receptor antagonist (IL-1RA) expression, as well as Casp 1 and IL-1β maturation, in the vital organs and blood of CFZ-treated mice, our results demonstrate that CFZ biocrystals in macrophages, but not the soluble form, is specifically associated with an IL-1RA-mediated anti-inflammatory response.

2.4 Materials and Methods

Reagents

Anti-caspase 1 and anti-IL-1β antibodies were purchased from Thermo Pierce (Rockford, IL) and Novus Biologicals (Littleton, CO), respectively. Anti-F4/80 and anti-CD68 antibodies were purchased from Abcam (Cambridge, MA). Anti-actin antibody and lipopolysaccharide (LPS; from *E. coli* O55:B5) were purchased from Sigma (St. Louis, MO).

Mice clofazimine treatment

Clofazimine (CFZ; Sigma-Aldrich, catalog no. C8895) was prepared in sesame oil (Shirakiku, Japan, or Roland, China) and Powdered Lab Diet 5001 (PMI International, Inc., St. Louis, MO) and orally administered to wild-type (WT) C57BL/6 mice or IL-1RA knockout mice (4 to 5 weeks old; Jackson Laboratory, Bar Harbor, ME) for up to 8 weeks *ad libitum* as previously described [8, 24]. Control mice were fed with the same diet without CFZ. The animal protocol was approved by the University of Michigan's Animal Care and Use Committee in accordance with the National Institutes of Health guidelines (UCUCA, no. PRO00005542).

Carrageenan footpad edema test

Footpad edema in response to carrageenan (CAR; Sigma) injection was measured in CFZ-treated and control mice as previously described [25]. In IL-1RA knockout (KO) mice, these experiments were performed at 6 weeks and not at 8 weeks because the IL-1RA KO mice weighed less than the WT mice and their livers were smaller (see Figure S2-4 in the Appendix A). In brief, the volume of each hind paw was measured before and after the intraplantar injection of 30 µl of 2% CAR (60 µg per paw) in phosphate-buffered saline (PBS) or an equal volume of PBS in the contralateral paw. Paw swelling was measured at 4 and 48 h after injection, after which the animals were euthanized by exsanguination while deeply anesthetized with an intraperitoneal injection of ketamine (100 mg/kg) and xylazine (10 mg/kg), and the skin

tissues of the plantar region were harvested for cytokine assay (see the Materials and Methods in Appendix A).

Acute lung injury and infrared pulse oximetry

Since C57BL/6 mice are relatively resistant toward a single dose of intratracheal (i.t.) LPS instillation [26], two i.t. injections of LPS (16 mg/kg; 50 μl) were administered, one on day 0 and the second on day 3. Briefly, mice treated with CFZ for 8 weeks (8-week-CFZ-treated mice) and control mice were anesthetized using intraperitoneal injections of xylazine (50 mg/kg) and ketamine (5 mg/kg). Under direct visualization of the vocal cords using an otoscope, either LPS or an equivalent volume of PBS in a 1-ml syringe attached to an oral gavage needle (22G) was instilled into the lungs via the oral route. The mouse was then placed in a temperature-controlled cage (37°C) for recovery from anesthesia.

The general health status of each PBS/LPS-instilled mice was monitored by measuring body weight and rectal temperature (microprobe thermometer; Physitemp Instruments, Clifton, NJ), and cardiopulmonary function (arterial oxygen saturation, respiratory rate, heart rate, and pulse distention) was monitored using MouseOx with a collar clip sensor (Starr Life Sciences Corp., Oakmont, PA) as previously described [27, 28]. In brief, 1 day before i.t. instillations (day -1), the hair around the neck of each mouse was removed using Nair (Church&Dwight, Princeton, NJ) to enable data acquisition using the collar clip sensor. The next day (day 0), immediately prior to the first LPS/PBS dose, and every 24 h afterward until day 6, the body weight, temperature, and MouseOx readings were recorded. MouseOx data were acquired by very brief anesthesia of the mouse using 5% isoflurane to facilitate the placement of the collar clip sensor. The mouse was then placed in an enclosed chamber with ambient light and allowed to acclimatize for 5 min, at which point the animals had recovered normal activities and

physiological readings. Arterial oxygen saturation, respiratory rate, heart rate, and pulse distention measurements were then simultaneously recorded for 6 min (15 readings/s), and any errors caused by motion during recording were excluded, after which the mean value of each parameter was used for further data analysis.

Terminal endpoint assessment

To objectively assess LPS-induced mortality, we used a multiparametric scoring system that relied on the daily changes in vital signs associated with inflammatory injury progression and mortality, which included arterial oxygen saturation [27], body weight, and temperature [29, 30]. First, the percent change from baseline (day 0) in arterial oxygen saturation, body weight, and temperature in each mouse caused by i.t. instillation of PBS/LPS were measured and calculated daily until day 6 after instillation. These data were then used in a vector equation to calculate the distance between each LPS-treated mouse and the mean of the PBS-treated mice to assess the terminal endpoint for each LPS-instilled mouse (see Materials and Methods in Appendix A). CFZ-treated and control mice were calculated separately, and LPS-instilled mice that scored a total of 18 or higher were determined as terminal, since these mice also displayed severe signs of sickness evidenced by impaired mobility, lack of grooming, hunched posture, and muscle weakness that could be felt while handling the mice. These mice were immediately euthanized with ketamine-xylazine (100 mg/kg, 10 mg/kg) and the bronchoalveolar lavage (BAL) fluid and lungs were harvested for cellular and biochemical analysis (see below). Remaining mice that did not reach terminal endpoint were all euthanized on day 6 after PBS/LPS instillation.

Cytokine measurements

The harvested organs (liver, spleen, lungs, and kidneys) and footpads designated for cytokine assays were cut and homogenized by sonication (2-s pulses repeated five times on ice, level 5; Fisher model 100) in radioimmunoprecipitation assay buffer (Sigma) with added protease inhibitors (Halt protease and phosphatase inhibitor cocktail and 0.5 M EDTA; Thermo Pierce, Rockford, IL). After centrifugation (18,000 x *g*, 15 min, 4°C), the supernatants were assayed for IL-1β, IL-1RA, and TNF-α by enzyme-linked immunosorbent assay (ELISA; Duoset; R&D Systems, Minneapolis, MN) in duplicate wells according to the manufacturer's instructions. Cytokines in the BAL were measured after the removal of the cells. Albumin was assayed by ELISA (Innovative Research, Novi, MI). The cytokine concentrations were expressed (i) as pico-, nano-, or micrograms per milligram of protein for the organs, (ii) as pico-, nano-, or micrograms of paw weight, or (iii) as pico- or micrograms per milliliter of BAL fluid.

Mouse BAL fluid harvesting, immunohistochemistry and imaging, and SDS-PAGE and Western blotting

The mouse BAL fluid harvesting, immunohistochemistry and imaging, and SDS-PAGE and Western blotting procedures are described in the Appendix A.

Data processing and statistics

All data are expressed as means ± the standard deviations (SD). For multiple comparisons, statistical analysis was performed with one-way analysis of variance (ANOVA) and Tukey's post *hoc* comparisons. For two-group comparisons, an unpaired Student *t* test was used. All statistical analyses employed the Sigmaplot version 13 (Systat Software, San Jose, CA) software and $P \leq 0.05$ was considered statistically significant.

2.5 Results

CFZ crystallization and bioaccumulation in the liver occurs after 2 weeks

During the first 2 weeks of CFZ treatment, CFZ-associated diffuse red staining was present throughout the liver (Figure 2-1A, brightfield). However, by 4 weeks, CFZ accumulated in the biocrystalline form. At 8 weeks, red CFZ biocrystals were evident throughout the liver (Figure 2-1A, top panel). Taking advantage of solvatochromic changes in the fluorescent excitation and emission spectra of CFZ [31, 32], fluorescence microscopy enabled *in vivo* detection of the soluble and biocrystalline forms of CFZ. After 2 weeks of CFZ treatment, the drug was mostly present in the soluble form with its fluorescence mostly detectable in the FITC channel (Figure 2-1A, fluorescein isothiocyanate [FITC] and Cy5 panels; Figure 2-1B). At later time points, the fluorescence signal in the FITC channel declined, while the fluorescence signal in the Cy5 channel increased, indicating the relative accumulation of the biocrystalline form (Figure 2-1A and B). By 8 weeks, most of the fluorescence signal was detectable in the Cy5 channel (Figure 2-1 A and B), indicating that CFZ was present almost entirely in biocrystalline form. Immunohistochemistry of 8-week-CFZ-treated liver sections showed that CFZ biocrystals are sequestered inside F4/80- positive macrophages (Figure 2-1C). Such targeted accumulation of CFZ biocrystals was also detected in other organs such as $CD68^+$ alveolar macrophages (see Figure S2-1 in Appendix A), and $F4/80^+$ splenic macrophages [8, 31].

CFZ biocrystal formation in the liver downregulates Casp 1/IL-1β processing while enhancing IL-1RA expression

Intracellular crystals, such as those formed by cholesterol or uric acid, have been implicated in the activation of the NLRP3-Casp 1 inflammasome, which plays a major role in the pathogenesis of chronic inflammatory disorders [14, 33, 34]. The uptake of other nano- and

microparticles has also been reported to cause inflammasome activation in macrophages [35-37]. Therefore, to assess whether the bioaccumulation of CFZ crystals leads to activation of the inflammasome, we measured and compared cleaved Casp 1 and IL-1β in organs that bioaccumulate CFZ - i.e., the liver, spleen, and lungs - and kidneys, that do not accumulate CFZ, after 2 and 8 weeks of either CFZ or control treatment. Two weeks of CFZ exposure resulted in only moderate cleavage of hepatic Casp 1 and IL-1β (Figure 2-2A, left panel, and Figure 2-2B). However, by 8 weeks, Casp 1 and IL-1β cleavage was significantly reduced by CFZ treatment (Figure 2-2A, right panel, and Figure 2-2B); IL-1β levels in the spleen, lung, and kidneys did not change (see Figure S2-2 in Appendix A). The expression of the proinflammatory cytokine, TNF-α, was unchanged by CFZ at both 2 and 8 weeks (Figure 2-2C), except in the liver, where it was decreased at 2 weeks compared to control livers.

Similar to previous observations [8], we found that after 8 weeks of oral administration CFZ caused a major upregulation of IL-1RA expression in CFZ biocrystal-accumulating organs, such as the spleen, the lungs, and especially the liver, which increased by 3-fold (Figure 2-2D). IL-1RA levels in the kidney were unaffected (Figure 2-2D). In contrast, after 2 weeks of oral CFZ administration there were more modest increases in only the spleen and lungs, while the liver was unaffected (Figure 2-2D). Since the liver is known to be the major source of circulating IL-1RA [38, 39], we observed a corresponding increase in serum IL-1RA levels in CFZ-treated mice at 8 weeks but not at 2 weeks (Figure 2-2E). Under all conditions, neither TNF-α nor IL-1β was detected in the serum. In aggregate, these findings suggest that crystallized CFZ, which is evident after 8 weeks of CFZ administration, decreased the activation of the inflammasome *in vivo*. In parallel with this decline, crystallized CFZ induced an upregulation of endogenous IL-1RA.

Systemic CFZ bioaccumulation and crystallization dampens CAR-mediated acute footpad inflammation

To test the physiological impact of the CFZ-induced serum IL-1RA levels, we tested the acute inflammatory response of CFZ-treated mice by using a well-established footpad injury model [25]. The paws of 8-week-CFZ-treated mice displayed strikingly reduced swelling at 48 h after the injection of CAR compared to the paws of untreated CAR-injected mice (Figure 2-3A). Paw volume measurements showed that there was a significant reduction (57%) in footpad swelling as early as 4 h after the injection of CAR in 8-week-CFZ-treated mice compared to control mice, and the animals continued to exhibit reduced swelling over the 48-h study period (Figure 2-3B). CAR-induced increases in footpad IL-1β and TNF-α levels were dramatically reduced by 8-week-CFZ treatment (Figure 2-3C and D). In contrast to the 8-week-treated mice, 2-week-CFZ-treated mice produced only a modest reduction in paw swelling compared to control mice (Figure 2-3E and F). The IL-1β and TNF-α levels in footpad homogenates from these animals were similar in both CFZ-treated and control mice at 48 h (Figure 2-3G and H). Accordingly, these results suggest that the accumulation of CFZ biocrystals modulated the immune response to profoundly dampen CAR-induced footpad inflammation, and this action is not evident for the soluble form of the drug after 2 weeks of treatment.

CFZ biocrystals dampen the acute inflammatory response in the footpad by increasing blood IL-1RA

IL-1RA is known to be an early-acting acute-phase anti-inflammatory cytokine [38], and circulating IL-1RA has been reported to dampen a broad spectrum of inflammatory conditions by inhibiting the activity of IL-1β at the site of injury [40, 41]. Therefore, we hypothesized that the anti-inflammatory response observed after 8 weeks of CFZ treatment may be mediated by

increased serum IL-1RA concentrations, which are not evident after 2 weeks of CFZ treatment (Figure 2-2E). Detection of serum IL-1RA in 2-week-CFZ-treated and control mice showed comparable IL-1RA levels before (0 h) and after (48 h) CAR injection (Figure 2-4A). However, serum IL-1RA levels in 8-week-CFZ-treated mice rapidly declined 4 h after CAR injection (Figure 2-4B). After 48 h, IL-1RA returned to similar levels in the plasma of control and 8-week-CFZ-treated mice (Figure 2-4B). For all mice, the plasma levels of TNF-α and IL-1β were below the detection limit of ELISAs (15 pg/ml). These results suggest that increased circulating IL-1RA levels associated with CFZ bioaccumulation and crystallization could be responsible for the anti-inflammatory activity observed in 8-week-CFZ-treated mice.

In order to test the possibility that elevated IL-1RA expression mediates the anti-inflammatory activity of CFZ after crystal formation, we administered oral CFZ to age-matched IL-1RA KO and WT mice and then subjected the animals to the CAR footpad injury model. IL-1RA KO mouse livers also increased in weight to an extent similar to that of WT mice after 6 weeks of CFZ treatment (see Figure S2-3B in Appendix A). Also, IL-1RA KO mice formed and accumulated CFZ biocrystals in the liver at a level similar to WT animals without noticeable differences in crystal shape or Cy5 fluorescence intensity (see Figure S2-3C and D in Appendix A). Remarkably, the anti-inflammatory action of CFZ bioaccumulation was greatly diminished in IL-1RA KO mice, since CFZ-treated and CAR-injected IL-1RA KO mice displayed similar swelling compared to untreated and CAR-injected IL-1RA KO mice (Figure 2-4C and D, right panels). In the CFZ-treated WT mice, we observed significantly reduced CAR-induced swelling compared to control mice at 4 and 48 h postinjury (Figure 2-4C and D, WT panels). As expected, the footpad IL-1β and TNF-α levels were significantly reduced in WT CFZ-treated and CAR-injected mice compared to WT untreated and CAR-injected mice (Figure 2-4E). However, the

IL-1β and TNF-α levels were comparable in the CAR-injected IL-1RA KO mice with or without CFZ treatment (Figure 2-4F). IL-1RA KO mice with or without CFZ treatment showed higher cytokine levels than the control WT mice after CAR injection (Figure 2-4E versus Figure 2-4F), but the footpad swelling was similar (Figure 2-4D). These results are consistent with CFZ bioaccumulation exerting a systemic anti-inflammatory action via the elevation of blood IL-1RA levels.

CFZ bioaccumulation enhances resistance to acute lung injury and improves mouse survival

Given the massive bioaccumulation of CFZ observed in the lungs, we proceeded to determine whether the presence of CFZ biocrystals in these organs may sensitize mice to a sublethal proinflammatory injury. Although CFZ treatment and bioaccumulation did cause some physiological changes, these changes were within ranges of normal physiological readings and overall mouse health was normal (see Table S2-1 in Appendix A).

To determine whether CFZ bioaccumulation induced a latent proinflammatory state in mouse lungs, a sublethal dose of LPS (16 mg/kg) was delivered i.t. to control and CFZ-treated mice. Strikingly, CFZ-treated mice were highly resistant to LPS-induced acute lung injury, with a 92% survival rate compared to the 42% survival rate of control mice (Figure 2-5A). The difference in the arterial oxygen saturation levels between control and CFZ-treated mice was more prominent after the second LPS injection. CFZ-treated mice displayed significantly higher arterial oxygen levels at days 5 and 6 than control mice because most control mice experienced levels of hypoxia that required euthanasia, indicating that control mice showed progressive deterioration in lung function compared to CFZ-treated mice (see Figure S2-4A in Appendix A). Paralleling the impaired lung function, LPS-injected control mice lost weight more rapidly than

CFZ-treated mice, such that six control mice lost >15% of their body weight compared to a similar weight loss in one CFZ-treated mouse (see Figure S2-4B in Appendix A). Both control and CFZ-treated LPS-injected mice displayed large drops in body temperature one day after LPS injection (days 1 and 4). However, CFZ-treated mice were more resistant to a decline in body temperature after the second injection compared to control mice (day 4) (see Figure S2-4C in Appendix A). CFZ-treated mice also displayed less reduction in heart rate, respiratory rate, and pulse distention after the second LPS injection (see Figure S2-4D to F in Appendix A) compared to control mice. Gross lung examination lungs after LPS-induced injury showed a notable reduction of hemorrhaging in CFZ-treated mice compared to control mice (Figure 2-5B). Cellular and biochemical analyses of BAL fluid to assess lung injury revealed that CFZ treatment reduced the LPS-induced BAL fluid cell count (Figure 2-5C) and reduced the BAL fluid albumin concentrations (Figure 2-5D). This CFZ-mediated reduction in lung injury was corroborated by CFZ-induced reductions in LPS-induced levels of BAL fluid TNF-α and IL-1β (Figure 2-5E and F). These results demonstrate that CFZ biocrystal accumulation in the lungs did not impair lung function but instead increased resistance to LPS-induced inflammatory lung injury.

2.6 Discussion

Previously, CFZ bioaccumulation has been associated with atypical pharmacokinetics, as well as more serious side effects, ranging from gastrointestinal problems to splenic infarcts [42]. Although expecting that CFZ bioaccumulation would lead to an upregulation of proinflammatory signaling pathways in macrophages, we were surprised to find the opposite. Instead, our experimental results indicate that long-term oral administration of CFZ and its sequestration as biocrystals within the macrophages of the lung, the spleen, and especially the liver can

dramatically suppress inflammation in peripheral tissues and increase mouse survival in response to acute lung injury. This systemic anti-inflammatory response parallels the accumulation of CFZ biocrystals throughout the animal and is accompanied by elevated IL-1RA levels in these organs and a corresponding boost in IL-1RA levels in serum. Of noteworthy significance, the formation and accumulation of cholesterol monohydrate and monosodium urate crystals have been implicated in the pathogenesis of chronic inflammatory diseases, such as atherosclerosis, nonalcoholic steatohepatitis (NASH) [34], and gout [43]. Moreover, other artificial nano- and microparticles, such as silica crystals [37], aluminum salt crystals [44], silver nanoparticles [35], poly(lactide-co-glycolide) (PLG), and polystyrene microparticles [36], have also been reported to cause inflammasome activation in macrophages. At the cellular level, the aforementioned particles or crystals are known to augment Toll-like receptor signaling and activate the NLRP3 inflammasome via lysosomal destabilization, which leads to Casp 1 activation and the production of cleaved IL-1β [13, 14]. Therefore, the finding that inflammasome activity was inhibited in the CFZ biocrystal-containing liver, evidenced by the suppression of Casp 1 activation and mature IL-1β processing, was unexpected. Moreover, the presence of CFZ biocrystals in the lung, spleen, or liver did not alter the TNF-α levels, a finding consistent with a lack of proinflammatory signaling.

These results prompt us to question whether CFZ bioaccumulation is an inherently toxic phenomenon. It is well known that soluble CFZ is toxic *in vitro*, with a 50% inhibitory concentration of approximately 5 μM, whereas the insoluble crystalline form of CFZ that bioaccumulates in macrophages leads to very few signs of toxicity even at 100 μM [23]. Indeed, in spite of its massive accumulation in the liver, the hepatotoxicity of CFZ in mice and human patients has not been a significant concern [45-47]. Like humans, mice treated with therapeutic

CFZ doses (10 mg/kg/day) did not show signs of deteriorated health. In fact, the CFZ-induced reduction of heart rate could be linked with increased longevity in mice [48]. Also, hypothermia, which is most often used as an indicator of drug toxicity in mice [49], was not seen in 8-week-CFZ-treated mice.

Regarding the therapeutic implications of these results, CFZ has proven to be highly effective for treating leprosy and active against a broad range of Gram-positive bacteria strains (*Staphylococcus*, *Streptococcus*, *Bacillus*, and *Listeria* spp.) [50] and even against drug-resistant *Staphylococcus aureus* clinical isolates that are methicillin resistant (MRSA) and vancomycin intermediate resistant (VISA) [51]. Indeed, CFZ has been clinically used since the 1960s and has helped cure over 16 million leprosy patients. Many of these microorganisms tend to infect and reside within macrophages. Interestingly, chemical analysis of CFZ biocrystals has revealed that they are composed of protonated hydrochloride salt of CFZ (CFZ-HCl) within membrane-bound intracellular compartments [9]. Therefore, the bioaccumulation of CFZ biocrystals in macrophages could serve to maximize the therapeutic efficacy of CFZ without significant side effects. Accordingly, it may be possible to reformulate CFZ as injectable micro- or nanocrystals to specifically target macrophages at sites of infection. Targeted local delivery could maximize CFZ benefit as a therapeutic agent while minimizing the systemic side effects that have curtailed the more widespread use of CFZ.

Considering possible signal transduction mechanisms underlying the anti-inflammatory activity of CFZ biocrystals, the cellular integrated stress response pathway is a candidate [52, 53]. Although soluble CFZ can cause membrane destabilization and cell death at high concentrations [54], lower concentrations of CFZ lead to accumulation within intracellular compartments. Previously, we observed that CFZ biocrystals can also be phagocytosed by

macrophages, where they are stable inside low-pH [4, 5] and counterion (Cl^-)-containing [9] membrane-bound compartments. As a weakly basic lysosomotropic drug, CFZ is prone to pH-dependent ion trapping in lysosomes and could therefore activate transcription factor EB (TFEB [55]), a master transcription factor of lysosomal biogenesis and homeostasis [56-58]. In turn, this could attenuate inflammasome activation pathways and IL-1β processing [59]. Alternatively, like intracellular protein aggregates and other crystalline inclusions that form in the endoplasmic reticulum [60], CFZ biocrystals may activate the unfolded protein response pathway, which could lead to downstream effects on inflammatory signaling [61, 62].

Our experiments indicate that CFZ biocrystals induce a considerable upregulation of IL-1RA production without triggering proinflammatory signaling. Since the evidence points to IL-1RA mediating the anti-inflammatory effects downstream of CFZ bioaccumulation in macrophages, future experiments aimed at elucidating the signaling pathway leading from CFZ biocrystals to IL-1RA expression should reveal further mechanistic details about the mechanism of action of CFZ and perhaps serve as the starting point for the development of new kinds of anti-inflammatory drugs. Thus, the present study strongly warrants further investigation into the mechanisms and therapeutic potential of CFZ for treating inflammatory and infectious diseases in humans. To conclude, CFZ biocrystal accumulation in macrophages could be triggering a previously unknown anti-inflammatory/immunomodulatory signaling pathway(s) of potential therapeutic value.

2.7 Acknowledgements and Funding

We thank Jean Nemzek (Medical School, University of Michigan) and Pathology Cores for Animal Research at the University of Michigan for histological support and Avery Lui for help with image analysis.

This study was supported by the National Institute of General Medical Sciences (NIGMS; R01GM078200 to G.R.R.), an MICHR B-to-B Pilot Seed grant (R.K.K., G.R.R.), and the University of Michigan MCubed Initiative (http://mcubed.umich.edu/). The contents of this report are solely the responsibility of the authors and do not necessarily represent the official views of the NIGMS or the National Institutes of Health.

2.8 Figures

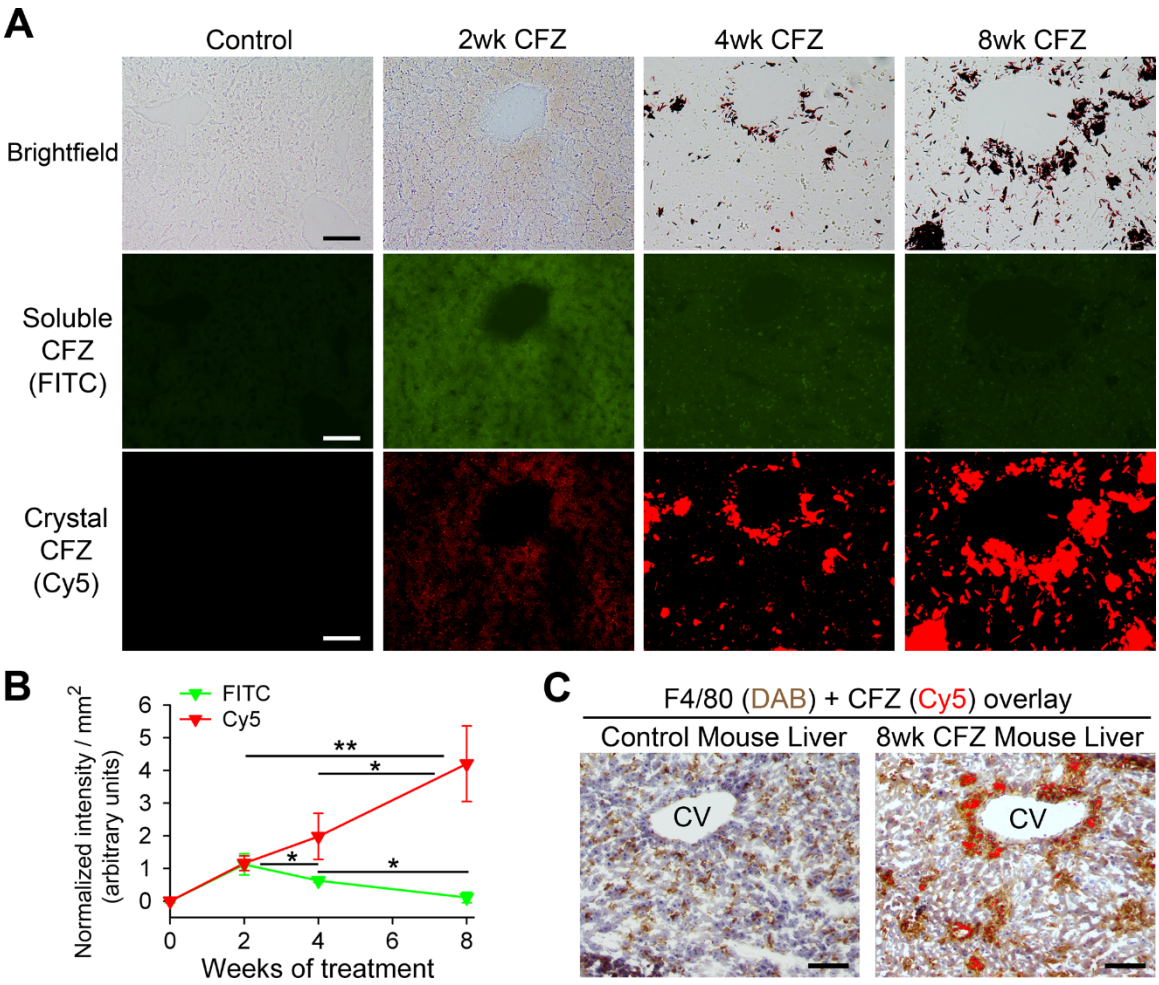

Figure 2-1. CFZ bioaccumulation and crystal formation in the liver occurs after 2 weeks. (**A**) Representative brightfield and fluorescence (FITC for soluble CFZ and Cy5 for crystalline CFZ) images of liver sections from control mice and mice treated with CFZ for 2, 4, and 8 weeks. Scale bar, 50 µm. (**B**) Fluorescence intensity values (FITC and Cy5 channels) of liver sections from control and CFZ-treated mice. Baseline (0 week) intensity values of controls were subtracted from CFZ-treated sections. The data are the means ± the SD of results from three to four images/time point. One-way ANOVA was used to compare fluorescence intensity between time points and $P \leq 0.05$ was considered statistically significant. *, $P \leq 0.05$; **, $P \leq 0.01$. (**C**) F4/80 (DAB) immunohistochemistry of a representative liver section from an 8-week-CFZ-treated mouse in which CFZ crystals (Cy5) are sequestered inside F4/80$^+$ macrophages. CV, central vein. Scale bar, 100 µm.

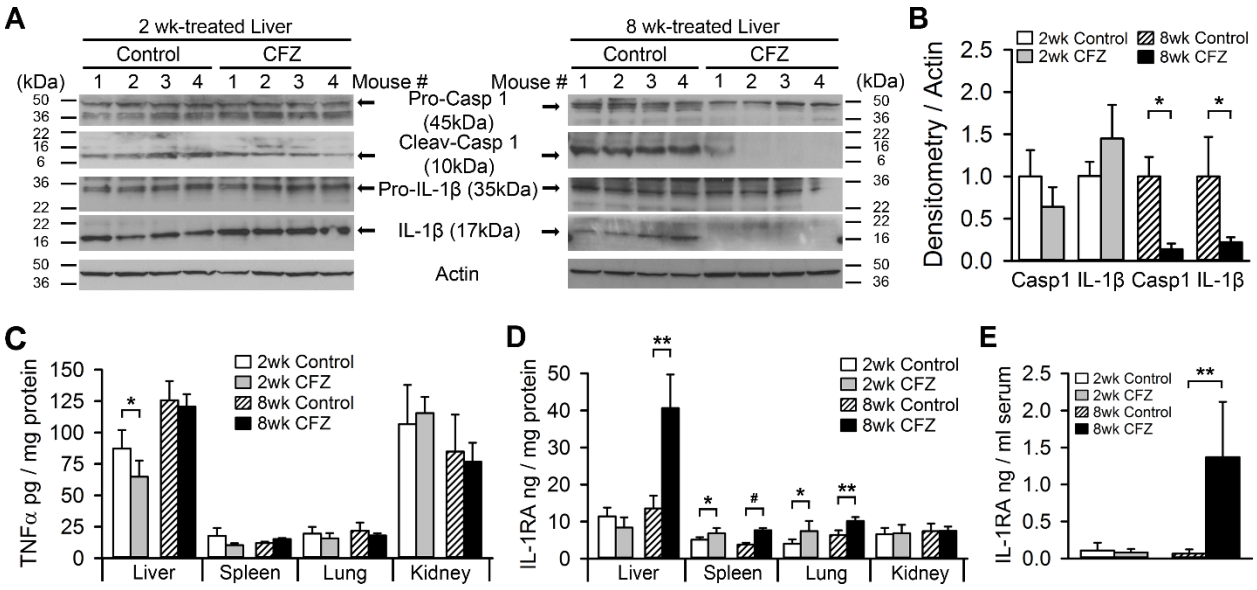

Figure 2-2. CFZ bioaccumulation reduces Casp 1 and IL-1β cleavage levels in the liver but increases IL-1RA expression. (**A**) Representative Western blots of liver homogenates showing that Casp 1 and IL-1β cleavage was not altered by 2 weeks of CFZ treatment but that 8 weeks of treatment reduced the detection of Casp 1 and IL-1β cleavage. (**B**) Densitometry of cleaved Casp 1 and IL-1β protein in 2- and 8-week-treated liver blots, normalized to actin ($n = 4$). Hepatic Casp 1 and IL-1β cleavage were reduced by 86 and 78%, respectively, in 8-week-CFZ-treated mice. (**C**) The levels of TNF-α in the spleen, lungs, and kidneys were unchanged by CFZ treatment, but there was a significant decrease in liver TNF-α from 2-week-CFZ-treated mice ($n = 4$ to 5). (**D**) The organs that bioaccumulate CFZ crystals – liver, spleen, and lung – displayed increased IL-1RA expression, whereas the kidney, which does not accumulate CFZ, did not show changes in IL-1RA expression ($n = 4$ to 5). (**E**) Serum IL-1RA levels were unchanged after 2 weeks but were increased 21-fold after 8 weeks of CFZ treatment. The serum TNF-α and IL-1β levels were below the limit of detection of the assay ($n = 6$). *, $P \leq 0.05$; **, $P \leq 0.01$; #, $P \leq 0.001$. Data are means ± the SD, and an unpaired Student *t* test was used to compare control mice versus CFZ-treated mice.

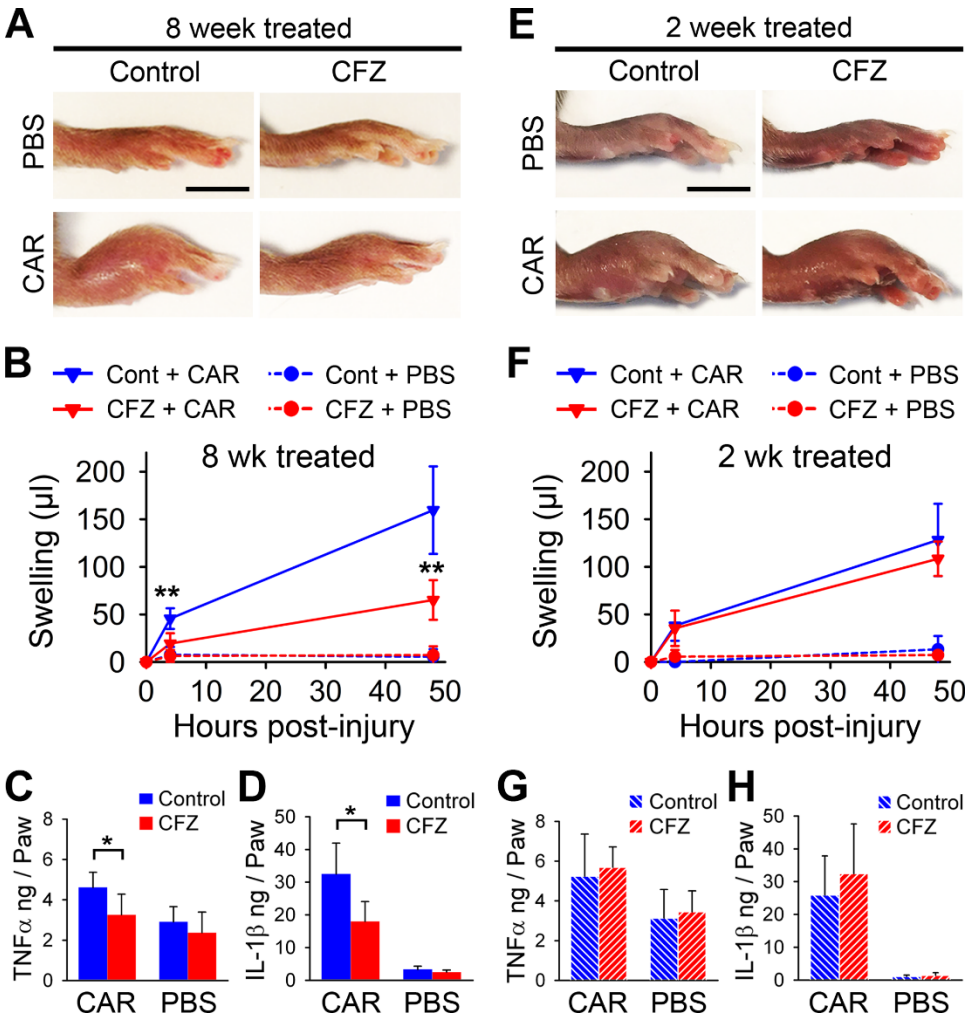

Figure 2-3. Systemic CFZ bioaccumulation and crystal formation dampens CAR-induced inflammatory response in the mouse footpad. (**A**) Representative photographs of paws 48 h after CAR or PBS footpad injection show markedly reduced paw swelling in 8-week-CFZ-treated mice compared to control mice. Scale bar, 5 mm. (**B**) Paw swelling, as measured by foot volume, was reduced on average by 57% as early as 4 h after CAR injection in 8-week-CFZ-treated mice compared to control mice and was sustained through 48 h. The footpad homogenate cytokine levels of IL-1β (**C**) and TNF-α (**D**) were reduced in 8-week-CFZ-treated mice at 48 h compared to untreated and injured paws. (**E** and **F**) Representative photographs of paws 48 h after CAR or PBS footpad injection in 2-week-CFZ-treated or control mice (**E**), which resulted in only a minor reduction in swelling at 4 and 48 h (**F**). Scale bar, 5 mm. (**G** and **H**) Associated footpad homogenate TNF-α (**G**) and IL-1β (**H**) levels were unchanged. PBS-injected paws did not show any difference in cytokine expression between CFZ-treated or control paws. Data are means ± the SD of $n = 5$ to 6/experiment. An unpaired Student t test was used to compare control versus CFZ-treated mice. *, $P \leq 0.05$; **, $P \leq 0.01$.

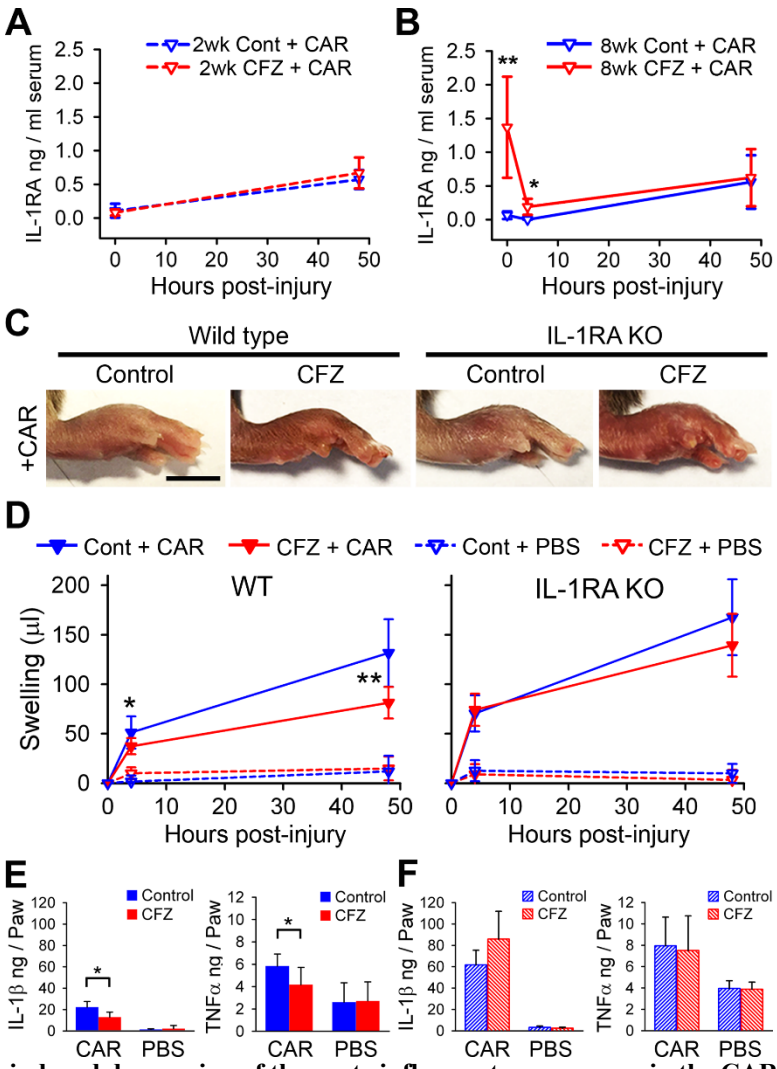

Figure 2-4. The CFZ-induced dampening of the acute inflammatory response in the CAR footpad model is mediated by circulating IL-1RA. (**A**) Two-week-CFZ-treated and control wild-type (WT) mice displayed similar serum IL-1RA levels before (0 h) and after (48 h) CAR injection. (**B**) Serum IL-1RA concentrations were significantly increased after 8 weeks of CFZ treatment compared to controls in WT mice (0 h). CAR injection in 8-week-CFZ-treated mice caused a sharp decline in serum IL-1RA concentrations by 4 h, whereas the levels in control CAR mice remained constant. At 48 h after CAR injection, the serum IL-1RA increased to similar levels in both control and CFZ-treated WT mice (data are means ± the SD of $n = 5$ to 8 animals/group/time point). (**C**) Representative images of inflamed paws of 6-week-CFZ-treated WT mice and IL-1RA KO mice at 48 h after CAR injection. (**D**) Footpad swelling, as measured by foot volume, was reduced by 27 and 38% at 4 and 48 h after CAR injection, respectively, in 6-week-CFZ-treated WT mice compared to control WT mice. In IL-1RA KO mice with CFZ treatment, paw swelling was similar at 4 h compared to untreated littermates, and at 48 h, swelling was marginally reduced (17%) compared to untreated IL-1RA KO mice. (**E**) Footpad homogenate levels of IL-1β and TNF-α were dampened in 6-week-CFZ-treated and CAR-injected WT mice at 48 h compared to control and CAR-injected paws. (**F**) Footpad homogenate levels of IL-1β and TNF-α were unaffected in 6-week-CFZ-treated and CAR-injected IL-1RA KO mice at 48 h compared to control and CAR-injected paws. Data are the compilation of two separate experiments and are presented as means ± the SD ($n = 7$ to 9). A Student t test was used to compare untreated versus CFZ-treated mice at each time point. *, $P \leq 0.05$; **, $P \leq 0.01$. Scale bar, 5 mm.

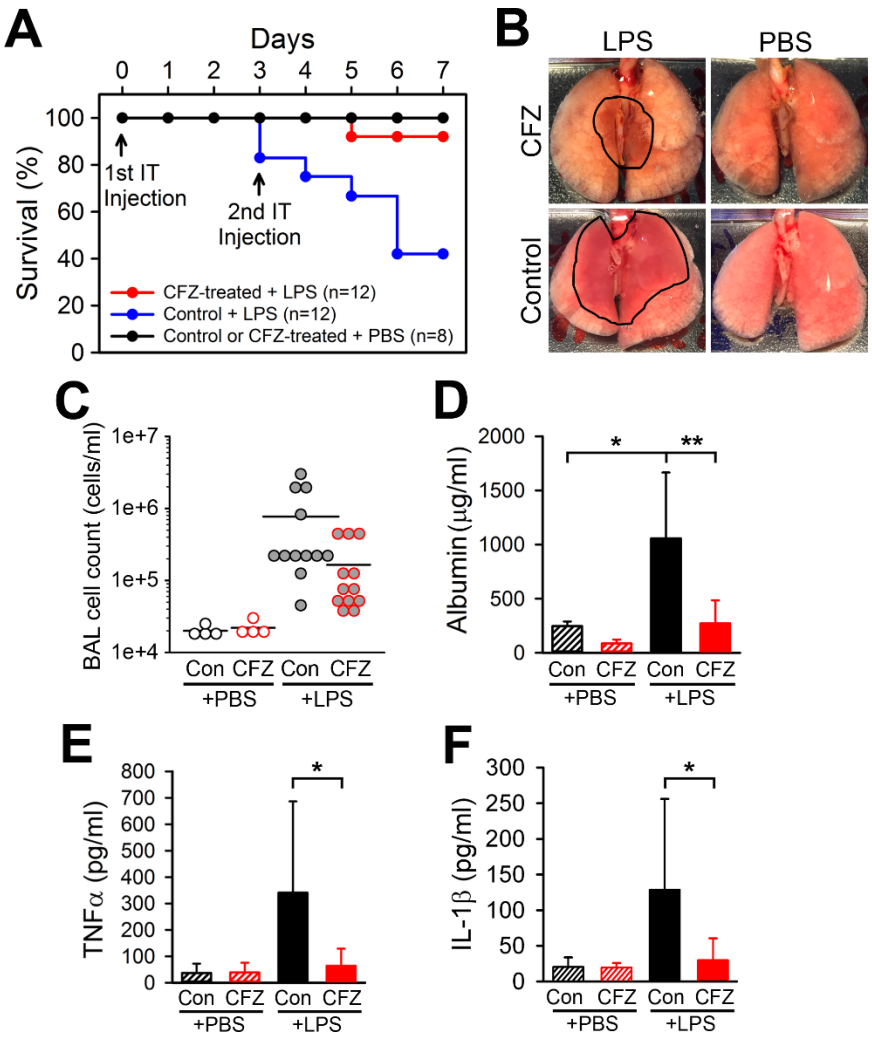

Figure 2-5. CFZ bioaccumulation enhances resistance to LPS-induced lung injury and improves mouse survival. (**A**) Kaplan-Meier survival curve showing the 92% survival rate of 8-week-CFZ-treated mice after LPS-induced acute lung injury compared to the 42% survival rate of control mice with LPS-induced injury. (**B**) A representative photograph shows the gross appearance of the lungs after PBS or LPS injection in control and CFZ-treated mice. Hemorrhaged areas caused by LPS injection are outlined in black lines. (**C** to **F**) CFZ treatment reduced LPS-induced increases in the BAL fluid cell count (**C**), albumin level (**D**), TNF-α level (**E**), and IL-1β level (**F**). The data are the compilation of two separate experiments and are presented as means ± the SD (PBS, $n = 4$; LPS, $n = 12$). One-way ANOVA was used to compare control versus CFZ-treated mice with PBS or LPS injections, and $P \leq 0.05$ was considered statistically significant. *, $P \leq 0.05$; **, $P \leq 0.01$.

2.9 Supporting Information

The supplemental methods and figures are available in the Appendix A.

2.10 References

1. Barry, V.C., et al., *A new series of phenazines (rimino-compounds) with high antituberculosis activity.* Nature, 1957. **179**(4568): p. 1013-5.

2. Cholo, M.C., et al., *Clofazimine: current status and future prospects.* J Antimicrob Chemother, 2012. **67**(2): p. 290-8.

3. Reibel, F., E. Cambau, and A. Aubry, *Update on the epidemiology, diagnosis, and treatment of leprosy.* Med Mal Infect, 2015. **45**(9): p. 383-93.

4. Tyagi, S., et al., *Clofazimine shortens the duration of the first-line treatment regimen for experimental chemotherapy of tuberculosis.* Proc Natl Acad Sci U S A, 2015. **112**(3): p. 869-74.

5. Lechartier, B. and S.T. Cole, *Mode of Action of Clofazimine and Combination Therapy with Benzothiazinones against Mycobacterium tuberculosis.* Antimicrob Agents Chemother, 2015. **59**(8): p. 4457-63.

6. Williams, K., et al., *Sterilizing activities of novel combinations lacking first- and second-line drugs in a murine model of tuberculosis.* Antimicrob Agents Chemother, 2012. **56**(6): p. 3114-20.

7. Banerjee, D.K., et al., *Some observations on the pharmacology of clofazimine (B663).* Am J Trop Med Hyg, 1974. **23**(6): p. 1110-5.

8. Baik, J., et al., *Multiscale distribution and bioaccumulation analysis of clofazimine reveals a massive immune system-mediated xenobiotic sequestration response.* Antimicrob Agents Chemother, 2013. **57**(3): p. 1218-30.

9. Keswani, R.K., et al., *Chemical Analysis of Drug Biocrystals: A Role for Counterion Transport Pathways in Intracellular Drug Disposition.* Mol Pharm, 2015. **12**(7): p. 2528-36.

10. Harbeck, R.J., et al., *Clofazimine crystals in the cytoplasm of pulmonary macrophages.* Ann Pharmacother, 1999. **33**(2): p. 250.

11. Sukpanichnant, S., et al., *Clofazimine-induced crystal-storing histiocytosis producing chronic abdominal pain in a leprosy patient.* Am J Surg Pathol, 2000. **24**(1): p. 129-35.

12. Jadhav, M.V., et al., *Tissue concentration, systemic distribution and toxicity of clofazimine--an autopsy study.* Indian J Pathol Microbiol, 2004. **47**(2): p. 281-3.

13. Tall, A.R. and L. Yvan-Charvet, *Cholesterol, inflammation and innate immunity.* Nat Rev Immunol, 2015. **15**(2): p. 104-16.

14. Martinon, F., et al., *Gout-associated uric acid crystals activate the NALP3 inflammasome.* Nature, 2006. **440**(7081): p. 237-41.

15. Gehring, U., et al., *Traffic-related air pollution and the development of asthma and allergies during the first 8 years of life.* Am J Respir Crit Care Med, 2010. **181**(6): p. 596-603.

16. Sint, T., J.F. Donohue, and A.J. Ghio, *Ambient air pollution particles and the acute exacerbation of chronic obstructive pulmonary disease.* Inhal Toxicol, 2008. **20**(1): p. 25-9.

17. Mackey, J.P. and J. Barnes, *Clofazimine in the treatment of discoid lupus erythematosus.* Br J Dermatol, 1974. **91**(1): p. 93-6.

18. Lo, J.S., R.E. Berg, and K.J. Tomecki, *Treatment of discoid lupus erythematosus.* Int J Dermatol, 1989. **28**(8): p. 497-507.

19. Chuaprapaisilp, T. and T. Piamphongsant, *Treatment of pustular psoriasis with clofazimine.* Br J Dermatol, 1978. **99**(3): p. 303-5.

20. Podmore, P. and D. Burrows, *Clofazimine--an effective treatment for Melkersson-Rosenthal syndrome or Miescher's cheilitis.* Clin Exp Dermatol, 1986. **11**(2): p. 173-8.

21. Bezerra, E.L., et al., *Double-blind, randomized, controlled clinical trial of clofazimine compared with chloroquine in patients with systemic lupus erythematosus.* Arthritis Rheum, 2005. **52**(10): p. 3073-8.

22. Venkateswarlu, B., et al., *Role of rifampin and clofazimine ointments in the treatment of leprosy.* Int J Lepr Other Mycobact Dis, 1992. **60**(2): p. 269-70.

23. Yoon, G.S., et al., *Phagocytosed Clofazimine Biocrystals Can Modulate Innate Immune Signaling by Inhibiting TNFalpha and Boosting IL-1RA Secretion.* Mol Pharm, 2015. **12**(7): p. 2517-27.

24. Baik, J. and G.R. Rosania, *Molecular imaging of intracellular drug-membrane aggregate formation.* Mol Pharm, 2011. **8**(5): p. 1742-9.

25. Otterness, I.G. and P.F. Moore, *Carrageenan foot edema test.* Methods Enzymol, 1988. **162**: p. 320-7.

26. Matute-Bello, G., C.W. Frevert, and T.R. Martin, *Animal models of acute lung injury.* Am J Physiol Lung Cell Mol Physiol, 2008. **295**(3): p. L379-99.

27. Lax, S., et al., *Using a non-invasive assessment of lung injury in a murine model of acute lung injury.* BMJ Open Respir Res, 2014. **1**(1): p. e000014.

28. Nayak, S., et al., *Immune responses and hypercoagulation in ERT for Pompe disease are mutation and rhGAA dose dependent.* PLoS One, 2014. **9**(6): p. e98336.

29. Toth, L.A., *Defining the moribund condition as an experimental endpoint for animal research.* ILAR J, 2000. **41**(2): p. 72-9.

30. Nemzek, J.A., et al., *Humane endpoints in shock research.* Shock, 2004. **21**(1): p. 17-25.

31. Baik, J. and G.R. Rosania, *Macrophages sequester clofazimine in an intracellular liquid crystal-like supramolecular organization.* PLoS One, 2012. **7**(10): p. e47494.

32. Keswani, R.K., et al., *A far-red fluorescent probe for flow cytometry and image-based functional studies of xenobiotic sequestering macrophages.* Cytometry A, 2015. **87**(9): p. 855-67.

33. Duewell, P., et al., *NLRP3 inflammasomes are required for atherogenesis and activated by cholesterol crystals.* Nature, 2010. **464**(7293): p. 1357-61.

34. Ioannou, G.N., et al., *Hepatic cholesterol crystals and crown-like structures distinguish NASH from simple steatosis.* J Lipid Res, 2013. **54**(5): p. 1326-34.

35. Simard, J.C., et al., *Silver nanoparticles induce degradation of the endoplasmic reticulum stress sensor activating transcription factor-6 leading to activation of the NLRP-3 inflammasome.* J Biol Chem, 2015. **290**(9): p. 5926-39.

36. Demento, S.L., et al., *Inflammasome-activating nanoparticles as modular systems for optimizing vaccine efficacy.* Vaccine, 2009. **27**(23): p. 3013-21.

37. Peeters, P.M., et al., *Silica-induced NLRP3 inflammasome activation in vitro and in rat lungs.* Part Fibre Toxicol, 2014. **11**: p. 58.

38. Gabay, C., et al., *Interleukin 1 receptor antagonist (IL-1Ra) is an acute-phase protein.* J Clin Invest, 1997. **99**(12): p. 2930-40.

39. Gabay, C., et al., *Production of IL-1 receptor antagonist by hepatocytes is regulated as an acute-phase protein in vivo.* Eur J Immunol, 2001. **31**(2): p. 490-9.

40. Dinarello, C.A. and J.W. van der Meer, *Treating inflammation by blocking interleukin-1 in humans.* Semin Immunol, 2013. **25**(6): p. 469-84.

41. Arend, W.P., *The balance between IL-1 and IL-1Ra in disease.* Cytokine Growth Factor Rev, 2002. **13**(4-5): p. 323-40.

42. McDougall, A.C., et al., *Splenic infarction and tissue accumulation of crystals associated with the use of clofazimine (Lamprene; B663) in the treatment of pyoderma gangrenosum.* Br J Dermatol, 1980. **102**(2): p. 227-30.

43. Shi, Y., A.D. Mucsi, and G. Ng, *Monosodium urate crystals in inflammation and immunity.* Immunol Rev, 2010. **233**(1): p. 203-17.

44. Riteau, N., et al., *ATP release and purinergic signaling: a common pathway for particle-mediated inflammasome activation.* Cell Death Dis, 2012. **3**: p. e403.

45. Bulakh, P.M., et al., *The effect of clofazimine on liver function tests in lepra reaction (ENL).* Lepr India, 1983. **55**(4): p. 714-8.

46. Cariello, P.F., et al., *Safety and tolerability of clofazimine as salvage therapy for atypical mycobacterial infection in solid organ transplant recipients.* Transpl Infect Dis, 2015. **17**(1): p. 111-8.

47. Kaluarachchi, S.I., B.M. Fernandopulle, and B.P. Gunawardane, *Hepatic and haematological adverse reactions associated with the use of multidrug therapy in leprosy--a five year retrospective study.* Indian J Lepr, 2001. **73**(2): p. 121-9.

48. Gent, S., et al., *Heart rate reduction and longevity in mice.* Basic Res Cardiol, 2015. **110**(2): p. 2.

49. Stokes, W.S., *Humane endpoints for laboratory animals used in regulatory testing.* ILAR J, 2002. **43 Suppl**: p. S31-8.

50. Van Rensburg, C.E., et al., *Antimicrobial activities of clofazimine and B669 are mediated by lysophospholipids.* Antimicrob Agents Chemother, 1992. **36**(12): p. 2729-35.

51. Oliva, B., et al., *Anti-staphylococcal activity and mode of action of clofazimine.* J Antimicrob Chemother, 2004. **53**(3): p. 435-40.

52. Fulda, S., et al., *Cellular stress responses: cell survival and cell death.* Int J Cell Biol, 2010. **2010**: p. 214074.

53. Kroemer, G., G. Marino, and B. Levine, *Autophagy and the integrated stress response.* Mol Cell, 2010. **40**(2): p. 280-93.

54. Fukutomi, Y., Y. Maeda, and M. Makino, *Apoptosis-inducing activity of clofazimine in macrophages.* Antimicrob Agents Chemother, 2011. **55**(9): p. 4000-5.

55. Sardiello, M., et al., *A gene network regulating lysosomal biogenesis and function.* Science, 2009. **325**(5939): p. 473-7.

56. Logan, R., A.C. Kong, and J.P. Krise, *Time-dependent effects of hydrophobic amine-containing drugs on lysosome structure and biogenesis in cultured human fibroblasts.* J Pharm Sci, 2014. **103**(10): p. 3287-96.

57. Parks, A., et al., *Autophagic flux inhibition and lysosomogenesis ensuing cellular capture and retention of the cationic drug quinacrine in murine models.* PeerJ, 2015. **3**: p. e1314.

58. Zhitomirsky, B. and Y.G. Assaraf, *Lysosomal sequestration of hydrophobic weak base chemotherapeutics triggers lysosomal biogenesis and lysosome-dependent cancer multidrug resistance.* Oncotarget, 2015. **6**(2): p. 1143-56.

59. Emanuel, R., et al., *Induction of lysosomal biogenesis in atherosclerotic macrophages can rescue lipid-induced lysosomal dysfunction and downstream sequelae.* Arterioscler Thromb Vasc Biol, 2014. **34**(9): p. 1942-1952.

60. Hasegawa, H., *Aggregates, crystals, gels, and amyloids: intracellular and extracellular phenotypes at the crossroads of immunoglobulin physicochemical property and cell physiology.* Int J Cell Biol, 2013. **2013**: p. 604867.

61. Hasegawa, H., et al., *In vivo crystallization of human IgG in the endoplasmic reticulum of engineered Chinese hamster ovary (CHO) cells.* J Biol Chem, 2011. **286**(22): p. 19917-31.

62. Bettigole, S.E. and L.H. Glimcher, *Endoplasmic reticulum stress in immunity.* Annu Rev Immunol, 2015. **33**: p. 107-38.

Chapter 3

Reverse Engineering the Intracellular Self-Assembly of a Functional Mechanopharmaceutical Device

3.1 Relevance to Thesis

This chapter was adapted from the following publication:

*Woldemichael T, Keswani RK, Rzeczycki P, **Murashov MD**, LaLone V, Gregorka B, Swanson JA, Stringer KA, Rosania GR. **2018**. Reverse engineering the intracellular self-assembly of a functional mechanopharmaceutical device. **Sci Rep.** 8(1):2934;doi:10.1038/s41598-018-21271-7*

This chapter incorporates the interdependence of lysosomal ion homeostasis and clofazimine drug biocrystal (Cy5(+) CFZ-HCl) accumulation. My contribution in this study involved studying the thermodynamic mechanism leading to differential stability of HCl salt form vs free base form of clofazimine by accurately measuring of the total solubility of CFZ-HCl as a function of pH, constructing a pH-dependent solubility profile of pure CFZ-HCl salt. By utilizing the data from this pH-dependent solubility profile of CFZ-HCl, the following physicochemical parameters were determined: $pH_{max,}$ apparent pK_a, CFZ-HCl aqueous solubility, CFZ free base intrinsic solubility, and K_{sp}. These key physicochemical parameters allowed us to discover the mechanism under which lysosomes of macrophages are able to accumulate and stabilize CFZ-HCl salt and not CFZ free base form of the drug. In fact, this study discusses the key lysosomal parameter for the physiological accumulation of biocrystal drug in a cell-type dependent manner by investigating the physicochemical properties of free base CFZ and CFZ-H^+Cl^- salt in relation to different cellular and subcellular conditions, such as pH and ion content,

and modeling the effects of various cell-type dependent lysosomal features, such as membrane proteins and ion content on biocrystal drug accumulation.

The results from this study enabled us to characterize the subcellular mechanism of a weakly basic drug (e.g. clofazimine) accumulation and stabilization in cells in a cell-type dependent manner, specifically in lysosomal environment of macrophages, *in vitro* and *in vivo*. Importantly, the findings supported our previously published results in regards to the unique accumulation and stabilization of CFZ self-assembled drug biocrystals, or crystal packing of CFZ-HCl salt *in vivo*, in macrophages.

3.2 Abstract

Weakly basic, poorly soluble chemical agents could be exploited as building blocks for constructing sophisticated molecular devices inside the cells of living organisms. Here, using experimental and computational approaches, we probed the relationship between the biological mechanisms mediating lysosomal ion homeostasis and the self-assembly of a weakly basic small molecule building block (clofazimine) into a functional, mechanopharmaceutical device (intracellular Crystal-Like Drug Inclusions – "CLDIs") in macrophage lysosomes. Physicochemical considerations indicate that the intralysosomal stabilization of the self-assembled mechanopharmaceutical device depends on the pH_{max} of the weakly basic building block and its affinity for chloride, both of which are consistent with the pH and chloride content of a physiological lysosomal microenvironment. Most importantly, *in vitro* and *in silico* studies revealed that high expression levels of the vacuolar ATPase (V-ATPase), irrespective of the expression levels of chloride channels, are necessary and sufficient to explain the cell-type dependent formation, stabilization, and biocompatibility of the self-assembled mechanopharmaceutical device within macrophages.

3.3 Introduction

Clofazimine (CFZ) is a weakly basic, poorly soluble, FDA-approved small molecule antibiotic that self-assembles [1, 2] into insoluble, biocrystalline structures known as Crystal Like Drug Inclusions (CLDIs) in macrophages of both mice and humans [3-5]. In mice, CFZ precipitates and accumulates in tissue macrophages as a biocrystalline hydrochloride salt (CFZ-H^+Cl^-). Remarkably, in Kupffer cells, splenocytes, alveolar macrophages, and peritoneal macrophages, the amount of intracellular CFZ-H^+Cl^- typically exceeds that of every other cellular component except water [5]. Known factors that contribute to this massive bioaccumulation and self-assembly phenomenon include the drug's high oral bioavailability, coupled with large daily doses, prolonged treatment regimens, and long elimination half-life [6].

The observed self-assembly, mechanical, and optical properties [7] of CFZ-H^+Cl^-, which can function as drug depots and photoacoustic contrast agents in macrophages, inspired our thinking about reverse engineering this weakly basic, small molecule chemical agent as a molecular building block for constructing other kinds of functional mechanopharmaceutical devices. Such devices could be used to influence the mechanical properties of cells. They could also be exploited as bio-responsive pharmaceutical or imaging agents by capitalizing on both physical and chemical interactions between cells and the self-assembled biocrystalline structures, *in vivo* [3, 5, 8]. In macrophages, CFZ-H^+Cl^- forms elastic structures, which bend and relax in response to biomechanical forces [7]. Furthermore, the presence of these mechanopharmaceutical devices inside macrophages is associated with augmented anti-inflammatory activity [9, 10]: upon phagocytosis, they lead to changes in cellular function, which include alterations in signal transduction pathways that affect the cell's inflammatory response [10]. Unlike the soluble form of CFZ, which tends to be cytotoxic, the phagocytosis of the self-assembled mechanopharmaceutical device does not lead to toxicity [8, 11].

Thus, given that macrophages express high levels of proton pumping vacuolar ATPase (V-ATPase) and chloride channels on their lysosomal membranes [12-14], and that weak bases are prone to accumulate inside lysosomes [15], we probed whether the expression levels of these lysosomal membrane proteins in macrophages actively drive the accumulation of CFZ-H^+Cl^- and its self-assembly in these cells. Using a well-established and published lysosomal ion regulation model [16], we studied how proton pumping and chloride transport mechanisms influenced cell-type specific stabilization of CFZ-H^+Cl^- inside lysosomes. In addition to verifying model predictions and further refining our understanding of the computational simulation results, we performed experiments using pharmacological inhibitors of V-ATPase [17] and chloride channels [18] to probe the biological mechanism underpinning the massive accumulation and self-assembly of the building block.

3.4 Materials and Methods

Solubility measurements

Freeze-dried CFZ-H^+Cl^- [11] samples were weighed and 25 mg was added to each of five scintillation vials. Mili-Q water (15 mL) was added to each vial to ensure that CFZ-H^+Cl^- crystals were in great excess. An aliquot of 0.1 M NaOH was added to each vial to achieve the initial equilibration pH measurements as follows: sample vials 1-5 initially contained 0, 40, 80, 120, and 200 μL of 0.1 M NaOH solution, respectively. After a 24-hour equilibration period, 10 μL of 0.1 M NaOH was added each day for a period of five days resulting in pH range of 4.5 to 8.9. The sample vials were placed on a magnetic stirrer plate in a 25 °C water bath. Each sample was allowed to equilibrate for at least 24 hours, after which 500 μL of sample was removed and filtered through a Spin-X centrifuge tube filter (0.45 μm cellulose acetate, 2 mL polypropylene tubes, non-sterile, Costar®, Cat # 8163) for 4 min @ 10,000 rpm. The pH of the filtered sample

was determined (UltraBasic pH meter, Denver Instrument, Bohemia, NY), after which the sample was subjected to HPLC analysis (see Supplementary Methods in Appendix B) (Waters Alliance, Separations Module 2695) to determine the total solubility of the drug at the measured pH. For each sample, solubility measurement was performed in triplicate, and the average was used to construct the total drug solubility-pH profile. The standard curve was generated using CFZ-H^+Cl^- crystals that were dissolved in the mobile phase at known concentrations (1-50 μM).

Thermodynamic equilibrium model of CFZ's solubility

For weak electrolytes, such as weakly basic drugs, the protonation state of the drug (B) is dictated by the relationship between the drug's association constant (K_a) and the acidity of its environment (H_3O^+). This is represented by the following equilibrium expression:

$$B + H_3O^+ \rightleftarrows BH^+ + H_2O \quad (1)$$

Where BH^+ is the protonated form of the drug as a result of the interaction of the free base form of the drug with hydronium ion, and H_2O is the byproduct of the reaction and remains constant. Thus, the equilibrium constant (K) is multiplied by H_2O to obtain K_a. Therefore, equation (1) is re-written using K_a.

$$B + H_3O^+ \rightleftarrows BH^+ \quad (2)$$

The mass law equilibrium equation is written as the following, assuming an ideal solution where the activity of a given species equals the concentration of the species (represented by the brackets):

$$K_a = \frac{[BH^+]}{[B][H_3O^+]} \quad (3)$$

By writing the logarithmic form of equation (3), we have the following relationship, which is the Henderson-Hasselbach equation:

$$pH - pK_a = \log\frac{[B]}{[BH^+]} \quad (4)$$

The equation is re-written as the following to express the concentrations of both the neutral and ionized forms of the drug:

$$[\mathrm{B}] = [\mathrm{BH}^+] \times 10^{\mathrm{pH}-\mathrm{p}K_a} \quad (5)$$

$$[\mathrm{BH}^+] = [\mathrm{B}] \times 10^{\mathrm{p}K_a-\mathrm{pH}} \quad (6)$$

According to thermodynamic laws of mass action, the total amount of drug is comprised of both the neutral and ionized forms at any given pH of its environment [19]. Thus, the total solubility (S_T) of the drug is written as:

$$S_T = [\mathrm{B}] + [\mathrm{BH}^+] \quad (7)$$

However, depending on the pH of the solution, the total drug solubility equation must be slightly modified to account for the distinction of the primary species in the solid versus solution phase [19]. For pH < pH_{max}, the ionized form of the drug is the saturated species that is in equilibrium with the salt from of the drug in the solid phase; therefore, its solubility remains constant while the solubility of the neutral form of the drug varies with respect to pH. Therefore, by substituting equation (5) into equation (7), the total drug solubility for pH < pH_{max} is re-written as:

$$S_T = [\mathrm{BH}^+]_S \times (1 + 10^{\mathrm{pH}-\mathrm{p}K_a}) \quad (8)$$

Where the solid phase is denoted by the subscript "s".

To the contrary, for pH > pH_{max}, the neutral form of the drug is in the solid phase; thus, its solubility remains constant whereas the solubility of the ionized form of the drug varies with respect to pH. Therefore, by substituting equation (6) into equation (7), the total solubility for pH < pH_{max} can be re-written as:

$$S_T = [\mathrm{B}]_S \times (1 + 10^{\mathrm{p}K_a-\mathrm{pH}}) \quad (9)$$

Moreover, at pH = pH_{max}, both the ionized and neutral forms of the drug are the saturating species, where both the salt and free base precipitate forms are in the solid phase. Thus, equation (7) can be re-written as:

$$S_T = [B]_S + [BH^+]_S \quad (10)$$

For our purpose, we substituted our model drug CFZ in the above equations (1-10). Rewriting equation (7) results in the following total CFZ-H^+Cl^- solubility equation:

$$S_T = [CFZ]_S + [CFZH^+] \quad (11)$$

Where the solid phase, which in this case is the free form of CFZ, is denoted by the subscript "s", and the ionized form of the drug, $[CFZH^+]$, is in the solution phase, and similar to equation (6), is dictated by pK_a and pH as follows:

$$[CFZH^+] = [CFZ]_S \times 10^{pK_a - pH} \quad (12)$$

Thus, by substituting equation (12) into equation (11), we obtain the following:

$$S_T = [CFZ]_S \times (1 + 10^{pK_a - pH}) \quad (13)$$

Furthermore, by using different combinations of any two solubility-pH data points from the experimental total solubility-pH measurements, the pK_a and the intrinsic free base solubility values were simultaneously solved using equation (13). Then, by substituting these values into equation (13), the total CFZ-H^+Cl^- solubility was calculated for the given range of pH 4.5 to 8.9, and the experimentally obtained total drug solubility-pH curve was fitted. Furthermore, in order to generate the total solubility-pH dataset for pH below pH_{max}, we used the following equation:

$$S_T = [CFZ] + [CFZH^+]_S \quad (14)$$

Similar to equation (8), equation (14) can be further expressed as:

$$S_T = [CFZH^+]_S \times (1 + 10^{pH - pK_a}) \quad (15)$$

However, we first had to determine $[CFZH^+]_S$. Because we only used one form of the drug (CFZ-H^+Cl^- salt) as the starting material in the experimental measurements of total drug solubility as a function of pH, we used a mathematical proof approach to determine $[CFZH^+]_S$ and thereby pH_{max} (see Supplementary Methods in Appendix B) without necessarily having to experimentally generate a total drug solubility-pH curve for pH below pH_{max}.

Moreover, the salt solubility product (K_{sp}) of CFZ-H^+Cl^- is given by the following equation:

$$K_{sp} = [\mathrm{CFZH^+}]_S \times [\mathrm{Cl^-}] \quad (16)$$

However, because of the 1:1 stoichiometric relationship of $CFZH^+$ and Cl^- in CFZ-H^+Cl^-[7], the K_{sp} of CFZ-H^+Cl^- in an aqueous media can be expressed as following:

$$K_{sp} = ([\mathrm{CFZH^+}]_S)^2 \quad (17)$$

Animal experiments

Mice (4 week old, male C57BL/6J) were purchased from the Jackson Laboratory (Bar Harbor, ME) and acclimatized for 1 week in a specific-pathogen-free animal facility. Clofazimine (CFZ) (C8895; Sigma, St. Louis, MO) was dissolved in sesame oil (Shirakiku, Japan) to achieve a concentration of 3 mg/mL, which was mixed with Powdered Lab Diet 5001 (PMI International, Inc., St. Louis, MO) to produce a 0.03% drug to powdered feed mix, which was orally administered *ad libitum* for up to eight weeks. A corresponding amount of sesame oil was mixed with chow for vehicle treatment (control). Mice were euthanized via CO_2 asphyxiation and exsanguination. Animal care was provided by the University of Michigan's Unit for Laboratory Animal Medicine (ULAM), and the experimental protocol was approved by the Committee on Use and Care of Animals (Protocol PRO00005542). All animal experiments were done according to the protocol guidelines.

Alveolar macrophage isolation

Following euthanasia, the trachea was surgically exposed and cannulated with a 20G needle, and the lungs were lavaged by instilling 1 mL DPBS (Life Technologies) containing 0.5 mM EDTA (Sigma) six times. Approximately 90% of the instilled bronchoalveolar lavage (BAL) was retrieved. BAL was centrifuged (10 min at 400 x g, 4 °C), the supernatant removed, and the cell pellet was resuspended in RPMI 1640 media (Life Technologies) with 5% FBS (Life Technologies) and Penicillin/Streptomycin (Thermofisher). Cells were plated onto 4 or 8 chamber coverglass (#1.5, Lab-Tek II, Nunc, Rochester, NY) in RPMI for imaging studies. The cells were allowed to attach overnight, washed, and imaged in fresh RPMI.

Peritoneal macrophage isolation

Following euthanasia, a small incision was made in the lower abdomen. The peritoneal cavity was then flushed with 10 mL of ice cold DPBS containing 5% FBS (Sigma) and collected. The peritoneal lavage was centrifuged for 10 min at 400 x g, 4 °C, and then re-suspended in DMEM media (Life Technologies) with 5% FBS and Penicillin /Streptomycin and counted. The cells were plated into Mat-tek dishes overnight in a serum-free growth media, and washed five times with phosphate-buffered saline (PBS).

Macrophage depletion

Mice were fed CFZ or control diet continuously for a four-week period. Following two weeks of feeding, mice were treated with either liposomes containing either 7 mg/mL of clodronate or PBS (FormuMax Scientific Inc., Sunnyvale, CA) for two weeks. Mice were initially treated with 200 µL of liposomes followed by 100 µL injections twice per week (or a matching volume of PBS) to ensure continual macrophage depletion. Liposomes were injected

intraperitoneally, as previously described [20]. After completing four weeks of feeding and two weeks of liposome treatment, mice were sacrificed and tissues were collected.

Biochemical analysis of CFZ in tissues

The concentration of CFZ in the organs of mice was determined spectrophotometrically. After four weeks of CFZ- or vehicle-diet treatment, mice were euthanized via CO_2 asphyxiation, and organs were collected. Tissue (20-30 mg) was homogenized in 500 μL of radioimmunoprecipitation assay buffer (Sigma) with added protease inhibitors (Halt protease and phosphatase inhibitor cocktail and 0.5 M EDTA; Thermo Pierce, Rockford, IL). Drug was extracted from homogenate (350 μL) with three washes with xylenes (1 mL). The drug was then extracted from the xylene with three 1 mL passes of 9 M sulfuric acid. The concentration of CFZ present in the tissue was determined using a 96-well plate reader (Biotek Synergy 2, Winooski, VT) (wavelength 540 nm). To account for extraction yield, untreated liver and spleen samples were spiked with known amounts of CFZ prior to extraction, and were analyzed in the same plate as the CFZ treated samples. The mass of CFZ per organ was determined using the yield-corrected concentration of CFZ in the mass of tissue analyzed, as determined through use of a standard curve with known concentrations of CFZ, and is reported as mg CFZ/g tissue.

Biochemical analysis of CFZ in plasma

Blood was collected and centrifuged (7,000 × g for 5 minutes). The resulting supernatant serum was extracted with acetonitrile (90% extraction efficiency) for 10 min at 4 °C with vortexing. After centrifugation (15,000 rpm, 4 °C), the supernatant was injected into a Waters Acquity UPLC H-Class (Waters, Milford, MA) equipped with an Acquity UPLC BEH C18 column (1.7 μm, 2.1 mm [inner diameter] by 100 mm; Waters, Milford, MA). Mobile phase A was 5 mM ammonium acetate, adjusted to pH 9.9 with ammonium hydroxide, and mobile phase

B was acetonitrile. The flow rate was 0.35 ml/min, with a linear gradient from 50 to 100% phase B over 1.5 min, followed by holding at 100% for 1.5 min, a return to 50% phase B, and then re-equilibration for 2.5 min. Standards were prepared by spiking untreated plasma samples with known amounts of clofazimine, ranging from 0 to 30 μM. Peak area was determined using Empower 3 Software (Waters, Milford, MA).

Sample preparation for microscopy

In preparation for cryosectioning, portions of each organ were removed, immediately submerged in OCT (Tissue-Tek catalog no. 4583; Sakura), and frozen (-80 °C). Cryosectioning (5 μm) was carried out using a Leica 3050S Cryostat (Leica Biosystems Inc., Buffalo Grove, IL). Immunohistochemistry of F4/80 (Abcam, 1:500 dilution) was performed using Alexa-Fluor 488 (Abcam, 1:500 dilution).

Deep-etch, freeze-fracture electron microscopy

At the time of euthanasia, the liver was collected and kept cold (4 °C). The organ was frozen against a copper block, cooled with liquid helium, and stored in liquid nitrogen. The sample was fractured with Balzers 400 nitrogen cooled vacuum evaporator and freeze-etched for two minutes (-100 °C). A rotary replica was generated with 2 nm platinum and backed with 10 nm carbon film support. It was cleaned with chromo-sulfuric cleaning solution (Fisher Scientific, cat# SC88) for twelve hours and rinsed with DI water. The sample was picked up on formvar coated grids and viewed on a JEOL 1400 electron microscope with an AMT camera (JEOL USA, Inc., Peabody, MA).

Spectral confocal microscopy

For the preparation of slides, CFZ-H^+Cl^- crystals suspended in PBS (20 μl) were placed on a glass slide and a cover-slip was applied onto the sample prior to imaging. Spectral confocal

microscopy was performed on a Leica Inverted SP5X confocal microscope system with two-photon FLIM (Leica Microsystems, Buffalo Grove, IL) using excitation wavelengths (470–670 nm). Image analysis and quantification were performed on Leica LAS AF. Several regions of interest of individual crystals were used to obtain fluorescence data, which were imported into MS-Excel for further analysis. All fluorescence yields were normalized to the maximum fluorescence yield measured across the tested spectral range, and background subtracted using data obtained from a blank slide.

Epifluorescence microscopy of cells incubated with CFZ and Lysotracker® Blue

Macrophage-derived RAW264.7 cells (ATCC, Manassas, VA, ATCC Number: TIB-71™) at a high seeding density of 100,000 cells/well, were grown in 8-chamber multiwell plates (Lab-Tek® II, Nunc, Rochester, NY) in Dulbecco's Modified Eagles Medium (DMEM) + 10% Fetal Bovine Serum (FBS) + 1% Penicillin/Streptomycin (P/S) (500 µl/well growth media); cells were pre-incubated with CFZ (20 µM) in DMSO for 24-72 hours. For lysosomal confirmation, RAW264.7 cells were seeded at 30,000 cells/well in an 8-chamber multiwell plate (500 µl/well growth media). Twenty-four hours later, the growth media was replaced with media containing varying concentrations (0, 1, 10, 20 µM) of Lysotracker® Blue DND-22 (Thermo Fisher Scientific, Waltham, MA, Catalog No. L7525, excitation/emission maxima ~ 373/422 nm) and CFZ (10 µM). Visualization of all samples (cells or crystals) was done on a Nikon Eclipse T*i* (Nikon Instruments, Melville, NY). Fluorescence filters (excitation/emission) were optimized for 4,6-diamidino-2-phenylindole dihydrochloride (DAPI) (350/405 nm, exposure - 550 ms, *violet*), fluorescein isothiocyanate (FITC) (490/510 nm, exposure - 100–500 ms, *green*), Texas Red (590/610 nm, exposure - < 500 ms, *red*), and Cy5 (640/670 nm, exposure - 500 ms, *far-red*). The Pearson's Co-localization Coefficient (PCC) was computed for each individual cell as ROIs

using the scatterplot distribution within the Nikon Elements AR software. Brightfield color photographs were acquired using a Nikon DS-Fi2 camera, whereas fluorescence photographs were acquired using a Photometrics CoolSNAP^{TM} *MYO* (Photometrics, Tucson, AZ) camera.

Quantitative cytometric analysis

Following macrophage staining, the population of macrophages was determined by taking the ratio of the total F4/80 signal to the total nuclear signal across an image. Because of the unique Cy5-specific fluorescence property of CLDIs [11], the prevalence of CLDIs was determined by taking the ratio of the total Cy5 signal to the total nuclear signal across an image. 5 images per mouse per organ were analyzed.

Drug stability in a lysosomal microenvironment

CLDIs were isolated from spleen and liver of 8-week CFZ treated mice based on previously published protocols [10, 21]. Free base CFZ crystals were pure CFZ crystals (Sigma-Aldrich, C8895). A speck (<< 1mg) of isolated CLDIs, CFZ-H^+Cl^- crystals, and free base CFZ crystals were placed in 2 mL of each of the stability testing medias: 1x PBS (pH 7.4), lysosomal buffer without sodium chloride (LB-, pH 4.5), and lysosomal buffer with sodium chloride (LB+, pH 4.5). Lysosomal buffers were prepared according to a previously published protocol [22]. Samples were stirred in media for 5-7 days; after which the stability of crystals from each sample was monitored using brightfield and fluorescence microscopy using a Nikon Eclipse Ti inverted microscope (Nikon Instruments, Melville, NY). Look-up-tables (LUTs) and exposure times were maintained the same throughout the samples.

Multi-parameter microscopy

Multi-parameter polarization, brightfield, and fluorescence microscopy was conducted using a Nikon Eclipse Ti inverted microscope (Nikon Instruments, Melville, NY). Polarization

microscopy was performed using the LC-PolScope [23], with the illuminating light narrowed to 623 nm by an interference filter (623 ± 23 nm, Semrock Optics, Rochester, NY). Polarization images were captured using an Abrio imaging system (Cambridge Research & Instrumentation, Inc, Woburn, MA). Brightfield images were captured using the Nikon DS-3 camera (Nikon Instruments) and fluorescence images were taken with the Photometrics CoolSnap MYO camera system (Photometrics, Tuscon, AZ) under the control of Nikon NIS-Elements AR software (Nikon Instruments). Illumination for fluorescence imaging was provided by the X-Cite 120Q Widefield Fluorescence Microscope Excitation Light Source (Excelitas Technology, Waltham, MA). Images were acquired and analyzed as previously described [24].

Raman sample preparation and measurements

Isolated mouse alveolar macrophages were transferred onto pre-sterilized silicon chips (16008; Ted Pella, Inc., Redding, CA) and incubated for 1h (@ 37 ºC and 5% CO_2) to allow adherence to chip. The cell-containing chips were washed by brief submersion into isotonic NaCl (0.9%) solution followed by DI water, then allowed to air-dry. Raman measurements were acquired with the WiTec alpha300R confocal Raman microscope (WITec, Ulm, Germany) equipped with two excitation lasers: a 532 nm solid-state sapphire and a 785 nm wavelength-stabilized diode (0-55 mW and 0-88 mW tunable intensity ranges, respectively). A 100X air objective (Zeiss Epiplan-NEOFLUAR, NA (numerical aperture) = 0.9) coupled to a CCD detector via a multi-mode fiber of 100 μm diameter serving as the confocal pinhole, produced 0.72 μm and 1.06 μm illumination spots (for 532 nm and 785 nm lasers respectively). To minimize fluorescence background from pure CFZ and CFZ-H^+Cl^- reference crystals, samples were excited with 785 nm. The 532 nm laser was utilized for excitation of biological samples due to its elicitation of a stronger Raman signal from the microscopic inclusions/CLDIs of

interest. Point spectra were acquired ($n \geq 40$ cells/group) by focusing a laser spot on cytoplasmic inclusions, CLDIs, or pure reference crystals: at each point, the laser was tuned to optimum intensity, and acquired point spectra over an integration time of 25 seconds. Individual raw spectra were baseline-subtracted and normalized using a MATLAB® processing algorithm developed in-house. For single-cell Raman imaging, the 532 nm excitation laser was raster-scanned across a 50×50 micron area with a step-size of 0.5 microns, yielding spectral datasets consisting of 10,000 spectra per cell. Exploiting the dramatic spectral differences arising from fluorescence of different CFZ forms, the un-processed Raman spectra were linearly deconvoluted via WiTec ProjectFOUR software's basis component analysis using representative un-processed reference spectra obtained from untreated cells, pure free base CFZ crystals, pure CFZ-H^+Cl^- crystals, and the silicon substrate. Dataset acquisition, processing, and image display parameters were performed equivalently for each cell specimen.

CLDI injection and stabilization assay

To determine how macrophages stabilize CLDIs, mice were treated with either liposomal PBS or liposomal clodronate, as previously described [25]. 48 hours after liposome administration, mice were injected I.P. with 200 μg of CLDIs suspended in 1 mL of PBS ($n = 3$ mice per group per time point). At time points ranging from 0 to 48 hours, the mice were euthanized, the peritoneal lavage was collected and pelleted, and the drug content within the pellet was analyzed using the previously described spectrophotometric analysis method. Using a simple exponential regression with recovered drug content, the half-life was estimated.

CLDI loading within individual macrophages

Using the total recovered mass of CLDIs within the liver and spleen, the CLDI loading within individual xenobiotic-sequestering macrophages was estimated using literature reported

values for macrophage numbers [26] within the liver and spleen, corrected for the percentage of cells which contained a CLDI. For the clodronate depleted organs, the reduction was accounted for with the quantified reduction in total F4/80 signal.

Cell culture and pharmacological treatment

For pharmacological inhibition experiments, macrophage-derived RAW264.7 cells (ATCC, Manassas, VA, ATCC Number: TIB-71^{TM}), at a very high seeding density of 50,000 cells/well grown in a 96 well tissue culture plate in 280 µl/well of DMEM + 10% FBS + 1% P/S (growth media), were pre-incubated (4h) with varying concentrations of Bafilomycin A1 (BafA1; Sigma-Aldrich, St. Louis, MO, Cat. No. B1793) (0-10 nM) and NPPB (Sigma-Aldrich, St. Louis, MO, Cat. No. N4779) (0-200 µM), after which CFZ (dissolved in DMSO) was added to achieve a final concentration range of 0-10 µM. The effect of the treatment on cell viability was assessed by an XTT assay (Roche, UK).

Drug uptake measurements

Measurement of CFZ uptake by RAW264.7 cells was performed using a modified absorbance spectroscopy method using 9 M H_2SO_4 (pH << 0.1) to digest the entire cell population and extract CFZ from the cells. At two time points (2 and 4h) after CFZ exposure, growth media was aspirated from the culture dish and the cells were washed twice with PBS before adding 9 M H_2SO_4 (100 µl/well). The plate was incubated at room temperature for 30 min before spectrophotometric quantification of CFZ using a Synergy 2 plate reader (BioTek, Winooski, VT) at 540 nm (Abs_{540}) and 750 nm (Abs_{750}) (for background). Standards were prepared on the same plate by adding 100 µl/well pre-determined standards of CFZ. Total CFZ uptake is reported as total intracellular drug (in picomoles) as measured and calculated using the standard curve. Assuming that the doubling time of 50,000 cells/well is ~ 11h [27], and that no

compromise of cell viability occurs because of the optimum dose used for both CFZ and the pharmacological inhibitors, the total number of cells/well at the time of cellular drug uptake measurement is ~ 68,000.

Experimental lysosomal pH measurements

Lysosomal pH was measured fluorometrically in peritoneal macrophages and macrophage-derived RAW264.7 cells, using methods described previously [28]. In brief, macrophages were incubated for 40h with CFZ crystals. 20h prior to measuring pH, cells were incubated for 15-18h with 150 µg/ml Oregon Green-labeled dextran-10kD (OGDx; Thermo-Fisher Scientific), and transferred to unlabeled culture medium for 3-5h to allow OGDx to traffic fully to lysosomes. Following transfer to Ringer's buffer, cells on Mat-tek dishes were observed in a Nikon TE300 microscope equipped for multichannel fluorescence microscopy with a 60X objective lens (N.A. 1.4). Phase contrast and three fluorescence images (excitation/emission: 440 nm/535 nm; 485 nm/535 nm; and 580 nm/630 nm) were collected from each field. The 580nm/630nm image was used to quantify clofazamine fluorescence. The ratio of the 485nm/525nm to 440nm/525nm images were used to measure lysosomal pH. Calibration of fluorescence ratios was obtained from cells incubated in ionophores and buffers as described in Davis and Swanson [28]. Average lysosomal pH was determined for individual cells.

Modeling lysosomal CFZ-H^+Cl^- accumulation

A Lysosomal ion regulation model which incorporates lysosomal membrane proteins, such as V-ATPase, CLC7, and membrane proton permeability was utilized [16], and further elaborated and modified (see Supplementary Methods in Appendix B) to explore the relationship between lysosomal ion homeostasis and lysosomal CFZ-H^+Cl^- accumulation and stabilization. In order to incorporate the lysosomal accumulation of CFZ-H^+Cl^- into the model as a function of

lysosomal proton and chloride ions, the rate of overall drug accumulation obtained from experimental findings [4, 29] was used to define the rates of both lysosomal proton ($H_{sequestered}$) and chloride ($Cl_{sequestered}$) sequestrations by CFZ, in units of molecules per second. We assumed these rates to be equal due to the proposed equal contribution of both proton and chloride ions in the intracellular formation and accumulation of CFZ-H^+Cl^- salt precipitates:

$$CFZH^+Cl^- = H_{sequestered} = Cl_{sequestered} \quad (18)$$

Model parameterization

The model incorporated 23 parameters: four were adjustable and the remaining 19 were fixed (Table S5-1 in Appendix B). Fixed parameters were given values obtained from the literature [16, 30-34], and are associated with physiological lysosomal ion homeostasis. Therefore, these parametric values are interchangeably referred hereon as "baseline input values" or "physiological baseline input values". The adjustable parameters are those values that were varied from their respective baseline input values in order to investigate their individual as well as combined effects on the physiological lysosomal pH, Cl^-, and membrane potential readout values, as discussed in the following subsections. These parameters include the number of active V-ATPase and CLC7 molecules per lysosome, as well as the cytoplasmic chloride concentration. In addition, the rates of proton and chloride sequestrations by CFZ are considered adjustable parameters as they are foreign to the lysosome.

Simulating lysosomal CFZ-H^+Cl^- accumulation

The previously mentioned rates of proton and chloride sequestrations by CFZ were adjusted to either 0.01 or 0.1 picomoles/cell/day [4, 29]. However, in our model simulations, we converted the units of these rates to picomoles/lysosome/day assuming there are ~ 100 lysosomes in a cell. From here onwards, we interchangeably refer to these rates, 0.01 and 0.1

picomoles/cell/day, as 1-fold (1X) and 10-fold (10X) rates of lysosomal CFZ-H^+Cl^- accumulation, respectively.

Simulating changes in lysosomal membrane proteins and cytoplasmic chloride amounts

In order to study the roles of V-ATPase, CLC7, and cytoplasmic chloride concentration on lysosomal accumulation of CFZ-H^+Cl^-, we varied the total numbers of active V-ATPase and CLC7 molecules per lysosome, and the cytoplasmic chloride concentration, while fixing the values of other lysosomal parameters at their baseline physiological input values in the presence as well as absence of lysosomal CFZ-H^+Cl^- accumulation. More specifically, to simulate the simultaneous inhibition of V-ATPase and CLC7, the total number of CLC7 molecules per lysosome was varied from 0 to 5,000 (resulting in 7-16 data-generating points) while, one parametric simulation at a time, the total number of V-ATPase molecules per lysosome was manually varied from 0 to 300 (resulting in 4-7 data-generating points). Moreover, to simulate the simultaneous inhibition of V-ATPase and cytoplasmic chloride, the cytoplasmic chloride concentration was varied from 0 to 10 mM (resulting in 16 data-generating points) while, one parametric simulation at a time, the total number of V-ATPase molecules per lysosome was manually varied from 0 to 300 (resulting in 4-7 data-generating points).

Using the aforementioned ranges of the adjustable lysosomal parameters, the corresponding lysosomal parameter inhibition range of 0 to 100% was calculated; where 0% represents no change from respective physiological baseline input value, and 100% represents the input value set to ~zero. The inhibition range was calculated as follows by comparing the corresponding input value (Adjusted Input Value) from the aforementioned given range with its respective physiological input value (Baseline Input Value):

$$\%\ \text{Inhibition} = \frac{\text{Baseline Input Value} - \text{Adjusted Input Value}}{\text{Baseline Input Value}} \times 100\% \quad (19)$$

Calculating the effect of lysosomal CFZ-H^+Cl^- accumulation on lysosomal ion homeostasis

Final lysosomal pH, chloride, and membrane potential were chosen as readout values because they are direct indicators of lysosomal ion homeostasis and physiology. Thus, parametric simulations of these variables were performed as a function of the aforementioned ranges of V-ATPase, CLC7, and cytoplasmic chloride in the absence and presence of lysosomal CFZ-H^+Cl^- accumulation at the rate of either 1X or 10X. Then, the readout values in the absence of lysosomal CFZ-H^+Cl^- accumulation were subtracted from those in the presence of lysosomal CFZ-H^+Cl^- accumulation in order to determine the effect of lysosomal CFZ-H^+Cl^- accumulation on lysosomal ion homeostasis.

Calculating the effects of V-ATPase, chloride channels, and cytoplasmic chloride on the physiological lysosomal accumulation of CFZ-H^+Cl^-

Time-plot simulations, where all of the lysosomal parameters were set to their respective baseline values in the absence of lysosomal CFZ-H^+Cl^- accumulation, were performed to obtain physiological final lysosomal pH, chloride accumulation, and membrane potential values, which from hereon we refer to as "physiological baseline readout values". Moreover, model parametric simulations of final lysosomal pH, Cl^-, and membrane potential as a function of simultaneous V-ATPase-CLC7 and V-ATPase-cytoplasmic chloride inhibitions were performed in the presence of lysosomal CFZ-H^+Cl^- accumulation at the rates of 1X and 10X. These were then subtracted from the physiological baseline readout values in order to calculate the effects of the simultaneous lysosomal parameter inhibitions on the dose-dependent lysosomal CFZ-H^+Cl^- accumulation.

Confirmation of steady-state and mass balance

For all of the aforementioned simulations, the final readout values were confirmed that they were steady-state values by performing the simulations for > 24h. We confirmed that mass balance was maintained in all of the simulations in the presence and absence of lysosomal CFZ-H^+Cl^- accumulation as long as a physiological pH gradient of up to 4.6 pH units was maintained across the lysosomal membrane.

3.5 Results

The weakly basic building block has pH-dependent solubility properties

CFZ is a weak base with two amines, which can be protonated depending on the pH of the immediate environment (Figure 3-1a). To study its pH-dependent solubility behavior, we used an established approach [19] (see Supplementary Methods in Appendix B for detailed explanation), which allowed an accurate measurement of the total solubility of CFZ-H^+Cl^- as a function of pH. From the experimental measurements, we calculated the solubility properties of CFZ, in an aqueous media at 25 ºC, which include its apparent p$K_{a,2}$ (p$K_{a'}$ = 6.08 ± 2.43x10^{-3}; 95% Confidence Interval = 6.07, 6.09) and intrinsic free base solubility (S_0 = 0.48 ± 4.05x10^{-6} µM; 95% CI = 0.48, 0.48) (Figure 3-1b). Moreover, to determine the effect of lysosomal Cl^- (Figure 3-1c) on the stability of the free base versus salt form of the drug, we performed drug stability experiments (Figure 3-1d) in the presence and absence of lysosomal buffer (pH 4.5, Cl^- concentration = 0-100 mM). We monitored drug stability by relying on the unique fluorescence profile of the different forms of CFZ: CFZ free base exhibits green and red fluorescence; peak excitation: 540–560 nm, peak emission: 560–600 nm, whereas CFZ-H^+Cl^- exhibits red and far red fluorescence; peak excitation: 560–600 nm, peak emission: 650–690 nm [11]. Indeed, the

fluorescence of CLDIs resembles the fluorescence of the synthesized CFZ-H^+Cl^- crystals (peak excitation: 560–600 nm, peak emission: 650–690 nm) (Figure S3-1 in Appendix B).

A low pH environment in the absence of Cl^- (LB-) induced the destabilization of both CFZ-H^+Cl^- and free base CFZ, without affecting the stability of CLDIs. To the contrary, a low pH environment in the presence of a physiological lysosomal Cl^- (LB+) induced the stabilization of CFZ-H^+Cl^- and CLDIs, whereas the free base CFZ precipitated out as CFZ-H^+Cl^- (Figure 3-1d). Thus, these findings reveal that the precipitation of CFZ as a hydrochloride salt was highly sensitive to small, but physiologically relevant variations in pH and chloride concentrations (pH_{max} = 4.5 ± 7.11x10^{-15}, 95% CI = 4.5, 4.5; and K_{sp} = 332.3 ± 3.71 μM^2, 95% CI = 323.1, 341.5) (Figure 3-1b, d); where the pH_{max} reveals the pH below which CFZ-H^+Cl^- salt formation occurs, and the K_{sp} elucidates the Cl^- concentration, which is > $(K_{sp})^{1/2}$ μM, that would further stabilize the salt form of the drug through a common-ion effect [35]. Thus, at the pharmacologically-relevant CFZ concentrations that have previously been measured in serum (1 to 20 μM), local variations in pH (~ 7.4 extracellular; ~ 7.2 cytosolic, and ~ 4.5 lysosomal) and chloride concentrations (~ 80 mM extracellular; ~ 10-20 mM in cytosol; and ~ 50-200 mM in lysosomes) can lead to a greater propensity of CFZ to precipitate as a hydrochloride salt in the lysosomal microenvironment (Figure 3-1c, d).

The intracellular organization of the self-assembled mechanopharmaceutical device

Prolonged administration of CFZ results in its accumulation in both human and animals as microscopic, insoluble, and membrane-bound aggregates, known as Crystal Like Drug Inclusions (CLDIs), which are primarily found within tissue macrophages [3-5]. CLDIs are primarily comprised of a protonated, hydrochloride salt of CFZ (Figure 3-2a) [7], which forms faceted structures possessing three orthogonal cleavage and multiple fracture planes with

lamellar spacing of 6 nm to 14 nm [21] (Figure 3-2b). These orthogonal cleavage and fracture planes correspond to the orthogonal crystallographic planes of the CFZ-H^+Cl^- unit cell (Figure 3-2c). When examined under polarized light (623 nm wavelength), the orthorhombic crystal structure of the deep red CLDIs [11, 29, 36] exhibits dichroism (Figure 3-2d) [24]. Due to the biological origin of the CLDIs [7], the interaction between the cell and crystal often leads to significant variations in its organization, impacting the manner in which it interacts with polarized light (Figure 3-2d). Furthermore, reference spectra of pure CFZ and CFZ-H^+Cl^- identified characteristic Raman peaks for clear distinction between the two forms (Figure 3-2e). Spectra obtained from cytoplasmic regions of untreated mouse alveolar macrophages were typical of biological specimens with no apparent contributions from drug. However, spectra obtained from cytoplasmic regions of 4- and 8-week CFZ-fed mouse alveolar macrophages revealed the presence of CFZ-H^+Cl^-, which dominated any Raman signal associated with biological specimens, and exhibited unique peak intensities and peak widths, which attribute to the geometric organization of the supramolecular structures: peaks generally become narrower and more intense with higher degree of order in samples, which suggests that by 8 weeks, the macrophages have organized the accumulated drug into supramolecular crystalline packages of CFZ-H^+Cl^- salt. Moreover, Raman imaging of single-cells revealed cytoplasmic accumulation of both forms of the drug after just 1 week and continuing through 4 weeks; at 8 weeks CLDI formation was apparent and clearly distinguishable from free base CFZ, as evidenced by non-overlapping Raman signals in the biocrystal regions of Raman image (Figure 3-2f).

Macrophages are necessary for the self-assembly of the mechanopharmaceutical device

To investigate whether macrophages play an active role in stabilizing CLDIs *in vivo*, macrophages were depleted by injecting mice (n = 3-4 per treatment group) intraperitoneally

with clodronate liposomes. This treatment depletes phagocytic cells without affecting non-phagocytic cells [20]. Moreover, the aforementioned CFZ's unique fluorescence characteristics were used to monitor the effect of macrophage depletion on the accumulation of CFZ-H^+Cl^- crystal. Following liposome therapy, the relative number of F4/80 positive macrophages within the liver and spleen of each treatment group was quantified using the total ratio of F4/80 to nuclear signal, revealing a significant reduction in the total macrophage population in the clodronate-CFZ fed group when compared to the PBS-CFZ treated group ($p < 0.05$, ANOVA, Tukey's HSD) (Figure 3-3a). Consequently, using the ratio between the intrinsic far-red fluorescence of CFZ-H^+Cl^- [37] and total nuclear signal, there was a significant reduction in the accumulation and stabilization of CFZ-H^+Cl^- within the liver and spleen ($p < 0.05$, ANOVA, Tukey's HSD) compared to the PBS-CFZ treated group (Figure 3-3b). More specifically, within the PBS-CFZ treated mice, the livers accumulated an average of 0.68 ± 0.27 mg CFZ/g tissue, while the clodronate-CFZ livers accumulated an average of 0.23 ± 0.09 mg CFZ/g tissue ($p < 0.05$, two-tailed Student's t-test); a reduction of nearly 66%. Similarly, the spleens of PBS-CFZ treated mice accumulated an average of 2.31 ± 0.40 mg CFZ/g tissue, compared to 0.70 ± 0.12 mg CFZ/g tissue in the clodronate-CFZ groups ($p < 0.01$, two-tailed Student's t-test); a reduction of 70%.

The individual drug loading within the macrophages of the liver and spleen was estimated based off of literature-reported values for macrophage populations in those two organs [26] and the total recovered drug within each organ, and there was no difference in total drug loading within either population of macrophage as a result of clodronate therapy (Figure 3-3c). Furthermore, there was no significant difference in mean plasma concentrations of CFZ at the end of therapy (Figure 3-3d). Taken together, this provides evidence that, while clodronate

therapy was reducing the macrophage population and subsequent bioaccumulation within the liver and spleen, it was not impacting the general bioavailability and absorption of CFZ in the body. To determine how macrophages stabilized the self-assembled mechanopharmaceutical devices, isolated CLDIs were injected I.P. into clodronate and PBS liposome treated mice and collected at time points from 0 to 48 hours (n = 3 mice per group per time point). Without macrophages present in the peritoneal cavity to internalize the CLDI, there was a significant reduction in the estimated half-life of the biocrystal ($p < 0.05$, ANOVA) (Figure 3-3e). This was confirmed via microscopic analysis of the peritoneal exudate 48 hours post-injection, with CLDIs becoming internalized by the macrophage and retaining their far-red fluorescence in the PBS-treatment group, while the clodronate-treated group showed reduced CLDI content within the exudate (Figure 3-3f).

Additionally, in order to confirm that clodronate did not impact drug accumulation within other macrophage populations, alveolar macrophages were collected and analyzed. Within the alveolar macrophage population, there was no significant difference in total cell number collected between the PBS and clodronate-treated groups ($p = 0.48$, two-tailed Student's t-test), as well as in the ability of the cells to accumulate CFZ in the form of a CLDI; where each alveolar macrophage population contained approximately 20% CLDI-positive cells ($p = 0.36$, two-tailed Student's t-test) (Figure 3-3g). Thus, the specific effect of clodronate liposomes on liver and spleen CLDIs and CFZ content, as well as the increased rate of CLDI destabilization and solubilization in the absence of peritoneal macrophages provide evidence that these cells are directly responsible for the *in vivo* accumulation, self-assembly, and stabilization of CFZ-H^+Cl^-.

The intracellular accumulation, protonation, and self-assembly of the building block in cytoplasmic vesicles does not interfere with lysosomal pH

Taking advantage of the aforementioned CFZ's unique fluorescence properties, we studied the accumulation of the un-protonated free base and protonated hydrochloride salt form of the drug in macrophages. Incubation of macrophages with CFZ *in vitro* revealed vesicular staining pattern consistent with CFZ free base (peak excitation: 540–560 nm, peak emission: 560–600 nm) as well as CFZ-H^+Cl^- (peak excitation: 560–600 nm, peak emission: 650–690 nm) [11]. Both fluorescent forms were visible in CFZ-treated cells and absent in untreated, control cells (Figure 3-4a and Figure S3-2 in Appendix B). Based on the observed little overlap of their orthogonal fluorescence signals, CFZ-H^+Cl^- did not co-localize with free base CFZ (Pearson's Colocalization Coefficient - PCC between green and far-red fluorescence = 0.30 ± 0.29) (Figure S3-3 in Appendix B). In addition, when cells were co-incubated with both CFZ and Lysotracker Blue (LB), LB fluorescence signal (excitation: 373 nm, emission: 422 nm) was inhibited in the cytoplasm and displaced [38] to the nucleus (based on the observed nuclear staining), whereas the punctate green and far-red fluorescence of CFZ were clearly visible in the cytoplasm of these cells (Figure 3-4c, and Figures S3-2 and S3-3 in Appendix B). As a control experiment, we measured the lysosomal pH of macrophages following phagocytosis of CLDIs in macrophage-derived RAW264.7 cells as well as in peritoneal macrophages of 8-week CFZ-fed mice (Figure 3-4d). In both cases, the lysosomal pH was not physiologically affected by the presence of the CFZ, as reflected by < 0.1 pH unit difference between the drug-free and drug-containing peritoneal macrophages and RAW264.7 cells. Thus, CFZ uptake in macrophage lysosomes does not perturb physiological lysosomal pH homeostasis, which is required for various lysosomal functions, such as lysosomal trafficking and degradation of intrinsic and extrinsic materials

within the lysosome by various pH-dependent hydrolytic lysosomal enzymes, which are essential for overall cellular homeostasis and viability [39]. Moreover, because the fluorescence signals of Lysotracker® probes are pH-independent [40], we interpret this to mean that intralysosomal CFZ accumulation interferes with Lysotracker probe accumulation through a mechanism that is independent of changes in lysosomal pH.

The building block's self-assembly mechanism is biocompatible with the lysosome

To identify the candidate mechanism driving CFZ-H^+Cl^- accumulation and stabilization in lysosomes, we used a well-established systems-based mathematical model of lysosomal ion regulation. We first performed a simultaneous variation of the number of active V-ATPase and chloride channels per lysosome (resulting in 0 to 100% inhibition of both parameters from their respective baseline physiological input values of 300 and 5000) in the presence and absence of dose-dependent lysosomal CFZ-H^+Cl^- accumulation (0 to 0.01 picomoles/cell/day), as measured *in vitro* [4, 29]. The simulation results indicated that CFZ-H^+Cl^- accumulates at the measured rate of 0.01 picomoles/cell/day exerting a negligible effect on lysosomal pH, Cl^-, and membrane potential from respective physiological baseline readout values (4.53 pH units, 224.6 mM, and 0.79 mV). Only a significant ($\geq$ 97%) reduction in the total V-ATPase amount per lysosome led to changes in these values (Figure 3-5a). Consistent with this, < 97% V-ATPase inhibition per lysosome was required for the physiological accommodation of lysosomal CFZ-H^+Cl^- accumulating at 0.01 picomoles/cell/day (Figure 3-5b). However, unlike the number of V-ATPase, the number of chloride channel molecules per lysosome did not show any effect on the physiological CFZ-H^+Cl^- accumulation unless this chloride current was completely absent (Figure 3-5b).

In dose-dependent simulations, CFZ-H^+Cl^- accumulating at a ten-fold greater (non-physiological) rate of 0.1 picomoles/cell/day led to more pronounced changes in lysosomal pH, Cl^-, and membrane potential (Figure 3-6a). At least < 68.3% V-ATPase inhibition per lysosome was required to sustain physiological ion concentrations in the presence of this 10-fold greater rate of CFZ-H^+Cl^- accumulation (Figure 3-6b). In contrast, variations in the numbers of chloride channels did not affect the physiological lysosomal accumulation of CFZ-H^+Cl^- at a rate of 0.1 picomoles/cell/day, unless there was a complete inhibition of the chloride current (Figure 3-6b).

V-ATPase is essential in the building block accumulation and self-assembly

To verify our model and simulation findings, we performed experiments to detect the effects of V-ATPase and chloride channels on the intracellular accumulation of CFZ. All experiments regarding the incubation and accumulation of CFZ were performed under conditions in which cellular viability was maintained. In the absence of any inhibitor, 8 μM extracellular CFZ accumulated at a rate of 0.01 picomoles/cell/day, as previously reported [4, 29]. However, inhibiting the V-ATPase with BafA1 reduced cellular CFZ accumulation by 80 ± 13% ($p < 0.01$) in a 4h incubation, relative to control, uninhibited cells (Figure 3-7a). This observation is consistent with our simulation results, where up to 50% V-ATPase inhibition resulted in a lysosomal pH increment (Figure 3-5a), which associates with a reduction in cellular drug accumulation. In contrast, when cells were treated with the chloride channel inhibitor NPPB and exposed to CFZ, no significant change was measured in the accumulation of CFZ following a 4h incubation (Figure 3-7b). This contrasts with the effect observed with BafA1 (Figure 3-7a), and is consistent with our simulation results (Figure 3-5a), thereby indicating that in the presence of CFZ uptake, lysosomal ion homeostasis is insensitive to chloride channel inhibition.

3.6 Discussion

As a weakly basic, poorly soluble small-molecule chemical that is FDA-approved, orally bioavailable, slowly cleared, and administered at high doses for prolonged periods of time, CFZ affords us the opportunity to reverse engineer the construction of a mechanopharmaceutical device that was found to form naturally inside cells. We report that, because of its physicochemical properties, CFZ is highly prone to precipitation in acidic endolysosomal compartments in macrophages, where it self-assembles into a highly ordered CFZ-H^+Cl^- biocrystalline, possessing many interesting optical and biomechanical features. Indeed, the preferential accumulation of CFZ in macrophage lysosomes is evident based on the displacement of Lysotracker Blue fluorescence from the cytoplasmic vesicles (Figure 3-4). Furthermore, fluorescence imaging revealed that CFZ was present both as a free base and hydrochloride salt form within intracellular vesicles (Figure 3-4). Thus, we performed computational simulations and experiments to probe the relationship between CFZ's pH-dependent solubility properties, the formation of salt and free base crystals, and the molecular, ion transport mechanisms responsible for this mechanopharmaceutical phenomenon, which could be exploited for developing other weakly basic small molecule building blocks as cell-targeted, self-assembling mechanopharmaceutical devices [41, 42].

Despite the complexities of lysosomal ion homeostasis, computational simulations and experimental results provide a straightforward explanation for the observed behavior of CFZ: the number of V-ATPase molecules that drive the lowering of macrophage lysosomal pH [43] plays a critical role in determining the intracellular bioaccumulation of CFZ in lysosomes without affecting lysosomal ion homeostasis. Our results show that very high levels of V-ATPase expression, that are typical of macrophages, are both necessary and sufficient to explain the

accumulation and stabilization of CFZ-H^+Cl^- salt in these cells because they allow the cells to maintain physiological lysosomal pH and membrane potential in spite of the accumulation of the drug. In addition, the intrinsic solubility properties of CFZ are such that the protonated form of the drug strongly interacts with chloride in a concentration range that is typically observed in lysosomes, which leads to the physiological accumulation of the drug in its hydrochloride salt form. Accordingly, V-ATPase expression establishes the ability of the cell to maintain physiological lysosomal pH [44], which, in relation to the drug's pH_{max} and K_{sp} (Figure 3-1), can sustain the continuous accumulation of the hydrochloride salt form of the drug [19] in the lysosome.

More importantly, we found that experimental results [4, 29] were highly consistent with model simulation results. First, the inhibition of V-ATPase activity resulted in the reduction of the total intracellular CFZ accumulation (Figure 3-7a), which was consistent with the model simulation results (Figures 3-5 and 3-6). In contrast, NPPB-mediated reduction of chloride channel activity did not affect the accumulation and stabilization of the salt form of the drug (Figure 3-7b), which was also consistent with the model simulation results (Figures 3-5 and 3-6, and Figures S3-5 and S3-6 in Appendix B). Furthermore, the measured K_{sp} of CFZ-H^+Cl^- and our CLDIs/CFZ-H^+Cl^- stability results (Figure 3-1) indicate that the physiological lysosomal chloride levels are sufficient to stabilize CFZ-H^+Cl^- salt formation through a common-ion "salting-out" mechanism [35]. Therefore, our findings collectively provide the first mechanistic framework that explains the accumulation of highly ordered, self-assembled CFZ-H^+Cl^- salt biocrystals in macrophages (Figures 3-2 and 3-3); which depends on the high levels of V-ATPase expression that is unique to this cell type[16].

It is also noteworthy that macrophages have lysosomes which are an order of magnitude greater in size than that of other cell types [45]. This provides them with the capability to accommodate massive accumulation of weakly basic drugs [46]. Even in cases where the initial lysosomal size is small (< 1 μm, in radius), the macrophage lysosomes can undergo biogenesis [47, 48]. A master regulator of lysosomal biogenesis and V-ATPase expression is transcription factor EB (TFEB) [39, 46, 49]. Moreover, given the recent findings regarding the role of TFEB in upregulating lysosomal genes during inflammation [50], the role of TFEB in the bioaccumulation and stabilization of CFZ-H^+Cl^- salt in macrophage lysosomes, in relation to CFZ's anti-inflammatory activity [9, 10], could be further investigated.

To conclude, we have discovered how lysosomal ion transport pathways play a major role in the self-assembly of a biocompatible, cell-targeted supramolecular structure formed by a weakly basic, small molecule building block. Together with the physicochemical properties of the freely soluble building blocks, these transport pathways can be exploited to develop novel types of drug depots and cell-directed drug delivery systems [51-53]. Indeed, interest has been raised in macrophages as drug delivery vehicles. As our studies have shown, macrophages may allow drugs to be locally stabilized and undergo a sustained release in a site-specific manner, offering a strategy for reducing off-target side effects [54, 55]. Macrophages are also one of the few cell types, which are primarily involved in the phagocytosis of foreign particles of different sizes and shapes, including drugs [56, 57], which offer yet another opportunity for loading these cells with massive amounts of chemotherapeutic agents. To this end, additional investigations into the manner in which these cells mechanically synergize with the self-assembled weakly basic small molecule building blocks in order to stabilize functional mechanopharmaceutical devices are warranted.

3.7 Acknowledgements and Funding

The authors acknowledge funding from M-Cubed and NIH grant R01GM078200 to GRR. We thank Dr. Nair Rodriguez-Hornedo (Department of Pharmaceutical Sciences, University of Michigan) for allowing the use of HPLC instrumentation in her lab.

3.8 Figures

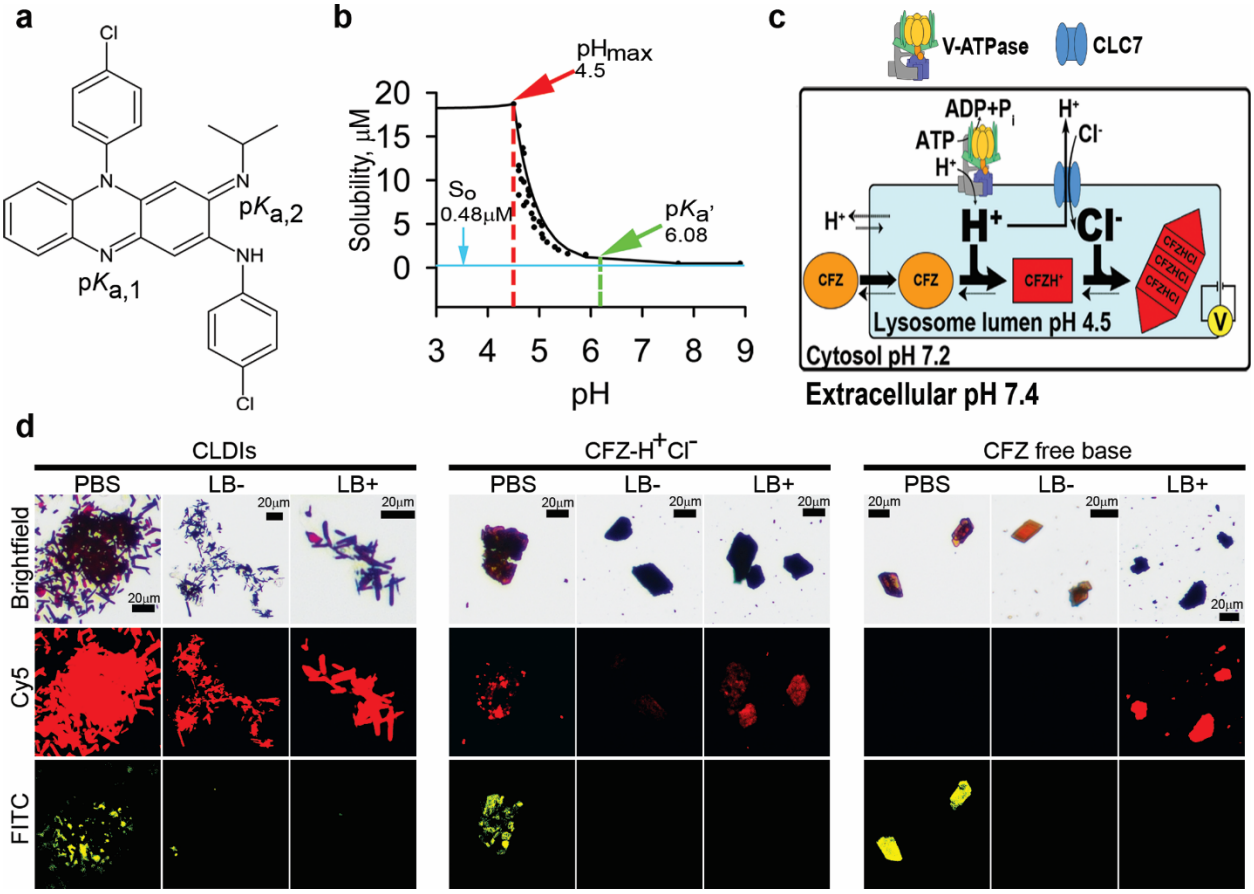

Figure 3-1. Chemical characterization of CFZ. a, Chemical structure of clofazimine (CFZ) with its two protonation sites and corresponding predicted (chemi-informatic) pK_a values (p$K_{a,1}$ = 2.31 and p$K_{a,2}$ = 9.29). **b**, CFZ-H^+Cl^- solubility-pH study revealed the solution pH dependence of the stabilization of the free base versus salt form of the drug with respect to its solubility parameters; which include the intrinsic free base solubility (S_o), apparent p$K_{a,2}$ (pK_a'), and pH_{max}. **c**, Illustration showing the cellular and subcellular accumulation of free base CFZ, its subsequent protonation ($CFZH^+$), and ion-ion interaction of $CFZH^+$ and cellular Cl^- to form CFZ-H^+Cl^-. This phenomenon depends on the drug's intrinsic solubility properties as well as the cellular pH and Cl^- levels, which are primarily regulated by membrane proteins: proton-pump known as V-ATPase and Cl^-/H^+ antiporter known as CLC7. **d,** Stability of CLDIs, CFZ-H^+Cl^-, and free base CFZ in PBS (pH 7.4), lysosomal buffer without sodium chloride (LB-, pH 4.5), and lysosomal buffer with 100 mM sodium chloride (LB+, pH 4.5) was monitored via brightfield and fluorescence microscopy.

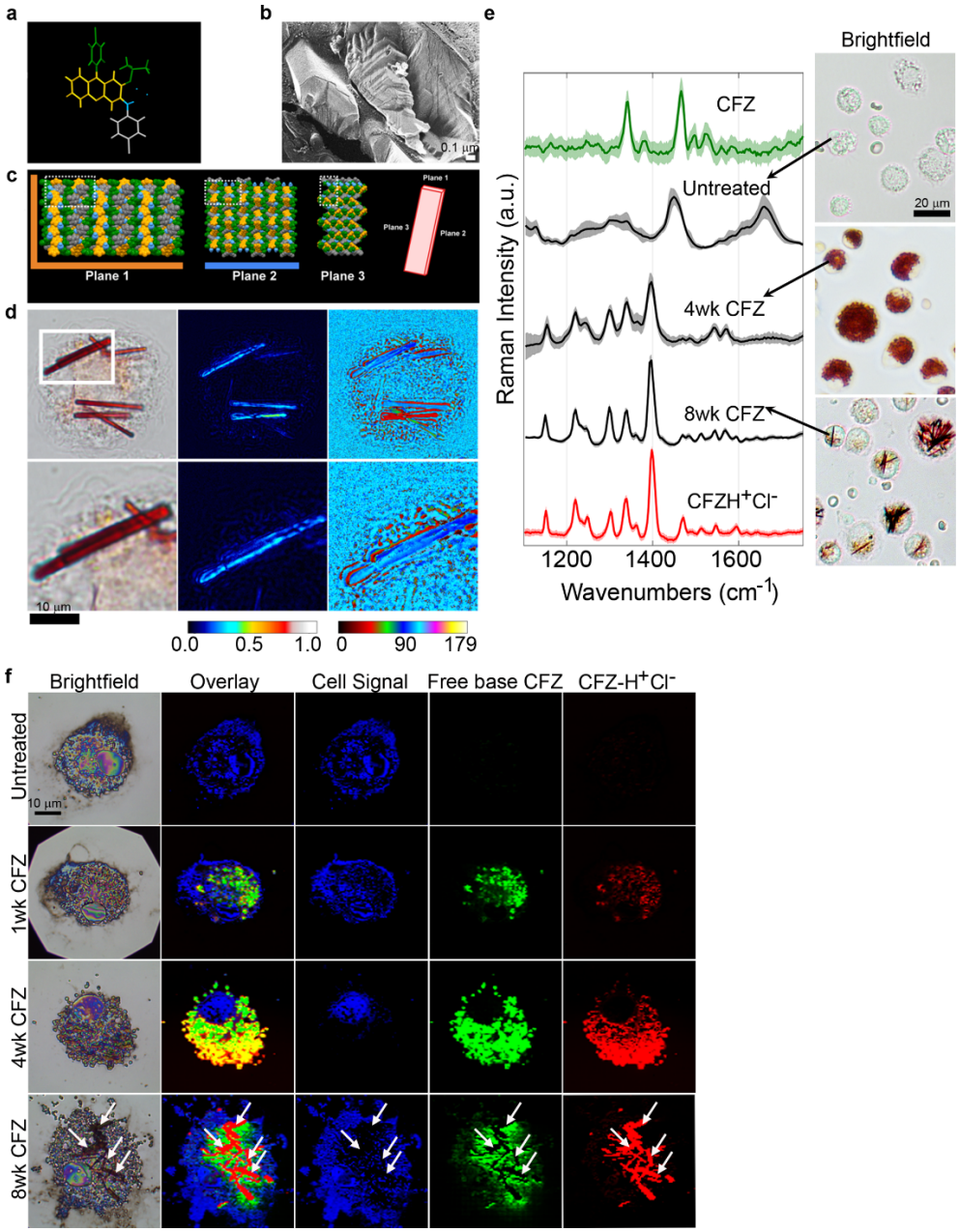

Figure 3-2. Intracellular self-assembled crystal organization of CFZ-H$^+$Cl$^-$. a, CFZ-H$^+$Cl$^-$ chemical structure with color coding corresponding to the regions of the structure in the crystal arrangement. **b**, Freeze-fracture electron micrograph of CLDIs within a Kupffer cell, showing that the CLDIs are sequestered inside the cell as multiple layered planes with lamellar spacing of 6 nm to 14 nm, by a double membrane of biological origin (~ 20 nm in thickness)[21]. **c**, Crystal packing of CFZ-H$^+$Cl$^-$ showing the three crystallographic planes of the crystal: a hydrophobic face in orange (plane 1), a hydrophilic face in blue (plane 2), and an amphipathic face (plane 3)[8]. **d**, CLDIs (100-1.5X magnification) zoomed in (zoom factor of 2) in alveolar macrophages show high dichroism and an axis of highest transmittance, with a different profile (represented by the different signal intensity associated with the color bar) observed specifically around the edges of the crystal. **e,** Raman spectra of free base CFZ, CFZ-H$^+$Cl$^-$, untreated and treated alveolar macrophages (4 and 8wks CFZ-fed mice) show distinct Raman peaks distinguishing between the different forms of the drug (red in the brightfield images): free base CFZ (1341 and 1465 cm^{-1}), CFZ-H$^+$Cl$^-$ (1399 cm^{-1}). **f,** Reflected brightfield and Raman images of alveolar macrophages from CFZ-fed mice prepared on silicon chip substrates; basis spectral fitting was used to show the temporal accumulation and cytoplasmic packaging of CFZ into highly ordered CLDIs.

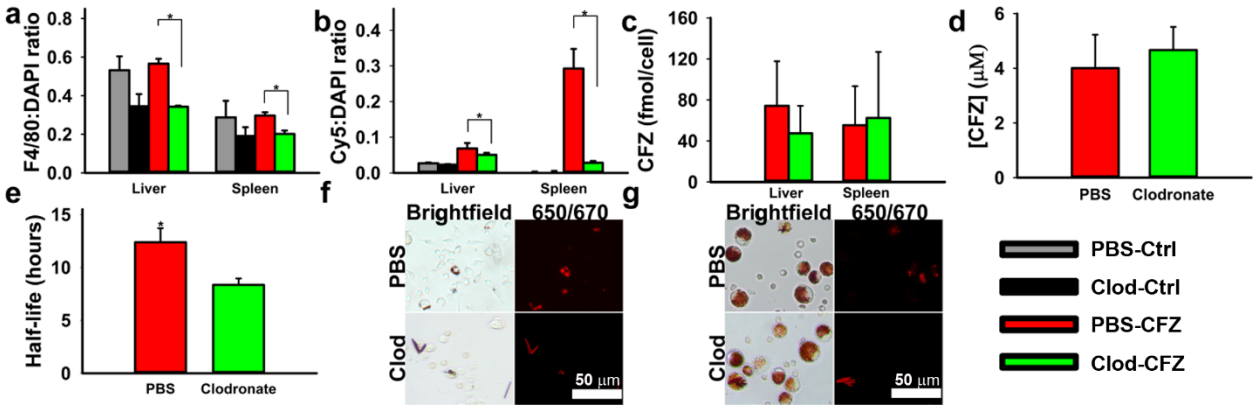

Figure 3-3. The role of macrophages on the intracellular accumulation of CFZ biocrystals *in vivo*. **a**, Clodronate depletion significantly reduces both hepatic and splenic macrophages in Clodronate-CFZ treatment group. **b**, Depletion of macrophages results in concomitant reduction in CLDI loading within the livers and spleens of treated animals. **c**, Clodronate depletion does not significantly reduce the estimated clofazimine loading per macrophage in the livers and spleen. **d,** Clodronate depletion does not significantly impact the serum concentrations of clofazimine following four weeks of treatment. **e,** Depletion of peritoneal macrophages significantly increases the rate of degradation of CLDIs injected intraperitoneally, leading to a significantly faster half-life. **f,** Peritoneal exudate of PBS- and clodronate-liposome treated mice 48 hours following CLDI injection showing brightfield and Cy5 fluorescence (red fluorescence and red in brightfield images correspond to CLDIs) (* = $p < 0.05$, ANOVA or ANOVA, Tukey's HSD when applicable). **g,** Alveolar lavage from PBS- and clodronate-liposome treated mice. Clodronate treatment did not impact CLDI accumulation (red fluorescence and red in brightfield images correspond to CLDIs) within alveolar macrophages.

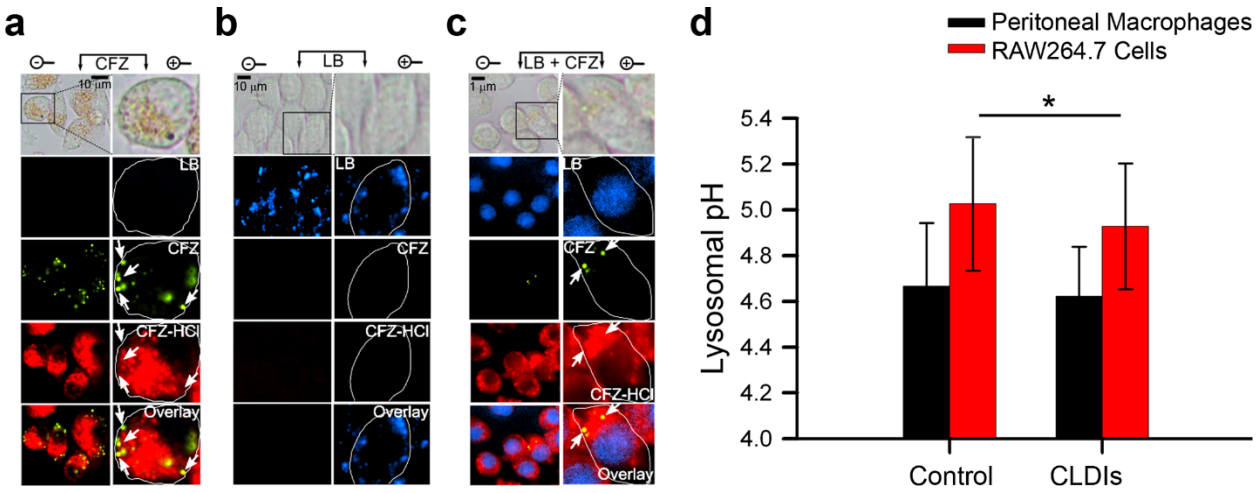

Figure 3-4. Evidence of lysosomal accumulation of CFZ via fluorescence staining patterns in RAW264.7 cells. **a**, Epifluorescence microscopy of RAW264.7 cells (40X magnification) zoomed in (zoom factor of 2.5) when incubated with (**a**) CFZ (10 μM), (**b**) Lysotracker Blue (LB, 1 μM), and (**c**) CFZ (10 μM) and LB (1 μM) together at t = 24 hours. Green fluorescence spots indicative of CFZ are also further annotated using white arrows for cross-referencing with other images. Note the lack of any far-red fluorescence positive signal in the direction pointed by the arrows. Vesicular staining pattern of LB visible as blue punctate spots in (**b)** are absent in (**c**), while nuclear staining becomes visible due to LB displacement from the lysosome to the nucleus because of CFZ accumulation in the lysosome. Cell boundaries are shown in white in the digitally zoomed panels. **d**, Lysosomal pH measurements of RAW26.7 cells in the presence and absence of CLDIs, and peritoneal macrophages of control versus 8-week CFZ-fed mice. Data are mean ± S.D. of 29-181 measurements; * p = 0.026; analyzed by unpaired two-tailed Student t-test.

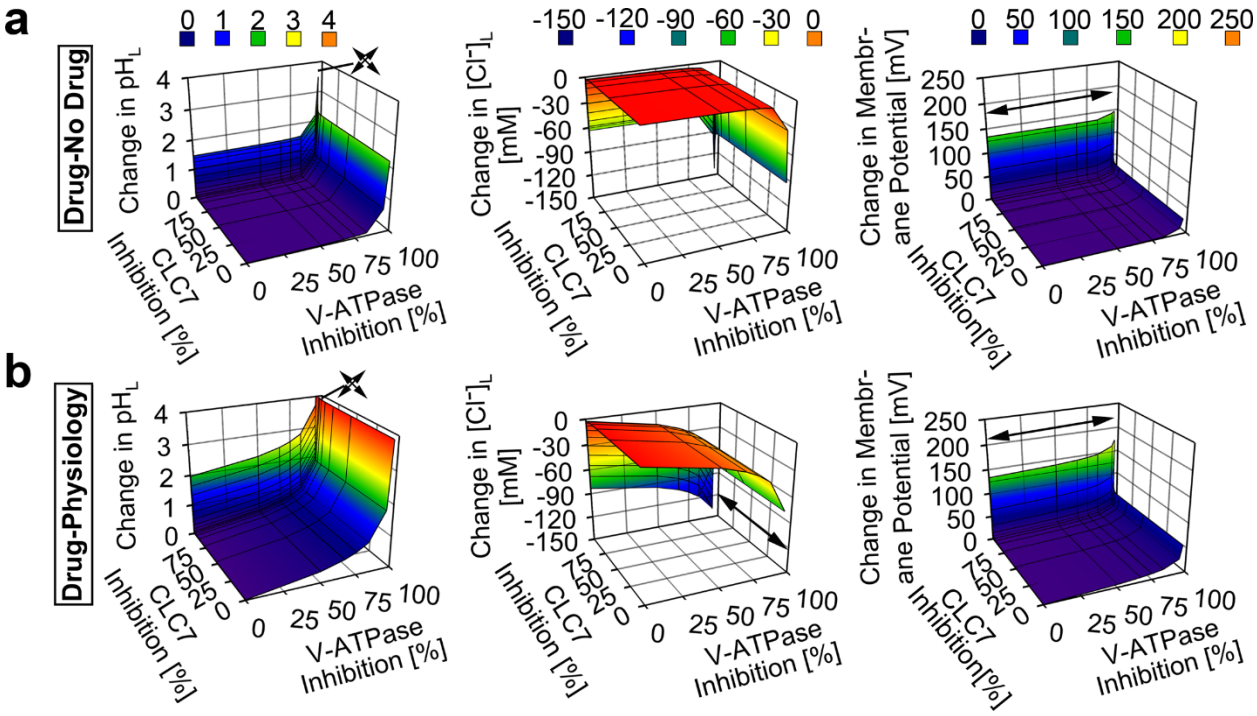

Figure 3-5. Model and simulation of the effects of V-ATPase and CLC7 on the lysosomal accumulation of CFZ-H^+Cl^-. a, V-ATPase inhibition showed a more substantial effect than CLC7 inhibition on the accumulation of CFZ-H^+Cl^- at the rate of 0.01 picomol/cell/day, as reflected by the changes in the lysosomal pH, Cl^-, and membrane potential values of the CFZ-H^+Cl^- containing lysosome from that of the CFZ-H^+Cl^- free lysosome. **b**, V-ATPase inhibition showed a more substantial effect than CLC7 inhibition on the physiological accumulation of CFZ-H^+Cl^- at the rate of 0.01 picomol/cell/day, as reflected by the changes in the lysosomal pH, Cl^-, and membrane potential values of the CFZ-H^+Cl^- containing lysosome from respective baseline physiological values. Arrow signs represent values outside of the axes plot range.

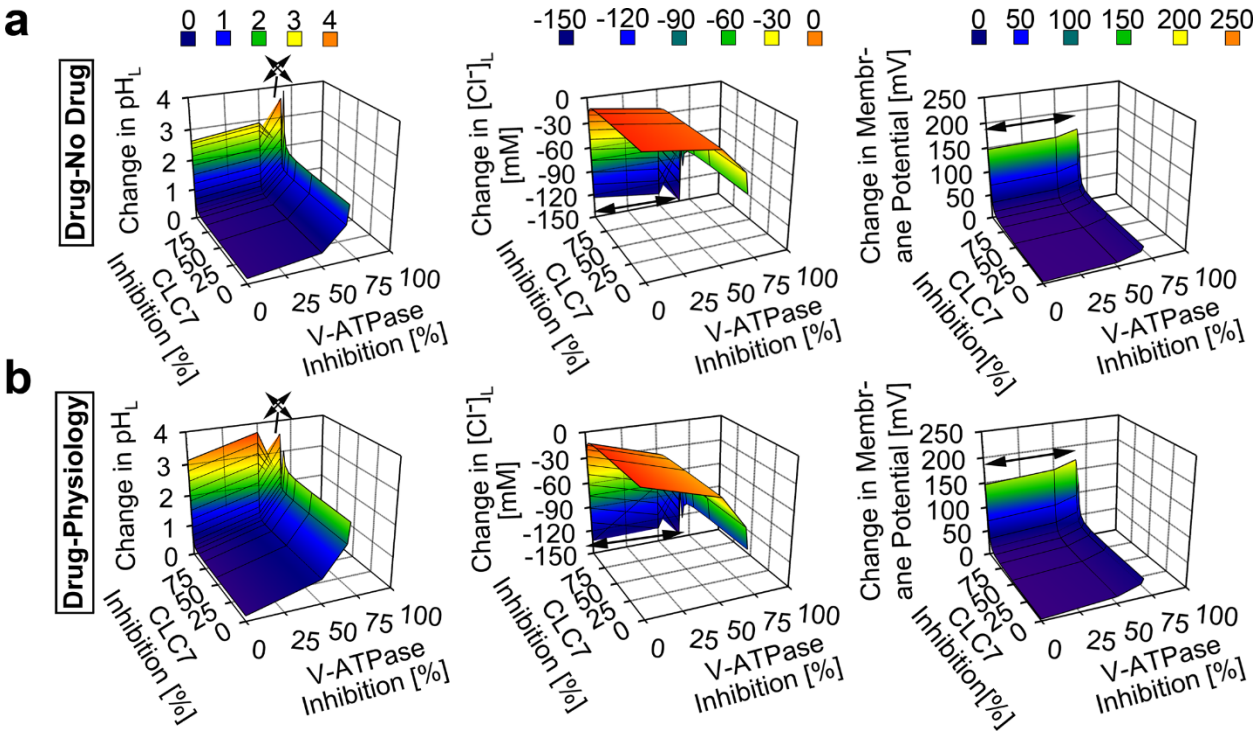

Figure 3-6. Model and simulation of the effects of V-ATPase and CLC7 on the lysosomal accumulation of CFZ-H$^+$Cl$^-$ at a higher dose. a, V-ATPase inhibition showed a more substantial effect than CLC7 inhibition on the accumulation of CFZ-H$^+$Cl$^-$ at the rate of 0.1 picomol/cell/day, as reflected by the changes in the lysosomal pH, Cl$^-$, and membrane potential values of the CFZ-H$^+$Cl$^-$ containing lysosome from that of the CFZ-H$^+$Cl$^-$ free lysosome. **b**, V-ATPase inhibition showed a more substantial effect than CLC7 inhibition on the physiological accumulation of CFZ-H$^+$Cl$^-$ at the rate of 0.1 picomol/cell/day, as reflected by the changes in the lysosomal pH, Cl$^-$, and membrane potential values of the CFZ-H$^+$Cl$^-$ containing lysosome from respective baseline physiological values. Arrow signs represent values outside of the axes plot range.

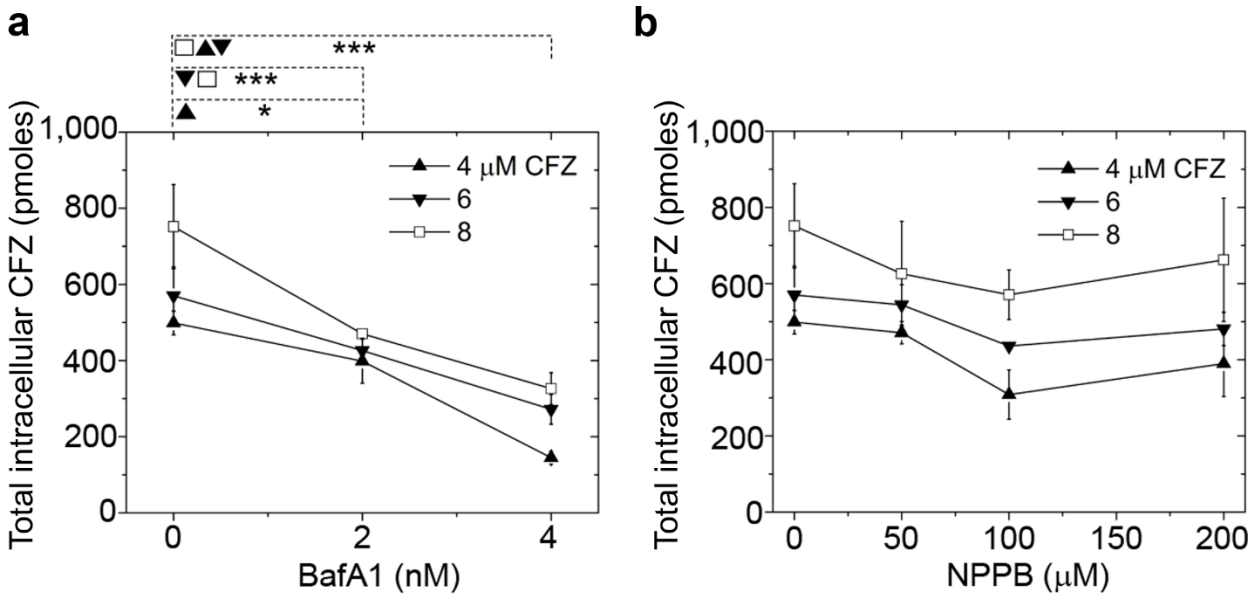

Figure 3-7. Intracellular CFZ accumulation. Total intracellular CFZ accumulation in picomoles (pmoles) in RAW264.7 cells (~ 68,000 cells/well) when pre-incubated with (**a**) BafA1 and (**b**) NPPB and initial concentration of CFZ = 4, 6, and 8 μM at t = 4 hours. Significant inhibition of CFZ accumulation was measured at t = 4 hours when cells were exposed to BafA1. To the contrary, no such inhibition was measured when cells were exposed to NPPB at t = 4 hours. Data are the mean ± S.D. of six experiments. * - $p < 0.05$, ** - $p < 0.01$, *** - $p < 0.001$. Each data point was compared in a pair-wise independent Student t-test.

3.9 References

1. Zhang, Z., et al., *Supersnowflakes: Stepwise Self-Assembly and Dynamic Exchange of Rhombus Star-Shaped Supramolecules.* J Am Chem Soc, 2017. **139**(24): p. 8174-8185.

2. Deng, Y., et al., *Multifunctional small molecule for controlled assembly of oligomeric nanoparticles and crosslinked polymers.* Org Biomol Chem, 2011. **9**(20): p. 6917-9.

3. Desikan, K.V., et al., *Autopsy findings in a case of lepromatous leprosy treated with clofazimine.* Lepr Rev, 1975. **46**(3): p. 181-9.

4. Baik, J. and G.R. Rosania, *Molecular imaging of intracellular drug-membrane aggregate formation.* Mol Pharm, 2011. **8**(5): p. 1742-9.

5. Baik, J., et al., *Multiscale distribution and bioaccumulation analysis of clofazimine reveals a massive immune system-mediated xenobiotic sequestration response.* Antimicrob Agents Chemother, 2013. **57**(3): p. 1218-30.

6. O'Connor, R., J.F. O'Sullivan, and R. O'Kennedy, *The pharmacology, metabolism, and chemistry of clofazimine.* Drug Metab Rev, 1995. **27**(4): p. 591-614.

7. Horstman, E.M., et al., *Elasticity in Macrophage-Synthesized Biocrystals.* Angew Chem Int Ed Engl, 2017. **56**(7): p. 1815-1819.

8. Keswani, R.K., et al., *Chemical Analysis of Drug Biocrystals: A Role for Counterion Transport Pathways in Intracellular Drug Disposition.* Mol Pharm, 2015. **12**(7): p. 2528-36.

9. Yoon, G.S., et al., *Clofazimine Biocrystal Accumulation in Macrophages Upregulates IL-1RA Production to Induce a Systemic Anti-Inflammatory State.* Antimicrob Agents Chemother, 2016.

10. Yoon, G.S., et al., *Phagocytosed Clofazimine Biocrystals Can Modulate Innate Immune Signaling by Inhibiting TNFalpha and Boosting IL-1RA Secretion.* Mol Pharm, 2015. **12**(7): p. 2517-27.

11. Keswani, R.K., et al., *A far-red fluorescent probe for flow cytometry and image-based functional studies of xenobiotic sequestering macrophages.* Cytometry A, 2015. **87**(9): p. 855-67.

12. Wang, S.P., et al., *Regulation of enhanced vacuolar H+-ATPase expression in macrophages.* J Biol Chem, 2002. **277**(11): p. 8827-34.

13. Hong, L., et al., *Alteration of volume-regulated chloride channel during macrophage-derived foam cell formation in atherosclerosis.* Atherosclerosis, 2011. **216**(1): p. 59-66.

14. Jiang, L., et al., *Intracellular chloride channel protein CLIC1 regulates macrophage function through modulation of phagosomal acidification.* J Cell Sci, 2012. **125**(Pt 22): p. 5479-88.

15. Kazmi, F., et al., *Lysosomal sequestration (trapping) of lipophilic amine (cationic amphiphilic) drugs in immortalized human hepatocytes (Fa2N-4 cells).* Drug Metab Dispos, 2013. **41**(4): p. 897-905.

16. Ishida, Y., et al., *A model of lysosomal pH regulation.* J Gen Physiol, 2013. **141**(6): p. 705-20.

17. Yoshimori, T., et al., *Bafilomycin A1, a specific inhibitor of vacuolar-type H(+)-ATPase, inhibits acidification and protein degradation in lysosomes of cultured cells.* J Biol Chem, 1991. **266**(26): p. 17707-12.

18. Wangemann, P., et al., *Cl−-channel blockers in the thick ascending limb of the loop of Henle Structure activity relationship.* Pflügers Archiv, 1986. **407**(2): p. S128-S141.

19. Kramer, S.F. and G.L. Flynn, *Solubility of organic hydrochlorides.* J Pharm Sci, 1972. **61**(12): p. 1896-904.

20. van Rooijen, N. and E. Hendrikx, *Liposomes for specific depletion of macrophages from organs and tissues.* Methods Mol Biol, 2010. **605**: p. 189-203.

21. Baik, J. and G.R. Rosania, *Macrophages sequester clofazimine in an intracellular liquid crystal-like supramolecular organization.* PLoS One, 2012. **7**(10): p. e47494.

22. Murashov, M.D., et al., *The Physicochemical Basis of Clofazimine-Induced Skin Pigmentation.* J Invest Dermatol, 2017.

23. Oldenbourg, R., *Polarized light microscopy: principles and practice.* Cold Spring Harb Protoc, 2013. **2013**(11).

24. Rzeczycki, P., et al., *Detecting ordered small molecule drug aggregates in live macrophages: a multi-parameter microscope image data acquisition and analysis strategy.* Biomed Opt Express, 2017. **8**(2): p. 860-872.

25. van Rooijen, N. and E. Hendrikx, *Liposomes for Specific Depletion of Macrophages from Organs and Tissues*, in *Liposomes*, V. Weissig, Editor. 2010, Humana Press. p. 189-203.

26. Lee, S., P. Starkey, and S. Gordon, *Quantitative analysis of total macrophage content in adult mouse tissues. Immunochemical studies with monoclonal antibody F4/80.* J Exp Med, 1985. **161**(3): p. 475-89.

27. Sakagami, H., et al., *Cell death induced by nutritional starvation in mouse macrophage-like RAW264.7 cells.* Anticancer Res, 2009. **29**(1): p. 343-7.

28. Davis, M.J. and J.A. Swanson, *Technical advance: Caspase-1 activation and IL-1beta release correlate with the degree of lysosome damage, as illustrated by a novel imaging method to quantify phagolysosome damage.* J Leukoc Biol, 2010. **88**(4): p. 813-22.

29. Min, K.A., et al., *Massive Bioaccumulation and Self-Assembly of Phenazine Compounds in Live Cells.* Adv Sci (Weinh), 2015. **2**(8).

30. Heuser, J., Q. Zhu, and M. Clarke, *Proton pumps populate the contractile vacuoles of Dictyostelium amoebae.* J Cell Biol, 1993. **121**(6): p. 1311-27.

31. Van Dyke, R.W., *Acidification of rat liver lysosomes: quantitation and comparison with endosomes.* Am J Physiol, 1993. **265**(4 Pt 1): p. C901-17.

32. Gambale, F., et al., *The Voltage-Dependent H+-Atpase of the Sugar-Beet Vacuole Is Reversible.* European Biophysics Journal with Biophysics Letters, 1994. **22**(6): p. 399-403.

33. Sonawane, N.D., J.R. Thiagarajah, and A.S. Verkman, *Chloride concentration in endosomes measured using a ratioable fluorescent Cl- indicator - Evidence for chloride accumulation during acidification.* Journal of Biological Chemistry, 2002. **277**(7): p. 5506-5513.

34. Alberts, B.J., A.; Lewis, J.; Raff, M.; Roberts, K.; Walter, P., *Moelcular Biology of the Cell. Fifth edition*. 2008: Garland Science, New York. 1601.

35. Serajuddin, A.T., *Salt formation to improve drug solubility.* Adv Drug Deliv Rev, 2007. **59**(7): p. 603-16.

36. Keswani, R.K., et al., *Repositioning Clofazimine as a Macrophage-Targeting Photoacoustic Contrast Agent.* Sci Rep, 2016. **6**: p. 23528.

37. Keswani, R., et al., *A Far-Red Fluorescent Probe For Flow Cytometric Xenobiotic-Sequestering Cell Functional Studies.* Cytometry Part A, 2015(Accepted Manuscript).

38. Lemieux, B., M.D. Percival, and J.P. Falgueyret, *Quantitation of the lysosomotropic character of cationic amphiphilic drugs using the fluorescent basic amine Red DND-99.* Anal Biochem, 2004. **327**(2): p. 247-51.

39. Samie, M.A. and H. Xu, *Lysosomal exocytosis and lipid storage disorders.* J Lipid Res, 2014. **55**(6): p. 995-1009.

40. Life Technologies. *LysoTracker and LysoSensor Probes*. 2013; Available from: https://tools.thermofisher.com/content/sfs/manuals/mp07525.pdf.

41. Huefner, A., et al., *Gold nanoparticles explore cells: cellular uptake and their use as intracellular probes.* Methods, 2014. **68**(2): p. 354-63.

42. Rajendran, L., H.J. Knolker, and K. Simons, *Subcellular targeting strategies for drug design and delivery.* Nat Rev Drug Discov, 2010. **9**(1): p. 29-42.

43. Beyenbach, K.W. and H. Wieczorek, *The V-type H+ ATPase: molecular structure and function, physiological roles and regulation.* J Exp Biol, 2006. **209**(Pt 4): p. 577-89.

44. Grabe, M., H. Wang, and G. Oster, *The mechanochemistry of V-ATPase proton pumps.* Biophys J, 2000. **78**(6): p. 2798-813.

45. Lüllmann-Rauch, R., *History and Morphology of the Lysosome*, in *Lysosomes*. 2005, Springer US: Boston, MA. p. 1-16.

46. Logan, R., A.C. Kong, and J.P. Krise, *Time-dependent effects of hydrophobic amine-containing drugs on lysosome structure and biogenesis in cultured human fibroblasts.* J Pharm Sci, 2014. **103**(10): p. 3287-96.

47. Emanuel, R., et al., *Induction of lysosomal biogenesis in atherosclerotic macrophages can rescue lipid-induced lysosomal dysfunction and downstream sequelae.* Arterioscler Thromb Vasc Biol, 2014. **34**(9): p. 1942-52.

48. Gao, Y., et al., *Comprehensive proteome analysis of lysosomes reveals the diverse function of macrophages in immune responses.* Oncotarget, 2017. **8**(5): p. 7420-7440.

49. Wang, W., et al., *Up-regulation of lysosomal TRPML1 channels is essential for lysosomal adaptation to nutrient starvation.* Proc Natl Acad Sci U S A, 2015. **112**(11): p. E1373-81.

50. Pastore, N., et al., *TFEB and TFE3 cooperate in the regulation of the innate immune response in activated macrophages.* Autophagy, 2016. **12**(8): p. 1240-58.

51. Brahler, M., et al., *Magnetite-loaded carrier erythrocytes as contrast agents for magnetic resonance imaging.* Nano Lett, 2006. **6**(11): p. 2505-9.

52. Wang, C., et al., *Red Blood Cells for Glucose-Responsive Insulin Delivery.* Adv Mater, 2017.

53. Paukner, S., et al., *Bacterial ghosts as a novel advanced targeting system for drug and DNA delivery.* Expert Opin Drug Deliv, 2006. **3**(1): p. 11-22.

54. Wang, C., et al., *Multifunctional theranostic red blood cells for magnetic-field-enhanced in vivo combination therapy of cancer.* Adv Mater, 2014. **26**(28): p. 4794-802.

55. Gutierrez Millan, C., et al., *In vitro studies of amikacin-loaded human carrier erythrocytes.* Transl Res, 2008. **152**(2): p. 59-66.

56. Rossi, L., et al., *Effect of listeriolysin O-loaded erythrocytes on Mycobacterium avium replication within macrophages.* J Antimicrob Chemother, 2004. **53**(5): p. 863-6.

57. Mishra, P.R. and N.K. Jain, *Surface modified methotrexate loaded erythrocytes for enhanced macrophage uptake.* J Drug Target, 2000. **8**(4): p. 217-24.

Chapter 4

An Expandable Mechanopharmaceutical Device for Measuring the Cargo Capacity of Macrophages in a Living Organism

4.1 Relevance to Thesis

This chapter was adapted from the following publication:

*Rzeczycki P, Woldemichael T, Willmer A, **Murashov MD**, Baik J, Keswani RK, Yoon GS, Stringer KA, Rodriguez-Hornedo N, Rosania GR. **2018**. An expandable mechanopharmaceutical device (1): measuring the cargo capacity of macrophages in a living organism. **Pharm. Res.** 36:12; doi: 10.1007/s11095-018-2539-6*

In this study, we asked whether specific accumulation of CFZ hydrochloride crystals in lysosomes could be explained as a passive, thermodynamic equilibrium phenomenon. To answer this, we further investigated the mechanism of CFZ-HCl salt formation and accumulation in lysosomes of macrophages (in the chapter referred to as CLDIs or mechanopharmaceutical device). In fact, we modeled the subcellular transport and precipitation properties of CFZ using a physiologically based pharmacokinetics approach to assess whether thermodynamics alone could explain the selective accumulation and stabilization of the drug in macrophage lysosomes. My contribution in this study involved experimentally determining the physicochemical properties (Chapter 3) and octanol solubility measurements of HCl salt form and free base form of CFZ that were used in the cellular pharmacokinetic model. The simulation results supported the notion that the proton and chloride ion concentrations of macrophage lysosomes are sufficient to drive the massive, cell type-selective accumulation and growth of CFZ hydrochloride biocrystals. It

was also determined that the solubility of CFZ-HCl in lysosomes was 3 nM, which is far lower than the free base solubility of CFZ free base due its K_{sp} and pH_{max}. Importantly, the CFZ-HCl salt form of the drug was used as a physical probe in this study, hence mechanopharmaceutical device, to measure the cargo loading capacity of different macrophage subpopulations *in vivo*.

4.2 Abstract

Clofazimine (CFZ) is an FDA-approved, poorly soluble small molecule drug that precipitates as crystal-like drug inclusions (CLDIs) which accumulate in acidic cytoplasmic organelles of macrophages. In this study, we considered CLDIs as an expandable mechanopharmaceutical device, to study how macrophages respond to an increasingly massive load of endophagolysosomal cargo.

First, we experimentally tested how the accumulation of CFZ in CLDIs impacted different immune cell subpopulations of different organs. Second, to further investigate the mechanism of CLDI formation, we asked whether specific accumulation of CFZ hydrochloride crystals in lysosomes could be explained as a passive, thermodynamic equilibrium phenomenon. A cellular pharmacokinetic model was constructed, simulating CFZ accumulation driven by pH-dependent ion trapping of the protonated drug in the acidic lysosomes, followed by the precipitation of CFZ hydrochloride salt via a common ion effect caused by high chloride concentrations.

While lower loads of CFZ were mostly accommodated in lung macrophages, increased CFZ loading was accompanied by organ-specific changes in macrophage numbers, size and intracellular membrane architecture, maximizing the cargo storage capabilities. With increasing loads, the total cargo mass and concentrations of CFZ in different organs diverged, while that of individual macrophages converged. The simulation results support the notion that the proton and

chloride ion concentrations of macrophage lysosomes are sufficient to drive the massive, cell type-selective accumulation and growth of CFZ hydrochloride biocrystals.

CLDIs effectively function as an expandable mechanopharmaceutical device, revealing the coordinated response of the macrophage population to an increasingly massive, whole-organism endophagolysosomal cargo load.

4.3 Introduction

In multicellular organisms, macrophages are well equipped to internalize extracellular solutes and particles through pinocytosis and phagocytosis, respectively. These processes allow them to execute a number of critical, immune surveillance functions, ranging from destruction of pathogens to removal and recycling of dead cells and aged tissue components [1-3]. In addition to being highly phagocytic, the endolysosomal system of the macrophage is especially adapted for accommodating and degrading foreign material due to higher expression levels of lysosomal acidification mechanisms [4], particularly the vacuolar-type proton ATP-ase (V-ATPase) [5]. However, there is no information about the extent of loading or the cargo storage capacity of macrophage populations *in vivo*, since the majority of measurements have been performed *in vitro* and in very short treatment periods by 'feeding' the cells with fluorescent tracer molecules [6] or inert beads of varying sizes [7,8] under artificial conditions.

Even though macrophages are found everywhere in the organism, their ability to influence the transport and disposition of small molecule drugs is mostly unknown. Due to their ubiquitous presence and high rates of endocytosis, pinocytosis, and phagocytosis, they are recognized to play a major role in the clearance of drug nano- or microparticles from the circulation [9,10]. Potentially, this action could be exploited for the delivery of small molecule drugs [11-14] , particularly those that are poorly soluble because they are prone to form insoluble

aggregates that may ultimately accumulate in macrophages [15,16]. Furthermore, cationic, amphiphilic molecules, particularly weakly basic molecules, can become trapped within lysosomes following protonation in the acidic lysosomal microenvironment [17-19]. The sequestration of weakly basic, hydrophobic drug molecules within acidic subcellular (ion-trapping) compartments of macrophages is a well-documented phenomenon [17].

To study the *in vivo,* cargo storage capacity of macrophages in an intact, living organism, we have co-opted an FDA-approved and biocompatible antibiotic, clofazimine (CFZ) [15,16]. CFZ is a weakly basic anti-mycobacterial agent that is clinically used to treat leprosy and multi-drug resistant tuberculosis [20-22]. It exhibits extensive bioaccumulation following oral administration, in both humans and animal models [23-25]. Because CFZ is both highly lipophilic (LogP = 7.66) [26,27] and contains an ionizable amine group ($pK_a = 6.08$) [28], it is poised to accumulates in adipose tissue, intracellular membranes, and acidic organelles such as lysosomes. In both human and animal models it has been shown that, following prolonged oral dosing, CFZ forms insoluble Crystal-Like Drug Inclusions (CLDIs) within macrophage lysosomes [15].

Here, by exploiting CFZ's self-assembly into CLDIs, we decided to further probe the macrophage's response to an increasing load of drug cargo. Experimentally, CLDIs were microscopically monitored to determine the numbers of drug-sequestering macrophages in different organs. From these same organs, CLDIs were then biochemically isolated and the drug content chemically analyzed to determine the average amount of drug per CLDI-containing cell [15,16]. Additionally, we modeled the subcellular transport and precipitation properties of CFZ using a physiologically based pharmacokinetics approach to assess whether thermodynamics alone could explain the selective accumulation and stabilization of the drug in macrophage

lysosomes. Based on the results, we propose that CLDIs function as an expandable mechanopharmaceutical device, which impacts the structural and functional properties of macrophages in different organs, and accounts for a drug loading-dependent increase in the volume of distribution (V_D) of the drug.

4.4 Materials and Methods

Animal Studies and Treatment Protocols

Animal care was provided by the University of Michigan's Unit for Laboratory Animal Medicine (ULAM), and the experimental protocol was approved by the Committee on Use and Care of Animals (Protocol PRO00005542). Mice (4 weeks old, male C57Bl6) were purchased from the Jackson Laboratory (Bar Harbor, ME) and acclimatized for 1 week in a specific-pathogen-free animal facility. Clofazimine (CFZ) (C8895; Sigma, St. Louis, MO) was dissolved in sesame oil (Shirakiku, Japan) to achieve a concentration of 3 mg/ml, which was mixed with Powdered Lab Diet 5001 (PMI International, Inc., St. Louis, MO) to produce a 0.03% drug to powdered feed mix, and orally administered *ad libitum*. Mice were fed for 2, 3, 4, and 8 weeks, which yielded estimated whole body cargo loads of 3.5mg, 5.25mg, 7mg, and 14mg, respectively. A corresponding amount of sesame oil was mixed with chow for vehicle treatment (control). For washout experiments, mice were fed with drug free, vehicle-containing diet for eight weeks, after an eight week loading period with the CFZ-containing diet. At the end of experimentation, mice were euthanized via carbon dioxide asphyxiation followed by exsanguination.

Macrophage Isolation

Following euthanasia, four different macrophage populations were isolated to study CFZ accumulation. Alveolar [16,29] and peritoneal macrophages [15], and bone marrow monocytes

[30] were all isolated using previously described techniques. To isolate Kupffer cells, the portal vein was injected with 10 mL of 1 mg/mL Collagenase D (Worthington Biochemical Corporation, Lakewood, NJ) in DMEM-low glucose (Life Technologies) with 15 mM HEPES (Life Technologies). The tissue was then removed, placed in a sterile petri dish, and minced into small (2-4 mm) pieces using a sterile scalpel blade. Collagenase solution (15 mL) was added, and the tissue was incubated (40 min, 37°C), with occasional pipetting to dissociate tissue. The suspension was then filtered through a 100 μm cell strainer (Fisher Scientific, Waltham, MA) and centrifuged (200 x g, 5 min). The supernatant was discarded, and the cells were resuspended in 15 mL DMEM-low glucose with 15 mM HEPES, and centrifuged (200 x g, 5 min). This was repeated for two additional washes. After the final wash, the cells were suspended in DMEM:F/12 (1:1) (Life Technologies) with 10% FBS and penicillin/streptomycin and macrophages were counted. For all cell groups, an aliquot was plated onto 4 or 8 chamber coverglass (#1.5, Lab-Tek II, Nunc, Rochester, NY), and for Kupffer cells, the plates were coated with Collagen 1 (Corning, Corning, New York) for imaging. The cells were allowed to attach overnight, washed with media, and imaged using a multi-parameter microscope imaging system (*vide infra*).

Multi-parameter Microscope Imaging and Analysis of Macrophage Sub-Populations

Multi-parameter polarization, brightfield, and fluorescence imaging and analyses of different macrophage subpopulations were performed using a custom-built imaging system, as previously described [16]. Brightfield, fluorescence, and polarization images were acquired on adherent cells. Images were analyzed using ImageJ software [31,32]. Values for dichroism and optical density are reported as an average signal per cell, from 0-1. At least 150 cells of each type were analyzed at each time point. Following loading with 7 and 14 mg of cargo, macrophages

were classified as xenobiotic sequestering based on whether or not they contained a detectable Cy5 signal from CFZ-HCl [15] using a K-means clustering analysis, with the clusters set to 2 based on of the Log_{10}(Intracellular Cy5 fluorescence).

Biochemical Analysis of Cellular Drug Cargo

The drug concentration in cells was calculated after measuring drug content in isolated macrophage populations and organ homogenates using established methods [15,24,33,34]. For isolated macrophage populations, cells were counted within each cell sample using a hemocytometer to determine the total recovered macrophage population. The cells were then centrifuged, and the media was removed. The cell pellet was suspended in 1 mL of DI water, and the drug was extracted and measured using a previously described spectrophotometric method [34-36]. Drug accumulation is reported as fmol CFZ/xenobiotic sequestering cell.

Sample Preparation for Microscopy

In preparation for microscopy, portions of the organ were removed, immediately submerged in OCT (Tissue-Tek catalog no. 4583; Sakura), and frozen (-80°C). For transmission electron microscopy, organs were prepared using previously described methods [23]. Immunohistochemistry of F4/80 (Abcam, 1:500 dilution) stained sections (5µm) was performed using Alexa-Fluor 488 (Abcam, 1:500 dilution).

Determination of Cargo Volume Occupancy

The volume occupied by biocrystalline drug molecules within a macrophage was estimated by using the reported crystal-packing density of 1.36 g/mL [34] for CFZ-HCl, which was then converted to a molar volume of 0.377 μm^3/ fmol. Cellular volume occupancy was then estimated using the measured drug content per cell and the calculated molar volume.

Determination of Vesicle Size and Shape

The size and shape of cargo loaded vesicles was microscopically measured within loaded macrophages obtained from CFZ-treated animals, using the Cy5 fluorescence channel to specifically monitor the vesicles containing CFZ-HCl. Using ImageJ [31,32], the radius of each vesicle was determined. Vesicles which showed Cy5 fluorescence were counted as CFZ sequestering. The vesicle volume was estimated assuming spherical shape, while CLDI volume was estimated assuming a cylindrical shape.

Analysis of Organ Macrophage Counts

To determine the macrophage population numbers in lung, liver, and spleen from animals treated with CFZ, cryosections were obtained (5μm). The change in the number of macrophages in a volume of tissue was determined by dividing the total F4/80 signal staining intensity between an 8 week CFZ-treated sample by the total F4/80 signal staining intensity of a vehicle-treated sample (the area and thickness of the sections analyzed were kept the same). The total macrophage population was then determined by multiplying literature reported (baseline) macrophage population values for each organ [37] by the relative expansion factor determined via increased intensity of the macrophage marker's fluorescence signal, via immunofluorescence. To determine the fraction of macrophages that contained CLDIs, the fraction of cells which were positive for Cy5 fluorescence and F4/80 staining were determined by visual inspection, using a mask of the F4/80 staining. Five images per organ per animal were analyzed for each measurement.

Measurement of Drug Accumulation based on Whole Organ Homogenates

For chemical analysis protocol development, organs were obtained from euthanized, untreated mice. Samples from the different organs (20-30 mg) were homogenized in radioimmunoprecipitation assay buffer (500 μL; Sigma) with added protease inhibitors (Halt

protease and phosphatase inhibitor cocktail and 0.5 M EDTA; Thermo Pierce, Rockford, IL). In order to determine the recovery yield, the organ homogenates were spiked with a known amount of drug. For analysis, homogenate (350 μL) was removed, and drug was extracted as described under "Biochemical Analysis of Cellular Drug Concentrations."

Determining the Fraction of Drug Sequestered by Macrophages of Different Organs

The total drug content of lung, liver, and spleen tissues at eight weeks of treatment was determined as described above, using established protocols [33]. Because CLDIs form and become stabilized exclusively within macrophages [23,28,34], we sought to determine the fraction of drug sequestered within macrophages of each organ. To accomplish this, tissues (n=3) were removed, weighed, and placed in a sterile petri dish, where they were manually minced and homogenized using a scalpel and syringe plunger. The resulting homogenate was filtered through a cell strainer (40 μm) to remove larger cellular clusters and debris. The filtrate was then centrifuged (300 *x* g, 10 min) to pellet the CLDIs. The supernatant was removed, and the CLDI pellet was resuspended in 10% sucrose in DPBS (Life Technologies, Carlsbad, CA) without calcium chloride or magnesium chloride, pH=7.4. CLDIs were further purified using a 3-layer sucrose gradient (50%, 30%, and 10% sucrose in DPBS) centrifugation method (3200 *x* g, 60 min). The pelleted CLDIs were then dissolved in 9 M H_2SO_4, and the mass of drug was determined using a plate reader (Biotek Synergy 2, Winooksi, VT) at wavelength 450 nm, and background corrected at wavelength 750 nm, which was determined using a standard curve with solutions of known concentration.

Determination of the Cargo Volume Occupied per Macrophage

Using the total recovered mass of drug associated with CLDIs isolated from the liver, lung, and spleen, the volume occupied by drug within individual xenobiotic-sequestering macrophages was estimated based on the number of CLDI containing cells, using the total

expanded macrophage population present in the measured tissue sample, multiplied by the fraction of cells which contained a CLDI (determined microscopically). Using literature reported values for cellular volume of the macrophage [38], the percentage of cellular volume occupied by drug was estimated by dividing the total recovered mass of drug associated within the isolated CLDIs, by the total (calculated) number of CLDI containing cells in the sample of tissue from which the CLDIs were isolated. The fraction of the phagocytic capacity occupied by cargo was calculated by dividing the measured cargo volume by the maximum phagocytic capacity of macrophages [8].

Biochemical Analysis of Drug Concentrations

The concentration of CFZ in plasma or organ homogenates was determined using a previously described method [24]. In brief, blood was collected in microtainer serum separator tubes (catalog no. 3659656; Becton Dickinson, Franklin lakes, NJ) and allowed to clot at room temperature and centrifuged (5,000 x g, 5 min). Samples (20 µl) were extracted with acetonitrile (60 µl, 90% extraction efficiency) for 10 min at 4°C with vortexing. After centrifugation (5,000 x g, 4°C), the supernatant was injected into Agilent 1200 RRLC coupled to 6410 Triple Quad LC-MS equipped with a Waters Xbridge C18 column (2.5 µm x, 2.1 mm x 100 mm). A standard curve was generated by extracting spiked drug samples using serum (or the organ homogenates) from a vehicle-only treated mouse mixed with CFZ stock solution from dimethyl sulfoxide, resulting in 10 different CFZ concentrations between 0 and 30 µM. The peak area was quantified using MassHunter Quantitative Analysis software, vB.04.00. This standard curve was then used to establish the concentration of drugs in experimental samples from blood of drug-treated mice (or from organ homogenates of these mice).

Determination of the Volume of Distribution of the Drug in Different Organs (V_{OD})

Following treatment with 5.25 or 14 mg of CFZ, mice (n=3 per time point) were euthanized and the liver, spleen, small intestine, fat, kidney, and lung were removed, weighed, and the mass of CFZ within each tissue and the concentration within plasma were determined as previously described [24]. The V_{OD} of the drug within macrophages, tissue, and the whole body at the different loading amounts was determined using the ratio between the total drug within tissues or individual cells and the measured plasma concentration.

Experimental Measurement of CFZ's Physicochemical Properties

Using Flynn and Kramer's methodology [39], the pH_{max}, apparent pK_a, intrinsic solubility, salt solubility, and solubility product constant (K_{sp}) of CFZ were experimentally determined as previously reported [28]. Briefly, an excess of CFZ-HCl (25 mg) was placed in 15 mL of Milli-Q water, and 0, 40, 80, 120, or 200 µL of 0.1 M NaOH were added to the vials to achieve an initial equilibration pH measurement. Following a 24 h equilibration period, 10 µL of 0.1 M NaOH was added daily over a five day period, leading to a pH range from 4.5 to 8.9. The samples were then stirred using a magnetic stirrer plate in a 25°C water bath to allow them to equilibrate for 24 h. A 500 µL sample was removed from each vial and filtered through a Spin-X centrifuge tube filter (0.45 µM cellulose acetate, 2 mL polypropylene tubes, non-sterile, Costar®, Cat #8163) for 4 min at 10,000 RPM. The pH of the filtrate was measured (UltraBasic pH meter, Denver Instrument, Bohemia, NY) both before and after the completion of the assay, prior to measurement of solubilized CFZ. The concentration of CFZ was then determined using HPLC analysis (Waters Alliance, Separations Module 2695). Each measurement was performed in triplicate and the average used to construct the pH-dependent solubility profile. Through mathematical manipulation of the Henderson-Hasselbalch equation and inputting different

combinations of the experimental, pH-dependent solubility measurements, the apparent pK_a, intrinsic free base solubility, pH_{max}, and K_{sp} were calculated, as previously described [28].

Solubility Measurements for CFZ and CFZ-HCl in Octanol

In order to determine the solubility values for CFZ and CFZ-HCl in 1-octanol (293245; Sigma-Aldrich), both forms of the drug were introduced in great excess to 1-octanol in glass scintillation vials. A small magnetic stir bar was added to each sample, and the samples were placed on the magnetic stirrer inside the incubator (37°C). After a 24-hour equilibration period, samples were removed from the incubator and immediately filtered using Spin-X centrifuge tube filters (0.45 μm cellulose acetate, 2 mL polypropylene tubes, Costar®) for 4 min at 5,000 x g. The concentration of the soluble drug in 1-octanol was spectrophotometrically determined (285 nm, 37°C; Synergy-2 plate reader; Biotek Instruments, Winooski, VT). For each sample, solubility measurement was performed in triplicate, and the average was reported. The standard curve was generated using CFZ crystals that were dissolved in 1-octanol at known concentrations (1-200 μM). Pure 1-octanol was used as a baseline absorbance.

Statistical Analysis of Experimental Data

All data are expressed as mean ± standard deviation (SD). For multiple comparisons, statistical analysis was performed with one-way analysis of variance (ANOVA) and Tukey's post hoc comparisons. All statistical analyses were performed using IBM SPSS Statistics version 24.0 (IBM Software, Armonk, New York). *p* values less than or equal to 0.05 were considered statistically significant.

Physiologically-based Drug Transport Modeling and Simulation of Intracellular Drug Supersaturation

We used an established, physiologically-based cellular pharmacokinetic modeling framework [39-41] to calculate the time-dependent changes in the concentration of a monovalent weakly basic small molecule drug inside each compartment within a cell following exposure of the cell to a constant extracellular drug concentration. For the present study, we used the open-source modeling software Virtual Cell®. All of the following models can be freely accessed at http://vcell.org. The model used here (*awillmer: Macrophage Cargo Capacity*) was built from the established Virtual Cell model: *jsbaik: 1-Cell PK acid/base/neut total*. For boundary conditions, we used the previously published, standard eukaryotic cell parameter values as input (Table S4-1).

Modeling the Passive Transport Properties of a Weakly Basic Drug that Stably Accumulates and Self-Assembles in Macrophage Lysosomes

We used CFZ as a weakly basic model drug to predict its subcellular phase-transition dependent accumulation. Even though it has two ionizable groups, it can be modeled as a monobasic compound because at physiological pH, the ionization of the amine with the lower pK_a of ~2 will not influence the transmembrane fluxes to any significant extent. In lysosomes, CFZ accumulates as CLDIs, which mostly contain hydrochloride salts of the weak base (CFZ-HCl). Thus, using predetermined physicochemical properties of the free base as well as the salt form of the drug (apparent pK_a = 6.08 [28], and octanol/water partition coefficient logP (logKow = 7.66 [26,27])) as input in the Virtual Cell model, we calculated the time-dependent subcellular distribution of both neutral and ionized molecular species as a function of an extracellular total drug concentration of 10 μM (concentrations in all subcellular compartments are linearly related

to the extracellular concentration). We set the extracellular volume to a high value (Table S4-1), so that the extracellular drug concentrations would remain nearly constant, without being affected by cellular drug uptake. In turn, the degree of supersaturation of the drug molecules in the different cellular compartments was calculated by dividing the concentrations of the protonated and unprotonated species of the drug in those compartments by the calculated solubility of the corresponding charged or neutral species in said compartments. Detailed theoretical calculations and equations used to determine the concentration of the ionized and unionized form of the weakly basic drug within subcellular compartments, and degree of supersaturation of the drug within various subcellular compartments can be found in the Supporting Information.

4.5 Results

Testing the *in vivo* adaptive response of different macrophage populations to a massive, whole organism cargo load

To determine how CFZ bioaccumulation as an expandable mechanopharmaceutical device affects macrophage function, we measured the response of different macrophage subpopulations to an increasingly massive CFZ load. Experimentally, at the smallest whole body cargo load measured (3.5 mg), the drug was mostly present in alveolar macrophages (Figure 4-1a). This cargo was associated with red, optically dense, cytoplasmic vesicles which exhibited little dichroism signal, corresponding to a disordered, amorphous, supramolecular organization [42,43] (Figure 4-1b). A 7 mg whole body cargo load resulted in a modest increase in accumulation in the alveolar macrophages (Figure 4-1c), and a small percentage of the drug was apparent in the peritoneal and liver macrophages (Figure 4-1a). However, the structure of the intracellular cargo became more organized with increasing amounts of drug as reflected in the

elevated optical density (Figure 4-1c) and dichroism (Figure 4-1d) of alveolar, peritoneal, and liver macrophages. At 14 mg, cargo loads redistributed into large, highly ordered CLDIs exhibiting strong dichroism signals in all macrophages (Figure 4-1b). Under all loading conditions, the less mature bone marrow monocytes were free of cargo. At a population level, these trends were confirmed by multi-parameter image-based cytometric analyses [16] (Figure 4-1c, d).

The results of chemical analyses paralleled the observed changes in loading dynamics and the redistribution of cargo among the different macrophage populations. At low (3.5 mg) cargo loading, alveolar macrophages sequestered 29.9 ± 12.4 fmol of CFZ/cell, while the other populations showed minimal loading (Figure 4-1e). After a whole body load of 3.5 mg, less than 0.3% of the maximal phagocytic capacity of the alveolar macrophages was reached (Figure 4-1f). At a larger (7 mgs) whole body cargo load, alveolar macrophages accumulated 34.0 ± 20.3 fmol CFZ/cell, which primarily remained in a disordered form as reflected in the low dichroism signal (Figure 4-1b, d). Peritoneal and liver macrophage populations, due to their differential accumulation pattern (Figure 4-1b), increased their cargo loading per cell to 105.7 ± 10.0 and 63.5 ± 16.2 fmol/cell, respectively. It is noteworthy that at the highest loads of cargo (14 mg), all tissue macrophage subpopulations exhibited similar levels of cargo loading (Figure 4-1e), except for monocytes. Thus, the formation of CLDIs facilitated intracellular cargo loading coincided with a systemic redistribution of cargo among all macrophage sub-populations, such that the load became more evenly distributed in the cell. In these isolated macrophages, the highest cargo volume corresponded to ~1% of the maximal phagocytic capacity of cell (Figure 4-1f) [8]. As such, only a small fraction of the potential intracellular cargo space was occupied even at the highest whole body loads that were measured *in vivo*.

To achieve an even distribution of cargo (which was observed in the most massively loaded condition), macrophages visibly adjusted their intracellular, cytoplasmic membrane organization. For example, with a relatively low amount of loading (3.5 mg), the alveolar macrophage population accumulated an average of 21.6 ± 5.0 vesicles per cell, with each vesicle occupying a mean volume of 0.43 ± 0.29 μm^3 (Table 4-1). Transmission electron micrographs of alveolar macrophages revealed numerous dark, lipid bound inclusions within the cytoplasm (Figure 4-2a). A larger (7 mg) whole body cargo load increased the number of cytoplasmic vesicles by >50% per cell (n=30 cells, $p<0.05$, ANOVA, Tukey's HSD), with the mean vesicular volume increasing by ~125% (Table 4-1). At the largest whole body cargo load tested (14 mg), an expansion of membrane-bound cytoplasmic vesicles was clearly visible (Figure 4-2b). At this point, the number of loaded vesicles per cell decreased by >40%. The expanded, membrane bound vesicles remained stable within the macrophages as long as eight-weeks following the discontinuation of drug administration (Figure 4-2c).

Of noteworthy significance, the amount of cargo in the isolated macrophage populations effectively accounted for most of the total cargo load measured in whole organ homogenates (Table 4-2). Based on the amount of cargo within each organ, the volume of blood that was cleared by the macrophages in the different organs was estimated (the organ-specific Volume of Distribution, V_{OD}; Table 4-3). In pharmacokinetic terms, the whole body V_D of a molecule is the ratio between the amount of drug in the organism and the plasma concentration of the drug [44]. V_D represents the extent of tissue distribution [45] as reflected in the theoretical volume required to contain an administered amount of drug at the same concentration found in plasma. With an increasing cargo load, each macrophage population significantly contributed to V_{OD} and consequently, to V_D (Table 4-3). Given that the volume of a single macrophage is ~1 pL, they

contribute to V_D via the solute-to-solid phase transition that accompanies CLDI formation. At the whole organ level, there was a nearly ~100-fold increase in the V_{OD} within the liver and small intestine, a ~60-fold increase within the spleen and ~10-fold increase within the lung, paralleling an increasing whole body cargo loading from 5.25 to 14 mg (Table 4-4). Adipose tissue and kidneys, neither of which contain large populations of tissue macrophages compared to other organs, had modest increases in the V_{OD} that were much lower than those observed in liver, spleen, lung, and intestine (Table 4-4).

The most important finding in the V_{OD} analysis pertains to the role of organ-specific macrophage subpopulations in the redistribution of cargo loads and its ultimate impact on the measured differences in the V_{OD} of the different organs. The difference in organ-specific V_{OD} (Table 4-4) between animals exposed to a moderate (5.25 mg) or a large (14 mg) cargo load, seemed to result in an increasingly divergent loading pattern. With a 14 mg load, for example, the spleen V_{OD} was >50 times greater than that of the kidney, while at a 5.25 mg load, the spleen V_{OD} was only ~3 times greater than kidney. However, when looking at the specific accumulation of drug in macrophages (Table 4-2 and 4-3; and Figure 4-1e, f), it was apparent that the divergence in the whole organ distribution was due to differences in the number of macrophages per organ mass, since the cargo became more evenly distributed among the resident macrophages of the respective organs.

Passive transport acting in concert with a pH and chloride-dependent phase transition is sufficient to explain the function of CFZ as an expandable mechanopharmaceutical device

In order to determine whether passive transport can explain the selective precipitation and growth of CFZ hydrochloride crystals in lysosomes, we proceeded to dissect the subcellular transport and self-assembly properties of CFZ using a physiologically based, cellular

pharmacokinetics modeling and simulation approach (Figure 4-3). Previous analyses have identified the hydrochloride salt form of CFZ as the major fraction of the bioaccumulated drug [28,34]. This hydrochloride salt form was specifically present in CLDIs, which are stabilized within acidic intracellular vesicles (as revealed by inhibiting the proton-pumping, V-ATPase which decreases CLDI formation and CFZ accumulation) [28]. Without macrophages, CLDIs also failed to form and CFZ accumulated in tissues to a much lesser extent [28].

Consistent with these previous experimental observations [28,34], our simulation results revealed how the unprotonated, neutral molecular species of CFZ accumulated intracellularly in the presence of a constant extracellular drug concentration (Fig. 4a). As expected, because of the higher pH (relative to the drug's pK_a) of the cytoplasm and mitochondria, the unprotonated free base concentration was highest in the cytoplasm (Fig. 4b) and mitochondria (Fig. 4c), relative to lysosomes (Fig. 4d). Simulating the distribution of the ionized (protonated) molecular species of the drug over time, we observed that the protonated form remained nearly constant in the extracellular medium (Fig. 4e). The concentration of protonated drug was lowest in cytoplasm (Fig. 4f) and mitochondria (Fig. 4g), but increased dramatically in the lysosomes (Fig. 4h) due to ion trapping [46]. In fact, lysosomes possessed the highest drug concentration of all cellular compartments (Fig. 4h). Because of the linearity of the model, the neutral and protonated, charged molecular species in all of the compartments proportionally decreased when the total initial extracellular CFZ concentration was reduced (for example, changing the units of micromolar to nanomolar).

In order to determine the propensity of the free base and ionized forms of the drug to precipitate in the different cellular compartments, we calculated the degree of supersaturation of both forms of the drug using their solubility properties obtained from experimental

measurements (Table 4-5). Degrees of supersaturation were calculated by determining the ratio of simulated steady state CFZ concentration to CFZ solubility (Equations 3 and 4 in the Appendix C). The greatest degree of supersaturation for the ionized form of the drug was observed in the lysosomal compartment (Table 4-5). Within the lysosomal lumen, the supersaturation of CFZ-HCl exceeded all other compartments by more than two orders of magnitude (Table 4-5). The primary reasons for the high supersaturation in the lysosomal lumen were the high chloride concentrations and a lysosomal pH lower than the pH_{max} of CFZ-HCl. Moreover, the degree of supersaturation of CFZ-HCl in the lysosome was exceeded by 3 to 6 orders of magnitude over that of CFZ free base (Table 4-5). This indicates that the conditions for salt precipitation would be most favorable in the lysosomal lumen, and as a result, would be the first location within the cell that precipitation would be expected to occur, as concentrations in all compartments increase following drug administration. Note that the intracellular concentrations predicted by the transport model were linearly dependent on the starting drug concentrations in the extracellular medium, so the model effectively predicted the most likely site of intracellular drug precipitation based on the lowest extracellular concentration necessary to achieve supersaturation in any intracellular compartment.

4.6 Discussion

In this study, we propose that CFZ accumulation in macrophages leads to physical alterations in cell structure and function that result from CFZ's self-assembly into an expandable mechanopharmaceutical device. This expandable mechanopharmaceutical device specifically accumulates in macrophage lysosomes following prolonged oral drug administration, and its effects are posited to result from a physical space occupied by the drug, independent of the drug's pharmacological activity. As an expandable mechanopharmaceutical device, we

considered CLDIs as a physical probe that can be used to measure the cargo loading capacity of different macrophage subpopulations *in vivo,* and used it to directly determine the V_D of the drug in different organs. While prior studies have determined that CLDI formation is compatible with the maintenance of normal ion homeostasis in lysosomes of macrophages [28], this is the first study to show that the mass and volume occupied by drug is specifically accumulating in lysosomes within these cells, while assessing its impact on the drug's volume of distribution (V_D) [16,34]. While it is often assumed that the V_D of a therapeutic agent is a constant, our measurements indicate that this is not necessarily the case. Furthermore, based on our mathematical modeling and simulation analysis, lysosomal pH and chloride content were found to be sufficient to account for the selective accumulation of CFZ in macrophage lysosomes accounting for the cell type selectivity of this phenomenon.

When studying the impact of macrophages on transport phenomena, fluid tracers or nanoparticles that are readily ingested by macrophages have been previously used as functional markers of macrophage-mediated clearance. To assess whole organism cargo capacity of macrophages *in vivo*, our results show how an expandable mechanopharmaceutical device that self-assembles from a small molecule building block could potentially be used to stretch the cell's cargo carrying capacity with the largest possible cargo load that can be accommodated by a living organism. This led us to consider the following question: how exactly does the organism respond to the massive build-up of a whole-body macrophage cargo load? In the experiments reported herein, the null hypothesis was that all macrophages would accumulate the drug to the same extent in all organs, and that at some point a toxicological effect may become manifested. However, our experimental results led us to reject this, in favor of an alternative hypothesis: different macrophage subpopulations initially vary in their ability to bioaccumulate drug, but

gradually respond to an increasingly massive amount of cargo so that the load does not exceed the cargo capacity of the individual cells and becomes more evenly distributed across all of the macrophage populations throughout the different organs of the body. Based on theoretical considerations, a physiologically-based cellular pharmacokinetic model indicated that this phenomenon may be entirely determined by an energetically-favorable, thermodynamically-driven loading state that decreases the total free energy of the drug while maximizing the volume-to-surface area ratio of intracellular drug inclusions. The significantly different rates at which this occurs in macrophage subpopulations do not simply reflect the extent of perfusion of the different organs, nor do they reflect the partitioning of soluble drug or trapping of circulating drug particles in these organs since it varied as the whole organism drug load increased. Since undifferentiated, bone marrow monocytes did not accumulate drug to any significant extent, we infer that differences in drug accumulation kinetics reflect organ-specific variations in the differentiation of macrophages into specialized, xenobiotic sequestering cells.

In terms of how these findings impact pharmacokinetics, CFZ induced changes in V_D which counters the underlying assumptions about the mechanistic underpinning of this pharmacokinetic parameter. V_D is usually considered the apparent volume that a systemically administered drug distributes in to reach a measureable concentration in the blood. For many poorly soluble, weakly basic drugs, the V_D can be in the order of thousands of liters, which greatly exceeds the volume of body water (60-100 liters). Large V_D is generally thought to be due to the preferential partitioning of hydrophobic drug molecules into adipose tissue or cellular membranes and lipids. For poorly soluble drugs that are administered at high doses for prolonged periods of time, if the drug molecules are metabolically stable and eliminated very slowly, bioaccumulation could eventually lead to a phase transition, with insoluble aggregates forming

throughout the organism, expanding the V_D. Accordingly, the experimental and theoretical analysis presented in this study suggests that the simple, thermodynamic partitioning mechanisms underlying the general concept of V_D may need to be revisited, especially for poorly soluble weakly basic drugs like CFZ which massively bioaccumulate in the organism.

Indeed, the experimental results presented in this study add support to the role of macrophage lysosomal pH and chloride ion regulation in contributing to, and accounting for, most of the accumulation and distribution of CFZ *in vivo* [28,34]. The results of our physiologically based model was consistent with CFZ precipitation occurring selectively in macrophage lysosomes, because the stability of CFZ hydrochloride precipitates in this organelle surpassed that of all other sites in the cell, as well as in the extracellular environment, by more than three orders of magnitude. Macrophages possess highly acidic lysosomes, which can expand to accommodate large cargo loads, and the macrophage population itself is able to undergo changes in structure and function to adapt to the cargo. In the future, the mathematical model could be used to predict the intracellular concentration and precipitation of ionized vs. neutral molecular species of other weakly basic small molecule drugs and to identify other small molecule chemical agents that have similar subcellular disposition characteristics as CFZ.

Regarding our use of the word “device”, it may sound unusual if one only considers the formation of a precipitate as a side-effect or as a toxic phenomenon arising from poor pharmacokinetics or inadequate dosing. In this particular case, the precipitation behavior of the drug is being purposefully co-opted as a volumetric instrument. It is being introduced as a tool to expand the macrophage cargo capacity and to probe how the organism responds to an increasing endophagolysosomal cargo load. In the scientific literature, one can find many references in which drugs are referred to as pharmacological “probes” or “tools” when used as inhibitors or

stimulators of endogenous molecular targets or pathways, with the goal of obtaining information about how these targets or pathways mediate biochemical signaling or physiological responses in living organisms [47–50]. The word "device" was purposefully chosen to highlight how CFZ was used as a self-assembling building block to construct a physical object to study the "cargo capacity" of macrophages. To use CLDIs as measurement "devices", we have developed methods to isolate and stabilize CLDIs [33] as well as microscopy instruments to monitor their optical [16], photoacoustic [51] and biomechanical properties [52]. Instead of engineering a new chemical compound to measure the cargo capacity in a living organism, CFZ was repurposed and administered to the animals to operate in this very physical manner, independently of the antimicrobial, redox, and other pharmacological interactions of freely soluble CFZ molecules.

4.7 Conclusion

To conclude, the results presented herein suggest a physical stimulus-dependent, macrophage-mediated biological response mechanism that is activated by the function of CFZ as a building block of an expandable mechanopharmaceutical device that accumulates within these cells. Macrophages actively stabilize intracellular CFZ as insoluble complexes that are trapped within their endophagolysosomal compartment. To accommodate increasingly massive loads of cargo, macrophages increased in numbers and adapted their intracellular membrane organization to expand the intracellular cargo space; this resulted in a gradual but dramatic increase in V_D. While resident macrophages of different organs demonstrate significant variations in their response to increasing loads of cargo, all differentiated macrophage populations were capable of sequestering very large loads. Of noteworthy significance, to our knowledge this is the first time that changes in the V_D of a small molecule drug has been directly linked to an adaptive, immune system-mediated, xenobiotic sequestration response.

4.9 Acknowledgements and Funding

This study was supported by NIH grant R01GM078200 awarded to GRR.

4.10 Figures and Tables

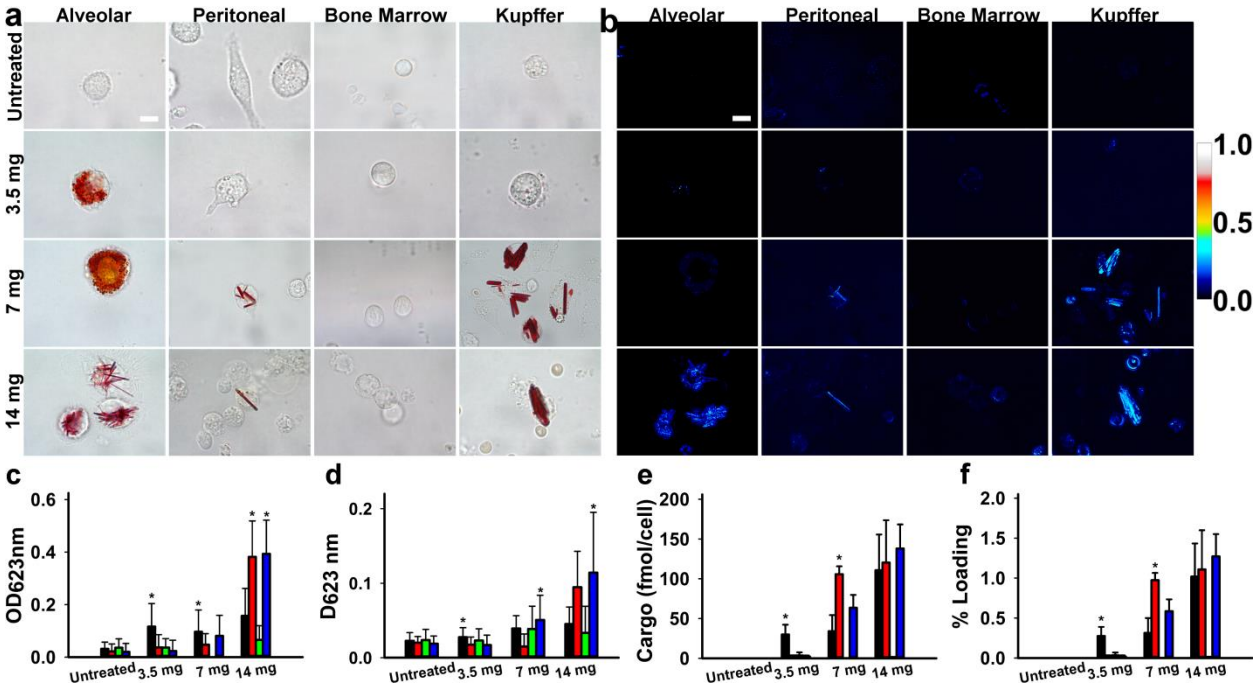

Figure 4-1: Microscopic imaging cytometry and quantitative chemical analysis indicate variations in cargo loading dynamics of different macrophage sub-populations. (**a**) Brightfield images of isolated macrophage and monocytes with increasing whole-body cargo loading. (**b**) Linear diattenuation images of isolated macrophage and monocytes with increasing whole-body cargo loading. Optical density (**c**), linear diattenuation (**d**), cargo loading per xenobiotic-sequestering cell (**e**), and percent of maximal cargo loading (**f**) of alveolar macrophages (black), peritoneal macrophages (red), bone marrow monocytes (green), and Kupffer cells (blue) with increasing cargo loading. Data are the mean (SD) of 150 cells per cell type and condition, for imaging studies, n=3 mice per cargo treatment for drug accumulation, (*=$p<0.05$, ANOVA, Tukey's HSD) (Scale bar = 10 μm).

Table 4-1: Vesicle number, size, and volume occupancy in alveolar macrophages following cargo loading.

Cargo Loading	Mean number of vesicles per cell ± SD (n=30 cells)	Mean vesicle volume ± SD (n=50 vesicles)	Mean total volume occupied by vesicles ±SD (n=50 vesicles)
3.5 mg	21.6 ± 5.0	0.43 ± 0.29 μm^3	9.2 ± 6.7 μm^3
7.0 mg	32.6 ± 6.8*	0.97 ± 0.96 μm^3	31.7 ± 32.1 μm^3
14.0 mg	18.4 ± 11.1	13.8 ± 10.4 μm^3*	253.8 ± 244.5 μm^3

* = $p < 0.05$, ANOVA, Tukey's HSD

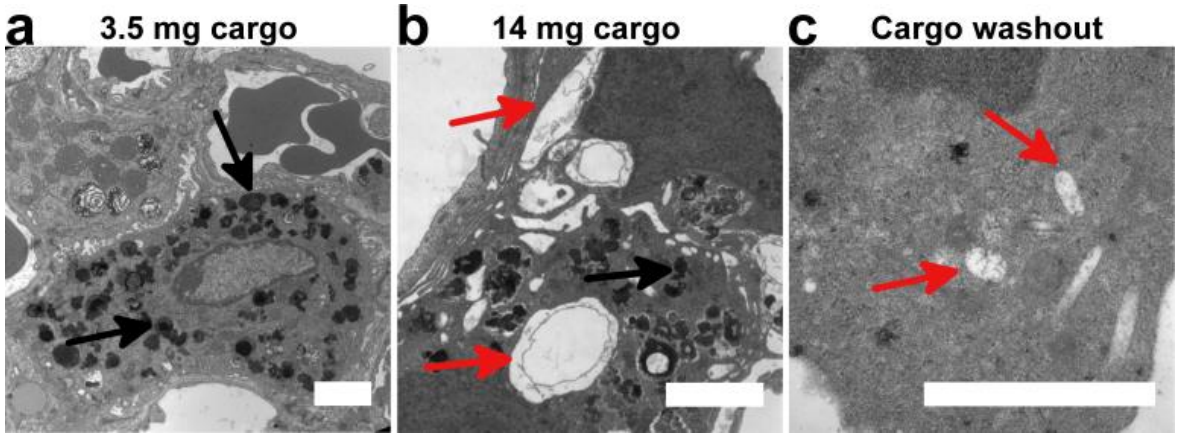

Figure 4-2: Macrophage cargo accumulation induces reorganization of internal membrane architecture. (**a**) Following whole-body cargo loading of 3.5 mg, small vesicles that fill the cytoplasm are apparent in alveolar macrophages. (**b**) A higher cargo load (14mg) results in accumulation of crystal-like drug inclusions (CLDIs) throughout the cytoplasm. (**c**) CLDIs remain stable even following an eight week washout period. Black arrows denote cargo-laden vesicles and red arrows denote cavities left from CLDIs removed during sample preparation. Scale bar is 2000 nm.

Table 4-2. Estimated cargo loads of liver, spleen, and lung macrophages, at a 14 mg whole body load.

Macrophage Population	Cargo mass (mg)	Percent Xenobiotic Sequestering	Total Xenobiotic Sequestering Cells (x 10^6)	Fmol Cargo/Xenobiotic Sequestering Cell	% Cell Volume Occupied by Cargo
Liver	4.57 ± 0.78	88.5 ± 3.3%	80 ± 19	120.9 ± 35.3	2.11 ± 0.62%
Spleen	3.23 ± 0.27	83.9 ± 12.5%	22 ± 5.9	310.5 ± 86.9	5.42 ± 1.52%
Lung	0.32 ± 0.06	81.1 ± 3.2%	3.7 ± 1.7	183.2 ± 91.5	3.20 ± 1.60%

Data represent the mean ± S.D., n = 3 mice.

Table 4-3. Volume of distribution in liver, lung, and spleen macrophage, at a 5.25 and 14 mg whole-body loads.

Macrophage Population	5.25 mg cargo V_{OD} (nL/macrophage)	14 mg cargo V_{OD} (nL/macrophage)
Liver	0.66 ± 0.08	33.51 ± 16.43*
Spleen	0.49 ± 0.03	64.25 ± 32.48*
Lung	5.51 ± 0.16	42.73 ± 31.58*

* = $p < 0.05$, Two-tailed Student's t-test

Table 4-4. Volume of distribution within specific organs, at a 5.25 and 14 mg whole-body load.

Tissue (n=3 per treatment)	5.25 mg cargo V_{OD} (L/kg tissue)	14 mg cargo V_{OD} (L/kg tissue)
Liver	33.9 ± 13.1	2232.5 ± 958.2*
Spleen	118.8 ± 85.4	6139.3 ± 2637.0*
Lung	91.2 ± 12.0	902.3 ± 524.1
Fat	91.8 ± 15.2	129.1 ± 61.1
Jejunum and Ileum	11.1 ± 6.3	1085.2 ± 606.2*
Kidney	31.1 ± 7.3	125.6 ± 55.5

* = $p < 0.05$, Two-tailed Student's t-test

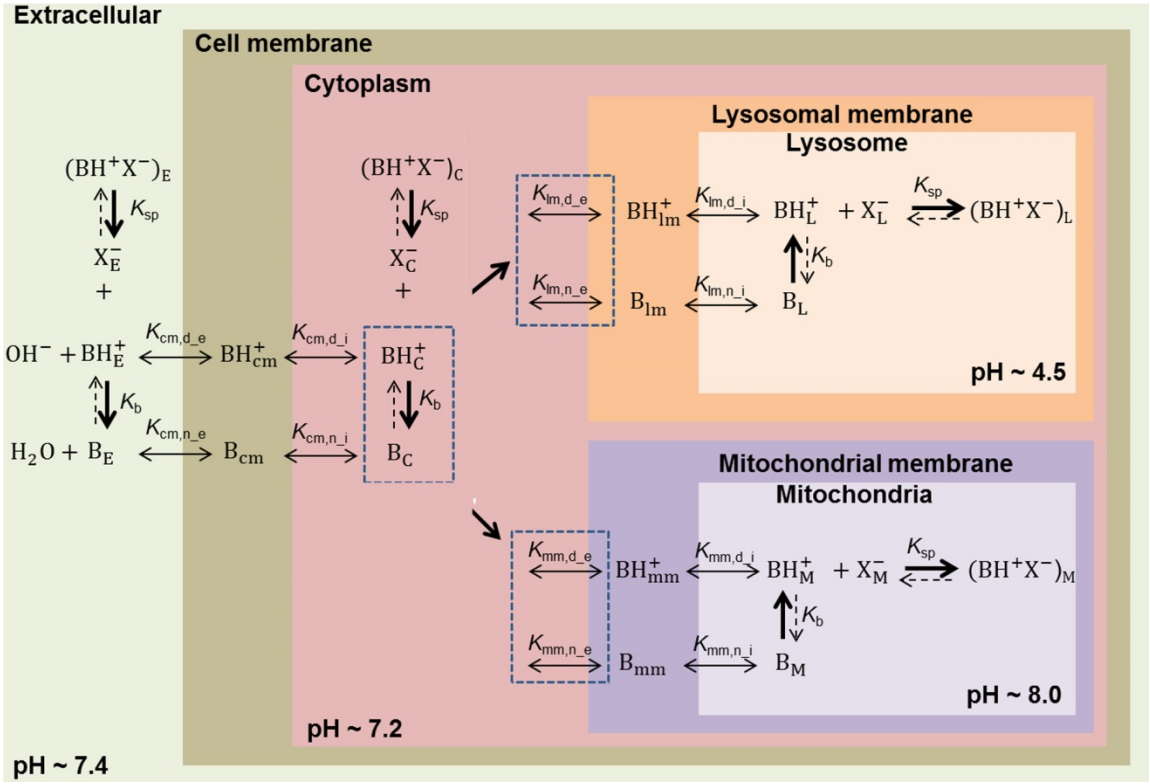

Figure 4-3: Diagrammatic representation of the integrated, transport and precipitation modeling approach used to determine the most likely cite of intracellular CFZ precipitation. The definition of each parameter value is given in Table S1 in the Supporting Information.

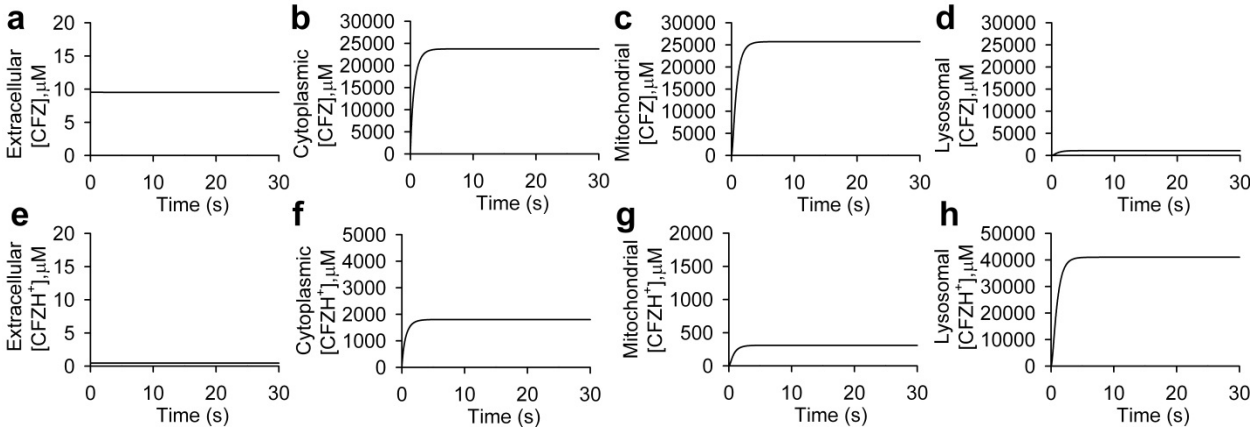

Figure 4-4: Time-plot simulations of intracellular concentrations of neutral and protonated species of clofazimine (CFZ) in different subcellular compartments. (**a**) Extracellular drug accumulation of neutral CFZ remains constant during the time course of the simulation; (**b**) neutral drug molecules enter and reach steady state in cytoplasm; (**c**) the mitochondrial compartment has the highest free base drug concentration due to a pH higher than the cytosol and significant lipid content; (**d**) lysosomes have low concentrations of the neutral species due to their low pH; (**e**) extracellular concentrations of ionized CFZ ($CFZH^+$) are much lower than neutral CFZ species, and remains constant; (**f**) due to the physiological pH of the cytoplasmic compartment, there is very little protonated drug, as well; (**g**) the high pH of the mitochondria leads to a low concentration of protonated free base, although the concentration is higher than in the extracellular medium due to the mitochondrial membrane potential-dependent uptake; (**h**) the lysosomal compartment has the highest ionized drug concentration due to ion trapping.

Table 4-5. Steady-state degree of supersaturation of free base CFZ and CFZ-HCl based on a simulated, initial extracellular concentration of 10 μM

Compartments	Estimated degree of supersaturation of free base CFZ at steady state	Estimated degree of supersaturation of CFZ-HCl at steady state
Extracellular	[b]1.98×10^{1}	0[a]
Cytosol	[b]4.95×10^{4}	0[a]
Mitochondrial lumen	[b]5.36×10^{4}	0[a]
Lysosomal lumen	[b]2.25×10^{3}	[c]1.36×10^{7}

[a]Because the local pH is higher than the pHmax, only the free base form is predicted to accumulate as the most stable precipitate.
[b]The simulated, steady state concentration of CFZ free base in the given aqueous compartment was divided by the experimentally measured, intrinsic aqueous solubility of CFZ (0.48 μM) [28].
[c]Based on this degree of supersaturation calculated with Equation 4 in the Appendix C, the solubility of CFZ-HCl in lysosomes, in the presence of 110 mM chloride at pH = 4.5, was 3 nM.

4.11 References

1. Epelman S, Lavine KJ, Randolph GJ. Origin and functions of tissue macrophages. Immunity. 2014;41(1):21–33.

2. Murray PJ, Wynn TA. Protective and pathogenic functions of macrophage subsets. Nat Rev Immunol. 2011;11(11):723–37.

3. Davies LC, Jenkins SJ, Allen JE, Taylor PR. Tissue-resident macrophages. Nat Immunol. 2013;14(10):986–95.

4. Mindell JA. Lysosomal acidification mechanisms. Annu Rev Physiol. 2012;74(1):69–86.

5. Wang S-P, Krits I, Bai S, Lee BS. Regulation of enhanced vacuolar H+-ATPase expression in macrophages. J Biol Chem. 2002;277(11):8827–34.

6. Hamczyk MR, Villa-Bellosta R, Andrés V. *In vitro* macrophage phagocytosis assay. In: Andrés V, Dorado B, editors. Methods in mouse atherosclerosis. New York, NY: Springer New York; 2015. p. 235–46.

7. Steinberg BE, Grinstein S. Analysis of macrophage phagocytosis: quantitative assays of phagosome formation and maturation using high-throughput fluorescence microscopy. Methods Mol Biol (Clifton, NJ). 2009;531:45–56.

8. Cannon GJ, Swanson JA. The macrophage capacity for phagocytosis. J Cell Sci. 1992;101(4):907–13.

9. Broz P, Ben-Haim N, Grzelakowski M, Marsch S, Meier W, Hunziker P. Inhibition of macrophage phagocytotic activity by a receptor-targeted polymer vesicle-based drug delivery formulation of pravastatin. J Cardiovasc Pharmacol. 2008;51(3):246–52.

10. Hirota K, Terada H. Endocytosis of particle formulations by macrophages and its application to clinical treatment. In: Ceresa B, editor. Molecular regulation of endocytosis. Rijeka: InTech; 2012. p. Ch. 16.

11. Lemaire S, Tulkens PM, Van Bambeke F. Cellular pharmacokinetics of the novel Biaryloxazolidinone Radezolid in phagocytic cells: studies with macrophages and Polymorphonuclear neutrophils. Antimicrob Agents Chemother. 2010;54(6):2540–8.

12. Carryn S, Chanteux H, Seral C, Mingeot-Leclercq MP, Van Bambeke F, Tulkens PM. Intracellular pharmacodynamics of antibiotics. Infect Dis Clin N Am. 2003;17(3):615–34.

13. Stamler DA, Edelstein MA, Edelstein PH. Azithromycin pharmacokinetics and intracellular concentrations in legionella pneumophila-infected and uninfected Guinea pigs and their alveolar macrophages. Antimicrob Agents Chemother. 1994;38(2):217–22.

14. Foulds G, Shepard RM, Johnson RB. The pharmacokinetics of azithromycin in human serum and tissues. J Antimicrob Chemother. 1990;25(suppl_A):73–82.

15. Keswani RK, Yoon GS, Sud S, Stringer KA, Rosania GR. A far-red fluorescent probe for flow cytometry and image-based functional studies of xenobiotic sequestering macrophages. Cytometry A. 2015;87(9):855–67.

16. Rzeczycki P, Yoon GS, Keswani RK, Sud S, Stringer KA, Rosania GR. Detecting ordered small molecule drug aggregates in live macrophages: a multi-parameter microscope image data acquisition and analysis strategy. Biomed Opt Express. 2017;8(2):860–72.

17. Logan R, Kong AC, Axcell E, Krise JP. Amine-containing molecules and the induction of an expanded lysosomal volume phenotype: a structure–activity relationship study. J Pharm Sci. 2014;103(5):1572–80.

18. Funk R, Krise J. Cationic amphiphillic drugs cause a marked expansion of apparent lysosomal volume: implications for an intracellular distribution-based drug interaction. Mol Pharm. 2012;9(5): 1384–95.

19. Kaufmann A, Krise J. Lysosomal sequestration of amine-containing drugs: analysis and therapeutic implications. J Pharm Sci. 2006;96(4):729–46.

20. Arbiser J, Moschella S. Clofazimine: a review of itsmedical uses and mechanisms of action. J Am Acad Dermatol. 1995;32(2):241–7.

21. Cholo M, Steel H, Fourie P, Germishuizen W, Anderson R. Clofazimine: current status and future prospects. J Antimicrob Chemother. 2011.

22. DrugBank. Clofazimine. In. drugbank.ca; 2013.

23. Baik J, Rosania GR. Macrophages sequester Clofazimine in an intracellular liquid crystal-like supramolecular organization. PLoS One. 2012;7(10):e47494.

24. Baik J, Stringer KA, Mane G, Rosania GR. Multiscale distribution and bioaccumulation analysis of Clofazimine reveals a massive immune system-mediated xenobiotic sequestration response. Antimicrob Agents Chemother. 2013;57(3):1218–30.

25. Sukpanichnant S, Hargrove NS, Kachintorn U, Manatsathit S, Chanchairujira T, Siritanaratkul N, et al. Clofazimine-induced crystal-storing histiocytosis producing chronic abdominal pain in a leprosy patient. Am J Surg Pathol. 2000;24(1):129–35.

26. Information NCfB. PubChem Compound Database; CID=2794. 2015 June 1. Available from: http://pubchem.ncbi.nlm.nih.gov/compound/2794

27. Quigley JM, Fahelelbom KMS, Timoney RF, Corrigan OI. Temperature dependence and thermodynamics of partitioning of clofazimine analogues in the n-octanol/water system. Int J Pharm. 1990;58(2):107–13.

28. Woldemichael T, Keswani RK, Rzeczycki PM, Murashov MD, LaLone V, Gregorka B, et al. Reverse engineering the intracellular self-assembly of a functional Mechanopharmaceutical device. Sci Rep. 2018;8(1):2934.

29. Yoon GS, Keswani RK, Sud S, Rzeczycki PM, Murashov MD, Koehn TA, et al. Clofazimine biocrystal accumulation in macrophages upregulates interleukin 1 receptor antagonist production to induce a systemic anti-inflammatory state. Antimicrob Agents Chemother. 2016;60(6):3470–9.

30. Zhang X, Goncalves R, Mosser DM. The isolation and characterization of murine macrophages. In. Current protocols in immunology: John Wiley & Sons, Inc.; 2001.

31. Schneider CA, Rasband WS, Eliceiri KW. NIH image to ImageJ: 25 years of image analysis. Nat Methods. 2012;9(7):671–5.

32. Abramoff MD, Magalhaes PJ, Ram SJ. Image processing with ImageJ. Biophoton Int. 2004;11(7):36–42.

33. Yoon G, Sud S, Keswani R, Baik J, Standiford T, Stringer K, et al. Phagocytosed Clofazimine biocrystals can modulate innate immune signaling by inhibiting TNF alpha and boosting IL-1RA secretion. Mol Pharm. 2015;12:2517–27.

34. Keswani R, Baik J, Yeomans L, Hitzman C, Johnson A, Pawate A, et al. Chemical analysis of drug biocrystals: a role for Counterion transport pathways in intracellular drug disposition. Mol Pharm. 2015;12:2528–36.

35. Trexel J, Yoon GS, Keswani RK, McHugh C, Yeomans L, Vitvitsky V, et al. Macrophage-mediated Clofazimine sequestration is accompanied by a shift in host energy metabolism. J Pharm Sci. 2017;106(4):1162–74.

36. Murashov MD, LaLone V, Rzeczycki PM, Keswani RK, Yoon GS, Sud S, et al. The physicochemical basis of Clofazimine-induced skin pigmentation. J Investig Dermatol. 2017;138:697-703.

37. Lee S, Starkey P, Gordon S. Quantitative analysis of total macrophage content in adult mouse tissues. Immunochemical studies with monoclonal antibody F4/80. J Exp Med. 1985;161(3):475–89.

38. Champion JA, Mitragotri S. Role of target geometry in phagocytosis. Proc Natl Acad Sci U S A. 2006;103(13):4930–4.

39. Trapp S, Rosania GR, Horobin RW, Kornhuber J. Quantitative modeling of selective lysosomal targeting for drug design. Eur Biophys J: EBJ. 2008;37(8):1317–28.

40. Min KA, Zhang X, Yu JY, Rosania GR. Computational approaches to analyse and predict small molecule transport and distribution at cellular and subcellular levels. Biopharm Drug Dispos. 2014;35(1):15–32.

41. Rodgers T, Rowland M. Physiologically based pharmacokinetic modelling 2: predicting the tissue distribution of acids, very weak bases, neutrals and zwitterions. J Pharm Sci. 2006;95(6):1238–57.

42. Mehta SB, Shribak M, Oldenbourg R. Polarized light imaging of birefringence and diattenuation at high resolution and high sensitivity. J Opt. 2013;15(9):094007.

43. Oldenbourg R. Polarized light microscopy: principles and practice. Cold Spring Harb Protoc. 2013;2013(11):pdb.top078600.

44. Toutain PL, Bousquet-MÉLou A. Volumes of distribution. J Vet Pharmacol Ther. 2004;27(6):441–53.

45. Smith DA, Beaumont K, Maurer TS, Di L. Volume of distribution in drug design. J Med Chem. 2015;58(15):5691–8.

46. de Duve C, de Barsy T, Poole B, Trouet A, Tulkens P, Van Hoof F. Commentary. Lysosomotropic agents. Biochem Pharmacol. 1974;23(18):2495–531.

47. Oswald S, Terhaag B, Siegmund W. *In vivo* probes of drug transport: commonly used probe drugs to assess function of intestinal P-glycoprotein (ABCB1) in humans. In: Fromm MF, Kim RB, editors. Drug Transporters. Berlin: Springer Berlin Heidelberg; 2011. p. 403–47.

48. Huguet J, Gaudette F, Michaud V, Turgeon J. Development and validation of probe drug cocktails for the characterization of CYP450-mediated metabolism by human heart microsomes. Xenobiotica. 2018:1–13.

49. Kivisto KT, Kroemer HK.Use of probe drugs as predictors of drug metabolism in humans. J Clin Pharmacol. 1997;37(S1):40s–8s.

50. Cermakova K, Hodges HC. Next-Generation Drugs and Probes for chromatin biology: from targeted protein degradation to phase separation. Molecules (Basel, Switzerland) 2018;23(8).

51. Keswani RK, Tian C, Peryea T, Girish G, Wang X, Rosania GR. Repositioning Clofazimine as a macrophage-targeting photoacoustic contrast agent. Sci Rep. 2016;6:23528.

52. Horstman EM, Keswani RK, Frey BA, Rzeczycki PM, LaLone V, Bertke JA, et al. Elasticity in macrophage-synthesized biocrystals. Angew Chem. 2017;56(7):1815–9.

Chapter 5

The Physicochemical Basis of Clofazimine-Induced Skin Pigmentation

5.1 Relevance to Thesis

This chapter was adapted from the following publication:

***Murashov MD**, LaLone V, Rzeczycki PM, Keswani RK, Yoon GS, Sud S, Rajeswaran W, Larsen S, Stringer KA, Rosania GR. **2018**. The physicochemical basis of clofazimine-induced skin pigmentation. **J Invest Dermatol** 138:697-703; doi: 10.1016/j.jid.2017.09.031*

This study allowed me to conclude Specific Aim 1 of this thesis. To test whether CFZ-induced skin pigmentation is due to CLDI formation, I identified a closely related clofazimine analog that does not precipitate under physiological pH and chloride conditions that are required for CLDI formation (Chapter 3). As a result, I developed methods to isolate, quantify, and analyze CFZ in mice skin tissues and determined that the major side effect from orally administered CFZ is associated with the CFZ free base, and not the accumulated drug biocrystals (e.g. CLDIs).

These results further validated the central hypothesis that even though CFZ-HCl and CFZ free base have the same API, the CFZ-HCl is a more therapeutically efficacious form of CFZ that could be potentially used in repurposing this drug for other indications. In fact, to reformulate and repurpose this drug for other indication and potentially circumvent the CFZ-induced skin pigmentation, I developed biomimetic formulation of CLDIs (synthetic, micronized

CFZ-HCl crystals) for parenteral administration (Chapter 6) and tested its efficacy in a different indication, gouty arthritis (Chapter 7).

5.2 Abstract

Clofazimine is a weakly basic, Food and Drug Administration-approved antibiotic recommended by the World Health Organization to treat leprosy and multi-drug-resistant tuberculosis. Upon prolonged treatment, clofazimine extensively bioaccumulates and precipitates throughout the organism, forming crystal-like drug inclusions (CLDIs). Due to the drug's red color, it is widely believed that clofazimine bioaccumulation results in skin pigmentation, its most common side effect. To test whether clofazimine-induced skin pigmentation is due to CLDI formation, we synthesized a closely related clofazimine analog that does not precipitate under physiological pH and chloride conditions that are required for CLDI formation. Despite the absence of detectable CLDIs in mice, administration of this analog still led to significant skin pigmentation. In clofazimine treated mice, skin cryosections revealed no evidence of CLDIs when analyzed with a microscopic imaging system specifically designed for detecting clofazimine aggregates. Rather, the reflectance spectra of the skin revealed a signal corresponding to the soluble, free base form of the drug. Consistent with the low concentrations of clofazimine in the skin, these results suggest that clofazimine-induced skin pigmentation is not due to clofazimine precipitation and CLDI formation, but rather to the partitioning of the circulating, free base form of the drug into subcutaneous fat.

5.3 Introduction

Drug-induced skin pigmentation corresponds to approximately 10-20% of all cases of hyperpigmentation [1]. It can be induced by a wide variety of drugs (i.e., nonsteroidal anti-inflammatory drugs, weakly basic drugs, heavy metals, psychotropic drugs, etc.) through several mechanisms that can involve an accumulation of melanin as a nonspecific postinflammatory

change in predisposed individuals, often worsened by sun exposure; an accumulation of the triggering drug itself and/or reacting with other substances in the skin; and due to deposits of certain heavy metals (i.e., iron) that can cause damage to the dermal vessels [1]. Hyperpigmentation caused by weakly basic drugs (i.e., chloroquine, amiodarone, and clofazimine) is of particular interest and importance because approximately 75% of drugs on the market are classified as weak bases [1-5]. One of the most extreme examples of weakly basic drugs that causes severe hyperpigmentation is clofazimine, and yet, the basis of clofazimine drug-induced skin pigmentation has never been investigated.

Clofazimine (CFZ) is a weakly basic, very lipophilic, phenazine antibiotic [6] that has been effectively used to treat leprosy for over 40 years. Curing more than 14 million people worldwide, this drug is on the World Health Organization's list of essential medications [7]. Furthermore, because of its potent activity against Mycobacterium tuberculosis, CFZ is now recommended by World Health Organization as a second line agent against multi-drugresistant tuberculosis, which is supported by *in vitro* animal and human studies [8, 9], including a randomized, prospective clinical trial [5].

Regardless of the indication, whether it is for leprosy or multi-drug-resistant tuberculosis, studies that have evaluated the clinical efficacy and tolerability of CFZ have reported that skin pigmentation is the most common and dominating side effect that is observed in more than 94% of the patients [3, 5]. Patients may also experience ichthyosis or gastrointestinal symptoms, but at the normal dosage of 50 to 100 mg/d, no other major side effects have been reported [3, 10-12].

In mice, long-term exposure (≥8 weeks) to orally administered CFZ has also been associated with extensive pigmentation of skin and internal organs (Figure 5-1) [13]. Solid drug

precipitates accumulate in tissue macrophages, forming crystal-like drug inclusions (CLDIs) that are most abundant in the liver and spleen [13-15]. CLDIs have also been reported in humans treated with the drug [16, 17]. Once inside the cell, these biocrystals display robust stability and remain in the body long after the discontinuation of treatment [13].

Microscopically, CLDIs show strong fluorescence in the Cy5 channel (650 nm excitation/670 nm emission) [18]. Furthermore, CLDIs are also detected via diattenuation because of the interaction of these supramolecular ordered structures with polarized light [19]. The analysis of isolated CLDIs revealed chemical and structural properties that are consistent with that of a specific CFZ hydrochloride salt (CFZ-HCl) polymorph [20].

Because orally administered CFZ has been associated with massive intracellular accumulation of CLDIs and strong red pigmentation of macrophage-containing organs [13], we hypothesized that skin pigmentation is associated with CLDI bioaccumulation in macrophages. To test this hypothesis, we identified a closely related CFZ analog that does not form CLDIs and determined its ability to cause skin pigmentation. In addition, we characterized the spectral properties of CFZ-induced skin pigmentation and conducted detailed microscopic analysis to identify the optical signature of CLDIs or precipitated CFZ hydrochloride salt in the skin of drug-treated mice.

5.4 Materials and Methods

Animal experiments

All animal care was provided by the University of Michigan's Unit for Laboratory Animal Medicine (ULAM), and the experimental protocol was approved by the Committee on Use and Care of Animals. As per previously established dosage regimen [13, 18, 21], 4- to 5-week-old Balb/c and C57BL/6 mice from Jackson Laboratory (Bar Harbor, ME) were given an

ad libitum drug powder feed diet, designed to target oral dose equivalent of 10 mg/kg/d CFZ (C8895, Sigma-Aldrich, St. Louis, MO) or CFZ analog 568. Compound 568 was synthesized in bulk using a previously established protocol [22]. After 3 to 4 weeks of dosing, photographs of mice were taken using an iPhone SE camera, the mice were euthanized via CO_2 asphyxiation, and a blood sample was acquired via cardiac puncture. The liver, spleen, and ears were harvested and washed in cold phosphate buffered saline. For microscopy analysis, a portion of each tissue was excised, submerged in an optimal cutting temperature compound (Sakura Finetek USA, Torrance, CA) before freezing (-80°C). Cryosectioning was carried out using a Leica 3050S Cryostat (Leica Biosystems, Buffalo Grove, IL) with a section thickness of 5 μm.

Physicochemical Parameters of CFZ and Analog 568

LogP and LogD determination

To predict pKa values and draw structures of CFZ and 568, ChemAxon MarvinSketch Software (Version 5.12.0) was used. LogP and LogD at pH 7.4 were determined experimentally for CFZ and 568 based on the established protocols from Quigley et al. (1990) for CFZ with minor modifications [23]. Briefly, the partition behavior of CFZ and the 568 analog was determined by mixing phosphate buffer at pH 3 and 1-octanol (293245; Sigma-Aldrich) 1:1 (v/v) system at 25°C. The partitioning process was carried out in a thermostatically controlled water bath with a magnetic stir bar. The stirring time of 24 hours was considered to be sufficient to produce equilibration. Each compound was introduced in organic solvent at its maximum solubility, and the concentration of drug in organic and aqueous layers was spectrophotometrically determined (285 nm; Synergy-2 plate reader; Biotek Instruments, Winooski, VT). CFZ and 568 concentrations were calculated from a standard curve. After concentrations were calculated and the apparent partition coefficient was determined, LogP and

LogD at pH 7.4 were determined using equations previously described by Quigley et al. (1990) [23].

CFZ and analog 568 hydrochloride salt synthesis

To synthesize the hydrochloride salt crystals for CFZ and 568, 7 mM drug solution in DMSO (67-68-5, Fisher Scientific, Fair Lawn, NJ) was added to 1 M NH_4Cl in 1:1 (v/v) ratio and left for 24 to 48 hours at room temperature in the dark. After 24 to 48 hours, the solution with crystals was washed three times with diminishing concentrations of aqueous NH_4Cl (100 mM, 10 mM, 1 mM) to reduce the amount of chloride in the solution. In between washing steps, samples were centrifuged (2,000*g* for 10 minutes at 4°C). After the last wash, crystals were resuspended in MilliQ water and immediately snap frozen in liquid nitrogen and then freeze-dried.

Absorbance profiles of CFZ and analog 568

To compare absorbance profiles among CFZ free base, 568 free base, CFZ-HCl salt, and 568-HCl salt, samples were dissolved in DMSO at the same concentrations (70 μM) and determined spectrophotometrically (200-550 nm with 5 nm steps; Synergy-2 plate reader; Biotek Instruments) in a UV 96-well plate (8404; Thermo Scientific, Rockford, IL). Blank DMSO was used to obtain the baseline absorbance profile.

Assay for HCl salt precipitation

To understand precipitation behaviors and the ability of CFZ and analog 568 to form hydrochloride salts, an *in vitro* assay was developed to mimic lysosomal conditions. Two buffer solutions were made: 10 mM sodium acetate buffer (pH 4.5) with 10 mM CTAB (solution A) and 10 mM sodium acetate buffer (pH 4.5) with 10 mM CTAB and 100 mM NaCl (solution B). In a UV 96-well plate (8404; Thermo Scientific) 1 μL of 7 mM CFZ / 568 in DMSO was added

to 99 μL of each buffer solution, and the precipitation was observed and quantified. The quantification of hydrochloride salt formation was done spectrophotometrically (2.5 hours of shake cycle – varying speeds, 285 nm, Synergy-2 plate reader; Biotek Instruments). Buffer solution with DMSO was used for baseline absorbance, and brightfield images of the hydrochloride salt precipitation were obtained based on the protocol described in the "Multiparameter microscopic imaging" section.

Imaging and quantification of pigmentation using various optical filters

Based on the absorbance profiles of CFZ and 568, three available single-band bandpass optical filters were used: 480 nm (D480/30x; Chroma, Bellows Falls, VT), 535 nm (D535/40m; Chroma), and 623 nm (FF01-623/24-25; Semrock, Brightline, Rochester, NY). These filters were attached to an iPhone SE camera for image acquisition. The flash and high dynamic range options on the camera were disabled, and the camera editing filters were not applied. Quantification analysis of pigmentation was performed using ImageJ image processing software [24].

Quantification of CFZ in tissues

Harvested tissues were thawed, weighed, cut, and homogenized by sonication (liver and spleen) and mechanical homogenizer (ear) (Pro200; Pro Scientific, Oxford, CT) in radioimmunoprecipitation assay buffer (89900; Thermo Scientific) containing protease inhibitor cocktail (78410; Thermo Scientific). Homogenates were centrifuged (15,000 rpm at 4°C for 5 minutes), and the supernatants were collected. The lipophilic tissue fraction was extracted with xylenes (CAS 1330-20-7/100-41-4; Fisher Chemical, Fair Lawn, NJ) in triplicates, followed by the second extraction in triplicates with 9 M H_2SO_4 of diprotonated CFZ from the xylenes extract. Samples were centrifuged (2,000*g* at 4°C for 10 minutes) to facilitate layer separation

during extractions. After acid fractions were collected, the volumes were recorded, and CFZ concentrations were determined spectrophotometrically. The absorbance of the supernatants was measured at λ = 540 nm (A_{540}) and 750 nm (A_{750}) using a Synergy-2 plate reader (Biotek Instruments). Corrected absorbance (A_{540} - A_{750}) was used to determine CFZ content via a standard curve of standards in 9 M H_2SO_4, and the concentration values were corrected for organ weight [25, 26]. To correct for extraction yield, known amounts of CFZ were added to tissue samples (untreated liver, spleen, and ear tissues) before extractions; these samples were processed and analyzed concurrently with the test samples. For liver and spleen tissues, the extraction yield averaged 90%; for skin tissues, the extraction yield averaged 62%.

Multiparameter microscopic imaging

Multiparameter polarization, brightfield, and fluorescence microscopy was carried out using a Nikon Eclipse Ti inverted microscope (Nikon Instruments, Melville, NY). Polarization microscopy was performed using the LC-PolScope [27], with the illuminating light narrowed to 623 nm by an interference filter (623 ± 23 nm, FF01-623/24-25; Semrock, Brightline). Polarization images were captured using an Abrio imaging system (Cambridge Research & Instrumentation, Woburn, MA). Brightfield images were captured using the Nikon DS-3 camera (Nikon Instruments), and fluorescence imaging was performed with the Photometrics CoolSnap MYO camera system (Photometrics, Tuscon, AZ) under the control of Nikon NIS-Elements AR software (Nikon Instruments). Illumination for fluorescence imaging was provided by the X-Cite 120Q Widefield Fluorescence Microscope Excitation Light Source (Excelitas Technology, Waltham, MA). An in-depth discussion of this multiparameter microscopic imaging method was recently described [19].

Statistics

Statistical analysis was performed using SPSS Statistics Software (Version 24; Armonk, New York). Data are expressed as the mean ± SD. A one-way analysis of variance single factor followed by a Tukey's honest significant difference or Games-Howell post hoc tests were used to determine significant differences when applicable.

5.5 Results and Discussion

In our previous study, we synthesized a focused library of phenazine derivatives of CFZ and assayed their bioaccumulation and self-assembly properties in RAW264.7 macrophages and Madin-Darby canine kidney epithelial cells [22]. As a result, three derivatives yielded cellular staining patterns comparable in morphology and intensity to those of CFZ; one of them was CFZ analog 568 [22], which was chosen to be used as an experimental control for this study. A comparison of key physicochemical parameters between CFZ and this analog revealed minor differences in molecular weights, physiologically relevant pKa values, and partition coefficients (logP and logD at pH 7.4) (Table 5-1).

Based on spectrophotometric comparison, absorbance profiles of CFZ and the 568 analog were nearly identical for both free base and salt forms (Figure 5-2b). Both compounds exhibited strong absorbance in the UV region at 285 nm due to their phenazine backbones; free base forms showed maximum visible absorbance at 450 nm, whereas the salt forms shifted the visible absorbance peak to 495 nm, which is consistent with our previous study [22].

Next, an *in vitro* precipitation assay that mimics the *in vivo* conditions that lead to CLDI formation was developed to screen for CFZ derivatives that do not form CLDIs. The rationale behind the assay is that CLDIs form by the precipitation of CFZ in the acidic lysosomal microenvironment (pH 4.5) and the formation of a hydrochloride salt in the presence of

physiological sodium chloride concentrations. Thus, a pH of 4.5 and chloride concentration of 100 mM were chosen to mimic the lysosomal environment [28]. Furthermore, to recapitulate lipophilic drug partitioning within lysosome membranes, cetrimonium bromide (CTAB) was used as a biorelevant surfactant because it does not interfere with absorbance at 285 nm – the UV wavelength of detection for phenazine derivatives (Figure 5-2b). The optimal concentration of CTAB was determined based on the calculated molar solubilization ratio between CFZ and CTAB at pH 4.5 (data not shown) [29]. Finally, this novel assay was calibrated so the presence of chloride would act as the driving force for the formation of hydrochloride salt. For this, two conditions were employed: solution A (no chloride) and solution B (100 mM chloride). The precipitation was measured as the decrease in absorbance in 285 nm wavelength that correlated with the drug concentration in the solution resulting from precipitation.

By screening the CFZ derivatives using the aforementioned assay, we identified the 568 analog as the most closely related CFZ derivative that did not precipitate out in the lysosomal microenvironment. CFZ and 568 share similar chemical structures (Figure 5-2a), spectral properties (Figure 5-2b), physicochemical characteristics (Table 5-1), and both can be solubilized by detergent in the absence of chloride due to the fact that CFZ and 568 remained soluble in solution A (no chloride) to a similar extent as in dimethyl sulfoxide (DMSO) (Figure 5-2c). Nevertheless, the 568 analog remains in solution in the presence of physiological chloride concentrations (solution B: 100 mM chloride), whereas CFZ precipitates out as hydrochloride salt, which was indicated by a 4-fold decrease in absorbance (Figure 5-2c) and by employing microscopy techniques (Figure 5-2d). Brightfield and positive Cy5 fluorescence confirmed CFZ precipitates as an HCl salt form of the drug; no precipitates were observed for analog 568 (Figure 5-2d).

On the basis of the differences in the behavior of CFZ and the 568 analog in the *in vitro* lysosomal microenvironment precipitation assay, we designed experiments to test the behavior of these compounds *in vivo*. After 3-4 weeks of treatment with a drug powder feed diet containing either a dose equivalent of 10 mg/kg/d CFZ or analog 568, skin pigmentation was visually evident, which was consistent with observations from previous CFZ studies [13]. Skin pigmentation in animals was quantitatively determined using 480 nm, 535 nm, and 623 nm optical filters. The reflectance spectra of the skin were compared with that of pure free base and hydrochloride salt solids of CFZ and analog 568 (Figure 5-3a). Images of CFZ and analog 568 free base and HCl salt forms of the drug powders revealed visual similarities in color and the extent of reflectance at different optical filters (Figure 5-3a). Both forms of each drug appeared similarly dark in 480 nm and 535 nm filter images (Figure 5-3a), supported by high optical density (OD) values (OD values > 0.5) at those wavelengths (Figure 5-3c) – making 480 nm and 535 nm filters ideal for detecting drug-induced skin pigmentation regardless of the drug form. In contrast, 623 nm optical filter distinguished free base from hydrochloride forms of both compounds, with high OD values (OD values > 0.5) indicative of the hydrochloride salt forms and low OD values (OD values < 0.2) indicative of the free base forms (Figure 5-3c). In this manner, we found that 568 analog-treated mice achieved an identical level of pigmentation as CFZ-treated mice (no significant difference in OD values; Figure 5-3b and c), and both were significantly higher than the untreated group ($P < 0.01$, analysis of variance single factor, Tukey honest significant difference, $n = 3$). Interestingly, the use of the 623 nm optical filter was unable to detect the skin pigmentation in CFZ- and 568 analog-treated mice, consistent with the spectra of the free base form of the compounds.

To further elucidate the distribution behaviors of these compounds, the tissues of interest from CFZ- and 568 analog-treated mice were harvested and cryosectioned for multiparameter microscopic imaging [19] (Figure 5-4). As previously reported, CLDIs were observed in the liver and spleen of CFZ-treated mice based on brightfield images and positive fluorescence and diattenuation signals [19]; however, CFZ skin sections did not contain CLDIs (Figure 5-4). A few dark spots present in both untreated animals and in drug-treated animals were attributed to melanosomes, which give mice skin its natural pigmentation [30, 31]. In contrast to CFZ, all tissues from 568 analog-treated animals had no evidence of CLDI accumulation due to the lack of fluorescence and dichroism signal in the liver and spleen, which are the main bioaccumulating organs (Figure 5-4). Because treatment with the 568 analog resulted in significant skin pigmentation, to the same extent as in CFZ treatment, we concluded that the skin pigmentation caused by both CFZ and 568 analog is not associated with CLDI bioaccumulation.

Lastly, the extent of drug bioaccumulation in the liver, spleen, and skin of CFZ-treated mice was compared. Tissue concentrations of the drug in the liver, spleen, and skin were determined to be 2.37 ± 0.62 mg/g, 4.34 ± 0.41 mg/g, and 0.16 ± 0.04 mg/g, respectively. The skin showed significantly lower concentrations compared with the liver and spleen ($P < 0.001$, analysis of variance single factor, Tukey honest significant difference, $n = 3$ [skin], $n = 4$ [liver and spleen]). Interestingly, because the skin is the biggest organ, representing 9.8% of total bodyweight [32], it accommodated a similar total CFZ mass as the spleen but at a 20-fold lower concentration. This much lower concentration of CFZ in the skin suggests that skin pigmentation is not associated with extensive bioaccumulation of the hydrochloride salt of CFZ and its precipitation into CLDIs, as is observed in the liver and spleen. Instead, the lower concentration of CFZ in skin is attributed to the soluble free base form of the drug that is expected to partition

into the subcutaneous fat [13]. In fact, the amount of clofazimine in skin (0.16 mgCFZ/gTissue) is consistent with an approximately 20% lipid content in skin, assuming that CFZ partitions into skin lipids similar to the measured concentration that is found in adipose tissue (0.74 mgCFZ/gFat) [13].

Overall, in case of oral or systemic administration of CFZ, our results suggest that skin hyperpigmentation should be expected because after absorption, the drug will naturally accumulate in the skin by partitioning from the systemic circulation. Therefore, the most viable alternative approach to reduce CFZ-induced skin hyperpigmentation would be to minimize the concentrations of drug in the circulation. This can be achieved through local administration and controlled release formulations. In this regard, an inhalable CFZ formulation has already been shown to be efficacious against *M. tuberculosis* in human monocyte-derived macrophage cultures and in a relevant animal model [33]. On the basis of our own findings, we are currently working toward reformulating CFZ, both as a locally injectable suspension of micronized, biomimetic crystals of CFZ hydrochloride and as an inhalable dry micronized powder. By advancing solid, micro- or nanoparticles of CFZ that mimic the solid form of the drug that naturally bioaccumulates in CLDIs on prolonged oral dosing [13, 14, 20], it may be possible to achieve prolonged, therapeutic drug concentrations at the site of action while avoiding CFZ-induced skin pigmentation that would result from high drug concentrations circulating throughout the body. Indeed, although the clinically used, oral formulation of CFZ is specifically indicated to treat leprosy, which primarily affects the skin, more targeted formulations and local delivery routes could be useful to repurpose the drug for other indications.

5.6 Acknowledgments and Funding

The study was supported by funding from the University of Michigan (MCubed; http://mcubed.umich.edu/) and a grant from the National Institute of General Medical Sciences (NIGMS) of the National Institutes of Health (R01 GM078200 to GRR). KAS effort was supported in part by R01 GM111400. The content is solely the responsibility of the authors and does not necessarily present the official views of the NIGMS or the National Institutes of Health.

5.7 Figures and Tables

Figure 5-1. Extent of skin pigmentation in CFZ-treated mice compared to untreated mice (control). CFZ, clofazimine.

Table 5-1. Physicochemical parameters of CFZ and 568.

	CFZ	**568**
M.W.	473.4 g/mol	475.4 g/mol
pKa	$pKa_1 = 9.29$[1] $pKa_2 = 2.31$[1]	$pKa_1 = 8.65$[1] $pKa_2 = 2.31$[1]
LogP	7.66[2]	6.69[2]
LogD @ pH 7.4	5.76[3]	5.42[3]

[1]Values were predicted by ChemAxon MarvinSketch Software (Version 5.12.0)

[2]CFZ mean ± 0.00 (n=3); 568 mean ± 0.04 (n=3)

[3]CFZ mean ± 0.00 (n=3); 568 mean ± 0.04 (n=3)

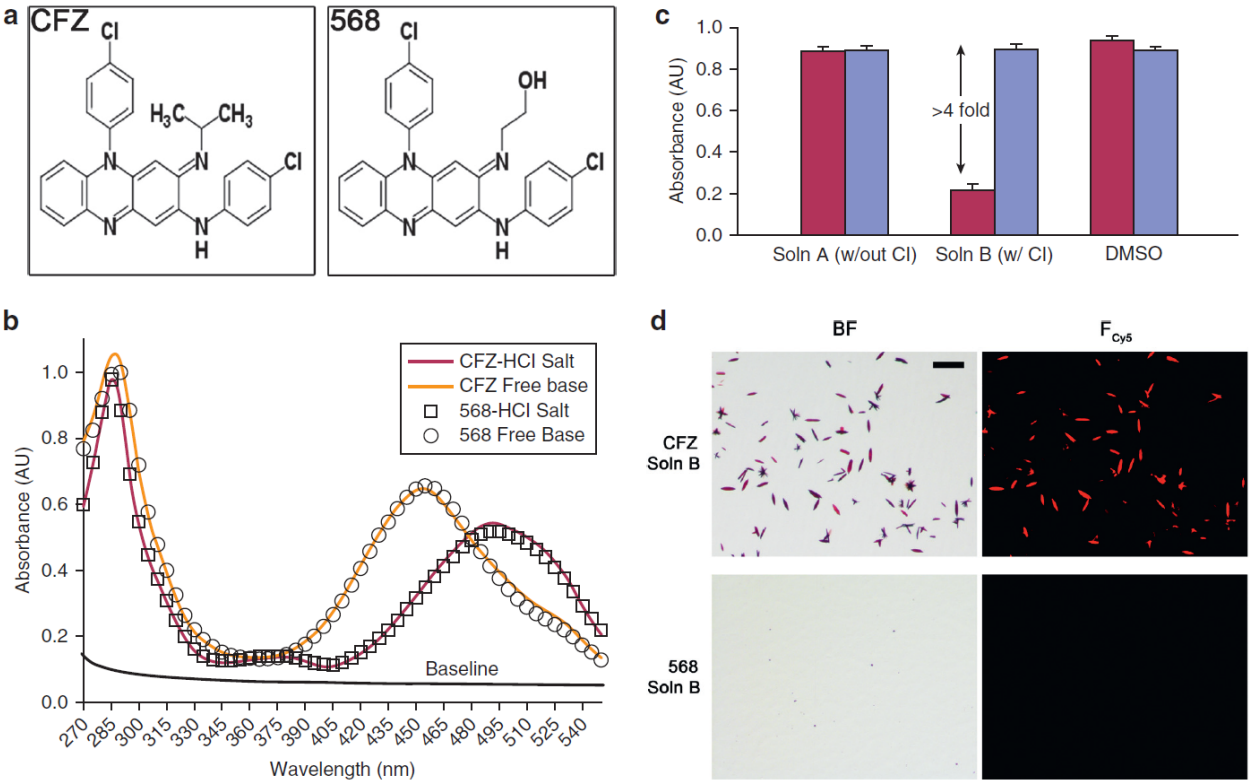

Figure 5-2. Comparison of CFZ and CFZ analog 568: structures, precipitation assay, and absorbance profiles. (a) The structural difference between CFZ and analog 568 at the tertiary amine is a specific substitution of the isopropyl group with a 2-hydroxyethyl. (b) The absorbance profiles (270 - 550 nm) show the similarity of CFZ and analog 568 free base and hydrochloride salt forms, respectively. (c) The ability of both CFZ and analog 568 to precipitate as hydrochloride salt in simulated lysosomal conditions (pH 4.5). This was determined by measuring the absorbance (285 nm) in different conditions: Soln A (no chloride), Soln B (100 mM chloride), and DMSO (red = CFZ, blue = 568). (d) Hydrochloride salt precipitation in the presence of chloride (Soln B) was verified by brightfield (BF) and fluorescence microscopy (F_{cy5}). Scale bar = 50 µm. CFZ, clofazimine; DMSO, dimethyl sulfoxide.

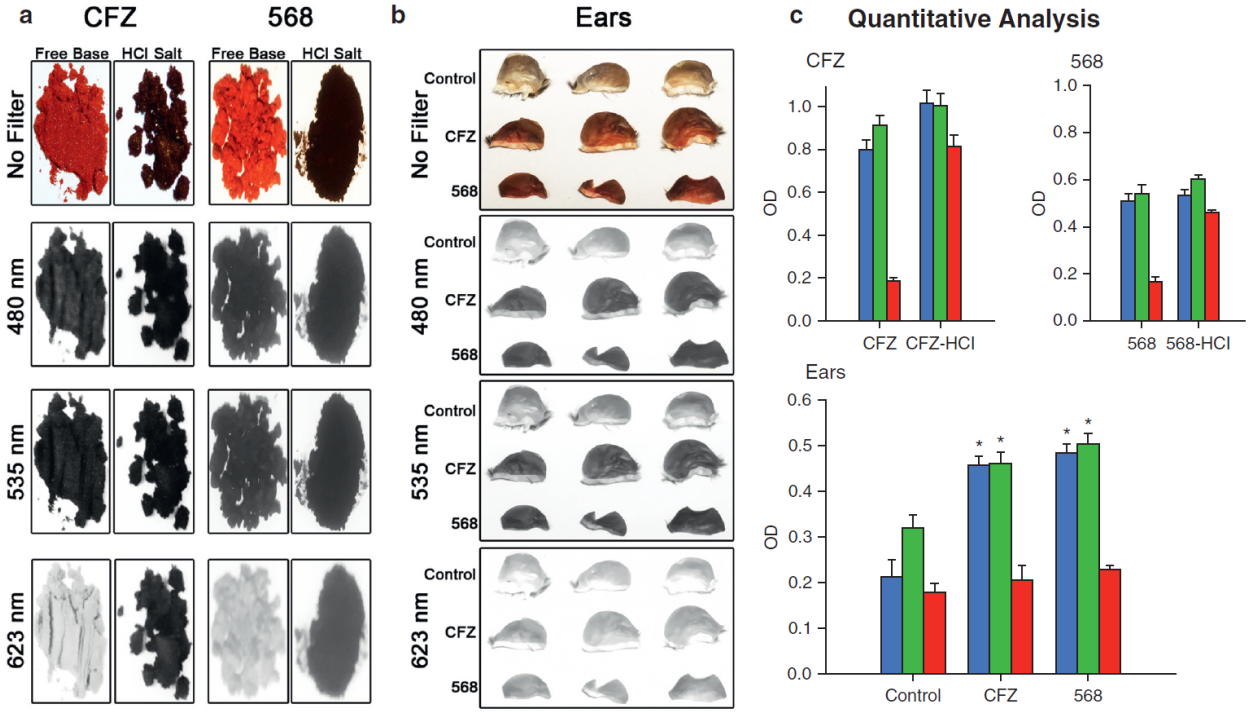

Figure 5-3. Optical properties of CFZ and CFZ analog 568 and quantitative analysis of skin pigmentation using various optical filters. (a) Images of CFZ and analog 568 free base and HCl salt powders and the extent of their reflectance using 480 nm, 535 nm, and 623 nm optical filters. (b) Images of mouse ears after 3-4 weeks of CFZ or analog 568 treatment and the extent of their reflectance using 480 nm, 535 nm, and 623 nm optical filters. (c) Quantitative analysis of the drug powder images (n = 7) and images of mouse ears after 3-4 weeks of CFZ or 568 treatment compared with untreated mice (n = 3) (blue = 480 nm filter; green = 535 nm filter; red = 623 nm filter; *P < 0.01, analysis of variance single factor, Tukey's HSD). CFZ, clofazimine; HSD, honest significant difference.

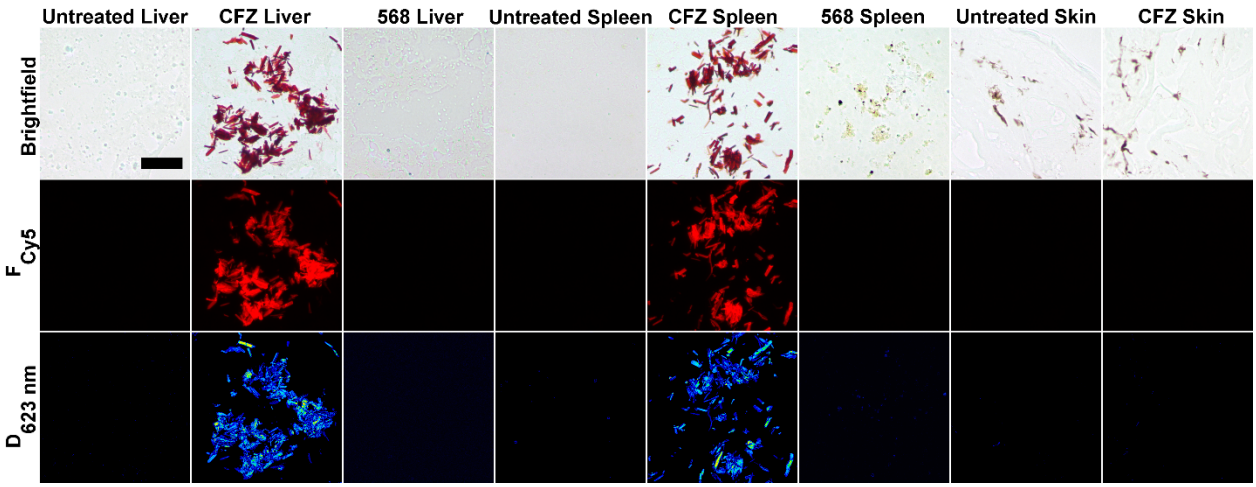

Figure 5-4. Multiparameter imaging of CFZ and CFZ analog 568 treated and untreated tissues. Images of liver, spleen, and skin sections were taken using brightfield, Cy5 fluorescence (F_{cy5}), and dichroism at 623 nm (D_{623nm}) to identify and compare for CFZ-HCl/CLDI signatures with corresponding untreated samples. Scale bar = 25 µm. CFZ, clofazimine; CLDI, crystal-like drug inclusion.

5.8 References

1. Dereure, O., *Drug-induced skin pigmentation. Epidemiology, diagnosis and treatment.* Am J Clin Dermatol, 2001. **2**(4): p. 253-62.

2. Gallo, C.B., et al., *Drug-induced pigmentation of hard palate and skin due to chronic chloroquine therapy: report of two cases.* Clin Exp Dermatol, 2009. **34**(7): p. e266-7.

3. Maia, M.V., G. Cunha Mda, and C.S. Cunha, *Adverse effects of alternative therapy (minocycline, ofloxacin, and clofazimine) in multibacillary leprosy patients in a recognized health care unit in Manaus, Amazonas, Brazil.* An Bras Dermatol, 2013. **88**(2): p. 205-10.

4. Manallack, D.T., *The pK(a) Distribution of Drugs: Application to Drug Discovery.* Perspect Medicin Chem, 2008. **1**: p. 25-38.

5. Tang, S., et al., *Clofazimine for the treatment of multidrug-resistant tuberculosis: prospective, multicenter, randomized controlled study in China.* Clin Infect Dis, 2015. **60**(9): p. 1361-7.

6. Arbiser, J.L. and S.L. Moschella, *Clofazimine: a review of its medical uses and mechanisms of action.* J Am Acad Dermatol, 1995. **32**(2 Pt 1): p. 241-7.

7. World Health Organization. *Leprosy Report*. 2014 [cited 2016 Aug 16]; Available from: http://www.who.int/mediacentre/factsheets/fs101/en.

8. Dooley, K.E., et al., *World Health Organization group 5 drugs for the treatment of drug-resistant tuberculosis: unclear efficacy or untapped potential?* J Infect Dis, 2013. **207**(9): p. 1352-8.

9. Gopal, M., et al., *Systematic review of clofazimine for the treatment of drug-resistant tuberculosis.* Int J Tuberc Lung Dis, 2013. **17**(8): p. 1001-7.

10. Hastings, R.C., et al., *Leprosy.* Clin Microbiol Rev, 1988. **1**(3): p. 330-48.

11. Jamet, P., et al., *Short-term trial of clofazimine in previously untreated lepromatous leprosy.* Int J Lepr Other Mycobact Dis, 1992. **60**(4): p. 542-8.

12. Singh, H., et al., *Adverse effects of multi-drug therapy in leprosy, a two years' experience (2006-2008) in tertiary health care centre in the tribal region of Chhattisgarh State (Bastar, Jagdalpur).* Lepr Rev, 2011. **82**(1): p. 17-24.

13. Baik, J., et al., *Multiscale distribution and bioaccumulation analysis of clofazimine reveals a massive immune system-mediated xenobiotic sequestration response.* Antimicrob Agents Chemother, 2013. **57**(3): p. 1218-30.

14. Baik, J. and G.R. Rosania, *Macrophages sequester clofazimine in an intracellular liquid crystal-like supramolecular organization.* PLoS One, 2012. **7**(10): p. e47494.

15. Baik, J. and G.R. Rosania, *Molecular imaging of intracellular drug-membrane aggregate formation.* Mol Pharm, 2011. **8**(5): p. 1742-9.

16. Belaube, P., et al., *Small bowel deposition of crystals associated with the use of clofazimine (Lamprene) in the treatment of prurigo nodularis.* Int J Lepr Other Mycobact Dis, 1983. **51**(3): p. 328-30.

17. Sukpanichnant, S., et al., *Clofazimine-induced crystal-storing histiocytosis producing chronic abdominal pain in a leprosy patient.* Am J Surg Pathol, 2000. **24**(1): p. 129-35.

18. Keswani, R.K., et al., *A far-red fluorescent probe for flow cytometry and image-based functional studies of xenobiotic sequestering macrophages.* Cytometry A, 2015. **87**(9): p. 855-67.

19. Rzeczycki, P., et al., *Detecting ordered small molecule drug aggregates in live macrophages: a multi-parameter microscope image data acquisition and analysis strategy.* Biomed Opt Express, 2017. **8**(2): p. 860-872.

20. Keswani, R.K., et al., *Chemical Analysis of Drug Biocrystals: A Role for Counterion Transport Pathways in Intracellular Drug Disposition.* Mol Pharm, 2015. **12**(7): p. 2528-36.

21. Yoon, G.S., et al., *Clofazimine Biocrystal Accumulation in Macrophages Upregulates Interleukin 1 Receptor Antagonist Production To Induce a Systemic Anti-Inflammatory State.* Antimicrob Agents Chemother, 2016. **60**(6): p. 3470-9.

22. Min, K.A., et al., *Massive Bioaccumulation and Self-Assembly of Phenazine Compounds in Live Cells.* Adv Sci (Weinh), 2015. **2**(8).

23. Quigley, J.M., et al., *Temperature-Dependence and Thermodynamics of Partitioning of Clofazimine Analogs in the Normal-Octanol Water-System.* International Journal of Pharmaceutics, 1990. **58**(2): p. 107-113.

24. Schneider, C.A., W.S. Rasband, and K.W. Eliceiri, *NIH Image to ImageJ: 25 years of image analysis.* Nat Methods, 2012. **9**(7): p. 671-5.

25. Trexel, J., et al., *Macrophage-Mediated Clofazimine Sequestration Is Accompanied by a Shift in Host Energy Metabolism.* J Pharm Sci, 2017. **106**(4): p. 1162-1174.

26. Yoon, G.S., et al., *Phagocytosed Clofazimine Biocrystals Can Modulate Innate Immune Signaling by Inhibiting TNFalpha and Boosting IL-1RA Secretion.* Mol Pharm, 2015. **12**(7): p. 2517-27.

27. Mehta, S.B., M. Shribak, and R. Oldenbourg, *Polarized light imaging of birefringence and diattenuation at high resolution and high sensitivity.* J Opt, 2013. **15**(9).

28. Stauber, T. and T.J. Jentsch, *Chloride in vesicular trafficking and function.* Annu Rev Physiol, 2013. **75**: p. 453-77.

29. Chakraborty, S., et al., *Assessment of solubilization characteristics of different surfactants for carvedilol phosphate as a function of pH.* J Colloid Interface Sci, 2009. **335**(2): p. 242-9.

30. Boissy, R.E., *The melanocyte. Its structure, function, and subpopulations in skin, eyes, and hair.* Dermatol Clin, 1988. **6**(2): p. 161-73.

31. Wu, X., et al., *Myosin V associates with melanosomes in mouse melanocytes: evidence that myosin V is an organelle motor.* J Cell Sci, 1997. **110 (Pt 7)**: p. 847-59.

32. Arms, A.D., et al., *Reference Physiological Parameters in Pharmacokinetic Modeling*. 1988: U.S. Environmental Protection Agency, Office of Health and Environmental Assessment.

33. Verma, R.K., et al., *Inhaled microparticles containing clofazimine are efficacious in treatment of experimental tuberculosis in mice.* Antimicrob Agents Chemother, 2013. **57**(2): p. 1050-2.

Chapter 6

Synthesis and Characterization of a Biomimetic Formulation of Clofazimine Hydrochloride Microcrystals for Parenteral Administration

6.1 Relevance to Thesis

This chapter was adapted from the following publication:

***Murashov MD**, Diaz-Espinosa J, LaLone V, Tan JWY, Wang X, Stringer KA, Rosania GR. **2018**. Synthesis and characterization of a biomimetic formulation of clofazimine hydrochloride microcrystals for parenteral administration. **Pharmaceutics** 10(4), 238; doi: 10.3390/pharmaceutics10040238*

This chapter investigated and concluded the Specific Aim 2 of this thesis. As a result, I developed a biomimetic formulation of CLDIs, micronized CFZ-HCl salt crystals for parenteral administration, and determined that RAW 264.7 macrophages internalized and stabilized CFZ-HCl microcrystals, just as well as isolated CLDIs, without any cytotoxicity *in vitro*.

Furthermore, these results led me to conclude that these drug microcrystals would also be prone to phagocytosis and stabilization by resident tissue macrophages in mouse model *in vivo*. As a result, all mice that were injected with the CFZ-HCl microcrystal formulation survived the injection (100% survival) and did not show any signs of toxicity. Importantly, injected CFZ-HCl microcrystals displayed the same distribution patterns as CLDIs (from orally administered CFZ treatment) and did not result in detectable skin pigmentation.

These findings further validated the central hypothesis and suggested that parenteral (injected or inhaled) biomimetic formulations of CFZ-HCl could be instrumental to avoid the pigmentation side effect of oral CFZ therapy.

6.2 Abstract

Clofazimine (CFZ) is a broad spectrum antimycobacterial agent recommended by the World Health Organization as a first line treatment for leprosy and second line treatment for multidrug resistant tuberculosis. Oral administration of CFZ leads to a red skin pigmentation side effect. Since CFZ is a weakly basic, red phenazine dye, the skin pigmentation side effect results from lipophilic partitioning of the circulating, free base (neutral) form of CFZ into the skin. Here, we developed a stable and biocompatible formulation of CFZ-HCl microcrystals that mimics the predominant form of the drug that bioaccumulates in macrophages, following long term oral CFZ administration. In mice, intravenous injection of these biomimetic CFZ-HCl microcrystals led to visible drug accumulation in macrophages of the reticuloendothelial system with minimal skin accumulation or pigmentation. In fact, no skin pigmentation was observed when the total amount of CFZ-HCl administered was equivalent to the total oral dose leading to maximal skin pigmentation. Thus, parenteral (injected or inhaled) biomimetic formulations of CFZ-HCl could be instrumental to avoid the pigmentation side effect of oral CFZ therapy.

6.3 Introduction

Clofazimine (CFZ) is a weakly basic, red-pigmented, FDA-approved, phenazine antibiotic that is included in the World Health Organization's (WHO) List of Essential Medications as part of the antibiotic cocktail used for the standard treatment for leprosy [1–5]. It has been in clinical use since the 1960s and has contributed to the cure of more than 16 million people worldwide [1–5]. Due to its potent activity against *Mycobacterium tuberculosis*, the WHO now recommends CFZ as a second line agent against multi-drug resistant tuberculosis

(MDR-TB) [3,6–10]. In humans, CFZ exhibits atypical pharmacokinetic properties [11,12]. In mice, following long-term (i.e., weeks) oral administration, solid drug precipitates accumulate in tissue macrophages, forming red crystal-like drug inclusions (CLDIs) that are most abundant in the liver and spleen [13–15]. This phenomenon has also been reported in humans treated with CFZ [11,12]. Interestingly, these biocrystals display robust stability inside macrophages and remain in the body long after discontinuation of treatment (>8 weeks) [13]. The preliminary analysis of isolated CLDIs from spleen and liver of CFZ treated mice revealed that CLDIs contained a hydrochloride salt form of the drug, which is stabilized by the acidic and high chloride concentrations present in macrophage lysosomes, while the orally-administered form of the drug is the free base [16].

In terms of its toxicological properties, the major side effect of orally administered CFZ is a strong red skin pigmentation, observed in more than 94% of patients [17,18]. CFZ-induced skin pigmentation is attributed to the circulating, soluble free base form of CFZ that partitions into the subcutaneous fat layer of the skin rather than CLDI formation and accumulation [19]. Even though prolonged CFZ treatment is associated with massive drug biocrystal accumulation within resident tissue macrophages, there are no obvious toxicological manifestations from these biocrystals. Instead, CLDIs are biocompatible, stable, long-lived, and relatively non-toxic [3,20]. Phagocytosed CLDIs modulate innate immune signaling by dampening pro-inflammatory and enhancing anti-inflammatory pathways via inhibition of tumor necrosis factor alpha (TNFα) and enhancement of interleukin 1 receptor antagonist (IL-1RA) secretion [3,20]. Specifically, CFZ inhibited carrageenan- and lipopolysaccharide-induced inflammation in the footpads and lungs, respectively, in 8-week-CFZ-treated mice, in an IL-1RA-dependent manner [3].

Since the skin pigmentation side effect is likely due to the free base form of the drug that partitions from the blood to the skin following oral administration, we decided to test whether parenteral administration of CFZ-HCl microcrystals could be used to avoid the drug's skin pigmentation side effect. We hypothesized that the injected, micronized CFZ-HCl particles would be ingested by macrophages and stabilized by the phagolysosomal microenvironment. In order to test this hypothesis, we developed and tested CFZ-HCl particles side-by-side with CLDIs and other solid forms of CFZ, in terms of their physicochemical characteristics. Furthermore, biological experiments were conducted to test the performance of biomimetic CFZ-HCl formulations following phagocytosis by macrophages *in vitro,* and *in vivo* after administering the drug via intravenous (IV) tail-vein bolus injection. The results indicate that a biomimetic formulation of CFZ-HCl can be effectively synthesized and delivered parenterally to circumvent the CFZ-induced skin pigmentation side effect.

6.4 Materials and Methods

Synthesis of different Clofazimine (CFZ) solids

Different CFZ salt crystals were synthesized by adding 1 M of ammonium salts in MiliQ water to 2 mM CFZ (C8895, Sigma-Aldrich, St. Louis, MO, USA) in methanol in a 1:1 ratio (*v*/*v*). Ammonium bromide, carbonate, citrate dibasic, nitrate, phosphate dibasic, and sulfate were all purchased from Sigma-Aldrich (213349; 207861; 25102; 221244; 215996; A4418 (respectively); Sigma-Aldrich, St. Louis, MO, USA). Ammonium acetate and chloride were purchased from Fisher Scientific (A639; A661 (respectively); Fisher Scientific, Fair Lawn, NJ, USA). Ammonium iodide was purchased from Acros Organics (448071000, Acros Organics, Morris Plains, NJ, USA).

Isolation of Crystal-Like Drug Inclusions (CLDIs)

CLDI purification and isolation were performed as previously described with minor modifications [13,14,21]. In brief, liver and spleen from mice that were fed CFZ for 8 weeks from previous experiments were homogenized by cutting the organs into smaller pieces and utilizing mechanical homogenizer (Pro200; Pro Scientific, Oxford, CT, USA). Liver and spleen homogenates were filtered through a 100 μm strainer, and the filtrate was collected in a 50 mL centrifuge tube and diluted up to 50 mL with 1× Phosphate Buffered Saline (PBS) (10010023, Gibco, Life Technologies, Carlsbad, CA, USA). The filtrate was then centrifuged at 250× *g* for 6 min. The supernatant was discarded, and fresh PBS was added up to 50 mL. This step was repeated twice, and after the final washing step, the red-CLDI containing pellet was resuspended in 2–5 mL of 10% sucrose. From the pellet, CLDIs were further purified using a three-layer discontinuous gradient (50%, 30%, and 10% sucrose in PBS) centrifugation method (3200× *g*, 60 min). After centrifugation, the top layers were discarded, and the CLDIs pellet was resuspended in PBS and snap frozen in liquid nitrogen in preparation for future analysis.

Bulk Synthesis of CFZ-HCl Salt Crystals

CFZ free base (10 g; Sigma-Aldrich, St. Louis, MO, USA) was placed in 2 L of 1 M HCl in an Erlenmeyer flask with a magnetic stir bar. After the addition of CFZ, the reaction was sealed with parafilm and stirred in the dark for 72 h. After 72 h, the stirring was turned off and CFZ salt crystals were allowed to precipitate. Following crystal precipitation, the HCl reactant was decanted and discarded. The residual acid containing the CFZ salt crystals was centrifuged (2000× *g*, 10 min, 4 °C), the supernatant was discarded, and the pellet was washed thrice with declining concentrations of HCl (100 mM, 10 mM, and 1 mM) to reduce the amount of chloride present in the solution. In between washing steps, samples were centrifuged (2000× *g*, 10 min, 4

°C). After the last wash, crystals were resuspended in MiliQ water and immediately snap frozen in liquid nitrogen and then freeze-dried.

Micronization (Jet Milling) and Sterilization

A SepSol, Sturtevant Inc. (Separation Solutions; SepSol Process Solutions, Kalamazoo, MI, USA) air jet mill was used to micronize the bulk synthesized CFZ-HCl crystals and CFZ free base crystals (control) to a particle size distribution within the desired range (0.5–5 μm). Following the company's specifications, the air jet mill was set at 50 psi grind pressure and 100 psi feed pressure. Filtered, dried, compressed air was used as the air source for the mill. Altogether, four batches of CFZ-HCl microcrystals (net weight ~40 g) and three batches of CFZ free base microcrystals (net weight ~20 g) were produced with ~80–90% yield from milling. Both types of micronized CFZ crystals were stored at −20 °C until the time of experimentation. Before each experiment, CFZ microcrystals were sterilized by dry heat at 170 °C for 1.5 h, using a bench top vacuum oven at 5 psi (Model 5831; National Appliance Co., Portland, OR, USA).

Particle Size Determination

The CFZ microcrystals particle size after synthesis and after micronization were analyzed using Zeta-Sizer (Malvern Instruments, Nano-ZS90, Malvern, UK) and brightfield microscopy using Nikon Eclipse Ti inverted microscope (Nikon Instruments, Melville, NY, USA).

Proton Nuclear Magnetic Resonance Spectroscopy Analysis

Proton (^{1}H) nuclear magnetic resonance (NMR) spectroscopy was performed as previously described [16]. Briefly, one-dimensional ^{1}H-NMR spectra of micronized CFZ-HCl crystals at different stages of manufacturing were acquired using an 11.74 T (500 MHz) NMR spectrometer with a VNMRS console and a 7510-AS autosampler system operated by host software VNMRJ 3.2 and equipped with a 5 mm Agilent One NMR probe with Z-axis gradients. The samples were dissolved in dimethyl sulfoxide-D6 (D, 99.9%) (DMSO-d_6; Cambridge

Isotope Laboratories, Inc., Andover, MA, USA). The NMR data were acquired at room temperature and processed using MestreNova 9.0 software (MestreLab, Santiago de Compostela, Spain).

Powder X-Ray diffraction Analysis

Powder X-ray diffraction (pXRD) spectra of micronized CFZ-HCl crystals at different stages of manufacturing were taken by Rigaku Miniflex X-ray diffractometer (Rigaku-USA Inc., Danvers, MA, USA) using Cu−Kα radiation, a tube voltage of 30 kV, and a tube current of 15 mA. Measurements were taken from 5° to 40° at a continuous scan rate of 2.5°/min.

Raman Microscopy

Raman spectra were acquired with a WiTec alpha300R confocal Raman microscope (WiTec, Ulm, Germany) equipped with a 532 nm solid-state sapphire excitation laser and charge coupled device (CCD) detector. For single point spectra, the laser was focused on the sample acquiring each Raman spectrum with an integration time of 75 s, using Zeiss EC EPIPLAN 50X objective (N.A. = 0.75). Alternatively, for large area scans, the laser rastered across a 100 μm by 100 μm area of the sample with a step size of 10 μm and an integration time of 2 s per pixel, using Zeiss 10 X objective. To measure quality and stability of individual CFZ microcrystals, single point spectra were taken from individual particles for micronized CFZ-HCl, micronized CFZ-HCl in diluent, and micronized CFZ free base that were dispersed on mica chips. Cosmic rays were removed from all spectra using the WiTec Project FOUR software. A MATLAB® processing algorithm developed in-house [22] was used to baseline-subtract, normalize, and overlay spectra to qualitatively identify the collected micronized sample spectra by comparing them to both CFZ-HCl and CFZ free base reference spectra.

Brightfield and Fluorescence Microscopy

Microscopy was performed using a Nikon Eclipse Ti inverted microscope (Nikon Instruments, Melville, NY, USA) as previously described [19,23]. Briefly, brightfield images were captured using the Nikon DS-3 camera (Nikon Instruments, Melville, NY, USA), and fluorescence imaging in FITC channel (490/510 nm, green) and Cy5 channel (640/670 nm, far-red) was performed with the Photometrics CoolSnap MYO camera system (Photometrics, Tuscon, AZ, USA) under the control of Nikon NIS-Elements AR software (Nikon Instruments, Melville, NY, USA). Illumination for fluorescence imaging was provided by the X-Cite 120Q Widefield Fluorescence Microscope Excitation Light Source (Excelitas Technology, Waltham, MA, USA).

Assaying Stability of CFZ-HCl in Aqueous Buffers

The stability of CFZ-HCl microcrystals was evaluated in IV diluent, synthetic lysosomal buffer [19], and PBS. A small amount of CFZ-HCl crystals (<1 mg) was placed in a large volume of test media (~20 mL) and gently stirred for 24 h to make sure that the equilibrium between the microcrystals and the test medium was reached. After 24 h, the small drop of test media with microcrystals was placed on the glass microscope slide, and the stability of CFZ-HCl microscrystals was evaluated using brightfield and fluorescence microscopy (see *"Brightfield and Fluorescence Microscopy"* section).

The diluent for the IV injectable formulation was made using polysorbate 80 (59924 Sigma-Aldrich, St. Louis, MO, USA), sodium chloride (BP358, Fisher Scientific, Fair Lawn, NJ, USA), and Milli-Q water. To coat, disperse, and adjust the size of the lipophilic CFZ-HCl microcrystals, the varying concentrations of polysorbate 80 (0–0.5%) was used [24]. Sodium chloride was added to maintain isotonicity. The pH was adjusted to pH 5 using 0.01 M HCl or

0.01 M NaOH to ensure the stability of CFZ-HCl microcrystals in the formulation. For experiments, the diluent was sterilized by sterile filtration with a syringe filter (09-719A; 0.22 μm, MCE, Sterile; Fisher Scientific, Fair Lawn, NJ, USA).

The synthetic lysosomal buffer was prepared as previously reported [19]. In brief, synthetic lysosomal buffer was made by preparing 10 mM sodium acetate buffer (pH 4.5) with 10 mM cetrimonium bromide (CTAB) and 100 mM NaCl to mimic lysosomal conditions [19].

Cell-based stability assays

The stability of CFZ-HCl microcrystals was evaluated following phagocytosis, using the RAW 264.7 murine macrophage cell line. The cell line was purchased from ATCC (Manassas, VA, USA) and maintained in Dulbecco's modified Eagle medium (DMEM) (11995-065, Gibco, Life Technologies, Carlsbad, CA, USA) supplemented with 10% fetal bovine serum (FBS) (16000-044, Gibco, Life Technologies, Carlsbad, CA, USA) and 0.1% penicillin/streptomycin (15140-122, Gibco, Life Technologies, Carlsbad, CA, USA). Cells were maintained at 5% CO_2 at 37 °C and passaged at 80% confluency. For the assay, the cells were seeded at 5×10^4 cells/well in 6-well plates and were allowed to grow for 24 h, at which point, isolated CLDIs, CFZ-HCl microcrystals, and CFZ free base microcrystals were added at 20 μg/mL in DMEM with 5% FBS to designated drug treatment plates. The same volume of DMEM with 5% FBS without drug treatment was added to wells of negative control plates. The cells were treated for 1 h, at which point, the media was removed, and the cells were thoroughly washed twice. DMEM with 10% FBS and 0.1% penicillin/streptomycin was then added back into the wells (t_0). Over the next 48 h (t_{8h}, t_{24h}, t_{48h}), total cell viability was assessed using trypan blue (0.4%) exclusion (15250-061, Gibco, Life Technologies, Carlsbad, CA, USA). At every time point, brightfield and

fluorescence images were taken, and the viability measurements were calculated in triplicate (# cells >100 per measurement).

Animal studies

Animal care was provided by the University of Michigan's Unit for Laboratory Animal Medicine (ULAM), and the experimental protocol was submitted to and approved by the University of Michigan's Institutional Committee on Use and Care of Animals (PRO00007593; 5 May 2017).

In order to assess of the skin pigmentation induced by micronized CFZ-HCl crystals following injection into the systemic circulation, 14 male mice (10–19 weeks old, C57BL6, Jackson Laboratory, Bar Harbor, ME, USA) were assigned to one of 3 groups: CFZ orally fed (OF) group (n = 5), CFZ-HCl IV injected group (n = 5), and the control group (n = 4). The CFZ orally fed group and control group mice were fed CFZ or vehicle chow for 9 weeks, respectively, as previously reported [13,14,20]. The CFZ-HCl IV injected group received a single IV bolus tail-vein injection with the formulation of CFZ-HCl microcrystals (200 mg/kg), using a 300 uL injection volume, which translates to an approximate total dose of 6 mg of drug microcrystals or 3 weeks of orally administered CFZ (assuming 100% bioavailability). Animals were sacrificed 24 h post injection. At the time of sacrifice, mice were euthanized with CO_2 inhalation and exsanguination.

Toxicological evaluation

The mice were monitored for behavioral changes and survival (e.g., lethargy, scruffy fur, squinted eyes, etc.) 24 h post-injection to evaluate the toxicity of the CFZ-HCl injections. In addition, plasma samples from the *in vivo* experiments were assayed for IL-1RA, IL-1β, and TNFα by enzyme linked immunosorbent assay (ELISA; Quantikine; R&D Systems,

Minneapolis, MN, USA) in duplicate according to the manufacturer's instructions. The cytokine concentrations were expressed as picograms per milliliter of plasma.

Immunohistochemistry

Immunohistochemistry was performed using a previously published protocol with some modifications [25]. In brief, following euthanasia, the liver and spleen were removed en bloc and embedded in Tissue-Plus Optimal Cutting Temperature (OCT) compound (4585, Fisher HealthCare, Houston, TX, USA). Frozen tissue blocks were sectioned (6 μm thick) using Leica 3050S cryostat, fixed in 4% paraformaldehyde (15710, Electron Microscopy Sciences, Hatfield, PA, USA) for 10 min, and blocked with 1% bovine serum albumin (BSA) (810033, MP Biomedicals, Solon, OH, USA), 5% goat serum (Sigma-Aldrich, St. Louis, MO, USA), and 0.3 M glycine (G8898, Sigma-Aldrich, St. Louis, MO, USA) in PBS for 2 h. The samples were then incubated with primary antibodies, anti-CD68 antibody (ab53444; 1 mg/mL stock; 1:200 dilution in 1% BSA; Abcam, Cambridge, UK) or purified rat IgG2a κ isotype control antibody (400502; 0.5 mg/mL stock; 1:100 dilution in 1% BSA; Biolegend, San Diego, CA, USA), overnight at 4 °C, followed by incubation with anti-rat IgG (H + L) Alexa Fluor® 488 conjugate secondary antibody (4416; 5 mg/mL stock; 1:500 dilution in 1% BSA; Cell Signaling Technology, Danvers, MA, USA) for 1 h at room temperature. Finally, the samples were incubated with Hoechst 33,342 solution (H3570; 1 μM stock; 1:10,000 dilution in PBS; Life Technologies, Carlsbad, CA, USA) for 10 min at room temperature for nuclear detection. After staining was complete, sections were mounted with a drop of ProLong® Gold antifade reagent (P36930, Life Technologies, Carlsbad, CA, USA) and sealed with a cover slip. Brightfield and fluorescence images were acquired as previously described in *"Brightfield and Fluorescence Microscopy"* section.

Imaging and Quantification of Skin Pigmentation

Imaging and quantification of mouse skin samples were performed using the previously published protocol [19]. Briefly, two single-band bandpass optical filters were used: 480 nm (D480/30x; Chroma, Bellows Falls, VT, USA) and 623 nm (FF01-623/24–25; Semrock, Brightline, Rochester, NY, USA). These filters were attached to an iPhone SE camera for image acquisition. The flash and high dynamic range options on the camera were disabled, and the camera editing filters were not applied. Quantification analysis of pigmentation was performed using ImageJ image processing software [26].

Statistics

Statistical analyses were performed using SPSS Statistics Software (Version 24; IBM Corp, Armonk, NY, USA). Data are expressed as the mean ± SD. A one-way analysis of variance single factor followed by either a Tukey's honest significant difference or Games-Howell post hoc test were used to determine significant differences when applicable.

6.5 Results and Discussion

First, we synthesized a focused library of CFZ salts (hydrochloride, hydrobromide, hydrogen sulfate, nitrate, citrate, hydroiodide, hydrogen phosphate, acetate, and carbonate salts) and compared their fluorescence and Raman spectral properties. For fluorescence analysis, image data were acquired with the standard FITC and Cy5 excitation/emission channels of an epifluorescence microscope; for Raman spectral data, single crystals were analyzed and compared to spectra of isolated CLDIs (Figure 6-1). By visual inspection, CLDIs and CFZ-HCl exhibited almost identical fluorescence and Raman spectra, sharing the CLDIs signature peak at 1400 cm^{-1} (red line). CFZ-hydrobromide, CFZ-hydrogen sulfate, and CFZ-nitrate had similar Raman spectra when compared to CLDIs and CFZ-HCl; however, the Cy5 signal was much less

prominent. Furthermore, based on CLDIs signature peak, the most prominent spectral peak of CFZ-hydrobromide, CFZ-hydrogen sulfate, and CFZ-nitrate showed a small shift in wavelength. All other CFZ salt crystals displayed a completely different Raman spectrum or possessed different visual/fluorescent profile compared to CLDIs. Thus, CFZ-HCl salt crystals most closely mimicked the optical properties of CLDIs.

To scale the synthesis of CFZ-HCl to multigram and larger quantities for manufacturing of a pharmaceutical-grade formulation for clinical trials, a new synthesis scheme was developed using hydrochloric acid for transforming clofazimine free base to hydrochloride salt crystals directly, without dissolving the free base in organic solvents. For free base particles of ~100 µm diameter or less, direct conversion hydrochloride crystals were complete by 72 h, as determined using microscopy, ^{1}H-NMR, and Raman (Figure 6-2).

The protonation state of the CFZ molecule in the different CFZ crystal forms was examined via solution ^{1}H-NMR studies, conducted in DMSO-d_6. ^{1}H-NMR data of newly synthesized CFZ-HCl crystals (CFZ-HCl*) depicts: ^{1}H NMR (400 MHz, DMSO-d_6) δ 9.29 (s, 1H), 8.94 (s, 1H), 8.26–8.17 (m, 1H), 8.04–7.95 (m, 2H), 7.79 (m, 4H), 7.60–7.53 (m, 2H), 7.49–7.41 (m, 2H), 7.37 (s, 1H), 7.15–7.07 (m, 1H), 5.82 (s, 1H), 3.68 (dq, J = 6.5 Hz, 1H), 1.23 (d, J = 6.3 Hz, 6H). ^{1}H-NMR data of control CFZ-HCl crystals depicts: ^{1}H NMR (500 MHz, DMSO-d_6) δ 9.18 (s, 1H), 8.86 (s, 1H), 8.25–8.18 (m, 1H), 8.05–7.95 (m, 2H), 7.79 (m, 4H), 7.62–7.54 (m, 2H), 7.49–7.42 (m, 2H), 7.37 (s, 1H), 7.16–7.08 (m, 1H), 5.82 (s, 1H), 3.68 (dq, J = 6.5 Hz, 1H), 1.23 (d, J = 6.4 Hz, 6H). Using our scalable synthesis method, the resulting CFZ-HCl* NMR spectra matched CFZ-HCl control spectra and was consistent with published spectra [16]. Both CFZ-HCl* and control CFZ-HCl crystals revealed the expected protonation of the tertiary amine (Figure 6-2A) by having an extra singlet peak at 9.29 and 9.18 ppm, respectively (minor

difference in chemical shift is attributed to the difference in the pH of the samples from different synthesis schemes). Furthermore, this protonation of the tertiary amine caused the chemical shift (+δ = 0.05–0.60 ppm) for all other protons in CFZ-HCl* to the same extent as in the control CFZ-HCl spectrum with respect to the CFZ free base spectrum, which confirmed the monoprotonated characteristic of the molecule (Figure 6-2C) [16]. Overall, the ^{1}H-NMR spectrum of CFZ-HCl* and control CFZ-HCl crystals reflected identical protonation states of the molecule.

The chemical "fingerprint" of CFZ-HCl* was further confirmed by Raman micro-spectroscopy due to the almost identical match of all of the peaks to CFZ-HCl control spectra, including the signature peak at 1400 cm^{-1}. Furthermore, the aqueous solubility of CFZ-HCl* matched the aqueous solubility of CFZ-HCl control crystals of approximately 18 μM at 25 °C (data not shown) [22]. In conclusion, the final product was verified to have the same optical and fluorescence properties (Figure 6-2B), as well as the same chemical characteristics, according to ^{1}H-NMR and Raman micro-spectroscopy, as the reference, pure CFZ-HCl salt crystals, synthesized using the established method [16,19] (Figure 6-2C,D).

To formulate micronized CFZ-HCl salt crystals and characterize the extent to which they mimicked CLDIs, ^{1}H-NMR, single crystal Raman micro-spectroscopy, and pXRD were used for comparative analysis. Following micronization and sterilization of bulk CFZ-HCl, chemical and structural characteristics of CFZ-HCl salt crystals remained relatively unchanged (Figure 6-3A–C). ^{1}H-NMR spectral (Figure 6-3A) and single crystal Raman micro-spectroscopy peaks (Figure 6-3B) were preserved with almost identical match, indicating that the chemical structure of CFZ-HCl crystals was not altered by micronization or sterilization. Furthermore, pXRD spectra revealed that the majority of diffraction peaks were preserved as well, including the CFZ-HCl

signature peak at $2\theta = 7.2°$ that is absent in CFZ free base, indicating the preservation of the crystal structure (Figure 6-3C) [16].

Following dispersion of individual drug crystals in IV diluent buffer, Raman spectral analysis quantitatively confirmed that the CFZ-HCl particles from the micronized, sterilized powder, had the same properties (Table 6-1).

In IV diluent buffer, the micronized, sterilized microparticles were completely dispersed. Ultimately, the size and the dispersion of the particles can be adjusted by varying the concentration of the detergent present in the diluent (e.g., polysorbate 80); the higher the concentration, the smaller and more dispersed the particles are (data not shown). In this case, the IV injection, the maximum concentration of polysorbate 80 was used (0.5%) to make the particles as small and as dispersed as possible [24]. As a result, the microcrystals exhibited the expected Cy5 and FITC fluorescence of CFZ-HCl and were homogeneous in size distribution (Figure 6-3D). By utilizing dynamic light scattering analysis (Figure 6-3E), there was one narrow particle distribution of 547 ± 160 nm, an ideal size for parenteral formulations. In contrast, prior to micronization, the starting material exhibited 2 major wide particle size distributions of 621 ± 300 nm and 5035 ± 592 nm, respectively (Figure 6-3E). Thus, air jet milling produced a stable micronized product that could be readily sterilized, preserving a desirable size distribution.

Following physical characterization, the sterilized CFZ-HCl microcrystals were tested for stability properties, by comparing fluorescence in the IV diluent, synthetic lysosomal buffer [19], and physiological saline media (PBS) (Figure 6-4). The micronized particles were stable in diluent (pH 5) and synthetic lysosomal buffer (pH 4.5) as evidenced by the preservation of a strong fluorescence signal in the Cy5 channel (indicative of CFZ-HCl salt) and absence of

fluorescence in the FITC channel (indicative of CFZ free base) (Figure 6-4). In PBS (pH 7.6), the CFZ-HCl microcrystals were unstable as evidenced by the increased fluorescence in the FITC channel and decreased fluorescence in the Cy5 channel, consistent with the conversion of CFZ-HCl to CFZ free base (Figure 6-4). Based on these results, we inferred that the diluent would be appropriate for *in vivo* injection and that the particles may be stabilized by macrophages following phagocytosis.

To confirm this, RAW 264.7 macrophages were incubated with isolated CLDIs and micronized CFZ-HCl. The stability of the phagocytosed drug particles in live cells was microscopically evaluated following ingestion, by visual inspection (Figure 6-5A). RAW macrophages internalized and stabilized CLDIs as well as CFZ-HCl microcrystals, based on the strong Cy5 fluorescence signal and the absence of a FITC fluorescence signal observed in macrophages during the course of a 48-h incubation period (Figure 6-5A). As a control for these experiments, macrophages were incubated with CFZ free base microcrystals which fluoresce in the FITC channel, but not in the Cy5 channel. Interestingly, brightfield and fluorescent images showed that the CFZ free base gradually lost their FITC fluorescence and gained the Cy5 fluorescence, suggesting that the macrophages can transform the free base to the protonated salt form of the drug (Figure 6-5A).

Most importantly, incubation with CFZ-HCl was not cytotoxic. In fact, cell viability was constant (~90–100%) throughout the 48 h incubation regardless of the treatment (Figure 6-5B). These results were further validated by the fact that the biomimetic formulation of CFZ-HCl microcrystals were phagocytosed and stabilized by macrophages, mimicking CLDIs, which led us to conclude that these drug microcrystals would also be prone to phagocytosis and stabilization by resident tissue macrophages *in vivo*.

In vivo studies were performed to assess the effect of injected CFZ-HCl on the spectral reflectance properties of the skin and also to determine whether the particles accumulate in macrophages of the different organs as reported in mice fed with oral CFZ (i.e., spleen and liver) [13–15,19]. Since this analysis was primarily focused on assessing the extent of skin pigmentation, the IV dose (200 mg/kg), which translates to an approximate total dose of 6 mg of CFZ-HCl microcrystals (assuming 100% bioavailability) was specifically chosen to be equivalent to the amount of orally administered CFZ (total of ~6 mg, based on a bioavailability of 10mg/kg/d) [3,13,19,21] under which the maximum CFZ-induced skin pigmentation occurs when CFZ is administered orally (~3 weeks of oral administration) [19].

All mice (n = 5 out of 5) that were injected with the CFZ-HCl microcrystal formulation survived the injection (100% survival) and did not show any signs of toxicity. Analyzing the distribution patterns of CFZ-HCl microcrystals in these animals, Cy5 fluorescence was observed in liver and spleen, form naturally in CFZ-fed mice (Figure 6-6).

In regards to the major side effect of oral CFZ therapy, the impact of the injected microparticles on skin pigmentation was quantitatively determined using a spectral reflectance assay as previously established [19]. Based on the skin reflectance signal acquired at the 480 nm and 623 nm optical filters, IV CFZ-HCl injected mice did not result in detected skin pigmentation (480 nm, no significant difference versus untreated mice, analysis of variance single factor, n = 4). Both untreated and IV injected mice exhibited significantly lower pigmentation than 9 week orally fed CFZ mice, with the 480 nm wavelength filter ($p < 0.05$, analysis of variance single factor, Games-Howell, n = 4) (Figure 6-7A,B). Importantly, the skin pigmentation of orally-fed mice is maximal at 3 weeks and then declines with continued feeding [19]; therefore, we can infer that IV injected mice are also less pigmented than mice fed with

CFZ for 3 weeks. Additionally, the 623 nm optical filter (indicative of the presence of CFZ-HCl) was also unable to detect any significant skin pigmentation that may have arisen from partitioning of circulating CFZ-HCl particles from blood to skin [19]. Of noteworthy significance, the lack of skin pigmentation observed in the CFZ-HCl injected mice cannot be explained by an overt toxicological effect of the drug leading to decreased mice viability, as all mice survived the injection without obvious toxicological consequences. As a caveat, it is important to note that the extent of skin pigmentation is not necessarily a direct reflection of CFZ accumulation in the skin, since the spectral reflectance properties of the skin can also be impacted by the amount of CFZ that circulates through the skin capillaries, as well as the optical (absorbance) properties of the CFZ molecules which can change depending on the molecules' ionization, aggregation, and redox states. Ultimately, the advantages of parenteral versus oral CFZ remain to be conclusively established under conditions leading to therapeutic efficacy, which will depend on the treatment regimen and clinical indication.

To further probe for the presence of toxic side effects resulting from the injected microparticles, TNFα, IL-1RA, and interleukin-1 beta (IL-1β) were measured. TNFα and IL-1β are pro-inflammatory cytokines that are released by cells, primarily macrophages, in response to inflammatory stimuli. IL-1RA is an early-acting acute-phase anti-inflammatory cytokine that dampens a broad spectrum of inflammatory conditions by inhibiting the activity of IL-1β, an important mediator of the inflammatory response [3,20]. However, none of these cytokines were significantly altered by an IV injection of CFZ-HCl (Figure 6-7C). In fact, IL-1RA levels were similar between treated and untreated groups ($p < 0.05$, analysis of variance single factor, Games-Howell, $n = 5$ (both CFZ groups), $n = 4$ (Control group); Figure 6-7C), while the plasma

IL-1β and TNFα concentrations were below the limit of detection (IL-1β LOD = 12.5 pg/mL; TNFα LOD = 10.9 pg/mL).

6.6 Conclusions

In conclusion, a biocompatible, biomimetic formulation of CFZ-HCl microcrystals proved suitable for parenteral, systemic administration, while avoiding the skin pigmentation and immunological response that accompanies oral CFZ administration. Based on our *in vitro* and *in vivo* data, micronized CFZ-HCl crystals were ingested by tissue macrophages and accumulated in liver and spleen, similar to CLDIs; yet, no skin pigmentation was evident, unlike oral administration of CFZ. IV administration did not result in overt toxicity and did not induce measurable changes in acute inflammatory response biomarkers. The anti-inflammatory cytokine, IL-1RA, which we have previously shown to be elevated following oral administration of CFZ [3,20], was not changed by the injected CFZ-HCl microparticles. Our findings support additional studies into the possible use of parenteral CFZ-HCl as a means to circumvent the skin pigmentation side effect of the oral drug. For example, an inhalable, aerosolized formulation of CFZ-HCl may be a good strategy for treating MDR-TB. Previously, Brunaugh et al. [27] and Verma et al. [28] investigated the feasibility of inhalable micronized CFZ free base microparticles against MDR-TB. Nevertheless, based on a more straightforward synthesis route, scalable manufacturing, and other practical considerations, an inhalable formulation of CFZ-HCl microcrystals could offer a more viable approach for pharmaceutical product development. As a wise man once said: “the most fruitful basis for the discovery of a new drug is to start with an old drug [29–31]”.

6.7 Acknowledgements and Funding

The authors are thankful to the University of Michigan's Biochemical NMR Core Laboratory.

This research was funded by the University of Michigan (MCubed, College of Pharmacy Upjohn Award, and MEDC Mi-TRAC (Kickstart) Award) and grants from the National Institutes of Health (NIH) (R01 GM078200; R01 GM111400; and P50 CA186786). The content is solely the responsibility of the authors and does not necessarily represent the official views of the National Institute of General Medical Sciences (NIGMS), National Cancer Institute (NCI), or the NIH.

6.8 Figures and Tables

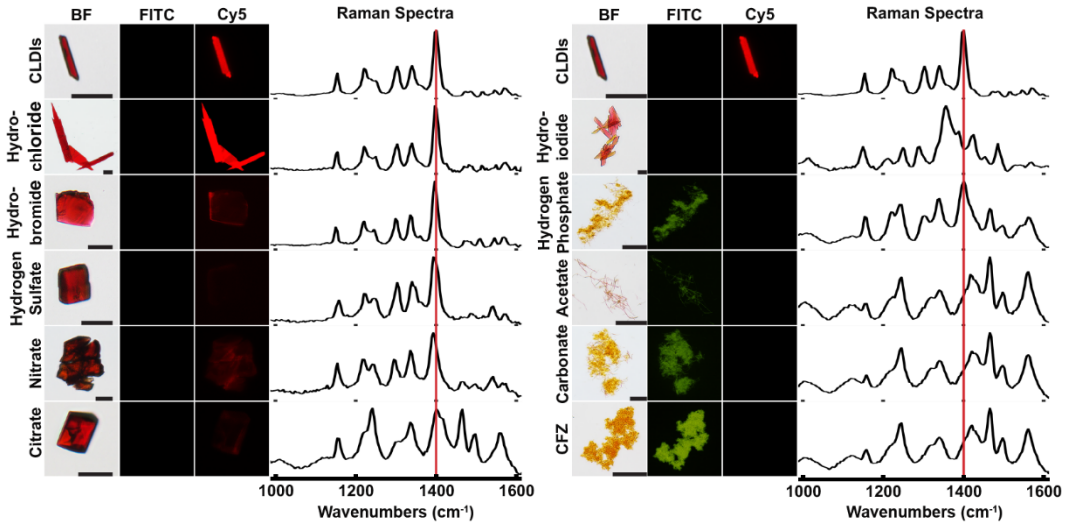

Figure 6-1. CFZ-HCl salt best resemble CLDIs. Single crystal Raman micro-spectroscopy spectra and brightfield (BF)/fluorescent (FITC, Cy5) microscopy images of various synthesized clofazimine (CFZ) salts compared to crystal-like drug inclusions (CLDIs) and CFZ free base. The red line represents the signature peak of CLDIs at 1400 cm^{-1}. Scale bar = 20 µm.

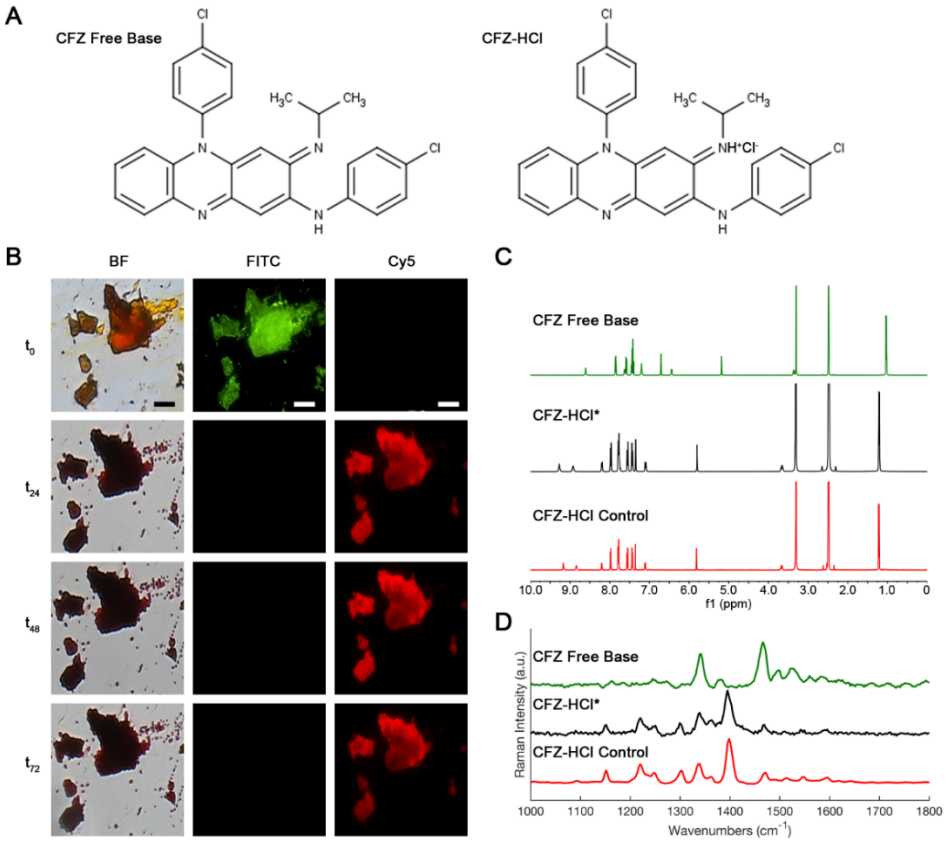

Figure 6-2. Validation of multigram synthesis of CFZ-HCl salt. Chemical structures of CFZ free base and CFZ-HCl (**A**). Brightfield (BF)/fluorescent (FITC, Cy5) microscopy images (**B**); ^{1}H-NMR (**C**), and Raman micro-spectroscopy spectra (**D**) of synthesized CFZ-HCl salt crystals via new synthesis scheme (*) compared to the established CFZ-HCl salt crystals and CFZ free base. Scale bar = 50 µm.

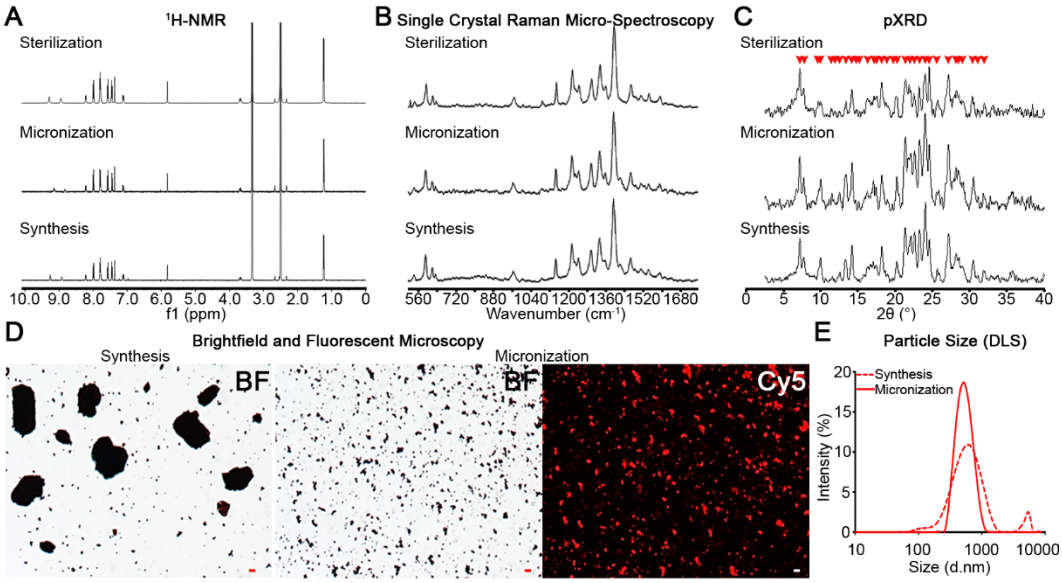

Figure 6-3. Characterization of CFZ-HCl salt crystals throughout the manufacturing process. The integrity of the salt crystals was maintained throughout the manufacturing process (synthesis, micronization, and sterilization) of a biomimetic formulation of micronized CFZ-HCl salt crystals. This is evidenced by the spectra from ^{1}H-NMR (**A**); single crystal Raman micro-spectroscopy (**B**); and powder X-ray diffraction (pXRD) (**C**). The red arrows in pXRD spectrum (**C**) indicate the peaks that are preserved after micronization and sterilization. The efficacy of micronization is depicted in brightfield and fluorescent images (**D**) and particle size distribution (**E**). Scale bar = 5 µm.

Table 6-1. Quality and stability of single CFZ-HCl and CFZ free base micronized drug crystals measured by single crystal Raman micro-spectroscopy.

Sample (n = 3)	# Drug Crystals Scanned	# CFZ-HCl Crystals	# CFZ Free Base Crystals	# Other Particles
Micronized CFZ-HCl	100	98 ± 1	0	2 ± 1
Micronized CFZ-HCl in Diluent *	100	98 ± 1	0	2 ± 1
Micronized CFZ Free Base	100	0	97 ± 1	3 ± 1

* Diluent in IV injectable formulation for *in vivo* studies

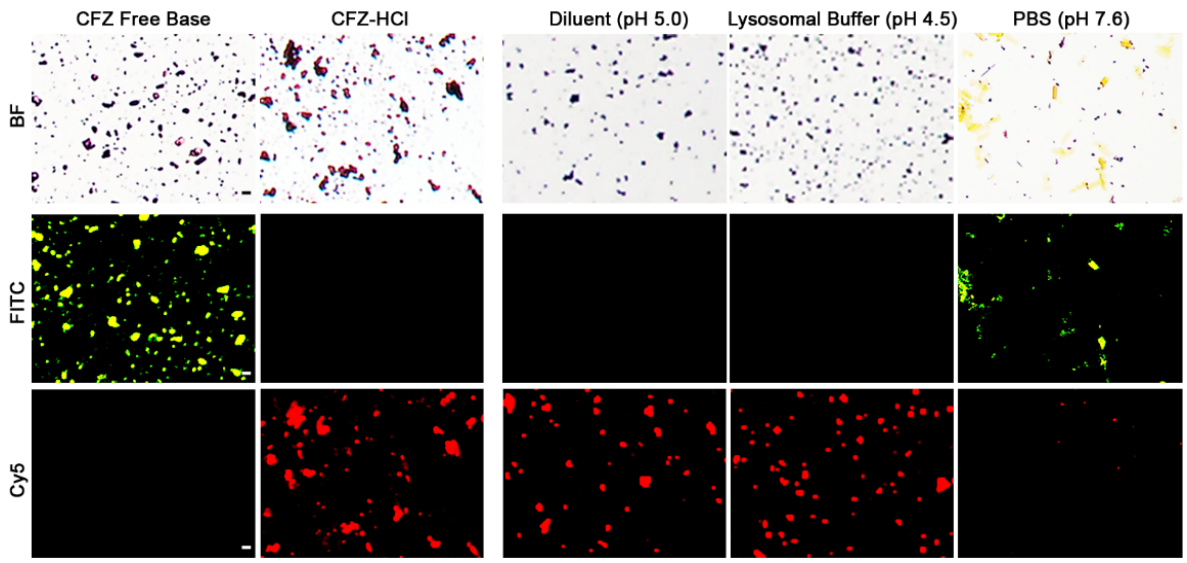

Figure 6-4. ***In vitro*** **stability of the biomimetic formulation of micronized CFZ-HCl salt crystals in IV diluent, synthetic lysosomal buffer, and PBS after 24 h utilizing brightfield and fluorescent (FITC, Cy5) microscopy.** Scale bar = 5 µm.

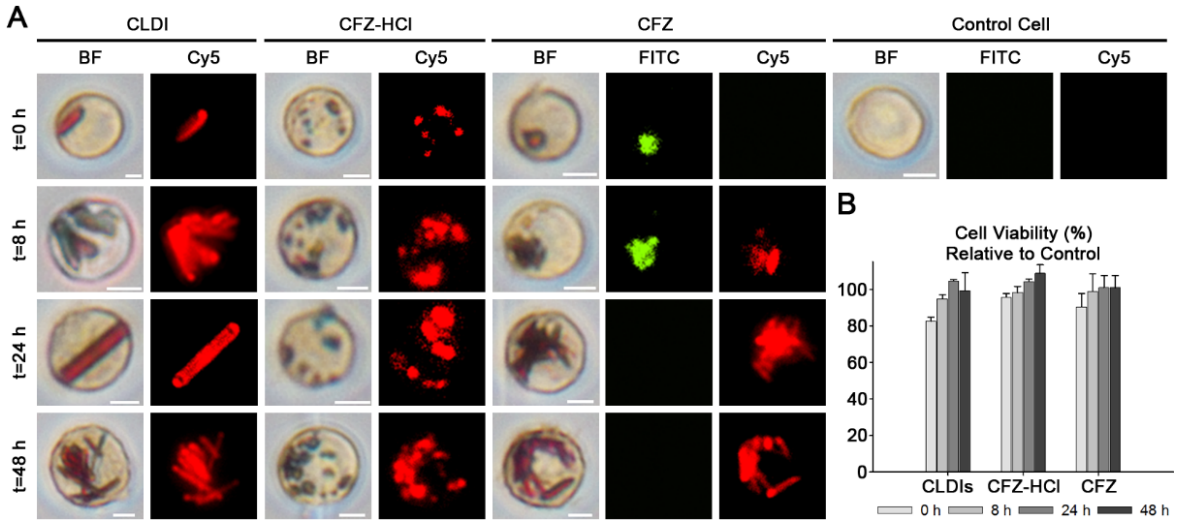

Figure 6-5. ***In vitro*** **stability of the micronized CFZ-HCl salt and CFZ free base drug crystals in RAW 264.7 murine macrophages over 48 hours compared to CLDIs.** The stability is depicted via brightfield and fluorescent images (FITC, Cy5) (**A**). Cell viability was not altered by 8, 24, and 48 hours of treatment with CLDIs, CFZ-HCl, or CFZ free base (**B**).

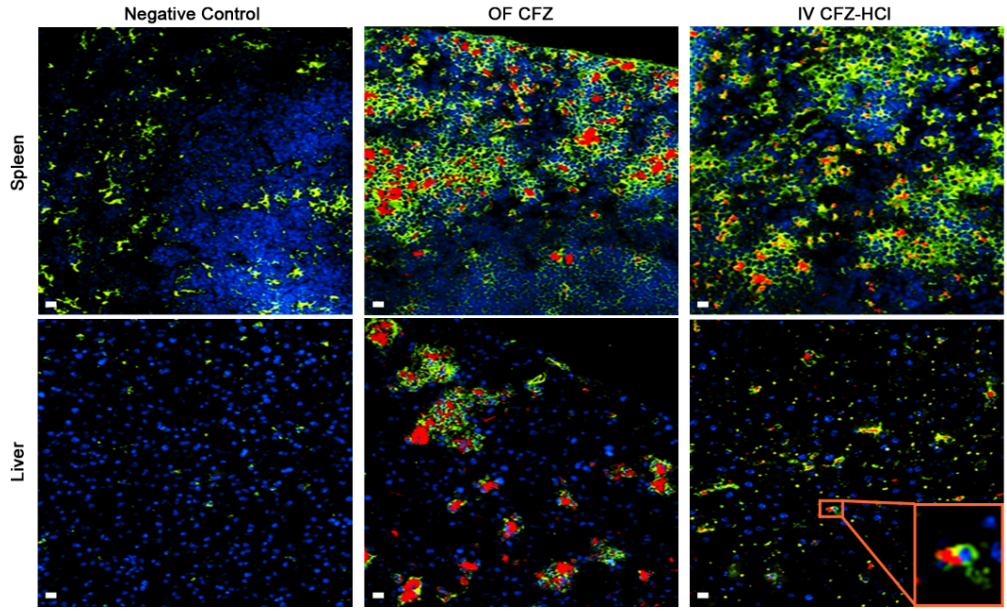

Figure 6-6. *In vivo* stability and phagocytosis of the biomimetic formulation of micronized CFZ-HCl salt crystals following IV injection to mice compared to orally fed (OF) CFZ mice. Images represent CD68 immunohistochemistry of cryo-sections of spleen and liver from OF CFZ and untreated (negative control) mice. Blue (DAPI) – nucleus; green (FITC) – CD68(+) macrophages; red (Cy5) – CLDIs / CFZ-HCl microcrystals. Scale bar = 20 μm.

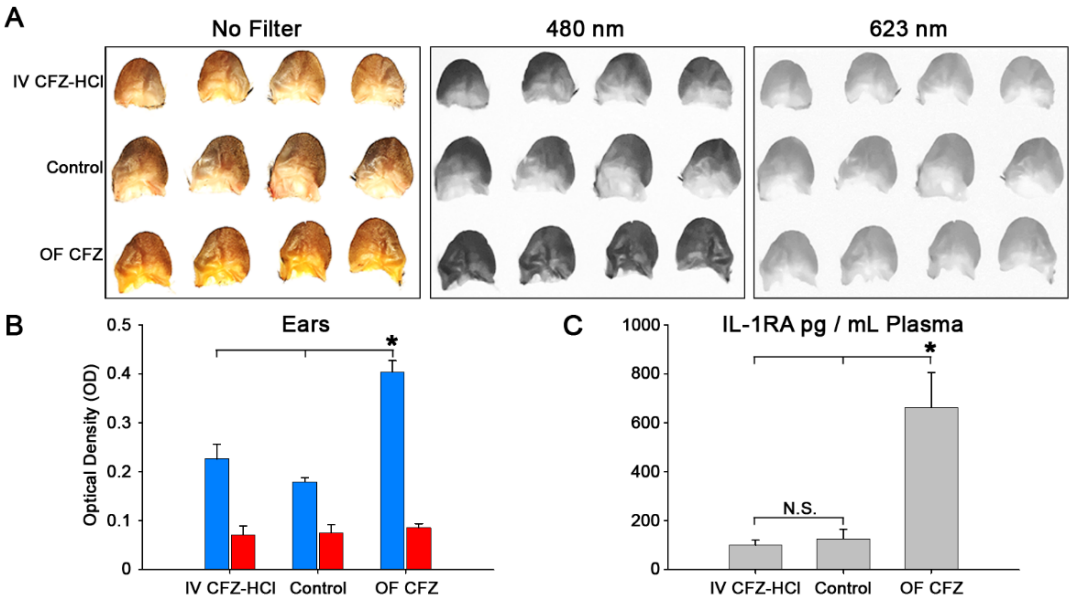

Figure 6-7. Quantitative analysis of skin pigmentation and plasma IL-1RA concentrations following IV administration of CFZ-HCl (IV CFZ-HCl) and oral administration of CFZ (OF CFZ) compared to untreated mice (control). Images of mouse ears from treatment groups and the extent of their reflectance using 480 nm and 623 nm optical filters (**A**). Quantitative analysis of the pigmentation of mouse ears from CFZ treated mice compared to untreated mice (n = 4) via reflectance spectroscopy (blue = 480 nm; red = 623 nm filter; * $p < 0.05$, analysis of variance (ANOVA) single factor, Games-Howell) (**B**). Plasma concentrations of IL-1RA in CFZ treated mice compared to untreated mice (n = 5 (CFZ groups); n = 4 (untreated group)) (* $p < 0.05$, analysis of variance (ANOVA) single factor, Games-Howell) (**C**).

6.9 References

1. Cholo, M.C.; Steel, H.C.; Fourie, P.B.; Germishuizen, W.A.; Anderson, R. Clofazimine: Current status and future prospects. *J. Antimicrob. Chemother.* **2012**, *67*, 290–298.

2. Barry, V.C.; Belton, J.G.; Conalty, M.L.; Denneny, J.M.; Edward, D.W.; O'Sullivan, J.F.; Twomey, D.; Winder, F. A new series of phenazines (rimino-compounds) with high antituberculosis activity. *Nature* **1957**, *179*, 1013–1015.

3. Yoon, G.S.; Keswani, R.K.; Sud, S.; Rzeczycki, P.M.; Murashov, M.D.; Koehn, T.A.; Standiford, T.J.; Stringer, K.A.; Rosania, G.R. Clofazimine Biocrystal Accumulation in Macrophages Upregulates Interleukin 1 Receptor Antagonist Production to Induce a Systemic Anti-Inflammatory State. *Antimicrob. Agents Chemother.* **2016**, *60*, 3470–3479.

4. World Health Organization Leprosy Report. Available online: http://www.who.int/mediacentre/factsheets/fs101/en (accessed on 26 October 2018).

5. Arbiser, J.L.; Moschella, S.L. Clofazimine: A review of its medical uses and mechanisms of action. *J. Am. Acad. Dermatol.* **1995**, *32*, 241–247.

6. Tyagi, S.; Ammerman, N.C.; Li, S.Y.; Adamson, J.; Converse, P.J.; Swanson, R.V.; Almeida, D.V.; Grosset, J.H. Clofazimine shortens the duration of the first-line treatment regimen for experimental chemotherapy of tuberculosis. *Proc. Natl. Acad. Sci. USA* **2015**, *112*, 869–874.

7. Lechartier, B.; Cole, S.T. Mode of Action of Clofazimine and Combination Therapy with Benzothiazinones against Mycobacterium tuberculosis. *Antimicrob. Agents Chemother.* **2015**, *59*, 4457–4463.

8. Williams, K.; Minkowski, A.; Amoabeng, O.; Peloquin, C.A.; Taylor, D.; Andries, K.; Wallis, R.S.; Mdluli, K.E.; Nuermberger, E.L. Sterilizing activities of novel combinations lacking first- and second-line drugs in a murine model of tuberculosis. *Antimicrob. Agents Chemother.* **2012**, *56*, 3114–3120.

9. Dooley, K.E.; Obuku, E.A.; Durakovic, N.; Belitsky, V.; Mitnick, C.; Nuermberger, E.L.; Efficacy Subgroup, R.-T. World Health Organization group 5 drugs for the treatment of drug-resistant tuberculosis: Unclear efficacy or untapped potential? *J. Infect. Dis.* **2013**, *207*, 1352–1358.

10. Gopal, M.; Padayatchi, N.; Metcalfe, J.Z.; O'Donnell, M.R. Systematic review of clofazimine for the treatment of drug-resistant tuberculosis. *Int. J. Tuberc. Lung Dis.* **2013**, *17*, 1001–1007.

11. Sukpanichnant, S.; Hargrove, N.S.; Kachintorn, U.; Manatsathit, S.; Chanchairujira, T.; Siritanaratkul, N.; Akaraviputh, T.; Thakerngpol, K. Clofazimine-induced crystal-storing histiocytosis producing chronic abdominal pain in a leprosy patient. *Am. J. Surg. Pathol.* **2000**, *24*, 129–135.

12. Belaube, P.; Devaux, J.; Pizzi, M.; Boutboul, R.; Privat, Y. Small bowel deposition of crystals associated with the use of clofazimine (Lamprene) in the treatment of prurigo nodularis. *Int. J. Lepr. Other Mycobact. Dis.* **1983**, *51*, 328–330.

13. Baik, J.; Stringer, K.A.; Mane, G.; Rosania, G.R. Multiscale distribution and bioaccumulation analysis of clofazimine reveals a massive immune system-mediated xenobiotic sequestration response. *Antimicrob. Agents Chemother.* **2013**, *57*, 1218–1230.

14. Baik, J.; Rosania, G.R. Macrophages sequester clofazimine in an intracellular liquid crystal-like supramolecular organization. *PLoS ONE* **2012**, *7*, e47494.

15. Baik, J.; Rosania, G.R. Molecular imaging of intracellular drug-membrane aggregate formation. *Mol. Pharm.* **2011**, *8*, 1742–1749.

16. Keswani, R.K.; Baik, J.; Yeomans, L.; Hitzman, C.; Johnson, A.M.; Pawate, A.S.; Kenis, P.J.; Rodriguez-Hornedo, N.; Stringer, K.A.; Rosania, G.R. Chemical Analysis of Drug Biocrystals: A Role for Counterion Transport Pathways in Intracellular Drug Disposition. *Mol. Pharm.* **2015**, *12*, 2528–2536.

17. Maia, M.V.; Cunha Mda, G.; Cunha, C.S. Adverse effects of alternative therapy (minocycline, ofloxacin, and clofazimine) in multibacillary leprosy patients in a recognized health care unit in Manaus, Amazonas, Brazil. *An. Bras. Dermatol.* **2013**, *88*, 205–210.

18. Tang, S.; Yao, L.; Hao, X.; Liu, Y.; Zeng, L.; Liu, G.; Li, M.; Li, F.; Wu, M.; Zhu, Y.; et al. Clofazimine for the treatment of multidrug-resistant tuberculosis: Prospective, multicenter, randomized controlled study in China. *Clin. Infect. Dis.* **2015**, *60*, 1361–1367.

19. Murashov, M.D.; LaLone, V.; Rzeczycki, P.M.; Keswani, R.K.; Yoon, G.S.; Sud, S.; Rajeswaran, W.; Larsen, S.; Stringer, K.A.; Rosania, G.R. The Physicochemical Basis of Clofazimine-Induced Skin Pigmentation. *J. Investig. Dermatol.* **2017**, *138*, 697–703.

20. Yoon, G.S.; Sud, S.; Keswani, R.K.; Baik, J.; Standiford, T.J.; Stringer, K.A.; Rosania, G.R. Phagocytosed Clofazimine Biocrystals Can Modulate Innate Immune Signaling by Inhibiting TNFalpha and Boosting IL-1RA Secretion. *Mol. Pharm.* **2015**, *12*, 2517–2527.

21. Keswani, R.K.; Yoon, G.S.; Sud, S.; Stringer, K.A.; Rosania, G.R. A far-red fluorescent probe for flow cytometry and image-based functional studies of xenobiotic sequestering macrophages. *Cytom. Part A* **2015**, *87*, 855–867.

22. Woldemichael, T.; Keswani, R.K.; Rzeczycki, P.M.; Murashov, M.D.; LaLone, V.; Gregorka, B.; Swanson, J.A.; Stringer, K.A.; Rosania, G.R. Reverse Engineering the Intracellular Self-Assembly of a Functional Mechanopharmaceutical Device. *Sci. Rep.* **2018**, *8*, 2934.

23. Rzeczycki, P.; Yoon, G.S.; Keswani, R.K.; Sud, S.; Stringer, K.A.; Rosania, G.R. Detecting ordered small molecule drug aggregates in live macrophages: A multi-parameter microscope image data acquisition and analysis strategy. *Biomed. Opt. Express* **2017**, *8*, 860–872.

24. U.S. Food & Drug Administration. Inactive Ingredient Search for Approved Drug Products. Available online: https://www.accessdata.fda.gov/scripts/cder/iig/index.cfm (accessed on 26 October 2018).

25. Trexel, J.; Yoon, G.S.; Keswani, R.K.; McHugh, C.; Yeomans, L.; Vitvitsky, V.; Banerjee, R.; Sud, S.; Sun, Y.; Rosania, G.R.; et al. Macrophage-Mediated Clofazimine Sequestration Is Accompanied by a Shift in Host Energy Metabolism. *J. Pharm. Sci.* **2017**, *106*, 1162–1174.

26. Schneider, C.A.; Rasband, W.S.; Eliceiri, K.W. NIH Image to ImageJ: 25 years of image analysis. *Nat. Methods* **2012**, *9*, 671–675.

27. Brunaugh, A.D.; Jan, S.U.; Ferrati, S.; Smyth, H.D. Excipient-Free Pulmonary Delivery and Macrophage Targeting of Clofazimine via Air Jet Micronization. *Mol. Pharm.* **2017**, *14*, 4019–4031.

28. Verma, R.K.; Germishuizen, W.A.; Motheo, M.P.; Agrawal, A.K.; Singh, A.K.; Mohan, M.; Gupta, P.; Datta Gupta, U.; Cholo, M.; Anderson, R.; et al. Inhaled microparticles containing clofazimine are efficacious in treatment of experimental tuberculosis in mice. *Antimicrob. Agents Chemother.* **2013**, *57*, 1050–1052.

29. Chong, C.R.; Sullivan, D.J., Jr. New uses for old drugs. *Nature* **2007**, *448*, 645–646.

30. Chen, H.; Wu, J.; Gao, Y.; Chen, H.; Zhou, J. Scaffold Repurposing of Old Drugs Towards New Cancer Drug Discovery. *Curr. Top. Med. Chem.* **2016**, *16*, 2107–2114.

31. Yella, J.K.; Yaddanapudi, S.; Wang, Y.; Jegga, A.G. Changing Trends in Computational Drug Repositioning. *Pharmaceuticals* **2018**, *11*, 57.

Chapter 7

Inhibition of Macrophage Recruitment Decreases the Stability of Injected Microcrystalline Particles in the Joint and Reduces the Associated Inflammatory Response

7.1 Relevance to Thesis

This chapter was adapted from the following manuscript:

***Murashov MD**, Stringer KA, Rosania GR. **2018**. Inhibition of Macrophage Recruitment Decreases the Stability of Injected Microcrystalline Particles in the Joint and Reduces the Associated Inflammatory Response. **Manuscript has not been submitted**.*

This chapter investigated and completed the Specific Aim 3 in this thesis. In one of new potential indications (e.g. gouty arthritis) for CFZ treatment, I explored the inflammatory status of the biomimetic formulation of micronized CFZ-HCl salt crystals (Chapter 2) under local administration in rat model, *in vivo*, and determined that the local injection of CFZ-HCl microcrystals leads to the recruitment of macrophages to the site of action, a pro-inflammatory response. Furthermore, micronized CFZ-HCl particles did not facilitate the dissolution and clearance of MSU crystals from the joint, main source of inflammation, by lowering the local pH of the synovium (Chapter 3).

7.2 Abstract

In macrophages, phagocytosis of monosodium urate crystals promotes the production of pro-inflammatory cytokines leading to pain, swelling and furthering monocyte recruitment. Here, we studied whether the inflammatory response induced by MSU crystals directly injected into

joints may be related to their alkalinizing effect on the local microenvironment or to their impact on macrophage recruitment. For this purpose, clofazimine hydrochloride (CFZ-HCl) microcrystals were injected into the rat knee, alone or in combination with MSU crystals. As a hypothesis, the micronized CFZ-HCl particles should lower the pH of the synovium upon dissolution, facilitating the dissolution and clearance of MSU crystals from the joint and reducing their alkalinizing effects. Contrary to expectations, the results indicated that CFZ-HCl injections significantly increased the severity of the inflammatory response induced by co-injecting MSU microcrystals. Furthermore, treatment with methylprednisolone, reduced both CFZ- and MSU-induced inflammation, while destabilizing the CFZ-HCl microcrystals through increased alkalinization. Because methylprednisolone is known to inhibit macrophage migration, we infer that macrophages exacerbate joint inflammation by stabilizing injected microcrystals; by reducing macrophage recruitment, methylprednisolone decreased injected microcrystal stability and lessened the inflammatory response.

7.3 Introduction

Gout is the most common inflammatory, crystal-induced arthropathy, characterized by severe pain, red, and swollen joint [1-3]. It is caused by hyperuricemia, which leads to the accumulation of monosodium urate (MSU) crystals in a joint, tendons, and surrounding tissues, resulting in an attack of gout [1]. Hyperuricemia is typically defined as a serum urate concentration that exceeds 6.8 mg/dL, which is above the saturation point of MSU [1]. Soluble urate is one of the final products of the metabolic breakdown of purine nucleotides [1, 4], and the body normally clears it via the enzyme uricase, which degrades urate to the more soluble molecule allontoin [1, 5-7]. However, several factors (i.e., genetic mutational inactivation of the gene for the uricase; renal underexcretion of urate; conditions of excessive cell and purine

turnover (e.g., leukemias, etc.) [4]; high purine dietary intake [8]; and/or genetic factors that result in primary urate overproduction [9]) can lead to hyperuricemia [1]. Even though gout may attack any single joint in the body (acute gout) or many joints at once with repeated episodes (chronic), in extreme cases, it may also result in tophi, kidney stones, and/or urate nephropathy [10].

Gout afflicts approximately 8 million patients every year, which is a prevalence of more than 10% in certain populations [11]. More than 10 pharmaceutical companies in world (e.g., AstraZeneca PLC, Novartis AG, Polaris Group, BioCryst Pharmaceuticals Inc., Teijin Pharma Limited, etc.) are currently working on treatments for gout that include: non-steroidal anti-inflammatory drugs (NSAIDs), colchicines, and corticosteroids that help with pain and inflammation; enzyme and protein inhibitors that ultimately reduce serum urate levels; and modified urate oxidase that metabolizes urate into highly soluble allantoin [12]. However, none of these treatments target the source of inflammation, the MSU crystals within the joint. Therefore, a treatment that facilitates the clearance of accumulated urate out of the joint by contributing to the dissolution of accumulated MSU crystals could lead to new and novel approaches to treating gout.

Under physiological conditions (pH 7.4), uric acid predominantly exists as a charged, urate anionic form. Urate has a pKa of 5.75, below which it turns into uric acid crystals (enol form, square-like crystals) [1]. In the most common form of gout, however, due to hyperuricemia and low affinity for sodium cation (Ksp), urate ions precipitate as monosodium urate salt crystals (needle-like crystals). Importantly, MSU salt crystals are more stable in joints of the extremities because they tend to be colder than the rest of the body; in these physiological conditions once

MSU salt crystals form, the only way to destabilize them is by lowering the pH and shifting the equilibrium to the enol form of urate.

Thus, as a means to lower and sustain the pH below the pKa of 5.75, we considered injecting micronized hydrochloride salt crystals of a weakly basic drug. Looking for the most biocompatible and stable weakly basic drug crystals that could function as a proton-donor to facilitate the dissolution of monosodium urate crystals, we selected clofazimine (CFZ). CFZ is a weakly basic, broad spectrum, orally administered, antimycobacterial agent recommended by the World Health Organization as a treatment for leprosy and multidrug resistant tuberculosis [13-21]. In patients, CFZ exhibits atypical pharmacokinetic properties, forming solid drug precipitates in tissue macrophages that display robust stability inside macrophages and remain in the body long after discontinuation of treatment [22-26]. The preliminary analysis of these biocrystals revealed that they contained a hydrochloride salt form of the drug, which is stabilized by the acidic and high chloride concentrations present in macrophage lysosomes, while the orally administered form of the drug is the free base [27]. Even though prolonged CFZ treatment is associated with massive drug biocrystal accumulation, there are no obvious toxicological manifestations from them. Instead, they were determined to be biocompatible, stable, long-lived, relatively non-toxic, and anti-inflammatory [28, 29].

Previously, we reported on the synthesis and characterization of a biomimetic formulation of CFZ hydrochloride microcrystals that proved suitable for parenteral, systemic administration without major toxicological consequences (Chapter 6). Thus, we proceeded to determine whether intra-articular (IA) injection of CFZ-HCl microcrystals could facilitate the dissolution of co-injected monosodium urate (MSU) crystals, by reducing the alkalinizing effects of MSU crystals and by destabilizing them by donating protons to the synovial fluid. As a

hypothesis, micronized CFZ-HCl particles should decrease inflammation, pain, and swelling associated with IA injections of MSU crystals, facilitating the dissolution and clearance of MSU crystals from the joint by lowering the local pH of the synovium. The schematic that depicts this hypothesis is shown in Figure 7-1.

7.4 Materials and Methods

Animals

All animal care conformed to the guidelines cited in the Guide for the Care and Use of Laboratory Animals (NIH Guide, 2011), the applicable standard operating procedures of Bolder BioPATH, Inc. Male Lewis rats were obtained from Charles River (Wilmington, MA). Rats weighed 245–310 grams (mean = 287 g) at enrollment Days (-12) and (-4) (Table 7-1). Animals were identified by a distinct mark at the base of the tail delineating group and animal number. After randomization, all cages were labeled with protocol number, group numbers, and animal numbers with appropriate color-coding.

Upon arrival, animals were housed 3–5/cage in shoe-box polycarbonate cages with wire tops, wood chip bedding, and suspended food and water bottles. An attending veterinarian was on site or on call during the live phase of the study. No concurrent medications were given. During the acclimation and study periods, animals were housed in a laboratory environment with temperatures ranging 67–76°F and relative humidity of 30%–70%. Automatic timers provided 12 hours of light and 12 hours of dark. Animals were allowed access *ad libitum* to Harlan Teklad Rodent Chow and fresh municipal tap water.

Upon completion of the study, the animals were euthanized for necropsy. Specifically, the rats were exsanguinated under deep anesthesia followed by bilateral pneumo-thoracotomy.

Test Article Identification and Preparation

Micronized CFZ Hydrochloride

Micronized CFZ-HCl crystals were synthesized as previously described (Chapter 6). To prepare a CFZ-HCl formulation for injection, the CFZ-HCl microcrystals were suspended in formulation diluent at different concentrations based on the treatment scheme (Table 7-2). The formulation diluent was made using polysorbate 80 (59924 Sigma-Aldrich, St. Louis, MO); polyethylene glycol 3350 (PEG; P146-3, Lot #174436, Fisher Scientific, Fair Lawn, NJ); sodium chloride (BP358, Fisher Scientific, Fair Lawn, NJ), and Milli-Q water. To coat and disperse the lipophilic CFZ-HCl microcrystals, the maximum concentrations of 0.2% polysorbate 80 and 3% PEG 3350 were used [30]. Sodium chloride was added to maintain isotonicity. The pH was adjusted to pH 4 using 0.01 M HCl or 0.01 M NaOH to ensure the stability of CFZ-HCl microcrystals in the formulation. Before suspending the CFZ-HCl microcrystals, the diluent was sterilized by sterile filtration with a syringe filter (09-719A; 0.22 μm, MCE, Sterile; Fisher Scientific, Fair Lawn, NJ). Micronized CFZ-HCl crystals were carefully mixed prior to injection via sonication and vortexing.

Methylprednisolone (DepoMedrol)

Methylprednisolone (DepoMedrol®, 40 mg/mL, 1 mL single-dose vial, Lot #T81737, Pfizer, NY) was purchased from the University of Michigan hospital pharmacy. DepoMedrol injections were carefully mixed prior to use via sonication and vortexing at the concentrations according to the treatment scheme (Table 7-2).

Monosodium Urate (MSU)

Bolder BioPATH supplied the MSU crystals (Invivogen, Cat #Tlrl-msu-25, Lot #MSU-39-04). MSU crystals were prepared at a concentration of 40 mg/ml in sterile endotoxin free

phosphate buffered saline (PBS, Lot #24317003). The MSU injections were carefully mixed prior to use via sonication and vortexing at the concentrations according to the treatment scheme (Table 7-2).

Experimental Study Design

The study was divided into two phases:

Phase 1: On Study Day (-12) (Table 7-1), Groups 1–2 received intra-articular (IA) injections of MSU vehicle and CFZ vehicle or CFZ injection into the right knee according to the treatment information (Table 7-2). Knee caliper measurement were taken at 0, 4, 8, and 24 h post-injection as described in Section 4a. Inflammatory activation was observed in animals treated with CFZ; therefore, a second injection was administered into the other (left) knee on Day (-8) to optimize formulation/dosing. Knees were calipered at 0, 4, 8, and 24h post-injection. After the final caliper measurements, animals in Groups 1–2 were necropsied as described in Section 4e.

Phase 2: On Study Day (-4) (Table 7-1), animals in Groups 3–6 were randomized by body weight into treatment groups, and baseline knee caliper, Von Frey, gait, and incapacitance (IC) measurements were taken. On Day (0), the animals were anesthetized with isoflurane and given IA injections of test article or vehicle and MSU crystals into the right knee joint as indicated in Table 7-2. Knee caliper, Von Frey, IC, and gait measurements were taken again on Day (0) and Day (1) (Table 7-1) as described in Sections 4a-d. The animals were euthanized for necropsy at 24 hours post-injection on Day (1) as described in Section 4e (neutrophil infiltration and knee swelling was expected to peak 24 hours post-injection).

Observations, Measurements, and Specimens

Knee Caliper Measurements

Right and left knee caliper measurements were made using a Digitrix II micrometer (Fowler & NSK). Caliper measurements for Groups 1–2 were taken on Study Day (-8, Table 7-1) as a baseline and at 4h and 8h post-injection and on Day (-7, Table 7-1) at 24h post-injection. The change in knee diameter from baseline was determined. Caliper measurements for Groups 3–6 were taken on Study Day (-4, Table 7-1) as baseline, Day (0, Table 7-1) at 4h and 8h post-injection, and Day (1, Table 7-1) at 24h post-injection. The change in knee diameter from baseline was determined.

Von Frey (VF) Testing Methods

Von Frey testing of Groups 3–6 was performed on Study Day (-4, baseline) and Day (1) (Table 7-1). The rats were habituated to the animal colonies for one week and handled four times for five minutes each after the week of habituation. The animals were habituated to the testing rack three times during this process.

A Von Frey (VF) testing kit for our purposes consisted of a set of hairs that ranged from 3.16 to 5.18 grams absolute threshold for rats. Each researcher used the same set of hairs to avoid variability between kits. Testing was done on the hind portions of the hind paw as the heel tends to give a more reliable and sensitive response. The purpose of testing was to determine which stiffness hair the rat would respond to 100% of the time. Data was entered into a spreadsheet and a separate program (psychofit) was used to translate the 100% response rate into a 50% threshold, which was used in reporting results. Testing began with three applications of the 4.31 hair. A response was recorded if the animal had an obvious reaction to the pressure of the hair, typically manifested as lifting of the hind paw from the grate to relieve the pressure. Responses

were recorded on a template as either a 0 (no response) or a 1 (response). If the animal did not respond to the hair three times in a row, the next larger hair in the kit was applied, and the process was repeated until the animal responded three times in a row. Following the response, the previous filament was re-tested to confirm lack of response. If the animal did respond, the next smaller filament was applied and the process was repeated until the animal no longer responded. Once a lack of response was observed, the previous filament was re-tested to confirm the response.

Incapacitance (IC) Testing Methods

Incapacitance (IC) testing of Groups 3–6 was performed on Study Day (-4, baseline) and Day (1) (Table 7-1). The animals were trained for the process at least twice prior to the actual evaluation date. The animals were placed in the plexiglass housing of the incapacitance meter. The plexiglass housing consisted of a tube situated at a 45 degree angle, which allowed the animal to elevate its torso. Each animal was allowed to acclimate for approximately 5 minutes or until the animal appeared to be calmly standing with both feet on the force plates. The position of the animal was such that each hind paw rested on a separate force plate. The force exerted by each hind paw was averaged over a 1 second interval, and the mean of three readings constituted 1 data point. The change in hind paw weight distribution was determined by the difference in the amount of weight between the right and left limbs [31].

Gait Evaluation Methods

Gait testing of Groups 3–6 was performed on Study Day (-4, baseline) and Day (1) (Table 7-1). Gait was evaluated by applying ink to the ventral surface of the foot and documenting weight bearing during movement (footprints) across paper. The rear feet of each rat were placed in ink, then rats were placed on paper and allowed to walk the full length. This

process was repeated as necessary to generate 4 clear, evenly inked footprint pairs representing the overall pattern of gait. Gait was scored visually as described in Table 7-3 (descriptions refer to diseased leg).

Necropsy Specimens

The animals were euthanized for necropsy 24h post-injection on Study Day (-7, Groups 1–2) and Day (1, Groups 3–6) (Table 7-1). Serum (≥200 µl/rat) was harvested and stored frozen (-80ºC for further analysis. Right and left knees were lavaged (50 µl of sterile saline per knee), and synovial fluid from each joint were collected, flash frozen in liquid nitrogen, and stored at (-80ºC) for future analysis. Right and left knees were also collected from all animals in Groups 1–2 and were flash frozen and stored (-80ºC) for future analysis. Non-injected knees were collected from Group 4 rats and were flash frozen and stored (-80ºC) for future analysis. Injected knees were collected from Groups 3–6 and non-injected knees were collected from Group 3 and were placed in 10% neutral buffered formalin (NBF) before being transferred to 70% ethanol and processed for histopathology.

Morphologic Pathology Methods

Histopathology was performed on knees from Groups 3–6 only. Knees were cut in half in the frontal plane, and the two halves were embedded together. Sections were cut from each block and stained with toluidine blue. The inflammation, pannus, cartilage damage, and bone resorption were evaluated and scored according to the indicated criteria (Tables 7-4, 7-5, 7-6, and 7-7).

Cytokine Measurements in Knee Lavage and Terminal Serum

Knee lavage and terminal serum samples were assayed for IL-1β and TNF-α by immunology multiplex assay (RECYTMAG-65K; MILLIPLEX Rat Cytokine/Chemokine

Magnetic Bead Panel, Burlington, MA) in triplicate according to the manufacturer's instructions. The cytokine concentrations were expressed as picograms per milliliter of either knee lavage or terminal serum. In addition, the pH of knee lavage samples was measured in triplicate using micro pH probe (Orion Star A211, Thermo Fisher, Waltham, MA) prior to cytokine measurements.

Brightfield and Fluorescence Microscopy

Microscopy was performed using a Nikon Eclipse Ti inverted microscope (Nikon Instruments, Melville, NY) as previously described [32, 33]. Briefly, brightfield images were captured using the Nikon DS-3 camera (Nikon Instruments), and fluorescence imaging in FITC channel (490/510 nm, green) and Cy5 channel (640/670 nm, far-red) was performed with the Photometrics CoolSnap MYO camera system (Photometrics, Tuscon, AZ) under the control of Nikon NIS-Elements AR software (Nikon Instruments). Illumination for fluorescence imaging was provided by the X-Cite 120Q Widefield Fluorescence Microscope Excitation Light Source (Excelitas Technology, Waltham, MA).

Statistical Analysis

Data were entered into Microsoft Excel, and arithmetic means and standard errors were calculated. Groups were compared to vehicle treated animals using a one-way analysis of variance (ANOVA) along with a Dunnett's post-hoc analysis or a Student's two-tailed t-test for measured data (parametric) or a Kruskal-Wallis (K-W) test along with a Dunn's post-hoc analysis for scored data (non-parametric). Statistical analysis was performed using Prism 7.0d software (GraphPad). Unless indicated, Bolder BioPATH, Inc. performed statistical analysis on raw (untransformed) data only. Statistical tests make certain assumptions regarding normality and homogeneity of variance, and further analysis may be required if testing resulted in

violations of these assumptions. P values were rounded to three decimal places. Significance for all tests was set at $p < 0.05$.

7.5 Results and Discussion

The study was divided into two phases: Phase 1 and Phase 2. The goal of Phase 1 of the experiment was to determine if CFZ-HCl injection on its own (CFZ-HCl microcrystals or the formulation diluent) causes an inflammatory response. To eliminate the possibility of the inflammatory response due to endotoxins in the CFZ-HCl injectable formulation, prior to Phase 1, both CFZ-HCl microcrystals and the formulation diluent were determined to be below the endotoxin limit by Charles River Labs (data not shown). Proceeding with the experiment, Phase 1 revealed that CFZ injection still resulted in inflammation (swelling) when injected IA at 50 µl/knee (equivalent to approximately 2.67 mg of CFZ-HCl per injection) (Figure 7-2A-B). In fact, CFZ injection resulted in significant increased knee caliper measurements 4-24 h post injection as compared to CFZ vehicle injection rat group (Figure 7-2A-B).

While Phase 1 revealed that CFZ-HCl causes an inflammatory response, we decided to proceed with Phase 2, which specifically intended to explore whether CFZ-HCl microcrystal dissolution may ameliorate MSU crystal induced inflammation through a pH-dependent mechanism. Thus, in Phase 2 (main study), MSU microcrystals were mixed with the drug treatments, and 50 µl of the resulting mixture was injected into each knee (equivalent of approximately 2.67 mg and 1.34 mg of CFZ-HCl (Groups 4 and 5, respectively), 1.34 mg of DM (Groups 5 and 6); and/or 0.67 mg of MSU microcrystals per injection). Inflammation was monitored through various assays, including knee caliper differentials, Von Frey analysis, Gait analysis, and incapacitance testing, was performed 24 hours post injection.

The knee caliper measurements compared the size of the injected knee to the uninjected knee of an animal, making a knee caliper differential value. As the result, the knee caliper differentials were significantly increased from Day (-4) to Day (1) (Table 7-1) in rats treated with CFZ alone compared to vehicle control rats (Figure 7-3A). Interestingly, knee caliper differentials were significantly reduced on Day (1) (Table 7-1) in rats treated with CFZ + methylprednisolone or DepoMedrol alone compared to vehicle treated, control rats (Figure 7-3A). In other words, CFZ on its own caused significant knee swelling compare to the vehicle treated group; methylprednisolone injection completely inhibited the CFZ-HCl effect on knee swelling.

The Von Frey analysis uses a set of hair or fibers, which are small pieces of nylon rod that approximately 50 mm in length and of varying diameters, to test a rodent's sensitivity to a mechanical stimulus. In this test, the animal stands on an elevated mesh platform, and the Von Frey hairs are inserted through the mesh to poke the animal's hind paw to evaluate the animal's reactions. As a result, in rats treated with CFZ, Von Frey absolute thresholds were significantly decreased on Day (1) (Table 7-1) compared to vehicle treated rats, meaning that CFZ injection caused additional pain to the animals relative to the pain that was already caused by the MSU injection alone (Figure 7-3B). Nevertheless, methylprednisolone alone significantly increased Von Frey absolute thresholds on Day (1) after both MSU and CFZ-HCl crystal injection compared to vehicle control rats, suggesting that methylprednisolone treatment was the most effective in eliminating the pain in the knee from the MSU induced gout (Figure 7-3B).

Gait analysis is the systematic study of animal and human locomotion that is used to assess and treat the patients with conditions affecting their ability to walk. In this case, the gait (foot prints) score is used to determine how well the rat can walk 24 hour post the injection. As a

result, the gait scores were significantly increased in rats injected with CFZ-HCl microcrsytals alone compared to vehicle treated rats, meaning that CFZ-HCl microcrystal-induced inflammation interfered with the rat's ability to walk properly (Figure 7-3C). Corresponding with the gait studies, incapacitence tests were performed, utilizing force plates to measure how much force is exerted by each hind paws in the plexiglass housing. The change in hind paw weight distribution was determined by the difference in the amount of weight between the right and left limbs (expressed as a percent of the combined total). As a result, the difference in weight bearing between left and right knees in vehicle treated rats increased from a mean of 5.54 g on Day (-4) to 24.46 g on Day (1) following injection of MSU crystals alone. Left-right weight bearing differentials were significantly increased on Day (1) in rats injected with MSU and CFZ-HCl crystals in combination and were significantly reduced on Day (1) in rats treated with methylprednisolone (Figure 7-3D). Again, these results indicated that CFZ-HCl and MSU combinations did not improve the inflammatory response relative to the MSU-injected joints. Again, methylprednisolone injection inhibited the effects of CFZ-HCl and MSU injections on the gait and incapacitance assays.

On Day (1) (Table 7-1), the animals were necropsied, and the injected knees were subjected to histopathological analysis for inflammation, pannus, cartilage damage, and bone resorption. As the result, the vehicle treated rats had mild to moderate knee inflammation compared to control (uninjected) knees with no cartilage damage or bone resorption (Figure 7-4A-C). One of 8 vehicle treated animals had very minimal pannus formation with the remaining animals in the group having none. Rats treated with CFZ had marked to severe knee inflammation with none to very minimal pannus formation and cartilage damage and no bone resorption. In fact, cartilage damage scores were significantly increased in rats treated with CFZ

compared to vehicle treated rats. Rats treated with methylprednisolone had none to very minimal inflammation with no pannus formation, cartilage damage, or bone resorption (Figure 7-4A-B). Knee inflammation and summed scores were significantly reduced in rats treated with methylprednisolone compared to vehicle treated animals (Figure 7-4A-C). Rats treated with CFZ + methylprednisolone had knee histopathology that did not differ significantly from vehicle treated animals rats (Figure 7-4A-C). Overall, Phase 2 results further confirmed that CFZ injection alone caused more inflammation, pannus, and cartilage damage than the vehicle treated mice with MSU induced gout (Figure 7-4A-C). On the other hand, CFZ injection in combination with methylprednisolone showed very similar scores as methylprednisolone alone, further suggesting that Depomedrol inhibits the effects of CFZ-HCl and MSU injections.

To study the molecular signaling mechanisms underlying the inflammatory response induced by CFZ-HCl and MSU injections alone or in combination, TNFα and IL-1β were measured in both terminal serum and knee lavage samples. It has been shown that MSU crystals activate resident tissue macrophages, which secrete inflammatory cytokines including TNFα and IL-1β locally and then make their way to the systemic circulation [34, 35]. Although blood cytokines were not significantly altered in Phase 1 and 2 experiments regardless of the sample type (Figure 7-5A-D), TNFα and IL-1β concentrations were elevated in knee lavage samples from CFZ-HCl treated groups in Phase 1 and 2 (Figure 7-5C-D), paralleling the functional and histopathological results.

Next, the pH was measured in the knee lavage samples (Figure 7-6A). At 80 mgs/ml, CFZ-HCl microcrystals did not lead to a decrease in the pH of the joints (Figure 7-6A), suggesting that there are proton transport mechanisms in the synovium that lead to fast pH equilibration with the blood. On the other hand, methylprednisolone treatment with and without

CFZ actually made synovium more alkaline by increasing the pH to around 8.2 (Figure 7-6A), which only would stabilize the MSU crystals within synovium.

Lastly, the knee lavage samples were subjected to the microscopic analysis. By visual inspection, no MSU crystals were present in the joints and that CFZ-HCl crystals could be clearly observed within macrophages, based on the fluorescence signal in Cy5 channel (Figure 7-6B-C). Some of the CFZ-HCl crystals were destabilized in CFZ-HCl + methylprednisolone injections.

7.6 Conclusion

In conclusion, an intra-articular injection of CFZ-HCl microcrystals promoted inflammation in response to co-injection with MSU microcrystals, based on evaluation of animal knee swelling, behavioral testing, and joint histopathology. Glucocorticoid activation inhibited the inflammatory response resulting from both CFZ-HCl and MSU injections, alone and in combination, based on swelling, incapacitance, and pain analyses. These results were consistent with the pathological results as well as the measured cytokine changes in response to the various different treatments. Because there were no major changes in the pH of the joint induced by injection of CFZ-HCl, MSU or combination of the two, it was apparent that the inflammatory responses were not elicited by the acidity of microcrystalline or alkalinizing formulations on the local microenvironment. Instead, CFZ-HCl injected with MSU crystals led to increased macrophage recruitment, with phagocytosis of CFZ-HCl crystals and increased stabilization of phagocytosed CFZ-HCl crystals. Nevertheless, methylprednisolone decreased the number of visible CFZ-HCl microcrystals associated with macrophages in the joint, suggesting that the stabilization of the injected microcrystals within macrophages may be primary factor driving the inflammatory response.

7.7 Acknowledgements and Funding

The authors are thankful to the Bolder BioPath, Inc. for performing the animal studies.

This research was funded by the University of Michigan (Mi-Kickstart Award) and grants from the National Institutes of Health (NIH) (R01 GM078200 and R01 GM111400). The content is solely the responsibility of the authors and does not necessarily represent the official views of the National Institute of General Medical Sciences (NIGMS), National Cancer Institute (NCI), or the NIH.

7.8 Figures and Tables

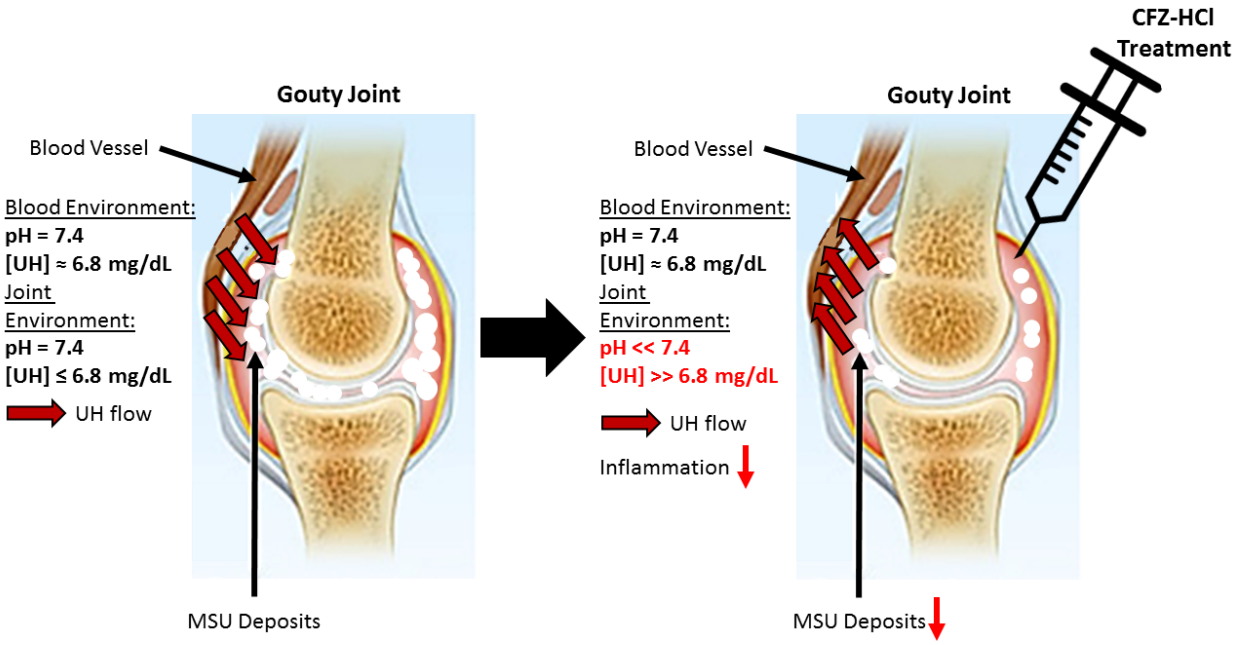

Figure 7-1. Study hypothesis schematic.

Table 7-1. Study calendar.

Mon	Tue	Wed	Thu	Fri	Sat	Sun
5/14/2018 Day (-15)	**5/15/2018 Day (-14)**	**5/16/2018 Day (-13)**	**5/17/2018 Day (-12)**	**5/18/2018 Day (-11)**	**5/19/2018 Day (-10)**	**5/20/2018 Day (-9)**
Distribute animals on arrival into groups for acclimation		Acclimate to VF Rack & IC Training	Grp 1-2: Inject CFZ / Vehicle Caliper Acclimate to VF Rack & IC Training	Grp 1-2: Caliper Acclimate to VF Rack & IC Training		
5/21/2018 Day (-8)	**5/22/2018 Day (-7)**	**5/23/2018 Day (-6)**	**5/24/2018 Day (-5)**	**5/25/2018 Day (-4)**	**5/26/2018 Day (-3)**	**5/27/2018 Day (-2)**
Grp 1-2: Inject CFZ / Vehicle* Caliper *Adjusted Dose	Grp 1-2: Caliper Necropsy			Grp 3-6: Randomize Baseline Caliper, VF, Gait, IC		
5/28/2018 Day (-1)	**5/29/2018 Day (0)**	**5/30/2018 Day (1)**	**5/31/2018 Day (2)**	**6/1/2018 Day (3)**	**6/2/2018 Day (4)**	**6/3/2018 Day (5)**
	Grp 3-6: Inject Test Article & MSU Caliper	Grp 3-6: Caliper VF Gait IC Necropsy	Grps 3-6: Inject MSU Caliper	Grp 3-6: Caliper VF Gait IC Necropsy		

Table 7-2. Groups and treatment information.

Group	N	MSU	Treatment	Dose Route	Dose Level (mg/mL)	Dose Vol.* (mg/mL)	Day 3 Reactivation
1	4	Vehicle	CFZ Vehicle	IA	--	--	--
2	4	Vehicle	CFZ	IA	80	50	--
3	8	Yes	CFZ Vehicle	IA	--	50	MSU
4	8	Yes	CFZ	IA	80	50	MSU
5	8	Yes	CFZ+DM	IA	40+40	50	MSU
6	8	Yes	DM	IA	40	50	MSU
*25 µl of 40 mg/ml MSU was mixed with 50 µl of treatment and only 50 µl of the total mixture was injected IA into the knee							
CFZ = Clofazimine; DM = Depo-Medrol; MSU = Monosodium Urate; IA = Intra-Articular							

Table 7-3. Gait evaluation scores.

Score	Meaning	Details
0	Normal	Approximately equal ink staining to normal paw
1	Slight limp/pain	Reduced inking area relative to the normal paw, but no full regions or structures are missing
2	Mild limp/pain	Print extends to the end or near to the end of the "curlicue" structure. If normal paw has very little heel staining (rat walks mainly on toes/ball of foot), then slightly less staining
3	Moderate limp/pain	Toes and full ball of foot, extending to the top of the "curlicue" structure are present. If normal paw has very little heel staining (rat walks mainly on toes/ball of foot), then toes with small portion of ball of foot
4	Marked limp/pain	Toes and partial ball of foot, no heel or posterior foot. If normal paw has very little heel staining (rat walks mainly on toes/ball of foot), then toes only
5	Severe limp/pain	Toes only, no ball of foot, no heel. If normal paw has very little heel staining (rat walks mainly on toes/ball of foot), then partial toes or non-specific marks
6	Hopping	Carrying leg, no footprint is evident

Table 7-4. Inflammation scores.

Score	Meaning	Details
0	Normal	--
0.5	Very Minimal	Generally focal or multifocal, very minor inflammation
1	Minimal	Multifocal, minor infiltration of inflammatory cells in synovium/periarticular tissue, no obvious distension of joint capsule
2	Mild	Diffuse mild infiltration of entire synovium, minor if any distension of joint capsule
3	Moderate	Moderate infiltration with moderate edema, diffuse with moderate distension of joint capsule usually on both medial and lateral sides
4	Marked	Marked infiltration and marked edema, diffuse with marked distension of joint capsule on both medial and lateral sides or may have just one side severely distended and the other is milder
5	Severe	Severe infiltration with severe edema, diffuse with severe distension of joint capsule on both medial and lateral sides
6	Very Severe	Very severe infiltration with very severe edema, diffuse with very severe distension of the joint capsule on both medial and lateral sides

The inflammatory infiltrate in rats with various types of arthritis consists of neutrophils and macrophages with smaller numbers of lymphocytes when the lesions are in the acute to subcute phase. Tissue edema and neutrophil exudates within the joint space are common in the acute to subacute phase. As the inflammation progresses to chronic, mononuclear inflammatory cells (monocytes, lymphocytes) predominate and fibroblast proliferation, often with deposition of metachromatic matrix, occurs in synovium and periarticular tissue. Exudate is less common in the joint space. Unless indicated in the comments area, the inflammation type is acute to subacute.

Table 7-5. Pannus scores.

Score	Meaning	Details
0	Normal	--
0.5	Very Minimal	Minimal infiltration of pannus in cartilage and subchondral bone, affects only marginal zones and affects only a few focal areas, less than 1% of area at risk affected
1	Minimal	Minimal infiltration of pannus in cartilage and subchondral bone, approximately 1–10% of cartilage surface or subchondral bone affected
2	Mild	Mild infiltration (extends over up to 1/4 of surface or subchondral area of tibia or femur), approximately 11–25% of cartilage surface or subchondral bone affected
3	Moderate	Moderate infiltration (extends over >1/4 but < 1/2 of surface or subchondral area of tibia or femur) approximately 26–50% of cartilage surface or subchondral bone affected
4	Marked	Marked infiltration (extends over 1/2 to 3/4 of tibial or femoral surface) approximately 51–75% of cartilage surface or subchondral bone affected
5	Severe	Severe infiltration approximately 76–100% of cartilage surface or subchondral bone affected

Table 7-6. Cartilage damage scores.

Score	Meaning	Details
0	Normal	--
0.5	Very Minimal	Minimal decrease in toluidine blue staining, affects only marginal zones
1	Minimal	Minimal to mild loss of toluidine blue staining with less than 1% cartilage loss on all combined surfaces
2	Mild	Mild loss of toluidine blue staining with focal mild (superficial) chondrocyte loss and/or collagen disruption, may have few small areas of 50% depth of cartilage affected, 1–10% cartilage loss on all combined surfaces
3	Moderate	Moderate loss of toluidine blue staining with multifocal to diffuse moderate (depth to middle zone) chondrocyte loss and/or collagen disruption, may have several areas of full thickness loss, 11–25% cartilage loss on all combined surfaces
4	Marked	Marked loss of toluidine blue staining with multifocal to diffuse marked (depth to deep zone) chondrocyte loss and/or collagen disruption, total overall loss 26–50% of all combined surfaces
5	Severe	Severe diffuse loss of toluidine blue staining with multifocal severe (depth to tide mark), total overall loss greater than 50% of width of all surfaces combined

Table 7-7. Bone resorption scores.

Score	Meaning	Details
0	Normal	--
0.5	Very Minimal	Minimal resorption affects only marginal zones, less than 1% of area at risk affected
1	Minimal	Small areas of resorption, not readily apparent on low magnification, approximately 1–10% of total joint width of subchondral bone affected
2	Mild	More numerous areas of resorption, definite loss of subchondral bone, approximately 11–25% of total joint width of subchondral bone affected
3	Moderate	Obvious resorption of subchondral bone approximately 26–50% of total joint width of subchondral bone affected
4	Marked	Obvious resorption of subchondral bone approximately 51–75% of total joint width of subchondral bone affected
5	Severe	Distortion of entire joint due to destruction approximately 76–100% of total joint width of subchondral bone affected

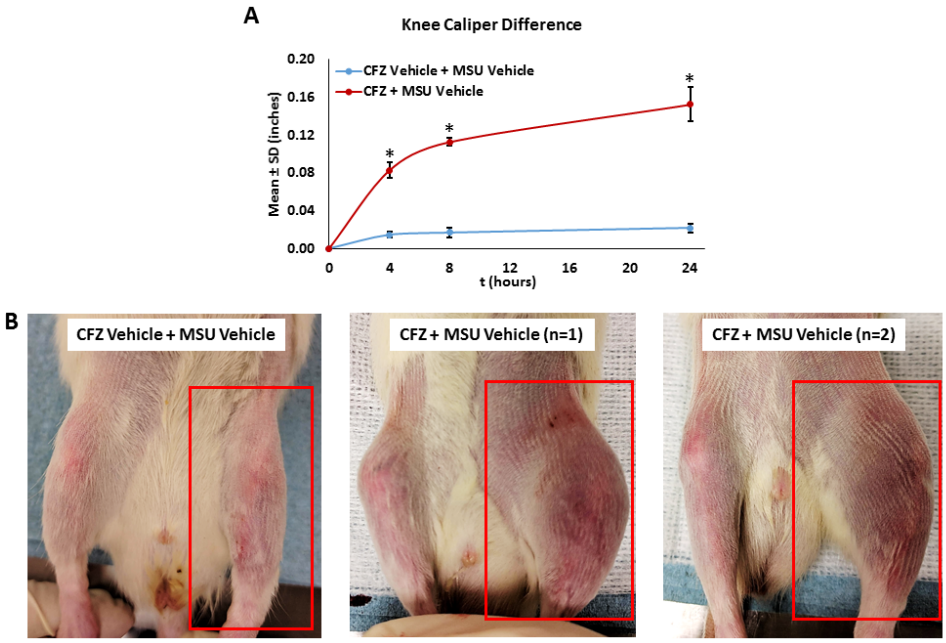

Figure 7-2. Phase 1 (Grp 1-2) – results. Knee caliper difference (**A**) and pictures (**B**) of the injected knees.

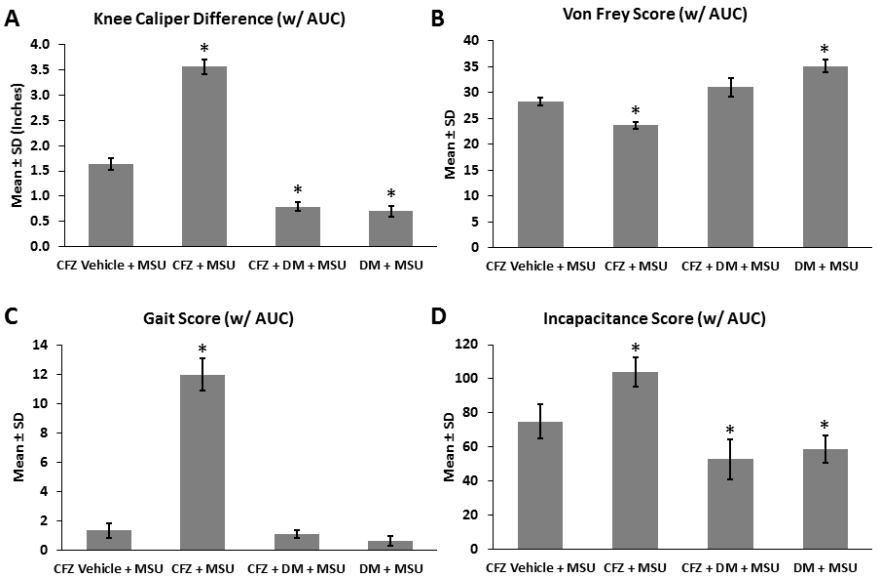

Figure 7-3. Phase 2 (Grp 3-6) – observational results. Knee caliper difference (**A**), Von Frey analysis (**B**), Gait analysis (**C**), and incapacitance scores (**D**).

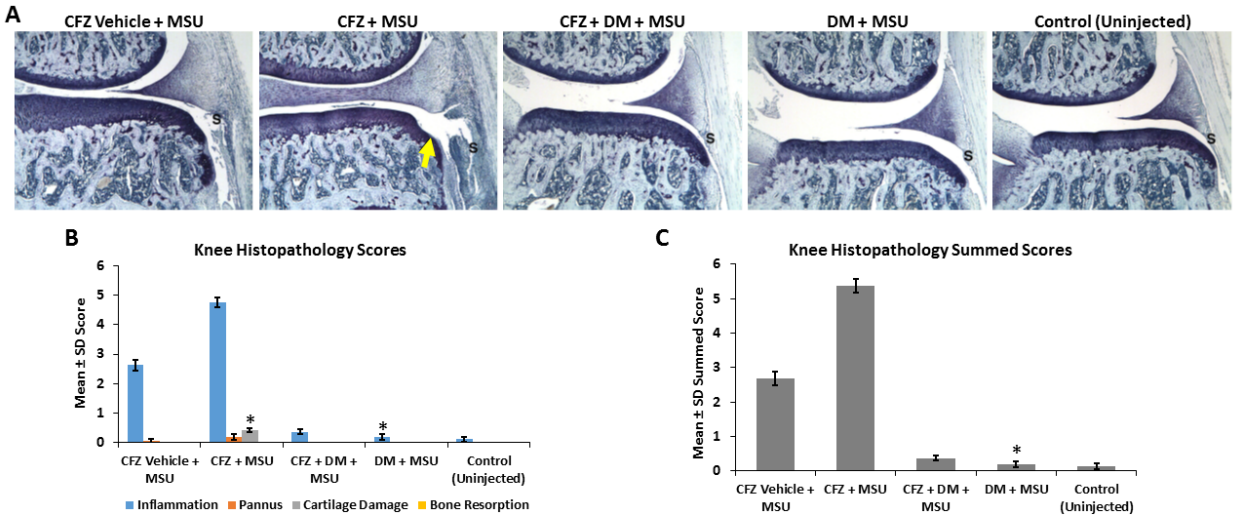

Figure 7-4. Phase 2 (Grp 3-6) – histopathological results. Histopathology photomicrographs (**A**) and inflammation, pannus, cartilage damage and bone resorption individual (**B**) and summed (**C**) scores.

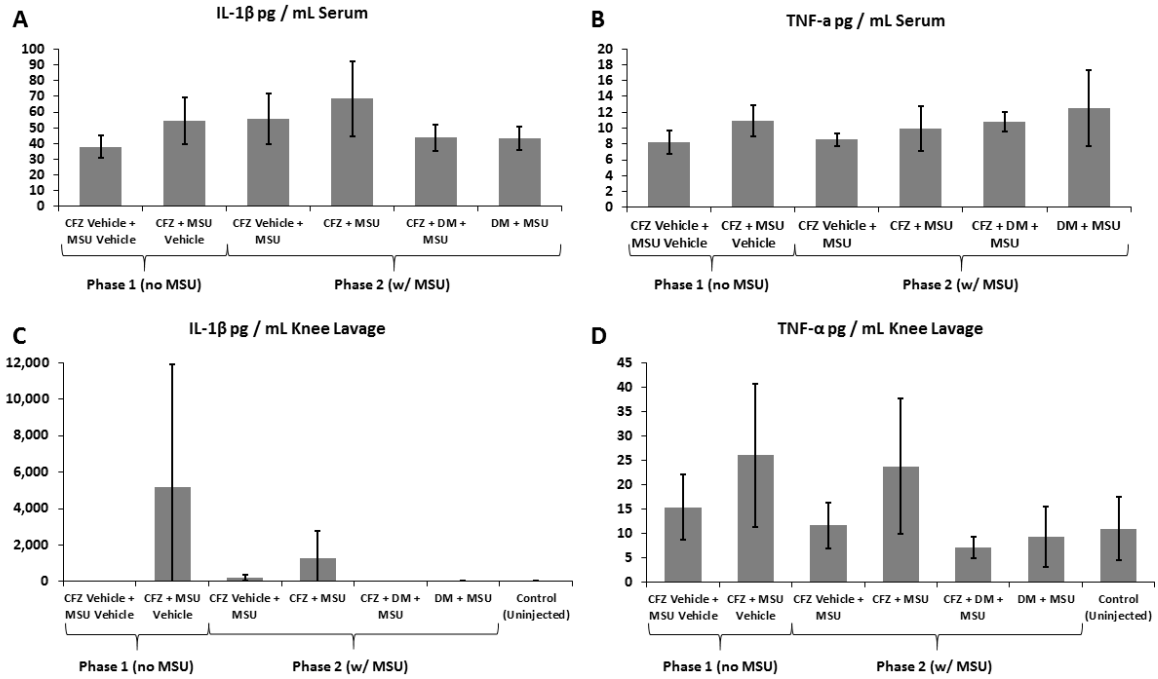

Figure 7-5. Phase 1 (Grp 1-2) and Phase 2 (Grp 3-6) cytokine measurements. Terminal serum (**A,B**) and knee lavage (**C,D**) IL-1β and TNF-α concentrations.

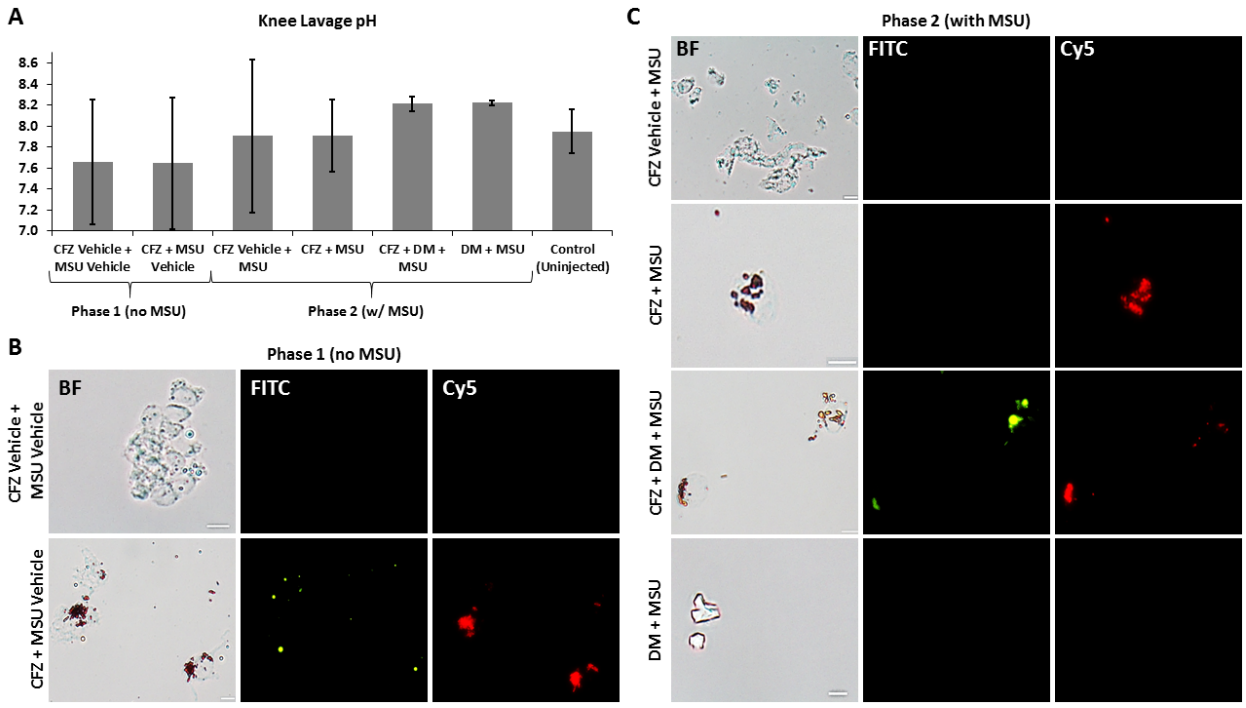

Figure 7-6. Phase 1 (Grp 1-2) and Phase 2 (Grp 3-6) pH and microscopic analysis of the knee lavage samples. The pH of knee lavage samples from Phase 1 and Phase 2 (**A**). Microscopic analysis of the knee lavage sample from Phase 1 (**B**) and Phase 2 (**C**). Scale bar = 10 µm.

7.9 References

1. Martillo, M.A., L. Nazzal, and D.B. Crittenden, *The crystallization of monosodium urate.* Curr Rheumatol Rep, 2014. **16**(2): p. 400.

2. Lawrence, R.C., et al., *Estimates of the prevalence of arthritis and other rheumatic conditions in the United States. Part II.* Arthritis Rheum, 2008. **58**(1): p. 26-35.

3. Roddy, E. and M. Doherty, *Epidemiology of gout.* Arthritis Res Ther, 2010. **12**(6): p. 223.

4. Choi, H.K., et al., *Pathogenesis of gout.* Ann Intern Med, 2005. **143**(7): p. 499-516.

5. Wu, X.W., et al., *Two independent mutational events in the loss of urate oxidase during hominoid evolution.* J Mol Evol, 1992. **34**(1): p. 78-84.

6. Wu, X.W., et al., *Urate oxidase: primary structure and evolutionary implications.* Proc Natl Acad Sci U S A, 1989. **86**(23): p. 9412-6.

7. Oda, M., et al., *Loss of urate oxidase activity in hominoids and its evolutionary implications.* Mol Biol Evol, 2002. **19**(5): p. 640-53.

8. Huang, H.Y., et al., *The effects of vitamin C supplementation on serum concentrations of uric acid: results of a randomized controlled trial.* Arthritis Rheum, 2005. **52**(6): p. 1843-7.

9. Sebesta, I., *Genetic disorders resulting in hyper- or hypouricemia.* Adv Chronic Kidney Dis, 2012. **19**(6): p. 398-403.

10. Richette, P. and T. Bardin, *Gout.* Lancet, 2010. **375**(9711): p. 318-28.

11. Oliviero, F., A. Scanu, and L. Punzi, *Metabolism of crystals within the joint.* Reumatismo, 2012. **63**(4): p. 221-9.

12. *Transparency Market Research. Gouty Arthritis Market - Global Industry Analysis, Size, Share, Growth, Trends and Forecast 2016 - 2024.*

13. Cholo, M.C., et al., *Clofazimine: current status and future prospects.* J Antimicrob Chemother, 2012. **67**(2): p. 290-8.

14. Barry, V.C., et al., *A new series of phenazines (rimino-compounds) with high antituberculosis activity.* Nature, 1957. **179**(4568): p. 1013-5.

15. World Health Organization. *Leprosy Report*. 2014 [cited 2016 Aug 16]; Available from: http://www.who.int/mediacentre/factsheets/fs101/en.

16. Arbiser, J.L. and S.L. Moschella, *Clofazimine: a review of its medical uses and mechanisms of action.* J Am Acad Dermatol, 1995. **32**(2 Pt 1): p. 241-7.

17. Tyagi, S., et al., *Clofazimine shortens the duration of the first-line treatment regimen for experimental chemotherapy of tuberculosis.* Proc Natl Acad Sci U S A, 2015. **112**(3): p. 869-74.

18. Lechartier, B. and S.T. Cole, *Mode of Action of Clofazimine and Combination Therapy with Benzothiazinones against Mycobacterium tuberculosis.* Antimicrob Agents Chemother, 2015. **59**(8): p. 4457-63.

19. Williams, K., et al., *Sterilizing activities of novel combinations lacking first- and second-line drugs in a murine model of tuberculosis.* Antimicrob Agents Chemother, 2012. **56**(6): p. 3114-20.

20. Dooley, K.E., et al., *World Health Organization group 5 drugs for the treatment of drug-resistant tuberculosis: unclear efficacy or untapped potential?* J Infect Dis, 2013. **207**(9): p. 1352-8.

21. Gopal, M., et al., *Systematic review of clofazimine for the treatment of drug-resistant tuberculosis.* Int J Tuberc Lung Dis, 2013. **17**(8): p. 1001-7.

22. Sukpanichnant, S., et al., *Clofazimine-induced crystal-storing histiocytosis producing chronic abdominal pain in a leprosy patient.* Am J Surg Pathol, 2000. **24**(1): p. 129-35.

23. Belaube, P., et al., *Small bowel deposition of crystals associated with the use of clofazimine (Lamprene) in the treatment of prurigo nodularis.* Int J Lepr Other Mycobact Dis, 1983. **51**(3): p. 328-30.

24. Baik, J., et al., *Multiscale distribution and bioaccumulation analysis of clofazimine reveals a massive immune system-mediated xenobiotic sequestration response.* Antimicrob Agents Chemother, 2013. **57**(3): p. 1218-30.

25. Baik, J. and G.R. Rosania, *Macrophages sequester clofazimine in an intracellular liquid crystal-like supramolecular organization.* PLoS One, 2012. **7**(10): p. e47494.

26. Baik, J. and G.R. Rosania, *Molecular imaging of intracellular drug-membrane aggregate formation.* Mol Pharm, 2011. **8**(5): p. 1742-9.

27. Keswani, R.K., et al., *Chemical Analysis of Drug Biocrystals: A Role for Counterion Transport Pathways in Intracellular Drug Disposition.* Mol Pharm, 2015. **12**(7): p. 2528-36.

28. Yoon, G.S., et al., *Clofazimine Biocrystal Accumulation in Macrophages Upregulates Interleukin 1 Receptor Antagonist Production To Induce a Systemic Anti-Inflammatory State.* Antimicrob Agents Chemother, 2016. **60**(6): p. 3470-9.

29. Yoon, G.S., et al., *Phagocytosed Clofazimine Biocrystals Can Modulate Innate Immune Signaling by Inhibiting TNFalpha and Boosting IL-1RA Secretion.* Mol Pharm, 2015. **12**(7): p. 2517-27.

30. FDA, *Inactive Ingredient Search for Approved Drug Products*. 2018, FDA/Center for Drug Evaluation and Research

31. Bove, S.E., et al., *Weight bearing as a measure of disease progression and efficacy of anti-inflammatory compounds in a model of monosodium iodoacetate-induced osteoarthritis.* Osteoarthritis Cartilage, 2003. **11**(11): p. 821-30.

32. Murashov, M.D., et al., *The Physicochemical Basis of Clofazimine-Induced Skin Pigmentation.* J Invest Dermatol, 2017. **138**(3): p. 697-703.

33. Rzeczycki, P., et al., *Detecting ordered small molecule drug aggregates in live macrophages: a multi-parameter microscope image data acquisition and analysis strategy.* Biomed Opt Express, 2017. **8**(2): p. 860-872.

34. Busso, N. and A. So, *Microcrystals as DAMPs and their role in joint inflammation.* Rheumatology (Oxford), 2012. **51**(7): p. 1154-60.

35. Martinon, F., et al., *Gout-associated uric acid crystals activate the NALP3 inflammasome.* Nature, 2006. **440**(7081): p. 237-41.

Chapter 8

Conclusions and Future Outlook

8.1 CFZ-induced skin pigmentation is associated with CFZ free base, not CFZ-HCl salt.

First, by using experimental and computational approaches, we probed the relationship between the biological mechanisms mediating lysosomal ion homeostasis and the self-assembly of a weakly basic small molecule building block (e.g. CFZ) into a functional, mechanopharmaceutical device (CFZ-HCl salt form) in macrophage lysosomes. Physicochemical considerations indicate that the intralysosomal stabilization of the self-assembled mechanopharmaceutical device depends on the pH_{max} of the weakly basic building block and its affinity for chloride, both of which are consistent with the pH and chloride content of a physiological lysosomal microenvironment. Most importantly, *in vitro* and *in silico* studies revealed that high expression levels of the V-ATPase, irrespective of the expression levels of chloride channels, are necessary and sufficient to explain the cell-type dependent formation, stabilization, and biocompatibility of the self-assembled mechanopharmaceutical device within macrophages. Moreover, to accommodate increasingly massive loads of cargo, macrophages increase in numbers and adapt their intracellular membrane organization to expand the intracellular cargo space.

To test whether CFZ-induced skin pigmentation is due to CFZ-HCl formation and accumulation, I identified a closely related CFZ analog that does not precipitate under physiological pH and chloride conditions that are required for CFZ-HCl accumulation and

stabilization. As a result, despite the absence of detectable Cy5(+) CFZ-HCl salt form in mice, administration of this analog still led to significant skin pigmentation. In CFZ treated mice, skin cryosections revealed no evidence of CFZ-HCl when analyzed with a microscopic imaging system specifically designed for detecting CFZ aggregates. Rather, the reflectance spectra of the skin revealed a signal corresponding to the soluble, free base form of the drug. Consistent with the low concentrations of CFZ in the skin, these results suggested that CFZ-induced skin pigmentation is not due to CFZ precipitation and CFZ-HCl formation and accumulation, but rather to the partitioning of the circulating, free base form of the drug into subcutaneous fat.

8.2 Biomimetic formulation of micronized CFZ-HCl crystals are stable under lysosomal conditions *in vitro* and *in vivo*

First, in order to distinguish between the potential adverse effects of insoluble drug biocrystals (e.g. Cy5(+) CFZ-HCl salt form) from those of the soluble molecules (CFZ free base), we designed an experimental strategy to compare how the accumulation of insoluble drug biocrystals might influence the immune signaling response of macrophages in live mice. Accordingly, we tested the specific hypothesis that CFZ biocrystals that accumulate in resident tissue macrophages can modulate (or activate) these cells' inflammatory signaling pathways *in vivo* that lead to systemic changes in the inflammatory response. By assessing tumor necrosis factor alpha (TNF-α) and IL-1 receptor antagonist (IL-1RA) expression, as well as Casp 1 and IL-1β maturation, in the vital organs and blood of CFZ-treated mice, the results demonstrated that CFZ biocrystals in macrophages, but not the soluble form (e.g. CFZ free base), are specifically associated with an IL-1RA-mediated anti-inflammatory response.

Knowing that CFZ drug biocrystals (e.g. Cy5(+) CFZ-HCl salt) are biocompatible, stable, long-lived, relatively non-toxic, and have anti-inflammatory properties, I developed a

biomimetic formulation of CFZ-HCl microcrystals. Based on the *in vitro* and *in vivo* data, micronized CFZ-HCl crystals were ingested by tissue macrophages and accumulated in liver and spleen, similar to CFZ biocrystals. In mice, IV injection of these biomimetic CFZ-HCl microcrystals led to visible drug accumulation in macrophages of the reticuloendothelial system with minimal skin accumulation or pigmentation. In fact, no skin pigmentation was observed when the total amount of CFZ-HCl administered was equivalent to the total oral dose leading to maximal skin pigmentation. Furthermore, IV administration did not result in overt toxicity and did not induce measurable changes in acute inflammatory response biomarkers. The anti-inflammatory cytokine, IL-1RA, which was previously shown to be elevated following oral administration of CFZ, was not changed by the injected CFZ-HCl microparticles. My findings support additional studies into the possible use of parenteral (injected or inhaled) CFZ-HCl as means to circumvent the skin pigmentation side effect of the oral CFZ administration. For example, an inhalable, aerosolized formulation of CFZ-HCl may be a good strategy for treating MDR-TB.

8.3 Local administration of biomimetic formulation of CFZ-HCl microcrystals *in vivo* leads to the recruitment of macrophages to the site of action, a pro-inflammatory response.

Since the biomimetic formulation of CFZ-HCl microcrystals proved suitable for parenteral administration without major toxicological consequences, I decided to determine its efficacy in one of possible indications – gout, most common inflammatory, crystal-induced arthropathy. Specifically, I studied whether the inflammatory response induced by MSU crystals directly injected into joints may be related to their alkalinizing effect on the local microenvironment or to their impact on macrophage recruitment. For this purpose, CFZ-HCl microcrystals were injected into the rat knee, alone or in combination with MSU crystals. As a

hypothesis, the micronized CFZ-HCl particles should lower the pH of the synovium upon dissolution, facilitating the dissolution and clearance of MSU crystals from the joint and reducing their alkalinizing effects. Contrary to my expectations, the results indicated that CFZ-HCl injections significantly increased the severity of the inflammatory response induced by co-injecting MSU microcrystals. This strong inflammatory response was attributed to increased macrophage recruitment from local CFZ-HCl treatment. Furthermore, treatment with methylprednisolone, reduced both CFZ- and MSU-induced inflammation, while destabilizing the CFZ-HCl microcrystals through increased alkalization. Because methylprednisolone is known to inhibit macrophage migration, I infer that macrophages exacerbate joint inflammation by stabilizing injected microcrystals; by reducing macrophage recruitment, methylprednisolone decreased injected microcrystal stability and lessened the inflammatory response.

Overall, the results of this study suggest that my formulation is not suitable for gouty arthritis and increases the severity of the local inflammatory response by facilitating macrophage recruitment, which can be explained by liver granulomas with macrophage recruitment around Cy5(+) CFZ-HCl precipitates in Chapter 2. Even though CFZ-HCl is associated with the systemic anti-inflammatory activity in Chapter 2, I now know that CFZ-HCl also exerts local pro-inflammatory effects at the site of action. Even though the results of this study suggested that my formulation is not suitable for gouty arthritis, further investigation is required to determine efficacy and anti-inflammatory action of my formulation in MDR-TB and other potential new indications.

8.4 Final Notes

The science and methodology portrayed in this dissertation can and should be applicable to the study of the accumulation, reformulation, and immunological side effects of other weakly

basic drugs. For example, amiodarone and nilotinib are also weak bases that accumulate and even precipitate out in macrophages. There are also at least a dozen of other drugs that lead to formation of granulomas in liver. One should investigate if these drugs are precipitating out due to stabilization of a specific ionized form by monitoring the protonation state of drugs using the novel methodology discussed in this thesis (e.g. Raman, ^{1}H-NMR, etc) and not necessarily have to rely on fluorescence techniques to distinguish between ionized forms that may accumulate in cells or tissues.

Overall, this dissertation augments the understanding of drug distribution and mechanism of action by effectively demonstrating how it is possible to distinguish the differential contribution of different ionization states of a drug (e.g. CFZ) to the drug's efficacy and toxicity properties. Furthermore, this dissertation has advanced the rational design of formulations, in terms of being the first to develop a biomimetic form of a small molecule drug and demonstrating how the role of macrophages in determining the stability of biomimetic formulations can be probed.

Appendices

Appendix A

Supporting Information in Chapter 2

A.1 Supplemental Materials and Methods

Mouse bronchoalveolar lavage (BAL) harvest

PBS/LPS-instilled and CFZ-treated or control mice were euthanized by exsanguination while deeply anesthetized with an intraperitoneal injection of ketamine/xylazine (100 mg/kg, 10 mg/kg). The trachea was surgically exposed and cannulated with an 18G needle and the lungs were lavaged by instilling 1 ml DPBS (Life Technologies, Carlsbad, CA) containing 0.5 mM EDTA (Sigma, St. Louis, MO). The retrieved BAL was then centrifuged (10 min at 400 x *g*, 4°C), and the supernatant was frozen (-80 °C), while the cell pellets were resuspended in 1 ml RPMI 1640 media (Life Technologies). To count total cells, the cells were stained with Trypan blue and counted using a hemocytometer.

Immunohistochemistry and imaging

After euthanasia with ketamine/xylazine and exsanguination, the liver, spleen and kidneys were removed *en bloc* and the lungs were inflated with 0.8 ml (50% OCT, 15% sucrose in PBS) and frozen in Tissue-Plus OCT compound (Fisher HealthCare, Houston, TX). Tissue blocks were sectioned at a thickness 6 μm, using Leica 3050S cryostat. For immunohistochemistry, sections were fixed in 4% paraformaldehyde for 10 min, blocked for 2 h and incubated with primary antibody at 1 ug/ml overnight (4°C) followed by HRP-conjugated secondary antibody for 1 h, DAB substrate incubation (intelliPATH FLX DAB chromogen kit,

Biocare Medical, Concord, CA) and hematoxylin counterstain. For fluorescence immunostaining, FITC-conjugated secondary antibody (Sigma) was incubated for 1 h, and Hoechst 33342 (Life Technologies) was used for nuclear detection. Non-fluorescence staining was performed by the Pathology Core for Animal Research (PCAR) in the Unit for Laboratory Animal Medicine (ULAM) at the University of Michigan. Sections were mounted on glass slides with ProlongGold (Life Technologies). Brightfield and fluorescence (DAPI, FITC and Cy5) images were acquired using the Nikon Eclipse Ti (Japan) inverted microscope equipped with a Nikon Digital Sight DS-Fi2 camera (Japan) for brightfield and Photometrics Coolsnap Myo camera (Tucson, AZ) for fluorescence.

SDS-PAGE and Western Blot

Harvested organs were washed in ice-cold DPBS and homogenized by sonication in radioimmunoprecipitation assay (RIPA) buffer (Sigma). Halt protease and phosphatase inhibitor cocktail and 0.5 M EDTA (Thermo Pierce) were added to the RIPA buffer (1:100 dilutions) before use. The protein concentration in homogenates was determined with a BCA assay (Thermo Pierce) and equal amounts of total protein were suspended in 4x sample buffer (Bio-Rad, Hercules, CA) and heated (4 min at 94°C). Proteins were separated by SDS-PAGE in 4-15% or 4-20% bis-acrylamide gels (Bio-Rad) and electroblotted onto PVDF membranes (Millipore, Billerica, MA) using the Criterion system (Bio-Rad). After blocking for 1 h in Tris-buffered saline/Tween (TBST, pH 7.6; 20 mM Tris-HCl, 150 mM NaCl, and 0.05% Tween20) containing 5% nonfat milk (Meijer), the blots were probed with primary antibodies diluted in 5% BSA or 5% nonfat milk overnight at 4°C. The membranes were washed with TBST and incubated with a 1:2000 dilution of HRP-conjugated anti-rabbit secondary antibodies (Millipore)

for 1 h at room temperature. Protein bands were visualized on X-ray film (Thermo) using chemiluminescence (Supersignal reagents; Pierce).

Equation for Mouse Terminal Endpoint Assessment

$$D_{LPS-\overline{PBS}} = \sqrt{(o_{LPS} - \bar{o}_{PBS})^2 + (w_{LPS} - \bar{w}_{PBS})^2 + (t_{LPS} - \bar{t}_{PBS})^2}$$

$D_{LPS-\overline{PBS}}$: total distance between LPS-instilled mouse and mean of PBS-instilled mice

$\bar{o}_{PBS}$: mean oxygen saturation change of PBS-instilled mice

o_{LPS}: oxygen saturation change of LPS-instilled mouse

$\bar{w}_{PBS}$: mean weight change of PBS-instilled mice

w_{LPS}: weight change of LPS-instilled mouse

$\bar{t}_{PBS}$: mean temperature change of PBS-instilled mice

t_{LPS}: temperature change of LPS-instilled mouse

- All changes represent percent changes from day 0 baseline measurements

A.2 Supplemental Figures and Tables

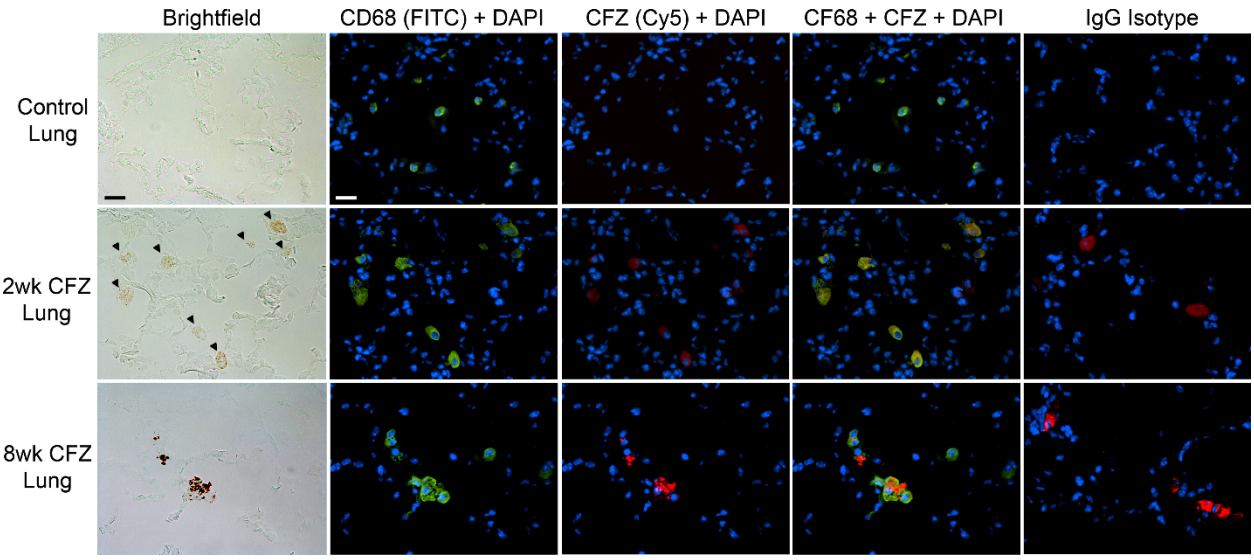

Figure S2-1. Clofazimine (CFZ) bioaccumulation and crystal formation in the lung occurs after 2 weeks in CD68 (+) macrophages. Representative brightfield and fluorescence (FITC for CD68 and Cy5 for CFZ) images of lung sections from control mice and mice treated with CFZ for 2 and 8 weeks. In the lung, CFZ can be seen accumulating inside macrophages after 2 week CFZ treatment with no crystallization (arrowhead). At 8 weeks, CFZ crystals can be seen located inside macrophages. Scale bar = 10 μm.

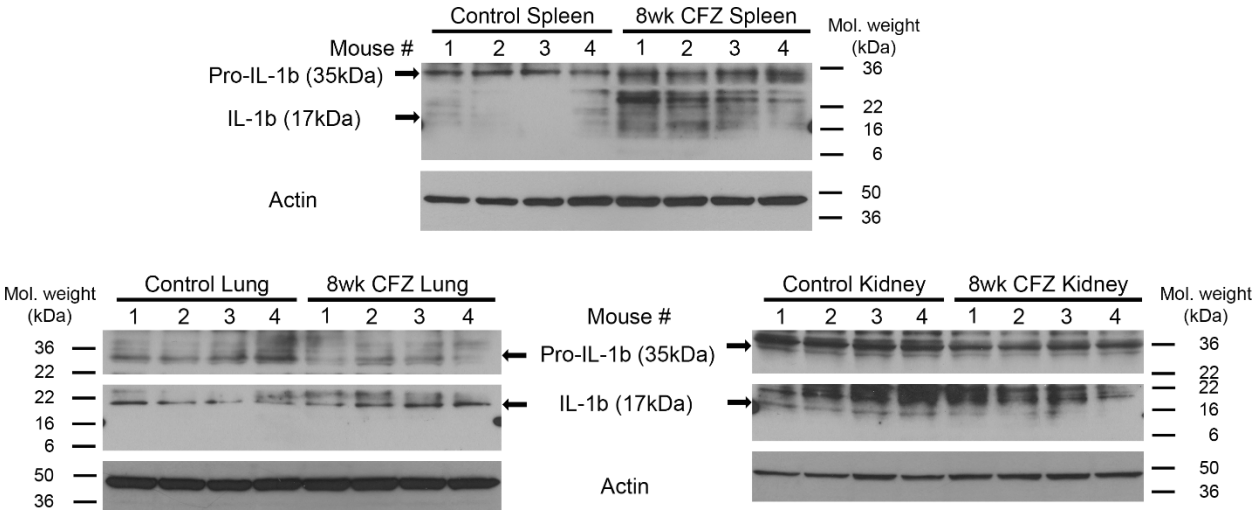

Figure S2-2. Clofazimine (CFZ) bioaccumulation does not affect IL-1β cleavage in the spleen, lung or kidney. Western blots of spleen, lung and kidney homogenates showing that IL-1β cleavage was not altered after 8 weeks of CFZ treatment.

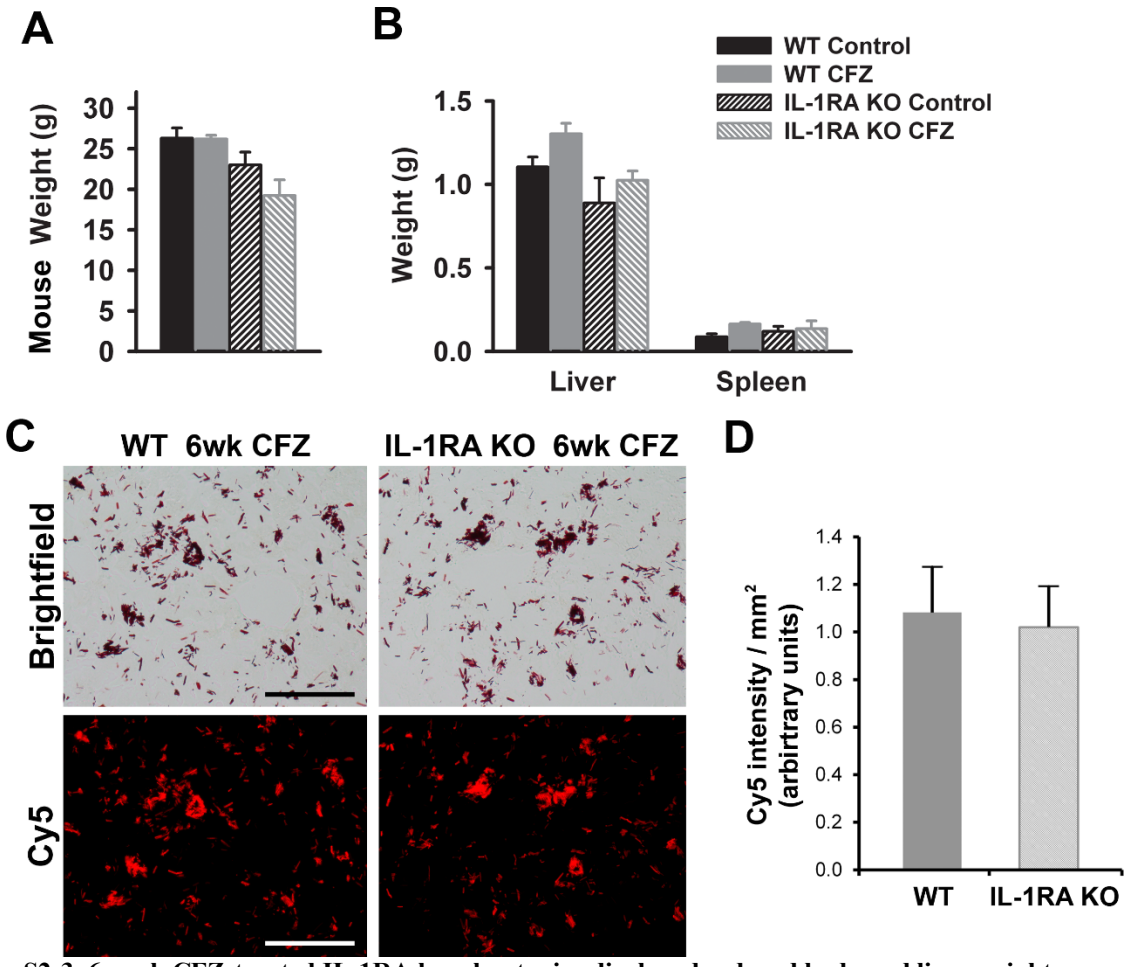

Figure S2-3. 6 week CFZ-treated IL-1RA knockout mice displayed reduced body and liver weights compared to control diet wildtype mice. (**A**) 6 week CFZ-treated IL-1RA knockout (KO) mice show reduced body weight compared to control diet treated littermates and wildtype (WT) mice. (**B**) IL-1RA KO mice display reduced liver weight compared to WT, but spleen are comparable. (**C**) Representative brightfield and fluorescence (Cy5 for crystalline CFZ) images of liver sections from WT and IL-1RA KO mice treated with CFZ for 6 weeks. Scale bar = 100 µm. (**D**) Cy5 fluorescence intensity values of liver sections from WT and IL-1RA KO and CFZ-treated mice. Data are the mean ± S.D. of 4 images. Scale bar = 100 µm.

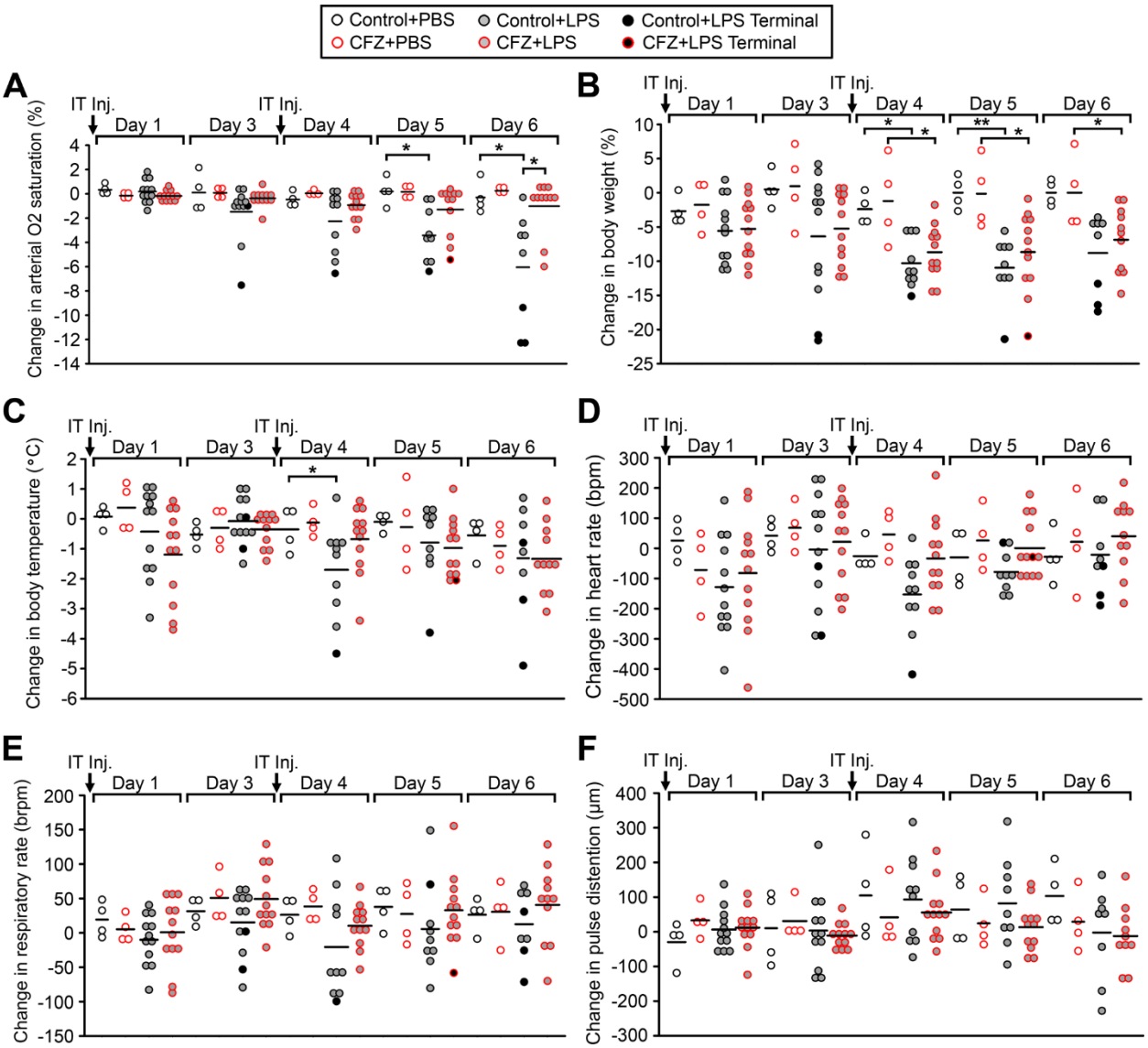

Figure S2-4. Daily monitoring of changes in bodily functions in 8 week CFZ-treated and control mice after PBS or LPS-induced acute lung injury. Daily monitoring of changes in arterial oxygen saturation (**A**), body weight (**B**), temperature (**C**), heart rate (**D**), respiratory rate (**E**), and pulse distention (**F**) in 8 week CFZ-treated and control mice after PBS (white circle) or LPS (grey circle)-induced acute lung injury. Control mice lung function progressively deteriorated at a higher rate than CFZ-treated mice as CFZ-treated mice displayed higher arterial oxygen levels at day 5 and day 6 (**A**). Control mice injected with LPS lost weight more rapidly compared to CFZ-treated mice (**B**). CFZ-treated mice were more resistant to hypothermia (**C**), drop in heart rate (**D**) and respiratory rate (**E**) after the second LPS injection compared to control-mice (day 4). Data is the compilation of two separate experiments and presented as mean ± S.D. (PBS n=4, LPS n=12). Black dots represent mice that reached terminal endpoint and were euthanized. One-way ANOVA was used to compare changes in parameters between control vs CFZ-treated mice with PBS or LPS injections per timepoint and $p \leq 0.05$ was considered statistically significant. *$p \leq 0.05$, **$p \leq 0.01$.

Table S2-1. Vital signs of control and clofazimine-treated mice (8 week treatment).

Vital signs	Control diet treated (n=16)	CFZ treated (n=16)	P value
Weight (g ± S.D.)	26.13 ± 1.49	24.39 ± 1.92	0.008
Body Temperature (°C ± S.D.)	35.30 ± 0.54	35.52 ± 0.76	0.35
Arterial O_2 Saturation (% ± S.D.)	97.52 ± 0.76	99.01 ± 0.24	0.00000064
Respiratory rate (brpm ± S.D.)	172.85 ± 18.25	154.29 ± 19.43	0.009
Heart rate (bpm ± S.D.)	632.91 ± 89.55	573.94 ± 85.28	0.066
Pulse distention (μm ± S.D)	512.22 ± 60.35	425.57 ± 52.32	0.00015

P values were calculated using Student's t-test (two-way, unpaired)

Appendix B

Supporting Information in Chapter 3

B.1 Supplementary methods

HPLC analysis

For the HPLC assay, the mobile phase was methanol:water (80:20) with 0.1% trifluoroacetic acid (1 ml/min flow rate). The stationary phase (column) was a C18 (unbonded silica particles) column (Atlantis® T3, 5 μm, 100Å), and the HPLC was equipped with a UV detector (Waters, Photodiode Array Detector 2996) @ 285 nm detection for CFZ. The retention time for CFZ was determined to be 4.75 min.

Determination of solubility parameters

We used a mathematical proof approach to determine $[CFZH^+]_S$ as detailed below:

First, we calculated $[CFZH^+]$ using the total solubility (S_T) at each pH value and the constant intrinsic free base solubility, $[CFZ]_S$, using the following equation, which was obtained by rearranging the terms in equation (14) (see main article):

$$[CFZH^+] = S_T - [CFZ]_S \qquad \text{(Supplementary Equation 1)}$$

Then, we chose a value, say "y", from the list of the computed $[CFZH^+]$ values, and let "y" equal $[CFZH^+]_S$. By substituting "y' in place of $[CFZH^+]_S$, we calculated for total solubility at the different pH values using equation (15) (see main article). Then, we compared this total solubility-pH dataset to that obtained using equation (13) (see main article). Then, we checked if there was the same total solubility value at a given pH in both datasets, which would represent

the intersection point of the two solubility-pH curves mentioned previously. This can be represented by the following equation:

$S_T' = [CFZ]_S + [CFZH^+]_S$ (Supplementary Equation 2)

Where S_T' is the total solubility value at the intersection of the two solubility-pH curves, and both forms of the drug, CFZ and $CFZH^+$, are present in equilibrium with their respective solid forms in the solid phase denoted by the subscript *s*.

Moreover, to prove if our earlier assumption ("y" is equal to $[CFZH^+]_S$) was valid, we calculated the total solubility by plugging "y" in place of $[CFZH^+]_S$, supplementary equation (2), and checked if it was equal to S_T'. Furthermore, by definition, the pH where both the intrinsic free base and salt forms of the drug are in the solid phase is known as pH_{max}. Thus, the pH associated with S_T' was deduced to be pH_{max}.

Modeling proton influx

V-ATPase is an electrogenic proton-pump, which inserts protons from the cytoplasm into the lysosome against an electrochemical gradient upon ATP hydrolysis [1, 2]. The rate at which a proton molecule is inserted per second (J_{HVATP}) was obtained from published experimental studies [2] as a function of transmembrane pH gradient (Δ pH) in units of pH unit and membrane potential difference, which is also interchangeably known as membrane potential (ΔΨ), in units of mV. This rate was multiplied by the total number of active V-ATPase molecules per lysosome (N_{VATP}) to obtain the total amount of proton molecules inserted into the lysosome in units of molecules per second, as follows:

$H_{pump} = N_{VATP} \times J_{HVATP}(\Delta pH, \Delta \Psi)$ (Supplementary Equation 3)

Where lysosomal ΔΨ is dictated by the total net change in lysosomal ion content and is represented by the following relationship [3]:

$$\Delta \Psi = (F \times V_L) / (C' \times S) \times [(\Sigma_i Z_i [\text{cations}]_i + \Sigma_i Z_i [\text{anions}]_i) - B] \quad \text{(Supplementary Equation 4)}$$

Where V_L is the lysosomal volume in units of L; Faraday's constant (F) which equals 96485 Coulomb/mol and is used to convert the lysosomal ion content in units of moles to units of Coulomb; C' is the specific membrane capacitance per unit area of a biological membrane, which is experimentally approximated to be 1 μF/cm2 and is multiplied by the lysosomal surface area S represented in units of cm^2 to obtain the total lysosomal membrane capacitance; Z_i is valence for ion i; [cation] the concentration of cation i at a given time *t* in units of Molar; [anion] is the concentration of anion i at a given time *t* in units of Molar; B is the Donnan particles in units of Molar, which are impermeable lysosomal contents defined by initial lysosomal ion concentrations and net change in the intrinsic surface potentials, supplementary equation (5). In the model and simulations communicated herein, the initial lysosomal ions consist of proton, potassium, sodium, and chloride with their respective charge (+ or -1) represented as a coefficient of their respective concentration, which is denoted by the square brackets, supplementary equation (5).

$$B = [H^+]_{L,initial} + [K^+]_{L,initial} + [Na^+]_{L,initial} - [Cl^-]_{L,initial} - (C \times S) / (F \times V_L) \times \{(\Psi_{in} - \Psi_{out}) + \Psi_{initial}\} \quad \text{(Supplementary Equation 5)}$$

Where Ψ_{in} and Ψ_{out} are the intrinsic inner and outer surface potentials, respectively, in units of mV, which contribute to the change in ion concentration at membrane surface as described later, $\Psi_{initial}$ is the initial lysosomal membrane potential which is set to zero mV in order to maintain initial lysosomal membrane electroneutrality.

Modeling chloride influx

V-ATPase mediated proton influx into the lysosome is followed by lysosomal membrane potential increase which consequentially arrests further proton influx. Thus, to lower the

membrane potential for the continuation of V-ATPase proton-pumping activity, which is essential to lower lysosomal pH to physiological pH, the removal of lysosomal cation or the insertion of lysosomal anion is required. Accordingly, CLC7 is considered as the primary membrane potential dissipating protein which transports two chloride ions from the cytoplasm to the lysosome for every proton it transports from the lysosome to the cytoplasm [4]. The rate ($J_{Cl,\,HClC7}$) at which the ion transportations occur was empirically derived from a current-voltage experimental data [3] as a function of chemical (ΔpH, ΔCl) and electric potential gradients, (ΔΨ), as detailed in supplementary equations (6) and (7). This rate was multiplied by the total number of CLC7 molecules per lysosome (N_{ClC7}) in order to obtain the total amount of proton and chloride molecules transported across the lysosomal membrane through CLC7, as follows:

$$H_{CLC7} = N_{CLC7} \times J_{Cl,HCLC7}(\Delta pH, \Delta Cl, \Delta \Psi) \quad \text{(Supplementary Equation 6)}$$

$$Cl_{CLC7} = 2 \times N_{CLC7} \times J_{Cl,HCLC7}(\Delta pH, \Delta Cl, \Delta \Psi) \quad \text{(Supplementary Equation 7)}$$

Where ΔCl is the chloride gradient comprised of the luminal chloride (Cl_L) and the cytoplasmic chloride (Cl_C). Moreover, the coefficient 2 in supplementary equation (7) defines the 2:1 stoichiometric relationship between the chloride and proton ions transported by CLC7 across the lysosomal membrane.

Modeling proton efflux

In addition to CLC7, the passive diffusion of protons across the lysosomal membrane can also contribute to the dissipation of membrane potential in order to facilitate the proton pumping activity of V-ATPase. This passive proton leak is modeled by supplementary equation (8), which is derived from the Goldman-Hodgkin-Katz (GHK) ion flux equation that is commonly used to describe the passive diffusion of a given ion across a biological membrane, assuming a linear potential gradient across a lipid membrane [3].

$$H_{leak} = [S \times P_{H+} \times Y \times Z \times [10^{-pHL} - (10^{-pHC} \times e^{-Z \times Y})] / (1 - e^{-Z \times Y})] \times N_{av}$$

(Supplementary Equation 8)

Where S is the total lysosomal surface area in units of cm^2 used to obtain the total amount of proton which passively diffuses across the lysosomal membrane; P_{H+} is the lysosomal membrane proton permeability in units of cm/s; Z is the valence of the ion (i.e. +1 for proton); pH_L is the luminal pH used to calculate the total free lysosomal proton based on the logarithmic relationship of pH and free proton ($pH_L = -\log[H^+]$); pH_c is the cytoplasmic pH used to calculate the total free cytoplasmic proton based on the logarithmic relationship of pH and free proton ($pH_C = -\log[H^+]$); N_{av} is Avogadro's number used to convert the amount of transported protons in unit of moles to unit of molecules; Y is used to convert proton transportation in unit of charge per second to moles per second and is defined as: $Y = (\Delta \Psi \times F) / (R \times T)$, where R is universal gas constant, F is Faraday's constant, and T is absolute temperature. Moreover, for cells at room temperature (25 °C), RT/F equals 25.69 mV, and is used for normalizing the lysosomal membrane potential communicated in this report.

Modeling the effect of membrane leaflet potentials on ions

In order to account for the effects of intrinsic external ($\Psi_{i,out}$) and internal ($\Psi_{i,in}$) leaflet potentials of the lysosomal membrane on cytoplasmic and lysosomal ion *i* concentrations, respectively, the individual cytoplasmic and lysosomal ion concentrations are computed using the following relationships, supplementary equations (9 and 10), derived from the GHK equation for a single ion concentration gradient, by setting net current flow equal to zero.

$$\Delta \Psi_{i,in} = (-Z \times R \times T) / F \text{ x } \ln (C_{i,in} / C_{i,L})$$ (Supplementary Equation 9)

$$\Delta \Psi_{i,out} = (-Z \times R \times T) / F \text{ x } \ln (C_{i,out} / C_{i,C})$$ (Supplementary Equation 10)

Where $C_{i,in}$ is the internal concentration of a given ion (i) at the membrane surface facing the lysosomal compartment, $C_{i,L}$ is the concentration of the ion (i) inside the lysosome, $C_{i,out}$ is the external concentration of the ion (i) at the membrane surface facing the cytoplasmic compartment, $C_{i,C}$ is the concentration of the ion (i) inside the cytoplasm. All units are molar.

Governing equations

Supplementary equations (3-10) were used in supplementary equations (11-13) to further define the ion movements as a function of time, in units of molecules per second.

$$dH^+/dt = H_{pump} - H_{CLC7} - H_{leak} - H_{sequestered} \quad \text{(Supplementary Equation 11)}$$

$$dCl^-/dt = 2 \times N_{CLC7} \times J_{Cl,HCLC7}(\Delta pH, \Delta Cl, \Delta \Psi) - Cl_{sequestered} \quad \text{(Supplementary Equation 12)}$$

Moreover, extending supplementary equation (11), we can denote the change in lysosomal pH with respect to time by following the relationship between the lysosomal lumen buffering capacity (β) of the Donnan particles, which sequester non-free lysosomal protons, and free lysosomal protons which give rise to lysosomal pH as follows:

$$dpH/dt = (-H_{pump} + H_{CLC7} + H_{leak} + H_{sequestered}) / (V \times N_{av} \times \beta) \quad \text{(Supplementary Equation 13)}$$

Where V is the lysosomal volume and is multiplied by N_{av} to convert the unit of molecules per second to molar per second, where the inverse of β is in units of pH units per molar.

Numerical analysis

Supplementary equations (11-13) were solved by numerical integration in Berkeley Madonna® using Rosenbrock stiff solver as a numerical integrator.

Data visualization

Multiple individual 2D datasets associated with the parametric simulations performed to generate simultaneous inhibitions of various lysosomal parameters were obtained. The datasets associated with each simultaneous inhibitions of lysosomal parameters were exported from

Berkeley Madonna and compiled into three separate matrices in a MS-Excel spreadsheet, such that the first rows and columns of the matrix correspond to the two parameters simultaneously varied in the model simulations to obtain the final lysosomal readout values (lysosomal pH, Cl^-, and membrane potential), where each makes up the rest of the rows and columns of a single matrix.

B.2 Figures and Tables

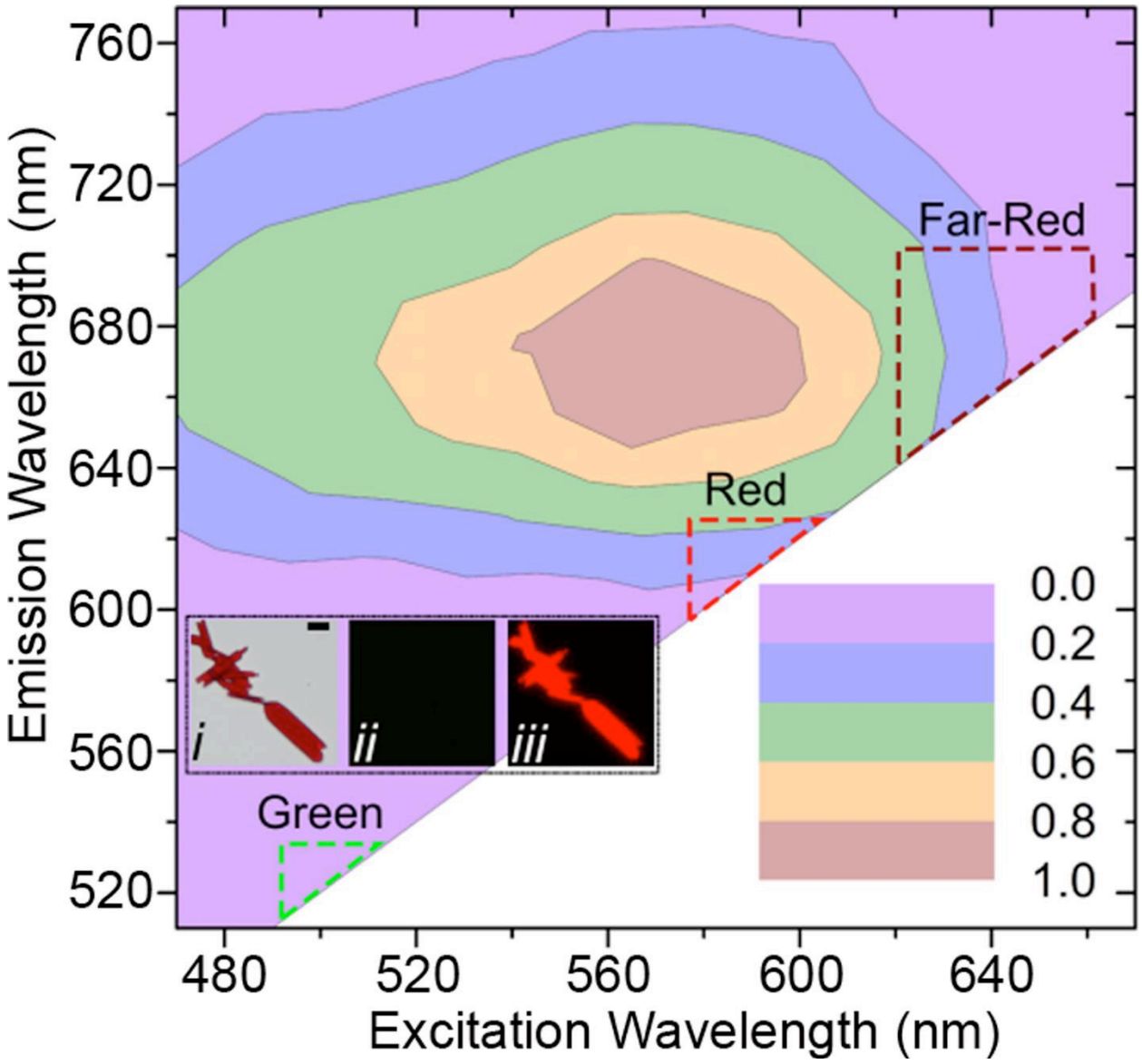

Figure S3-1. Fluorescence Microspectroscopy and (inset, *i* = brightfield, *ii* = green fluorescence, *iii* = far-red fluorescence) Epifluorescence Microscopy of CFZ-H^+Cl^- crystals indicating the lack of green fluorescence while being fluorescent in the far-red fluorescence range. The excitation wavelength (nm, Ex) and emission wavelength (nm, Em) are shown on the X-axis and Y-axis, respectively. The normalized fluorescence yield is shown by a contour plot that was normalized using a control slide first and then to the maximum measured fluorescence yield. The colors as shown represent contour levels from 0-1 in steps of 0.2. The green, red, and far-red fluorescence bandwidths are overlaid on top of the normalized fluorescence spectra.

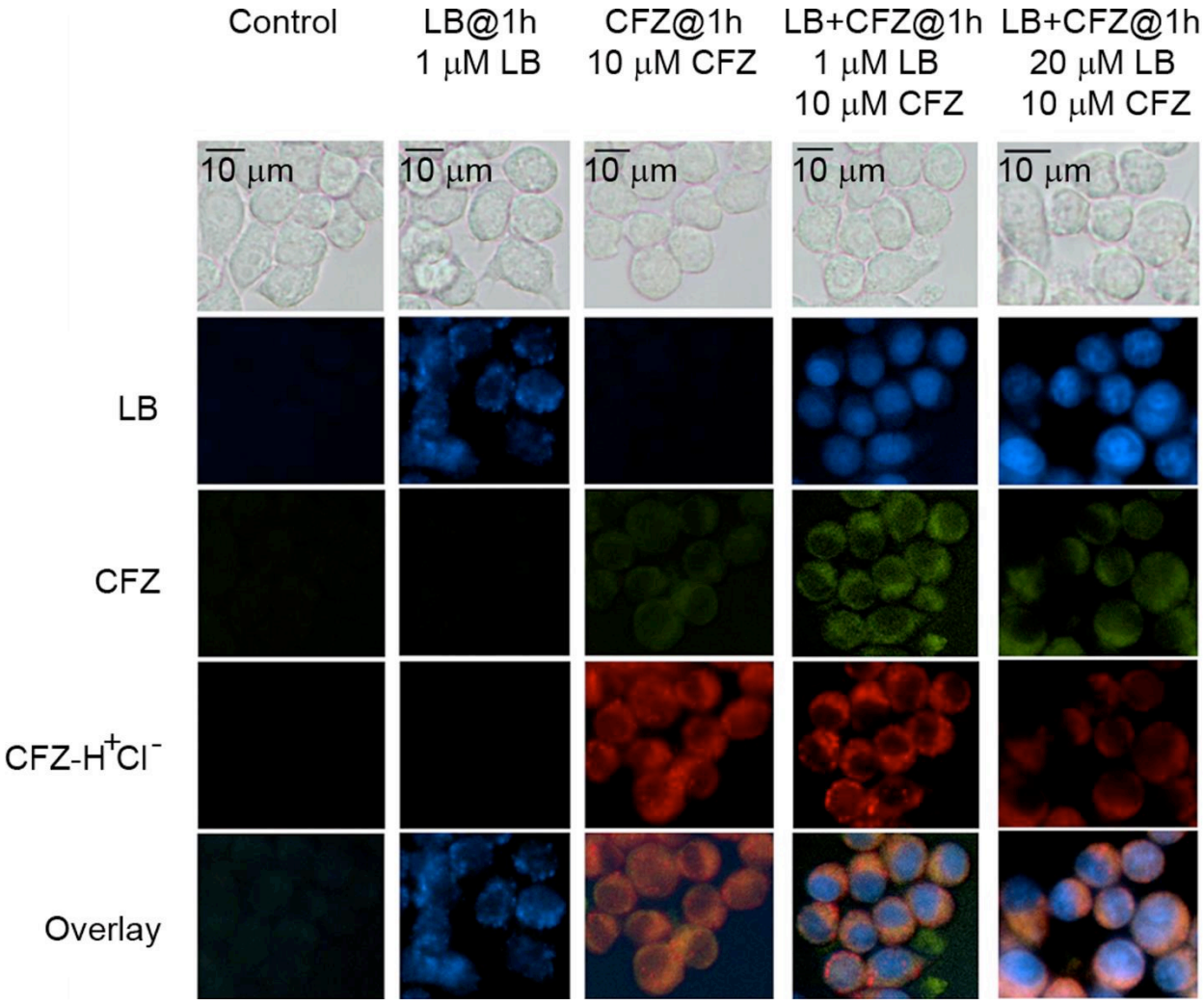

Figure S3-2. Epifluorescence microscopy of RAW264.7 cells when incubated with CFZ (10 μM), Lysotracker® Blue (LB, 1 and 20 μM) at *t* = 1 hour. Scale bar, 10 μm. At 1 hour, green fluorescence spots indicative of CFZ are visible as mild diffuse staining rather than punctate staining observed at *t* = 24 hours. Vesicular staining pattern of LB, visible as blue punctate spots when incubated on its own, are absent when co-incubated with CFZ at both LB = 1 and 20 μM. The control images were taken at *t* = 24 hours post initiation of experiments.

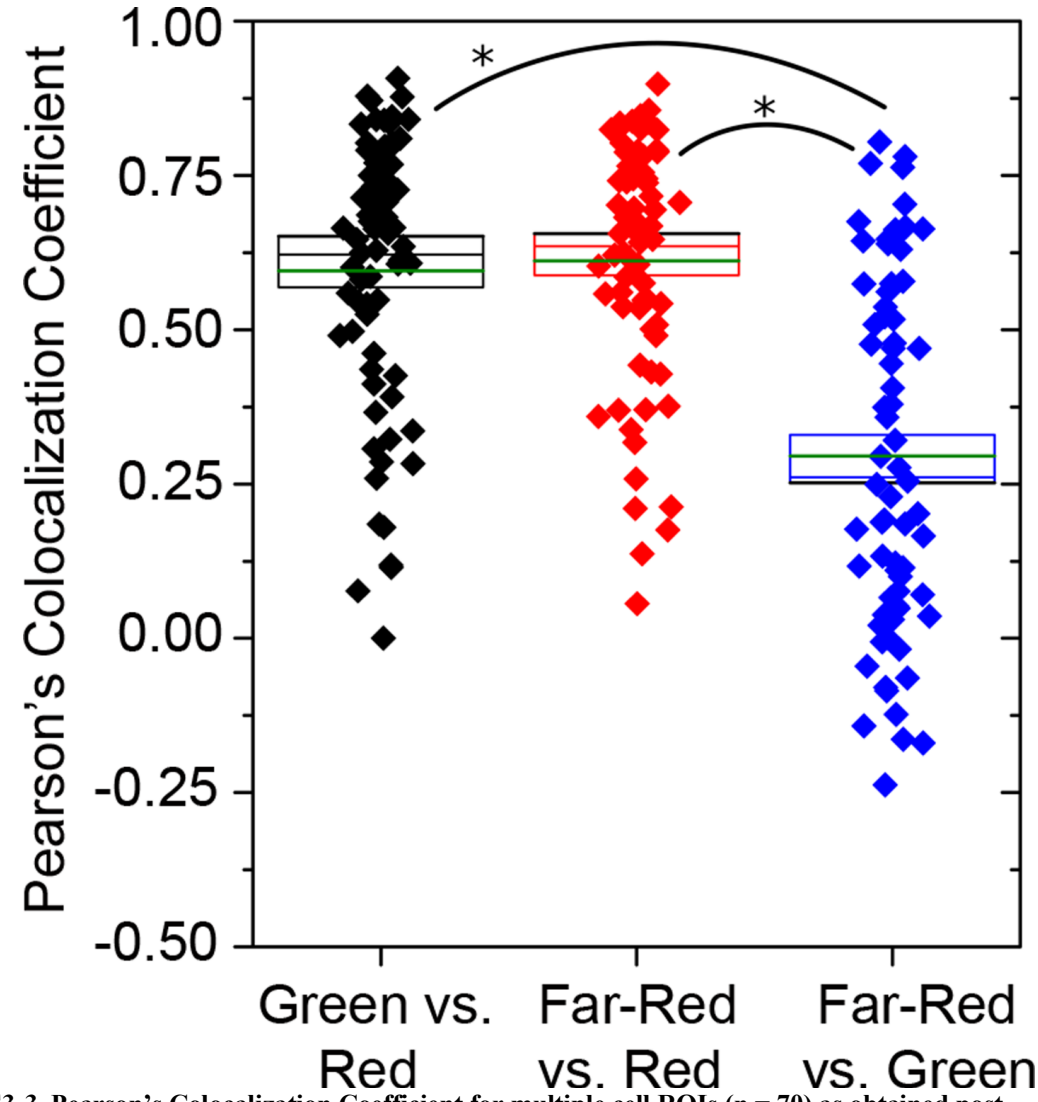

Figure S3-3. Pearson's Colocalization Coefficient for multiple cell ROIs (n = 70) as obtained post epifluorescence microscopy of RAW264.7 cells incubated with CFZ (10 µM) at *t* = 24-72 hours. Fluorescence channel description is provided in Supplementary Table S3-2. The scatter distribution is further annotated with four horizontal lines denoting the Mean ± S.E. (same color lines as the distribution), Mean (green line) and the Median (black line) of the distribution. * -$p < 0.005$.

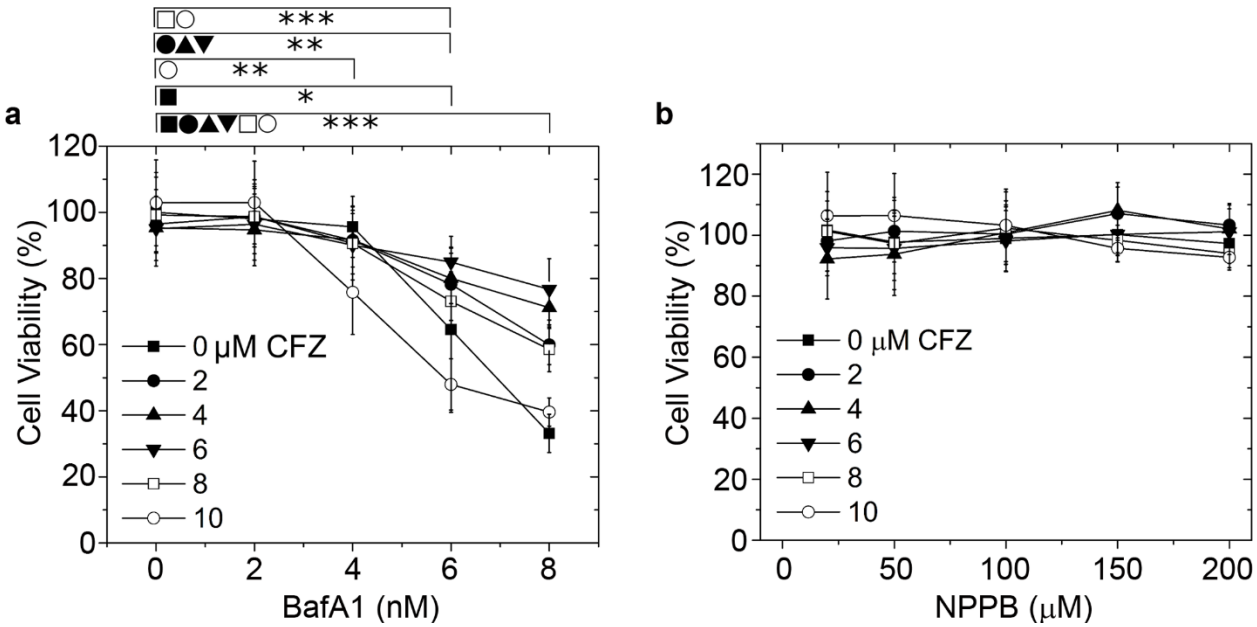

Figure S3-4. Viability of RAW264.7 cells treated with a) BafA1 and b) NPPB in the presence of CFZ (0-10 μM). Data was collected at n = 6 with * - $p < 0.05$, ** - $p < 0.01$, *** - $p < 0.001$. Each point is compared in a pair-wise independent Student *t*-test.

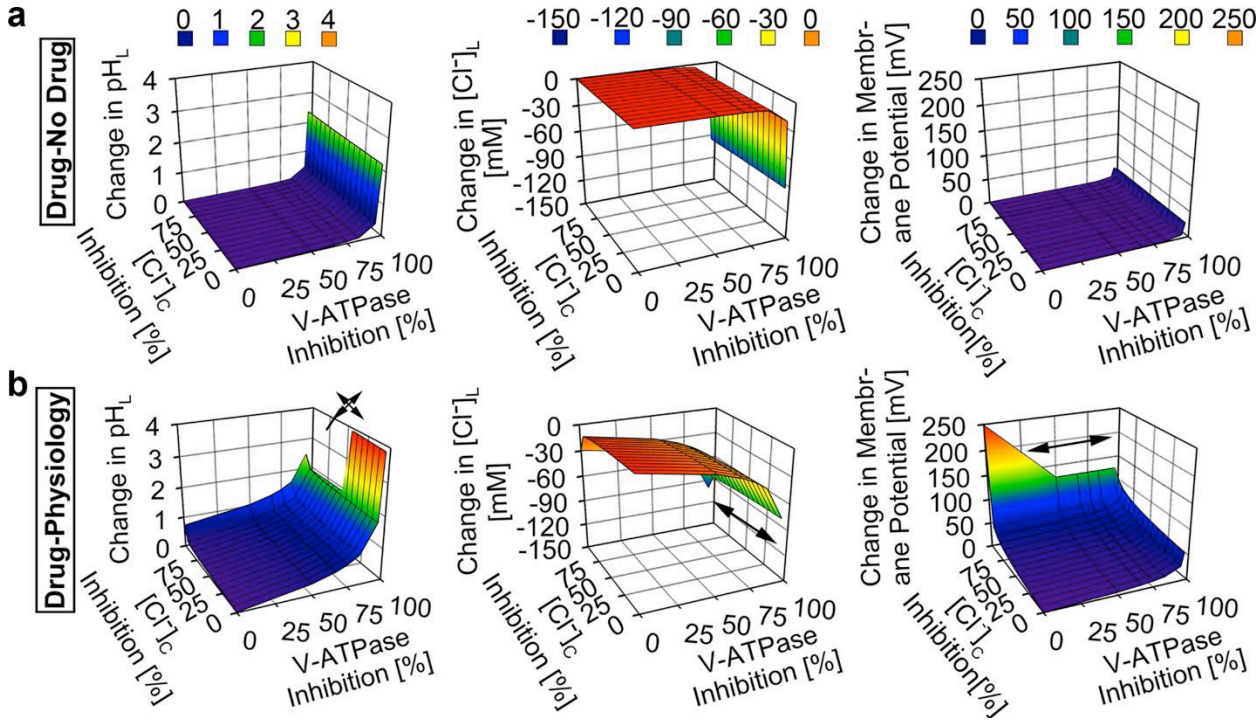

Figure S3-5. **Model and simulation of the effects of V-ATPase and cytoplasmic chloride on the lysosomal accumulation of CFZ-H$^+$Cl$^-$. a**) V-ATPase inhibition showed a more substantial effect than cytoplasmic chloride inhibition on the accumulation of CFZ-H$^+$Cl$^-$ at the rate of 0.01 picomol/cell/day, as reflected by the changes in the lysosomal pH, Cl$^-$, and membrane potential values of the CFZ-H$^+$Cl$^-$ containing lysosome from that of the CFZ-H$^+$Cl$^-$ free lysosome. **b**) V-ATPase inhibition generally showed a more substantial effect than cytoplasmic chloride inhibition although the simultaneous inhibition of both parameters showed even more pronounced effect on the physiological accumulation of CFZ-H$^+$Cl$^-$ at the rate of 0.01 picomol/cell/day, as reflected by the changes in the lysosomal pH, Cl$^-$, and membrane potential values of the CFZ-H$^+$Cl$^-$ containing lysosome from respective baseline physiological values. Arrow signs represent values outside of the axes plot range.

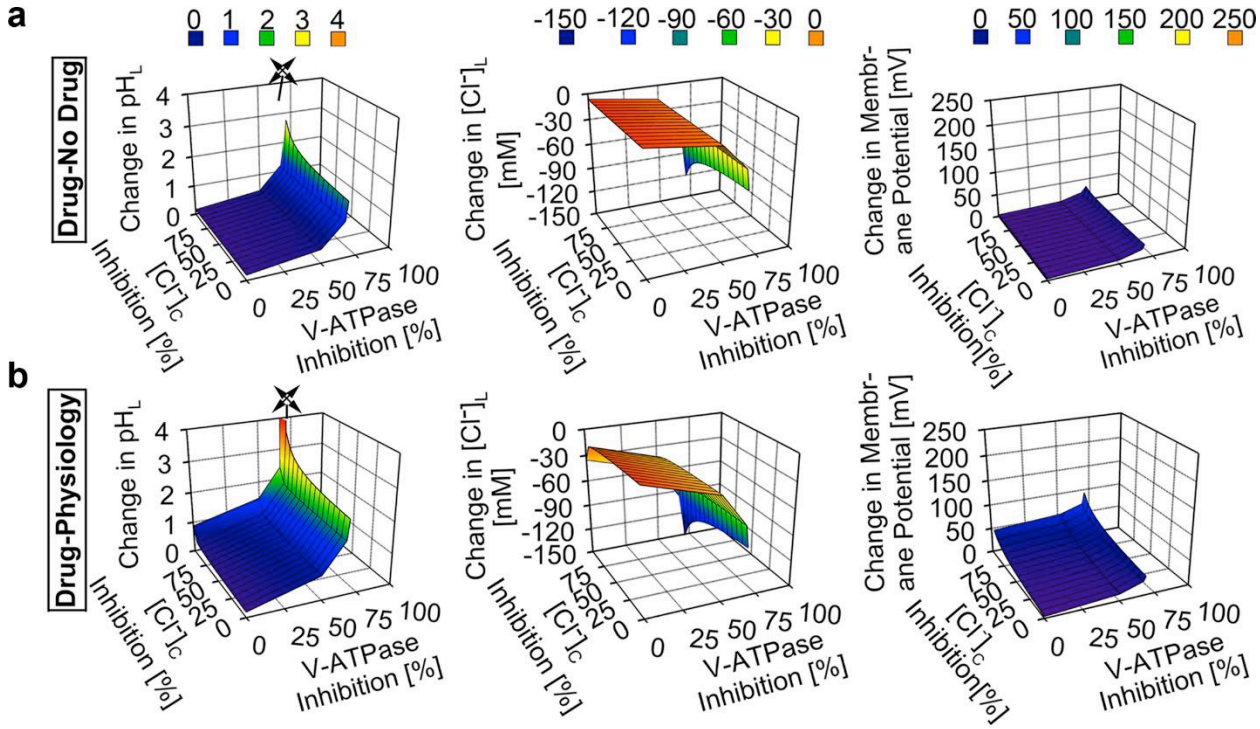

Figure S3-6. Model and simulation of the effects of V-ATPase and cytoplasmic chloride on the lysosomal accumulation of CFZ-H$^+$Cl$^-$ at a higher dose. a) V-ATPase inhibition showed a more substantial effect than cytoplasmic chloride inhibition on the accumulation of CFZ-H$^+$Cl$^-$ at the rate of 0.1 picomol/cell/day, as reflected by the changes in the lysosomal pH, Cl$^-$, and membrane potential values of the CFZ-H$^+$Cl$^-$ containing lysosome from that of the CFZ-H$^+$Cl$^-$ free lysosome. **b**) V-ATPase inhibition generally showed a more substantial effect than cytoplasmic chloride inhibition although the simultaneous inhibition of both parameters showed even more pronounced effect on the physiological accumulation of CFZ-H$^+$Cl$^-$ at the rate of 0.1 picomol/cell/day, as reflected by the changes in the lysosomal pH, Cl$^-$, and membrane potential values of the CFZ-H$^+$Cl$^-$ containing lysosome from respective baseline physiological values. Arrow signs represent values outside of the axes plot range.

Table S3-1. Model parameters.

Symbol	Description	Baseline Input Value	Range of Input Value	Units
pH_C	Cytosolic pH	7.2	Fixed	pH Unit
pH_L	Luminal pH	7.4	Fixed	pH Unit
$[Cl^-]_C$	Cytosolic chloride concentration	10	1×10^{-5} - 10	mM
$[Cl^-]_L$	Luminal chloride concentration	110	Fixed	mM
$[Na^+]_L$	Luminal sodium concentration	145	Fixed	mM
$[K^+]_L$	Luminal potassium concentration	5	Fixed	mM
$[H^+]_L$	Luminal proton concentration	0	Fixed	mM
P_{H+}	Membrane proton permeability	6×10^{-5}	Fixed	cm/s
V	Lysosomal volume	1.65×10^{-16}	Fixed	L
S	Lysosomal surface area	1.45×10^{-8}	Fixed	cm^2
C'	Specific bilayer capacitance	1	Fixed	$\mu Farad/cm^2$
B	Buffering capacity	40	Fixed	mM/pH unit
N_{VATP}	V-ATPase number	300	1×10^{-4} - 300	
N_{CLC7}	CLC7 number	5000	1×10^{-4} - 5000	
Ψ_{out}	Outer surface potential	-50[b]	Fixed	mV
Ψ_{in}	Inner surface potential	0[b]	Fixed	mV
CLC_Cl	CLC7 Cl^- stoichiometry	2	Fixed	
CLC_H	CLC7 H^+ stoichiometry	1	Fixed	
R	Gas constant	8.314	Fixed	$J.K^{-1}.mol^{-1}$
T	Absolute temperature	0	Fixed	Kelvin
F	Faraday's constant	96485	Fixed	J/Volt
N_{av}	Avogardro's number	6.02×10^{23}	Fixed	molecules/mol
a	Rate of proton and chloride sequestration by CFZ to form CFZ-H^+Cl^-	0	1.16×10^{-21} - 1.16×10^{-20}	Moles/day

a = Baseline input values are literature values [5-8] representing physiological lysosomes and are in agreement with previously published model [1, 3].
b = Estimated intrinsic surface potentials for inner (Ψ_{in}) and outer (Ψ_{out}) leaflets of the lysosomal membrane accounted for when modeling membrane transporter mediated dynamic lysosomal and cytoplasmic ion concentrations at the membrane surface [1].

Table S3-2. Fluorescence in RAW264.7 cells. (Channels (Ex/Em)) – Blue (350/405 nm), Green (490/510 nm), Red (590/610 nm), and Far-Red (640/670 nm).

	Blue	Green	Red	Far-Red
CFZ	-	+	+	-
CFZ-H^+Cl^-	-	-	+	+
Lysotracker® Blue	+	-	-	-

B.3 References

1. Grabe, M. and G. Oster, *Regulation of organelle acidity.* J Gen Physiol, 2001. **117**(4): p. 329-44.

2. Grabe, M., H. Wang, and G. Oster, *The mechanochemistry of V-ATPase proton pumps.* Biophys J, 2000. **78**(6): p. 2798-813.

3. Ishida, Y., et al., *A model of lysosomal pH regulation.* J Gen Physiol, 2013. **141**(6): p. 705-20.

4. Graves, A.R., et al., *The Cl-/H+ antiporter ClC-7 is the primary chloride permeation pathway in lysosomes.* Nature, 2008. **453**(7196): p. 788-92.

5. Van Dyke, R.W., *Acidification of rat liver lysosomes: quantitation and comparison with endosomes.* Am J Physiol, 1993. **265**(4 Pt 1): p. C901-17.

6. Gambale, F., et al., *The Voltage-Dependent H+-Atpase of the Sugar-Beet Vacuole Is Reversible.* European Biophysics Journal with Biophysics Letters, 1994. **22**(6): p. 399-403.

7. Heuser, J., Q.L. Zhu, and M. Clarke, *Proton Pumps Populate the Contractile Vacuoles of Dictyostelium Amebas.* Journal of Cell Biology, 1993. **121**(6): p. 1311-1327.

8. Sonawane, N.D., J.R. Thiagarajah, and A.S. Verkman, *Chloride concentration in endosomes measured using a ratioable fluorescent Cl- indicator - Evidence for chloride accumulation during acidification.* Journal of Biological Chemistry, 2002. **277**(7): p. 5506-5513.

Appendix C

Supporting Information in Chapter 4

C.1 Supplemental Materials and Methods

Theoretical calculations of the concentration of neutral and protonated (charged) species of a weakly basic drug molecule in different subcellular compartments

The total drug concentration output obtained after running the Virtual Cell model is comprised of the concentration of the neutral and ionized forms of the drug:

$$C_T = [B] + [BH^+] \quad (1)$$

Where C_T is the total drug concentration, [B] is the concentration of the neutral drug, and $[BH^+]$ is the concentration of the ionized drug.

Thus, using equation (1) and the Henderson-Hasselbalch equation (equation 2), we calculated the concentrations of the neutral and ionized forms of the weak base drug from the total drug concentration in the extracellular, cytoplasm, mitochondria, and lysosome:

$$pH - pK_a = \log\frac{[B]}{[BH^+]} \quad (2)$$

Determining the degree of supersaturation of the neutral and protonated drug species in the different subcellular compartments

Drug concentration above thermodynamic drug solubility leads to supersaturation(3). Thus, using experimentally determined thermodynamic solubility value of the free base and protonated species of drug in aqueous media and octanol, we estimated the degree of supersaturation –DS(n)- of the free base as follows(3):

$$\mathrm{DS(n)} = \frac{[\mathrm{B}]}{[\mathrm{B}]_s} \quad (3)$$

Where [B] is the steady state, free base drug concentration in aqueous compartment, and $[B]_s$ is the experimentally measured thermodynamic solubility of the free base drug in water. Similarly, we estimated the degree of supersaturation (DS+) of the charged protonated species in aqueous media as follows:

$$\mathrm{DS(+)} = \frac{[\mathrm{BH^+}]\times[\mathrm{Cl^-}]}{K_{\mathrm{sp}}} \quad (4)$$

Where K_{sp} is the solubility product of the salt form of the drug, $[BH^+]$ is the dissolved concentration of the ionized drug, and $[Cl^-]$ is the chloride concertation that interacts with the ionized drug through ion-ion interaction, producing the salt solubility product of the drug. Using pH_{max} and the intrinsic free base solubility of CFZ obtained from the literature(4), the K_{sp} was calculated assuming the counterion forms a 1:1 complex with the drug, using the following relationship:

$$K_{\mathrm{sp}} = \left(\frac{[\mathrm{B}]_s}{10^{\mathrm{pH_{max}-pK_a}}}\right)^2 \quad (5)$$

Biochemical Analysis of Drug Concentrations in Plasma

Mobile phase A was 5 mM ammonium acetate, adjusted to pH 9.9 with ammonium hydroxide, and mobile phase B was acetonitrile. The flow rate was 0.35 ml/min, with a linear gradient from 50 to 100% phase B over 1.5 min, followed by holding at 100% for 1.5 min, a return to 50% phase B, and then re-equilibration for 2.5 min. The mass spectrometer source conditions were set as follows: 325°C, gas flow at 10 liters/min, nebulizer at 40 lb/in2, capillary at 4,000 V, and positive ion mode. The MS acquisition parameters were as follows: MRM mode, transition 1 set at 473.1 to 1:431.1, a dwell time of 400 ms, fragmentor set at 180, a collision

energy of 40; transition 2 set at 473.1 to 429.1, a dwell time of 100 ms, fragmentor set at 180, and a collision energy of 40.

C.2 Supplemental Table

Table S4-1: Cellular drug accumulation parameters for the Virtual Cell model (*awillmer: Macrophage Cargo Capacity*)

Symbol	Description	Value	Units
init $C_{T,E}$	Initial total extracellular drug concentration	10	μM
init $C_{T,C}$	Initial total cytoplasmic drug concentration	0	μM
init $C_{T,M}$	Initial total mitochondrial drug concentration	0	μM
init $C_{T,L}$	Initial total lysosomal drug concentration	0	μM
init $C_{T,CM}$	Initial total cell membrane drug concentration	0	μM
init $C_{T,MM}$	Initial total mitochondrial membrane drug concentration	0	μM
init $C_{T,LM}$	Initial total lysosomal membrane drug concentration	0	μM
$[Cl^-]_L$	Lysosomal chloride concentration	110	mM
pH_E	Extracellular pH	7.4	
pH_C	Cytoplasmic pH	7.2	
pH_M	Mitochondrial pH	8	
pH_L	Lysosomal pH	4.5	
L_E	Extracellular lipid fraction	0	
L_C	Cytoplasmic lipid fraction	0.05	
L_M	Mitochondrial lipid fraction	0.05	
L_L	Lysosomal lipid fraction	0.05	
W_E	Extracellular water fraction	1	
W_C	Cytoplasmic water fraction	0.95	
W_M	Mitochondrial water fraction	0.95	
W_L	Lysosomal water fraction	0.95	
γ_n*	Activity coefficient of unionized drug	1	
γ_d*	Activity coefficient of ionized drug	0.74	
Ψ_{CM}	Cell membrane potential	-70	mV
Ψ_{MM}	Mitochondrial membrane potential	-160	mV
Ψ_{LM}	Lysosomal membrane potential	10	mV
V_E	Extracellular volume	$1x10^{-4}$	L
D_C	Cytoplasmic diameter	12.4	μm
D_M	Mitochondrial diameter	5.76	μm
D_L	Lysosomal diameter	5.76	μm

* activity coefficients of unionized and ionized molecules were obtained from the literature(1). The physicochemical properties were obtained from experimental data fitting (2) for CFZ free base and CFZ-HCl salt. The diameters of the cellular compartments were used to calculate volume and surface area, assuming spherical geometry.

C.3 References

1. Zhang X, Shedden K, Rosania GR. A cell-based molecular transport simulator for pharmacokinetic prediction and cheminformatic exploration. Mol Pharm. 2006;3(6):704-716.

2. Woldemichael T, Keswani RK, Rzeczycki PM, Murashov MD, LaLone V, Gregorka B, Swanson JA, Stringer KA, Rosania GR. Reverse Engineering the Intracellular Self-Assembly of a Functional Mechanopharmaceutical Device. Scientific reports. 2018;8(1):2934.

3. Hens B, Brouwers J, Corsetti M, Augustijns P. Supersaturation and Precipitation of Posaconazole Upon Entry in the Upper Small Intestine in Humans. J Pharm Sci. 2016;105(9):2677-2684.

4. Bergstrom CA, Luthman K, Artursson P. Accuracy of calculated pH-dependent aqueous drug solubility. Eur J Pharm Sci. 2004;22(5):387-398.